University of Arkansas, Fayetteville
ScholarWorks@UARK

Theses and Dissertations

5-2011

An Analysis of the Stability and Transport of CO_2 on Mars and Iapetus: Increasing Accuracy via Experiments and Photometry

David Garrison Blackburn
University of Arkansas

Follow this and additional works at: http://scholarworks.uark.edu/etd

Recommended Citation
Blackburn, David Garrison, "An Analysis of the Stability and Transport of CO_2 on Mars and Iapetus: Increasing Accuracy via Experiments and Photometry" (2011). *Theses and Dissertations*. 204.
http://scholarworks.uark.edu/etd/204

This Dissertation is brought to you for free and open access by ScholarWorks@UARK. It has been accepted for inclusion in Theses and Dissertations by an authorized administrator of ScholarWorks@UARK. For more information, please contact scholar@uark.edu, ccmiddle@uark.edu.

AN ANALYSIS OF THE STABILITY AND TRANSPORT OF CO_2 ON MARS AND IAPETUS: INCREASING ACCURACY VIA EXPERIMENTS AND PHOTOMETRY

AN ANALYSIS OF THE STABILITY AND TRANSPORT OF CO_2 ON MARS AND IAPETUS: INCREASING ACCURACY VIA EXPERIMENTS AND PHOTOMETRY

A dissertation submitted in partial fulfillment
of the requirements for the degree of
Doctor of Philosophy in Space and Planetary Sciences

By

David Garrison Blackburn
Arkansas Tech University
Bachelor of Science in Computer Science, 2007

May 2011
University of Arkansas

ABSTRACT

Volatile transport of carbon dioxide is most relevant on two planetary bodies in our solar system: Mars and Iapetus. We experimentally measured the sublimation rate of CO_2 ice under simulated martian conditions and developed a model based on our experimental results. We experimentally verified that solar irradiance is the primary control for the sublimation of CO_2 ice on the martian poles with the amount of radiation striking the surface being controlled by variations in the optical depth, ensuring the formation and sublimation of the seasonal cap. Our model, supported by comparison of MGS-MOC and MRO-HiRISE images, shows that ~ 0.4 m is currently being lost from the south perennial cap per martian year. In order to build a similar model for Iapetus, one key parameter was needed: the bolometric Bond albedo. We used photometry of *Cassini* VIMS observations of Iapetus to produce the first phase integrals calculated directly from solar phase curves of Iapetus for the leading hemisphere and to estimate the phase integrals for the trailing hemisphere. Our phase integrals, which are lower than previous results, have profound implications for the analyses of the energy balance and volatile transport on this icy satellite. We also utilized *Cassini* VIMS and ISS and *Voyager* ISS observations of Iapetus to produce the first bolometric Bond albedo map of Iapetus; the average albedo values for the leading and trailing hemispheres are 0.25 ± 0.03 and 0.05 ± 0.01 respectively. On Iapetus, which has no detectable atmosphere, any carbon dioxide sublimating from the dark material, where it was discovered by reflectance spectroscopy, would either escape the body or migrate on ballistic trajectories to a possible polar cold trap. However, through proof by contradiction, we show that if dry ice is the source of the detected signal in the dark material, it produces an impossible

scenario where an extensive polar cap is produced along with incorrect temperatures for the dark material at equatorial latitudes. After ruling out surface dry ice as the source, we set upper limits on the amount of CO_2 transport that can occur on Iapetus without forming a polar cap.

This dissertation is approved for
Recommendation to the
Graduate Council

Dissertation Director:

_____
Dr. Larry Roe

Dissertation Committee:

_____
Dr. Richard Ulrich

_____
Dr. John Dixon

_____
Dr. Jason Tullis

_____
Dr. Julia Kennefick

_____
Dr. Bonnie J. Buratti (*ex officio*)

DISSERTATION DUPLICATION RELEASE

I hereby authorize the University of Arkansas Libraries to duplicate this dissertation when needed for research and/or scholarship.

Agreed _____
David Garrison Blackburn

Refused _____
David Garrison Blackburn

ACKNOWLEDGEMENTS

Portions of this research were carried out at the Jet Propulsion Laboratory, California Institute of Technology, and the University of Arkansas and sponsored by the National Aeronautics and Space Administration's Space Grant Program. I would also like to thank the University of Arkansas and the Arkansas Space Grant Consortium for financial support, as well as helpful conversation with Mike Hicks, Ken Lawrence, Karly Pitman, and Edgard Rivera-Valentin.

Special thanks to my advisor Dr. Richard Ulrich and my JPL mentor Bonnie J. Buratti for their excellent and avid support throughout my research.

Also, special thanks to Edgard Giovanni Rivera-Valentin, Richard Boardman Wright, Jr., and Maci Edwards for their tremendous friendship and encouragement during this process. I would also like to thank Betty Barnett, my high school physics teacher, who inspired me to pursue this career.

DEDICATION

This dissertation is dedicated to my loving parents:
James and Phyllis Blackburn

And my aunt who saved my life as a child:
Grace Lancaster

And my grandmother whose spirit still guides me:
Francis Blackburn

And my grandmother who gave up her own chance at college to help her family:
Novelene Garrison

TABLE OF CONTENTS

LIST OF FIGURES

LIST OF TABLES

LIST OF PAPERS

Blackburn, D.G., Bryson, K.L., Chevrier, V.F., Roe, L.A., White, K.F., 2010. Sublimation kinetics of CO2 ice on Mars. Planetary and Space Science, 58, 780-791.

Blackburn, D.G., Buratti, B. J., Ulrich, R., Mosher, J. A., 2010. Solar phase curves and phase integrals for the leading and trailing hemispheres of Iapetus from the *Cassini* Visual Infrared Mapping Spectrometer. Icarus, 209, 738-744.

Blackburn, D.G., Buratti, B.J., Ulrich, R., 2011. A bolometric Bond albedo map of Iapetus: Observations from *Cassini* VIMS and ISS and *Voyager* ISS. Icarus, 212, 329-338.

CHAPTER 1

INTRODUCTION

This chapter gives an introduction to carbon dioxide stability in the Solar System, the martian polar caps, Iapetus, planetary photometry, the science questions pertinent to this study, objectives of this dissertation, and an outline for the succeeding chapters.

1.1 Carbon Dioxide Stability in the Solar System

Carbon dioxide has been detected through remote sensing on most bodies in our solar system in gaseous form such as the immense atmosphere of Venus, in solid state such as the martian polar caps, in an unknown condition on the dark material of Iapetus and various other icy satellites of Saturn and Jupiter (Cruikshank *et al*., 2010), on the surfaces of Neptune's satellite Triton and Uranus's satellite Titania, in trace amounts in the atmospheres of the gas giants, and even on the surface of Pluto. On our own planet, it plays an important role in regulating our climate, providing the extra warmth through the greenhouse effect, and participating in metabolic pathways to facilitate the current life forms present on Earth. Yet, of all the present bodies, solid carbon dioxide is of interest currently on four bodies in particular because of its semi-stable status (Fig 1.11): Mars, Titania, Ganymede, and Iapetus. However, Ganymede does not remain cold enough for extended periods of time to allow for any substantial deposits of CO_2 frost to be relevant. Carbon dioxide has also been detected on various other minor satellites; however, the amount of carbon dioxide on these is not enough to merit attention in this study. Even though Titania would also be of interest here, it lacks sufficient resolution albedo maps to perform an in-depth study, and there is no possibility of producing them from the current mission data available. On Mars and Iapetus, conditions on the surface warrant carbon

dioxide to be a volatile that transports over the bodies allowing it the potential to shape their surfaces and be an active geological process. Thus, the role that carbon dioxide plays in shaping those bodies' surfaces is of prime interest to this study.

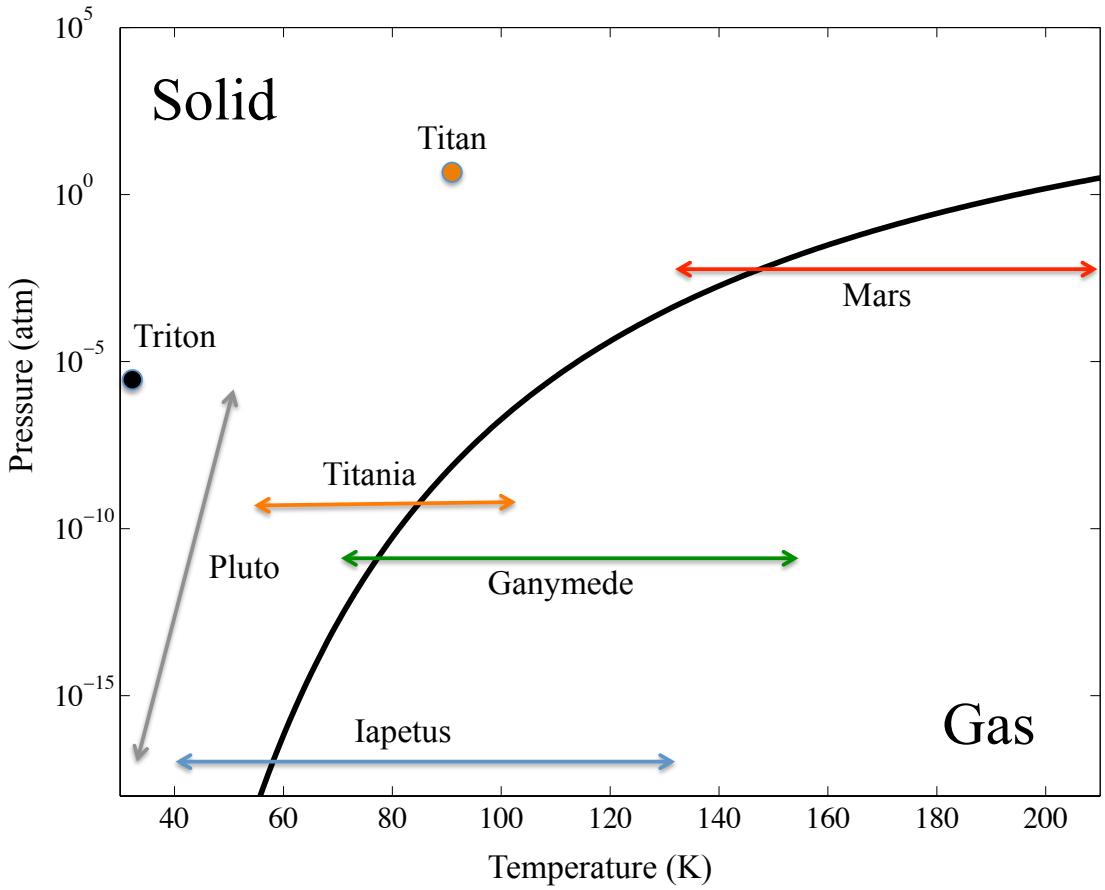

Figure 1.1 *Carbon dioxide phase diagram for conditions relevant to planetary bodies in our solar system in which CO_2 has been detected on their surfaces. For Pluto, Triton, and Titan, conditions always warrant dry ice (also potentially carbon dioxide clathrate). For Mars, Ganymede, Titania, and Iapetus, their surfaces all allow for dry ice on at least a temporary basis or concentrated in their polar regions but also have the ability for temperatures to rise where CO_2 becomes a gas. Even though Earth and Venus have substantial CO_2 inventories, their surface conditions only allow CO_2 to exist in a gaseous state and have temperature ranges much higher than what is expressed in this figure.*

1.2 Martian Polar Caps

Mars, the fourth planet in our Solar System, contains an atmosphere composed mostly of carbon dioxide at about seven millibars of total pressure. Although a telluric planet, Mars' total inventory of CO_2 detectable by remote sensing is reduced compared to the other inner planets. While most of the carbon dioxide in the atmosphere was probably lost due to solar wind stripping after loss of the martian magnetic field, there is still a mystery as to the degree of reduction (Malin *et al*., 2001; Byrne and Ingersoll, 2003). A large portion of the surface CO_2 is locked up in the martian polar ice caps, though mostly in the southern residual cap. The southern residual cap is mostly H_2O covered with a layer of carbon dioxide while the southern seasonal cap contains mostly CO_2 ice (Fig 1.2). In the north, the residual cap is water ice, and temperatures only decrease enough in winter to form a seasonal cap of CO_2 and water ice. Recently, some have concluded that the southern caps are currently receding (Malin *et al.* 2001; Thomas *et al*., 2009), which makes understanding the kinetics of this evaporation vital to understanding the seasonal long-term and stability of the martian polar caps. Specifically, previous thermal models have mostly relied on a purely heat-transfer limited approach in describing the kinetics of sublimation, which should be tested on an experimental level and is a secondary objective of this dissertation (see section 1.6). On Mars, carbon dioxide is in constant transport between the two polar caps via the martian atmosphere, as well as many other suggested sources and sinks like adsorption onto the surface (Blackburn *et al*. 2010). Thus understanding seasons on Mars and long-term stability of the polar caps are of key interest to this project and a primary objective.

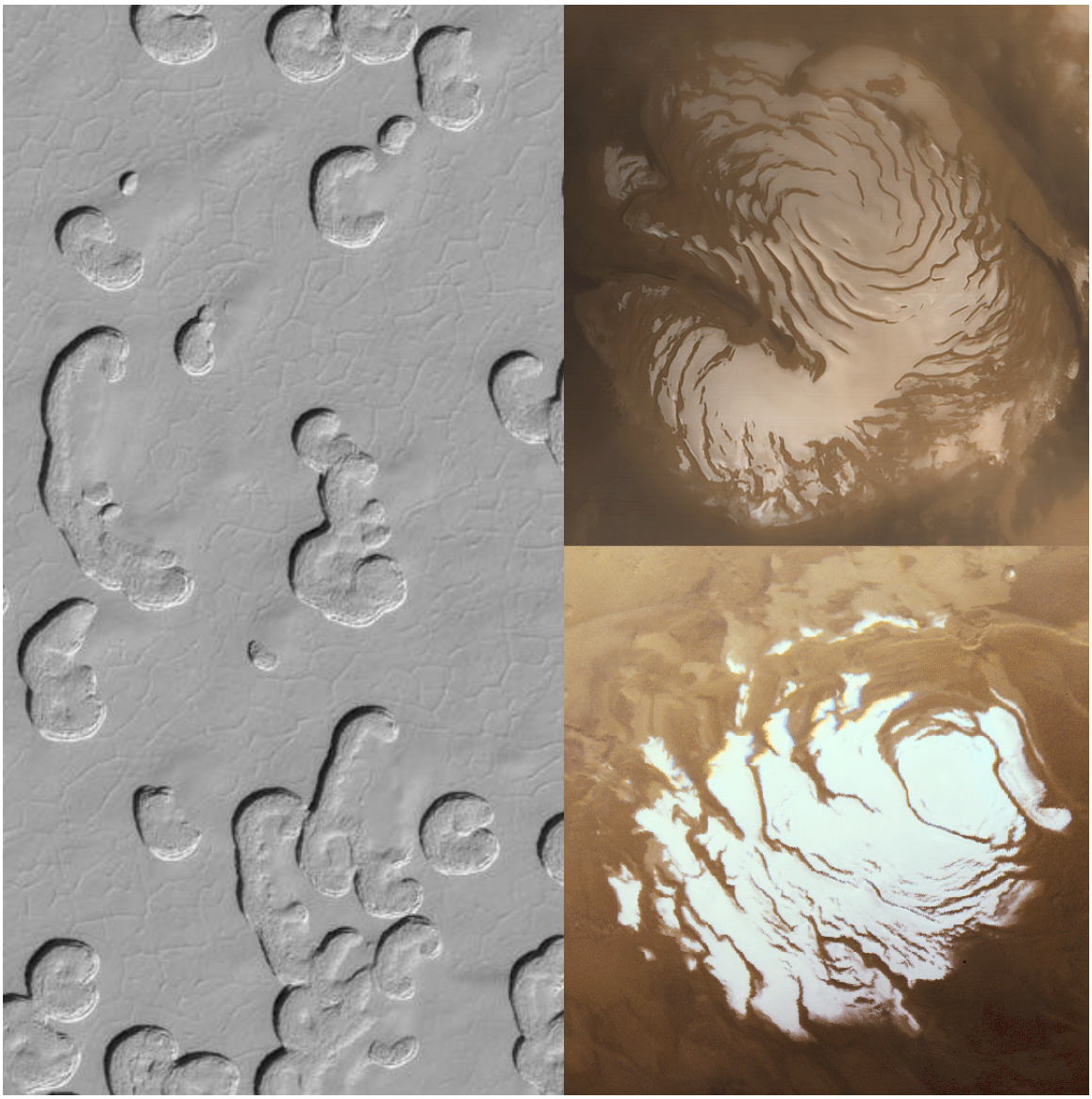

Figure 1.2 (Left) *Swiss cheese terrains in martian southern residual cap on November 3, 1999 (MGS MOC2-216).* ***(Top Right)*** *Martian northern polar cap on March 13, 1999. (MGS MOC2-231).* ***(Bottom Right)*** *Martian southern polar cap on April 17, 2000 (MGS MOC2-225; All images courtesy of NASA Planetary Data System).*

1.3 Iapetus

Giovanni Domenico Cassini discovered Saturn's moon Iapetus in 1671; at the time he recognized that one hemisphere was darker than the other and correctly deduced that it must have a different surface composition than the other hemisphere. The *Cassini* spacecraft revealed many mysteries about this satellite, including a sharp albedo transition and an equatorial ridge that runs around most of the satellite (Fig. 1.3). The albedo dichotomy has been explained to be either deposition of purely exogenic material (Verbiscer, 2009) or a result of thermal segregation triggered by an exogenic seeding of material (Mendis and Axford, 1974; Spencer and Denk, 2010). Yet, the greater mystery of the ridge is thought to be either: 1) the remnant of the oblate shape of the young Iapetus that rotated more rapidly than today (Kerr, 2006), 2) a result of icy material that welled up from beneath the surface and then solidified or 3) the leftover from a former ring that accreted onto the surface (Ip, 2006). This dissertation is primarily concerned, though, with one of the main compositional mysteries of Iapetus. In 2005, Buratti *et al.* discovered a carbon dioxide signature concentrated heavily in the dark material (Fig 1.3). On Iapetus, surface dry ice is not stable for long periods (Lebofsky, 1975), yet Palmer and Brown (2008) showed that with the help of gravity, carbon dioxide can remain in the local system long enough to allow for polar caps under the right conditions, especially during certain periods in Iapetus' history when the obliquity relative to the Sun's ecliptic is lowest. In order to investigate the potential for CO_2 transport accurately on Iapetus and the stability of polar caps, better approximations for bolometric Bond albedo for thermal models were needed. Therefore, this study also sought out to improve upon the current albedo of the surface by deriving from *Cassini* and *Voyager* results the phase integrals

and normal reflectance values required for the most accurate albedo map of Iapetus to date.

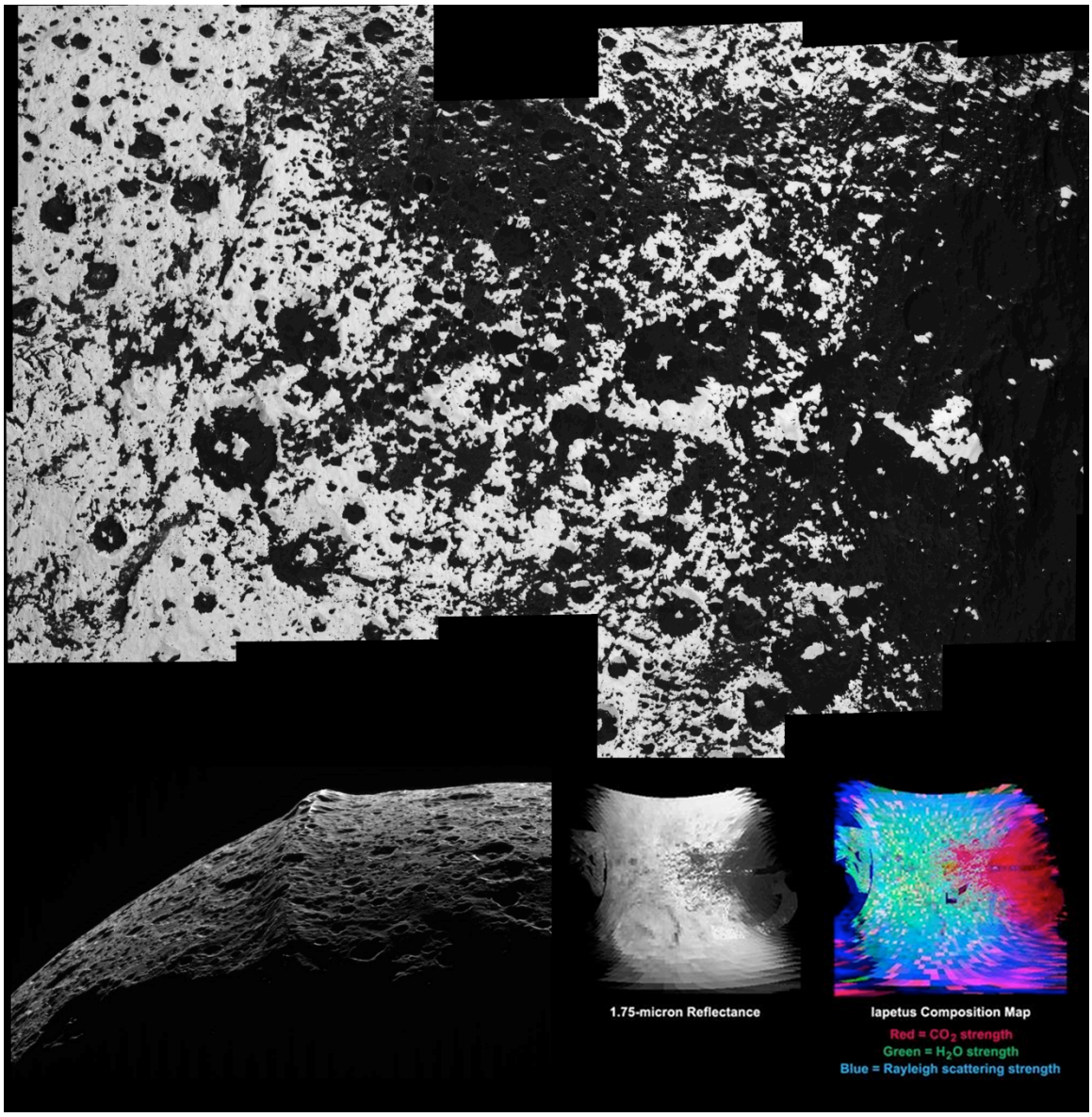

Figure 1.3 (Top) *Border region mosaic of Cassini ISS images highlighting the stark contrast between dark and light material.* ***(Bottom Left)*** *Cassini ISS image (1_W1568120778.121) of the equatorial ridge that is one of the most intriguing unsolved mysteries of the satellite* ***(Bottom Right)*** *Compositional mosaic map of Iapetus from Cassini VIMS showing that carbon dioxide is concentrated in the dark terrains (Courtesy: NASA).*

1.4 Planetary Satellite Photometry

Photometry is the study of the intensity of an astronomical object's electromagnetic radiation, and more specifically, planetary photometry focuses on radiation of the full disks and surfaces of bodies in the Solar System. Planetary photometry is also concerned with the scattering properties of the surface of a planetary body, as surfaces of planetary bodies scatter light in different ways, depending on the surface composition, structure, and macroscopic roughness. A Lambert surface, where the reflectance is diffuse, scatters an equal intensity of light in all directions, yet no surface is purely "Lambertian." Many saturnian satellites scatter light unevenly at some wavelengths (Buratti, 1984).

1.4.1 Solar Phase Curves

The solar phase angle is the angle between the Sun, the surface of the body being studied, and the observer (the spacecraft). At zero degrees phase angle, the body being observed is a full disk, which occurs for Earth's "full" moon about every 28 days. From the earth, only 0 to 6 degrees of solar phase angles are observable for the saturnian system. In order to derive the full solar phase curve for Iapetus, which extends up to 180 degrees and is the brightness versus phase angle, observations from an orbiting spacecraft are required. The *Cassini* tour provided an unprecedented opportunity to achieve a broad range of phase angles coupled with the ability to characterize the difference in the solar phase curve with wavelength via the Visual and Infrared Mapping Spectrometer (VIMS) instrument (0.34-5.12 μm). The normalized solar phase curve allows the calculation of a key value: the phase integral. The phase integral is a numerical representation of the directional scattering properties of light. Defined mathematically in equation 3.1 (p. 64),

it effectively represents the "beam pattern" of the object. For example, a "Lambertian" surface has a larger area under the normalized solar phase curve, resulting in a higher phase integral.

1.4.2 Albedo

Albedo, which is derived from the Latin word for whiteness and is also known as the reflection coefficient, is a dimensionless fractional value representing the reflecting power of a surface. Although there are several other forms, there are two types of albedo of interest here: geometric and Bond. The geometric albedo is a ratio of the actual brightness of a planetary body at zero degrees phase angle to that of an idealized flat, totally reflecting, "Lambertian" disk. The Bond albedo is the fraction of power on a planetary body that is scattered back out into space, taking into account the directional scattering properties of the surface, and is the product of the phase integral and the geometric albedo. For distant and small targets, knowledge of albedo can aid in identifying physical properties of the regolith (composition, size, shape, degree of compaction). In particular for airless bodies in the outer Solar System, one can infer how much and what type of ice is present on the surface from albedos. The spectral geometric albedo and the phase integral contribute to the bolometric Bond albedo, a quantity that is extremely important for determining the energy balance on planetary bodies, identifying the composition of geologic units, and finding volatile deposits. The bolometric Bond albedo (eq. 4.6, p. 96) is the Bond albedo across all wavelengths, taking into account the proper weighting of the intensity of the solar flux with wavelength.

1.5 Science Questions Pertinent to this Study

This dissertation seeks to answer or shed light on the following questions:

1) How stable are the martian polar caps? Are they in a state of growth or retraction?

2) Which model for sublimation most accurately describes the kinetics? On Mars? On Iapetus?

3) What are the phase integrals on Iapetus' surface? Do they change by wavelength? What is their relationship with the geometric albedo?

4) What is the bolometric Bond albedo of the surface of Iapetus?

5) Does Iapetus have a polar cap of CO_2?

6) In what form is the CO_2 on the dark material of Iapetus?

7) How does CO_2 transport on Mars and Iapetus differ?

1.6 Objectives of this Study

Therefore, in order to answer these questions, this dissertation has the following objectives:

1) Determine the limiting-rate factor for CO_2 kinetics on Mars experimentally.
2) Examine the short- and long-term stability of the martian polar caps.
3) Determine the phase integrals for Iapetus.
    a. Characterize the surface texture.
    b. Determine the relationship between geometric albedo and phase integral.
    c. Examine the wavelength dependence of the phase integral.
4) Build a bolometric Bond albedo map of Iapetus.
5) Limit the choices for the form of CO_2 present in the dark material.
6) Examine the stability of a dry ice polar cap on Iapetus.

While the albedo for the polar caps on Mars is well known from maps provided from Mars Global Surveyor and Mars Reconnaissance Orbiter, prior to this dissertation

albedo maps for Iapetus were insufficient to fully study CO_2 transport. In Chapters 3 and 4, we provide the description of how a full-scale bolometric Bond albedo map was produced as a tool to answer these questions for Iapetus.

1.7 Outline of Chapters

Chapter 2 explains the study of CO_2 sublimation kinetics on Mars and its results on the martian polar caps, which is published in the journal *Planetary and Space Science.* Chapter 3 details the results of the investigation of solar phase curves and phase integrals for Iapetus and is published in the journal *Icarus*. Chapter 4 shows the bolometric Bond albedo map for Iapetus and is also published separately in the journal *Icarus*. Chapter 5 details the study of the possible state of CO_2 present in the dark material and the stability of a potential polar cap on Iapetus; it is in manuscript format and ready for submission to the journal *Planetary Science*. Chapter 6 contains the summary and conclusions as well as future work.

1.8 References

Blackburn, D.G., Bryson, K.L., Chevrier, V.F., Roe, L.A., White, K.F., 2010. Sublimation kinetics of CO2 ice on Mars. Planetary and Space Science, 58, 780-791.

Buratti, B.J., 1984. Voyager disk resolved photometry of the saturnian satellites. Icarus 59, 392-405.

Buratti, B.J., and 28 co-authors, 2005. Cassini Visual and infrared mapping spectronomer observations of Iapetus: Detection of CO2. The Astrophysical Journal, 622, L149-L152.

Byrne, S., Ingersoll, A.P., 2003. A Sublimation Model for Martian South Polar Ice Features. Science. 299, 1051-1053.

Cruikshank, D.P. and 17 co-authors, 2010. Carbon dioxide on the satellites of Saturn: Results from Cassini VIMS investigation and revisions to the VIMS wavelength scale. Icarus, 206, 561-572.

Ip, W.-H, 2006. On a ring origin of the equatorial ridge of Iapetus. Geophysical Research Letters 33, L16203.

Kerr, R.A., 2006. How Saturn's icy moons get a (geologic) life. Science 311, 29.

Lebofsky, L.A., 1975. Stability of frosts in the solar system. Icarus, 25, 205-217.

Malin, M.C., Caplinger, M.A., Davis, S.D., 2001. Observational Evidence for an Active Surface Reservoir of Solid Carbon Dioxide on Mars. Science. 294, 2146-2148.

Mendis, D. A., Axford, W. I., 1974. Satellites and magnetospheres of the outer planets. Annu. Rev. of Earth & Planet. Sci. 2, 419-474.

Palmer, E.E. and Brown, R.H., 2008. The stability and transport of carbon dioxide on Iapetus. Icarus 195, 434-446.

Spencer, J.R. and Denk, T., 2010. Formation of Iapetus' extreme albedo dichotomy by exogenically triggered thermal ice migration. Science 327, 432-435.

Thomas, P.C., James, P.B, Calvin, W.M., Haberle, R, Malin, M.C., 2009. Residual south polar cap of Mars: Stratigraphy, history, and implications of recent changes. Icarus. 203, 352-375.

Verbiscer, A. J., M. Skrutskie, Hamilton D., 2009. Saturn's largest ring. Nature 461, 1098-1100.

.

CHAPTER 2

SUBLIMATION KINETICS OF CO_2 ICE ON MARS

In this chapter, we begin our study of CO_2 ice kinetics by investigating its sublimation from the surface of Mars with a three-pronged approach that includes experimental measurement in a planetary simulation chamber, modeling of the surface evaporation, and remote sensing measurements of CO_2-related geologic features on the surface of the planet. This chapter is published in the journal *Planetary and Space Science.* Dr. Larry Roe assisted with the theory behind heat transfer of evaporation in the chamber and on Mars, and Dr. Vincent Chevrier provided assistance with the theory of evaporation and other helpful conversation. Dr. Katie Bryson performed one-third of the experiments and all of the remote sensing measurements. Krista White participated in the project as her REU experience for the Space Center and performed another one-third of the experiments. I finished the remaining third of the experiments and redesigned the model to account for atmospheric opacity, thermal emission from the surface, and more accurate albedos; I also wrote the manuscript and finished the remainder of the project.

2.1 Abstract

Dynamic models of the martian polar caps are in abundance, but most rely on the assumption that the rate of sublimation of CO_2 ice can be calculated from heat transfer and lack experimental verification. We experimentally measured the sublimation rate of pure CO_2 ice under simulated martian conditions as a test of this assumption, developed a model based on our experimental results, and compared our model's predictions with observations from several martian missions (MRO, MGS, Viking). We show that sun irradiance is the primary control for the sublimation of CO_2 ice on the martian poles with

the amount of radiation penetrating the surface being controlled by variations in the optical depth, ensuring the formation and sublimation of the seasonal cap. Our model confirmed by comparison of MGS-MOC and MRO-HiRISE images, separated by 2-3 martian years, shows that ~0.4 m are currently being lost from the south perennial cap per martian year. At this rate, the ~2.4 meters-thick south CO_2 perennial cap will disappear in about 6-7 martian years, unless a short-scale climatic cycle alters this rate of retreat.

2.2 Introduction

The martian polar caps represent the most active geological features on the surface of Mars today. The polar caps are composed predominately of water ice at their base, covered by a seasonal cap of CO_2 and H_2O ice in the North and a perennial and seasonal CO_2 cap in the South (Bibring *et al.*, 2004; Langevin *et al.*, 2005). Early modeling of the polar caps suggested that they were in equilibrium with the ~6 mbar CO_2 atmosphere (Leighton and Murray, 1966), and various observations have shown a cyclicity of growth and retreat, following martian seasons (Smith *et al.*, 2001). Other studies show that CO_2 ice is only a thin veneer on the surface of a probably much thicker ice layer (Bibring *et al.*, 2004; Zuber *et al.*, 2007). This veneer is too small for the caps to be in equilibrium with the atmosphere (Byrne and Ingersoll, 2003; Malin *et al.*, 2001), suggesting that the polar caps are very young (Fishbaugh and Head III, 2001). Therefore, either larger unidentified CO_2 reservoirs in the martian subsurface are required, including possibly adsorbed CO_2 in the regolith (Fanale *et al.*, 1982; Fanale and Cannon, 1971), to buffer the much larger atmosphere or the total budget of CO_2 is present in the atmosphere. With the latter case, it requires that Mars today has much less CO_2 than other terrestrial planets.

Dynamic models of the polar caps on Mars are in abundance, and the majority are based on energy gain/loss to estimate the mass balance. A radiative energy balance as the primary modeling mechanism was first suggested by Leighton and Murray (1966). Forget *et al.* (1998) introduced the emissivity of the ice as an important component to the radiation balance, and Schmidt *et al.* (2009) demonstrated an albedo control on the cap recession.

The majority of dynamic models of the polar caps are based on CO_2 ice sublimation, lacking laboratory confirmation that heat transfer controls the rate of sublimation. Experimental verification of this process under simulated martian conditions is of interest, as it has been shown previously (Ingersoll, 1970; Moore and Sears, 2006; Sears and Chittenden, 2005; Sears and Moore, 2005) that the kinetics of water ice sublimation into a CO_2 atmosphere is best modeled by ice surface temperature and diffusion limitation. We report in this paper the experimentally measured sublimation rate of pure CO_2 ice under simulated martian conditions and derive an experimentally based model of CO_2 sublimation on Mars. Finally, we compare our predictions to data from Mars Global Surveyor (MGS) Mars Orbiter Laser Altimeter (MOLA), Mars Orbiter Camera (MOC), Mars Express Observatoire pour la Mineralogie l'Eau les Glaces et l'Activite (OMEGA), and Mars Reconnaissance Orbiter (MRO) High Resolution Imaging Science Experiment (HiRISE) and Compact Reconnaissance Imaging Spectrometer for Mars (CRISM).

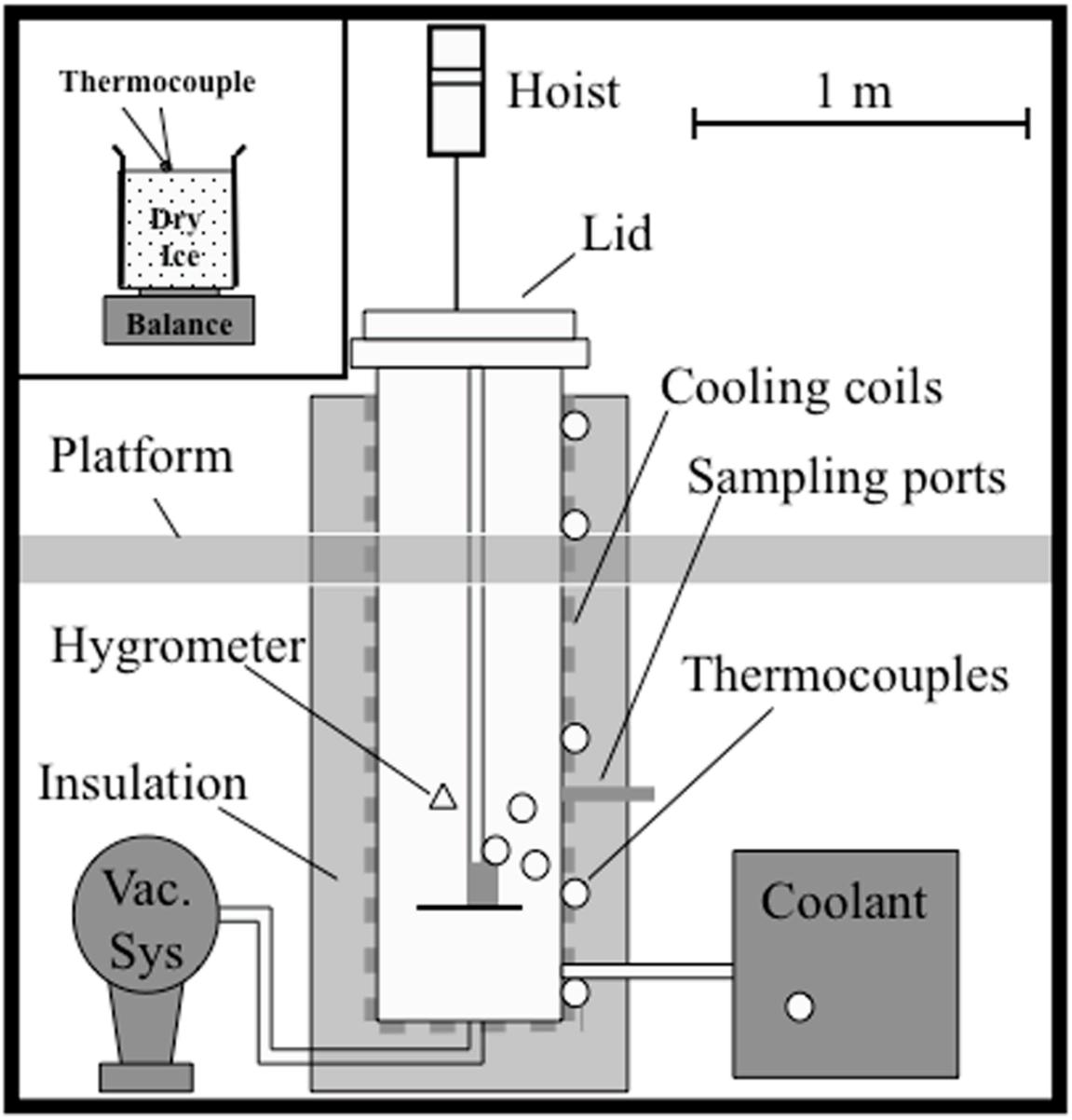

Figure 2.1 *– Schematic diagram of the simulation chamber. (Inset) Experimental setup for the present experiments, which is placed on the platform inside the chamber. The 61 cm diameter and 208 cm deep chamber is equipped with cooling system, vacuum system, thermocouples, and hygrometer.*

2.3 Experimental

We performed ten experiments where we determined the rate of CO_2 ice sublimation on a variety of grain sizes. In these experiments, we compared the differences between CO_2 powder, gravel or pellets, and solid blocks. CO_2 ice pellets (on average 1-2 cm in radius) were acquired from VMR International and solid blocks from Airgas. In the case of the CO_2 powder, we ground pellets of CO_2 ice down with a mortar and pestle to below 1 cm radii to a snow-like consistency. The CO_2 samples were packed into a beaker with a thermocouple above the surface of the dry ice and, in some experiments a second thermocouple was inserted inside the dry ice in order to look for any thermal variation by depth within the ice itself. We used a 0.6 m^3 environmental chamber (Fig. 2.1), previously described in several publications (Chevrier *et al.*, 2007; Sears and Chittenden, 2005; Sears and Moore, 2005). The chamber was evacuated to < 0.09 mbar, filled with dry gaseous CO_2 (g) to 1 atm, and cooled to ~263 or 273 K. The chamber was then opened, and the sample was placed on top a loading analytical balance. The platform supporting the balance and the sample were then lowered into the chamber. The chamber was evacuated to 7 mbar (700 Pa) and allowed to equilibrate for 30 minutes, and the mass, pressure, temperature (of the atmosphere, walls, sample, and coolant), and humidity were recorded every 1 to 2 minutes for ~1 hour, but the results were only considered significant for the mass loss rates after equilibration indicated by zero on the x-axis in Fig. 2.2B. Pressure and atmospheric temperature were maintained between 6.7 and 7.2 mbar and at 263 ± 1 K or 273 ± 1 K, respectively. Before and after each experiment, the height and diameter of the dry ice were measured, as well as the surface area and volume.

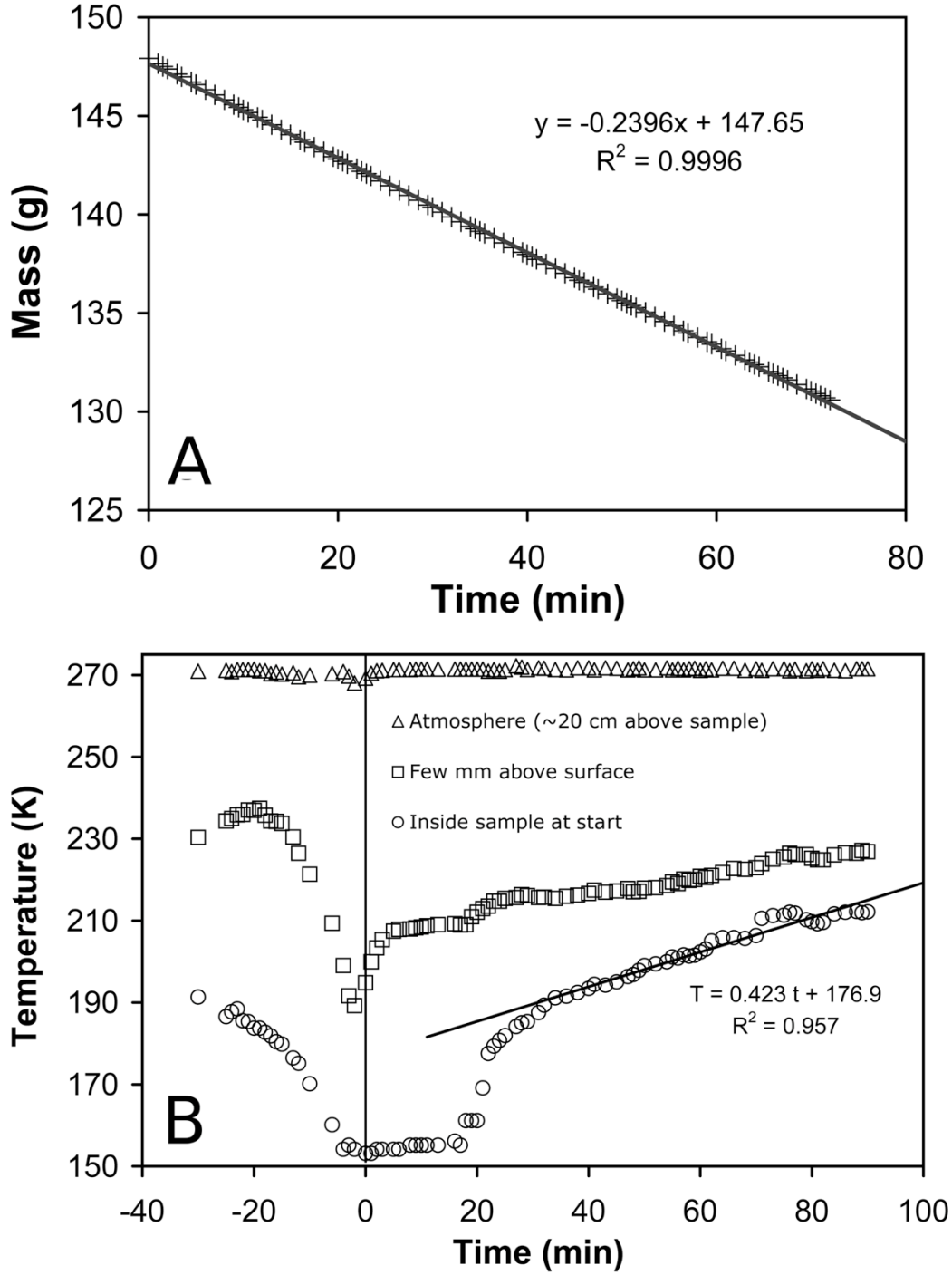

Figure 2.2 *– Experimental results of the sublimation of CO_2 ice.* ***A.*** *Mass of CO_2 ice as a function of time. Dividing the mass loss (slope of the regression line) by the surface area of the sample and the density of CO_2 ice (ρ_{ice} = 1562 kg m^{-3}) gives the sublimation rate in mm h^{-1}.* ***B.*** *Evolution of temperature measured at three different locations: triangles: atmosphere temperature (20 cm above the sample), squares: a few mm above the sample, circles: the thermocouple is initially a few mm below the surface, in the dry ice; with time, the surface regresses due to sublimation, and the thermocouple reaches the surface (~ 20*

min). Then, the thermocouple measures the hear transfer by conduction from the atmosphere, and t=0 corresponds to the end of the pumping period when the pressure reaches 7 mbar.

Table 2.1. *Experimental data of solid CO_2 ice sublimation. T_s is the temperature inside the sample near the surface; T_{S*} is the temperature a few mm above the surface; T_{atm} is the temperature 20 cm above the sample; and R_h is the relative humidity (defined as the measured water vapor pressured divided by the saturation pressure at the atmospheric temperature).*

Type	Grain Size Radius	Avg. T_S (K)	Avg. T_{S*} (K)	Avg. T_{atm} (K)	Avg. R_h (%)	Duration (min)	Sublimation Rate E_S (mm h^{-1})
Gravel	~ 1 cm	-	218 ± 6	261 ± 1	2.86 ± 0.60	110	1.06
Solid Block	N/A	-	219 ± 1	265 ± 1	5.08 ± 0.52	79	1.01
Solid Block	N/A	-	218 ± 2	264 ± 1	4.46 ± 0.34	92	0.99
Powder	~ 1 mm	-	213 ± 3	263 ± 1	2.06 ± 0.24	92	1.36
Powder	~ 1 mm	-	214 ± 4	263 ± 1	2.64 ± 0.36	81	1.63
Powder	~ 1 mm	-	208 ± 4	264 ± 1	3.40 ± 0.53	85	1.68
Loose Powder	~ 2 mm	186 ± 20	218 ± 10	271 ± 1	3.30 ± 2.17	67	1.22
Loose Powder	~ 2 mm	159 ± 13	193 ± 7	271 ± 1	3.33 ± 2.08	90	1.09
Packed Powder	~ 1 mm	151 ± 1	240 ± 4	272 ± 1	2.28 ± 0.09	78	0.91
Packed Powder	~ 1 mm	152 ± 2	238 ± 7	272 ± 1	2.16 ± 0.12	82	1.04

2.4 Results

The mass loss of CO_2 appears extremely linear, with R^2 coefficients systematically above 0.99 (Fig. 2.2A). The mass loss in g min^{-1} was converted into sublimation rate, E_S, in mm h^{-1} using the density (ρ_{ice} = 1562 kg m^{-3}) and surface area of the sample. Results are summarized in Table 2.1 and show remarkably constant values, validating the reproducibility of our experiments. We compared the differences between CO_2 powder, gravel, and solid blocks and observed that the effect of particle size was considered negligible, yet the rate for the powdered samples was slightly higher (up to 1.66 mm h^{-1}) than for larger blocks (up to 1.06 mm h^{-1}). No noticeable difference of sublimation rate was observed between the experiments performed at atmospheric temperature of 263 and 273 K. We determined that the average sublimation rate of CO_2 ice is 1.20 ± 0.27 mm h^{-1}.

2.5 Temperature Profile

We measured the temperature profiles below the surface of the sample (~0.5 cm), ~0.5 cm above the surface and 20 cm above the sample (Fig. 2.2B). The temperature of the atmosphere (i.e. 20 cm above the sample) remained very constant during the experiments (either at 263 K or at 273 K), as well as the sample temperature at ~153 K, which corresponds to the equilibrium temperature of CO_2 at 7 mbar. This is exactly what is observed on the surface of Mars, where the polar caps are usually at ~150 K (Titus *et al.*, 2003), thus in thermal equilibrium with the atmospheric pressure. The temperature a few mm above the surface was 30 to 60 K higher, as a result of the strong temperature gradient between the surface and the atmosphere (Fig. 2.2B). The sudden increase in the near-surface temperature at t ~ 20 min (Fig. 2.2B) resulted from the fact that the

thermocouple, which is initially inside the sample, reaches the surface when the ice is recessing due to sublimation. After this sudden transition, the temperature increased linearly at an average rate of 0.3 ± 0.1 K min^{-1} or about 4.7 ± 1.9 K mm^{-1}, which was obtained by dividing the rate of temperature increase by the sublimation rate.

2.6 CO_2 Sublimation Process

We modeled the CO_2 sublimation process as being governed by heat transfer between the chamber and the ice and by diffusion of the sublimated molecules away from the surface. There are three possible heat transfer processes: conduction from the ice surface into the ice interior, heat transfer from the warmer atmosphere to the cooler ice surface, and radiation from the chamber walls to the ice surface. From conservation of energy, the net heat transfer to the surface will equal the rate at which the ice is sublimated:

$$Q_{solid} + Q_{gas} + Q_{rad} = J \times \Delta H^{sub}_{150K,0.07bar} \quad (2.1.)$$

where Q_{solid} is the rate at which energy is transferred between the surface and the body of the ice, Q_{gas} is the rate at which the surface receives energy from the chamber atmosphere, Q_{rad} is the rate of radiative heat transfer from the warmer chamber walls to the surface, J is the sublimation rate in mol s^{-1}-m^{-2}, and $\Delta H^{sub}_{150K,0.07bar}$ is the enthalpy of sublimation of CO_2 ice, which is 590 x 10^3 J kg^{-1} at 155 K (Schmidt *et al.*, 2009). At the beginning of the experiment (t = 0), the temperature measured below the ice surface is 148-153 K (Fig. 2.2B), indicating that conduction has caused the ice to reach internal thermal equilibrium during the approximately 30 min pump-down. As a result, the surface and interior of the ice were at the same temperature. At this point, the ice surface reached the solid - vapor equilibrium temperature associated with the chamber pressure (7 mbar, 150 K, Fig. 2.2B).

This condition is maintained by sublimation of the surface: any heat input to the surface causes a constant-temperature sublimation of the affected layer, preventing a thermal gradient in the ice, thus eliminating conduction into the solid. This leaves conduction from the gas phase or radiation as the possible drivers for the sublimation process.

Heat transfer from the chamber atmosphere to the ice surface is purely gaseous conduction. Since the ice surface is considerably colder than the atmosphere, there are no buoyancy effects creating free convection, and there is no wind to create forced convection. In this case, the heat conduction is defined by the following equation:

$$\frac{Q_{gas}}{A} = k_{CO_2} \frac{\left(T_{atm} - T_S\right)}{L} \qquad (2.2.)$$

where A is the sample surface area, k_{CO_2} is the thermal conductivity of CO_2 gas at the average temperature of the thermal boundary layer (4.48×10^{-3} W m^{-1} K^{-1}), and L is the thermal boundary layer thickness. The measured temperature gradient (4.7 K mm^{-1}, Fig. 2.2B) allows us to estimate that the average conductive flux from the atmosphere to the surface Q_{gas}/A is 66 ± 26 W m^{-2}. Therefore, sublimation occurs because the atmosphere is too warm compared to the cold ice surface (263 to 273K against 150K). Thermal conduction in the CO_2 atmosphere is too low to be the dominant process in the chamber, as its contribution alone corresponds to a sublimation rate of 0.26 ± 0.10 mm h^{-1}.

Neglecting atmospheric absorption and re-radiation and assuming a shape factor of one, the radiative heat transfer between the ice surface (treating the ice as an opaque material, a condition verified in our experiments) and chamber walls is defined by:

$$\frac{Q_{rad}}{A} = \sigma\left(1-\alpha\right)\left(T_W^4 - T_S^4\right) \qquad (2.3.)$$

where T_W is the temperature of the walls of the chamber, T_S is the temperature of the ice surface, σ is the Stefan-Boltzmann constant and (1 - α) is the absorptivity of CO_2 ice at the characteristic wavelength of the emitted radiation (α being the albedo). Equation 2.3 can be utilized, in this case, because we are assuming that the ice is a gray body and that the walls of our chamber represent a blackbody, which makes the absorptivity equal to the emissivity and is a common technique in heat transfer (Kaviany, 2002). Using Wien's displacement law, we calculated that the peak in the blackbody radiation spectrum for the wall surface at 263 K is 11 μm. At this wavelength, the estimated surface absorptivity of CO_2 ice is ~ 0.9 (Warren *et al.*, 1990). The calculated radiative heat flux Q_{rad}/A under these assumptions is 220 ± 20 W m^{-2}. Therefore, in our experiments, the sublimation of CO_2 ice is in majority controlled by radiation from the walls (220 W m^{-2}), with a minor contribution due to conduction from the gas phase (66 W m^{-2}). Combining eq. 2.1, 2.2 and 2.3 leads to the following equation describing CO_2 ice sublimation:

$$E_S = \frac{\sigma(1-\alpha)\left(T_W^4 - T_S^4\right) + k_{CO_2}\dfrac{\left(T_{atm} - T_S\right)}{L}}{\rho_{ice}\Delta H^{sub}_{150K,0.07bar}} \qquad (2.4.)$$

In eq. 2.4, ρ_{ice} is the measured density of the CO_2 ice (1562 kg m^{-3}) and $\Delta H_{sub,\ 150K,\ 0.07\ bar}$ is the measured heat of sublimation for CO_2 at 150K and 0.07 bar (590 x 10^3 J kg^{-1}, Giauque and Egan, 1937; Schmidt *et al.*, 2009).

Combining the radiative energy from the walls at 263 K (~ 220 W m^{-2}), with the conductive flux from the atmosphere (~ 66 W m^{-2}), gives a sublimation rate of 1.12 ± 0.18 mm h^{-1}, a value identical to our experimental results (1.20 ± 0.27 mm h^{-1}) within the error margin.

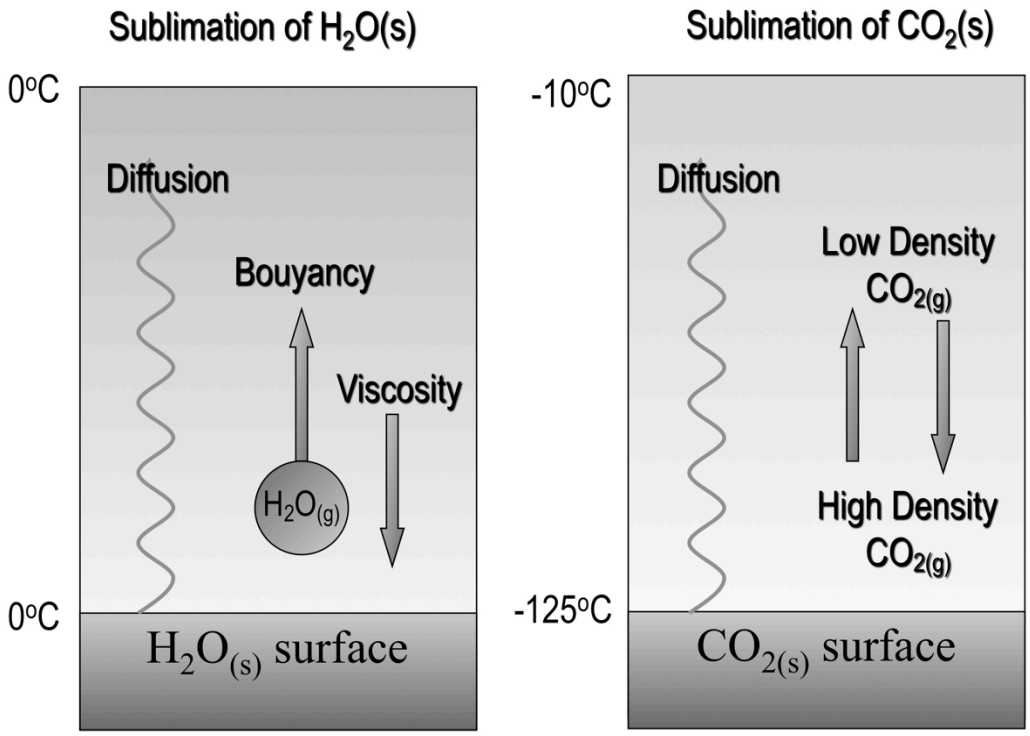

Figure 2.3 *– Comparison between sublimation processes of H_2O and CO_2 ice on Mars. Water ice sublimation is mostly driven by diffusion and buoyancy into the heavier CO_2 atmosphere (Ingersoll, 1970; Sears and Moore, 2005). In our experiments, the density gradient is reversed since the CO_2 atmosphere is warmer than the surface. This situation simplifies the heat transfer to radiation from the walls only (no possible convection, and very low conduction from the gas phase, see section 5 for details).*

2.7 Comparison to H_2O Ice Sublimation

It has been shown previously that ice surface and gas boundary layer temperatures control the sublimation rate of water ice (Chevrier *et al.*, 2007; Chittenden *et al.*, 2008; Ingersoll, 1970). This is due to the strong temperature dependency of the saturation pressure of the gas phase on the surface of the solid, which determines the concentration gradient. However, in the case of the CO_2 ice, there is no concentration gradient, since CO_2 is the dominant gas. This effect helps to simplify prediction of the sublimation rate of CO_2 ice by heat transfer control as illustrated in Fig. 2.3, while the sublimation rate for water ice depends on temperatures and includes terms for the diffusion of water into a CO_2 atmosphere, gravity, and humidity (Ingersoll, 1970).

2.8 Application to the Martian Polar Caps

Now that we have experimentally confirmed that the kinetics are heat-transfer limited, we can use our experimentally derived equation as a basis for a new model for change in the elevation of the seasonal and residual CO_2 cap of the south pole of Mars by correcting to the appropriate heat flux on Mars. In addition to confirm our model and heat-transfer limitation, we chose to compare our predictions with observational data from MOLA, MOC, HiRISE and CRISM.

2.8.1 Sublimation Model

On Mars, there is no blackbody emission like the walls of our chamber. Instead, the irradiance of the surface comes predominately from the sun with a minor contribution from infrared emission of the atmosphere. In this case eq. 2.4 becomes:

$$E_S = \frac{Q_{DirectSolar} + Q_{IndirectSolar} + Q_{IR} - Q_{Emission}}{\rho_{ice}\Delta H^{sub}_{150K,0.07bar}} \qquad (2.5.)$$

In eq 5, $Q_{DirectSolar}$ is the radiation from direct solar illumination; $Q_{IndirectSolar}$ is the scattering component, due to the presence of dust in the atmosphere; Q_{IR} is the infrared emission from the atmosphere that strikes the surface; and $Q_{Emission}$ is the infrared emission of the ice itself. The conduction from the martian atmosphere is not included in eq. 2.5 and can be neglected (as a first approximation) since the maximum difference of temperature between the martian atmosphere and the CO_2 surface is ~70 K (Titus *et al.*, 2003), which is less than the 110-120 K difference in our experiments and corresponds to a maximum heat input of ~42 W m^{-2}. In eq 5, $Q_{DirectSolar}$ is defined as follows:

$$Q_{DirectSolar} = (1-\alpha_{VIS})S_0 \cos(z)\left(\frac{\bar{r}}{r}\right)\psi \qquad (2.6.)$$

S_0 is the mean irradiance at Mars' distance from the sun (590 W m^{-2}), $\bar{r}/r$ is the normalized distance to the sun, z is the zenith angle, ψ is the atmospheric transmission coefficient, and α_{VIS} is the albedo of the CO_2 ice in the visible wavelengths. The transmission coefficient is taken from Pollack *et al.* (1990) and is a function of the zenith angle and optical depth, calculated by dividing the net downward flux in Pollack *et al.* (1990) by ($1 - \alpha$). This result is presented in Rapp (2008) in table format for varying optical depths and zenith angles. From their data, we produced polynomial best fits for various optical depths. For example, for $\tau = 0.5$, the resultant degree four polynomial as a function of zenith angle is:

$$\psi = -0.36459z^4 + 0.65774z^3 + 0.46207z^2 + 0.076182z + 0.89927 \qquad (2.7.)$$

The indirect solar irradiance is taken from Rivera-Valentin *et al.* (2009), which is an adaption of Kieffer *et al.* (1977), Aharonson and Schorghofer (2006) and Schmidt *et al.* (2009):

$$Q_{IndirectSolar} = (1-\alpha_{VIS}) f_{ID} S_0 \left(\frac{\bar{r}}{r}\right)^2 (1-\psi)\cos^2\left(\frac{\gamma}{2}\right), \text{ for } \cos(z) > 0 \qquad (2.8.)$$

For indirect solar, γ is the slope angle of the terrain, and f_{ID} is the 2 percent contribution used by Kieffer *et al.* (1977), Aharonson and Schorghofer (2006), Schmidt *et al.* (2009), and Rivera-Valentin *et al*. (2009). $Q_{IndirectSolar}$ is zero when cos(z) is below zero, i.e. during the night time. The infrared emission from the atmosphere on the surface of the ice is defined as:

$$Q_{IR} = (1-\alpha_{IR}) f_{IR} S_0 \left(\frac{\bar{r}}{r}\right)^2 \cos^2\left(\frac{\gamma}{2}\right)\cos(z_{noon}), \text{ for } \cos(z_{\text{noon}}) > 0 \qquad (2.9.)$$

Infrared emission from the atmosphere (eq. 2.9) was approximated in the same manner as previous models (Aharonson and Schorghofer, 2006; Kieffer *et al.*, 1977; Schmidt *et al.*, 2009) as 4 percent of the noon direct sunlight (f_{IR}), and α_{IR}, the ice albedo in the infrared, is equal to 1-ε (Warren *et al.*, 1990), where ε is the emissivity. The z_{noon} is the zenith angle at noon. The infrared emission of the ice $Q_{Emission}$ is defined as:

$$Q_{Emission} = \varepsilon\sigma T_{ice}^4 \qquad (2.10.)$$

where σ is the Stephan-Boltzman constant and T_{ice} is the mean CO_2 ice temperature (148 K, Titus *et al.,* 2003). We used a standard value of 0.91 for the emissivity, measured by Eluszkiewicz and Moncet (2003), used by Pollack *et al.* (2003) and Schmidt *et al.* (2009) and within the range of Haberle *et al.*'s (2008) model for considering ground ice effects.

For our model, we determined the daily average flux for $Q_{DirectSolar}$ by using the following equation:

$$\overline{Q}_{DirectSolar} = (1-\alpha_{VIS})\frac{S_0}{\pi}\left(\frac{\bar{r}}{r}\right)\left[\cos\delta\cos\phi\sin H + H\sin\delta\sin\phi\right]\Psi_{avg} \qquad (2.11.)$$

where,

$$\cos H = -\tan\phi \tan\delta \tag{2.12.}$$

In this daily average for direct solar insolation, δ is the solar declination, ϕ is the latitude, and H is the hour angle defined in eq. 2.12. In eq. 2.11, ψ_{avg} is the value for the transmission coefficient at the average zenith angle during a day.

Schmidt *et al.* (2009) determined a relationship between L_S and the bolometric albedo at visual wavelengths (α_{VIS}) from OMEGA images. In the south polar cap, the albedo relationship with L_S differs between the cryptic (between longitude 60ºE and 260ºE) and the anti-cryptic sectors (between longitude 100ºW and 60ºE). Using a weighted average from the extent of these sectors, we derived the following equation to describe the change in the CO_2 ice visible bolometric albedo over a martian year for 178 < L_S < 368 (when the average daily flux from the sun is above zero and visible albedo becomes relevant):

$$\alpha_{VIS} = \left(\frac{200}{360}\right)\left(-0.1967 + 0.0029 L_S\right) + \left(\frac{160}{360}\right) MIN\left(-0.392 + 0.0044 L_S, 0.63\right) \tag{2.13.}$$

In eq. 2.13, the *MIN* means to take the minimum of the two values in the series, and values for visible bolometric albedo span from 0.33 to 0.76 for L_S from 178 to 368, respectively. While Schmidt *et al.* (2009) only used this relation though L_S 320, we found that continuing the model though 368 fit well with albedo observations of the residual cap, which is exposed after ~ L_S 320 (Byrne *et al.*, 2008).

Our experiments showed that the behavior of CO_2 ice on Mars is largely dependent on the intensity of surface insolation, which is heavily dependent on optical depth τ, our remaining free parameter due to the variation in dustiness from year to year (Vincendon *et al*., 2009; Vincendon *et al.*, 2008; Bonev *et al.*, 2008). We used the

measurements of optical depth over the southern cap provided by Vincendon *et al.* (2009) spanning three martian years (27, 28 and 29) as a baseline to constrain our model (Fig. 2.4A). For our model, we calculated the average E_S corresponding to all L_S values. Once the averages were determined by L_S, the result was integrated over a martian year to produce a predicted change in elevation for the south polar cap (Fig. 2.4B). All three years showed very similar trends with two general periods: (1) sublimation of ~1.3 m of cap thickness during the summer between L_S 180 and 330 and (2) condensation of CO_2 ice the rest of the year. Also, we observed for all three years a net loss of CO_2 ice between condensation and sublimation of 0.43 ± 0.04 m for each martian year. The slight difference in year 28 compared to the two other years is due to a peak in atmospheric dust at L_S 270, which reduced the sublimation rate during that period.

After comparing a yearly-averaged optical depth of 0.3 with the variation in optical depth over season provided by Vincendon *et al.* (2009), we found the difference in net loss of elevation negligible (<0.05 m/yr). Thus, to compare the changes with more and less dusty years than the three sampled by Vincendon *et al.* (2009), we calculated the net change in height Δh over a martian year for various latitudes and yearly-averaged optical depths between 0.1 and 1.0 (Fig. 2.5). We observed that for optical depths below 0.7-0.8, there is a net loss over one martian year, while higher optical depths result in a net gain.

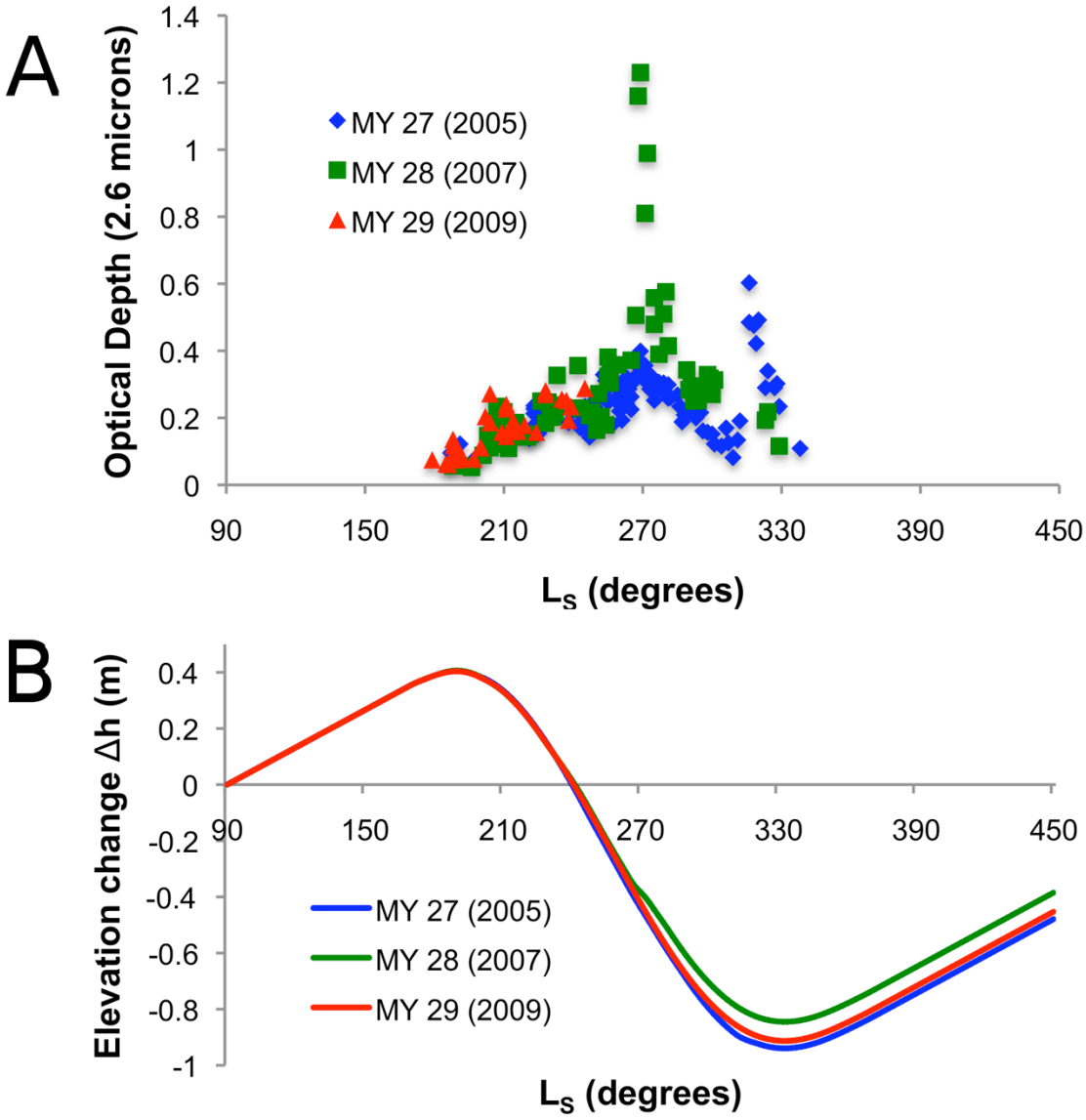

Figure 2.4 *– **A.** Optical depth vs. L_S for Mars years (MY) 27, 28, and 29, using the measured optical depth from Vincendon et al. (2009). **B.** Predicted elevation change of the CO_2 seasonal cap vs. L_S for Mars years 27, 28, and 29, using the measured optical depth from Vincendon et al. (2009), showing a net loss of 0.47 m, 0.38 m, and 0.45 m over these martian years, corresponding to an average of 0.43 ± 0.04 m/yr that may manifest itself in the residual cap.*

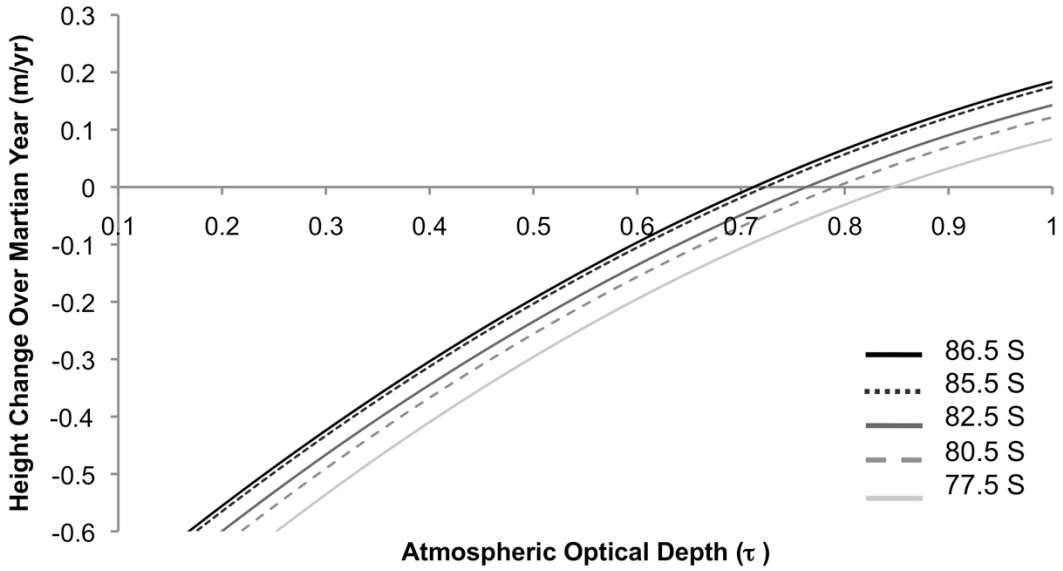

Figure 2.5 *– Elevation change of the CO_2 seasonal cap vs average yearly atmospheric optical depth for the latitutdes 86.5 S, 86.5 S, 82.5 S, 80.5 S, and 77.5 °S. In the case of latitude 86.5 S, for optical depths above ~ 0.71, the CO_2 cap would experience a net growth over a martian year and a net loss for values lower than 0.71. Note: At much higher optical depths (approaching ~2), dust storms would provide a source of heat for sublimation by themselves (Bonev et al., 2008).*

2.8.2 Comparison to MOLA Data

We applied our model to height changes of the south polar seasonal caps determined from longitudinally averaged MOLA observations over varying ranges of latitudes (Fig. 2.6A). These observations were acquired by MGS during martian years 24 and 25, for which there is no detailed optical depth measurement. Therefore, we fitted optical depths that allowed our model to match the highest and lowest point for the elevation change throughout the year. Since we wanted to compare these values to longitudinally averaged MOLA data (Smith *et al.*, 2001), we used a zero value for the slope angle to get an average for all topographies. Our model applied over one martian year (Fig. 2.7) predicts a net loss of 0.12 m yr^{-1} of CO_2 from the south polar cap at 86.5 °S when the optical depth is set to 0.6. This higher number for the optical depth than the ~0.3 yearly average value found by Vincendon *et al.* (2009) is expected, considering the regional dust storms during MOLA data acquisition. However, the elevation changes analyzed in the MOLA altimeter data expressed in Smith *et al.* (2001) may be inaccurate and altered by compaction of CO_2 snow, which lowers the elevation over time (Smith, 2009, personal communication). Our model predicts that sublimation starts at L_S ~198 (Fig. 2.7), which is later than L_S ~ 163 predicted by the CO_2 mass loss from the Ames GCMS and from time variations in Mars' gravitational field (Smith *et al.*, 2009); yet they were based on total mass loss of the poles, and at 86.5 °S latitude, we are far from the polar cap edge that will begin sublimating first. Regional dust storms occurred in the southern hemisphere between L_S ~ 225° and 245°, most likely dramatically affecting global-scale advection, providing an early heat source, and resulting in sublimation of the south seasonal cap about 35° L_S prior to the start of

substantial solar insolation.

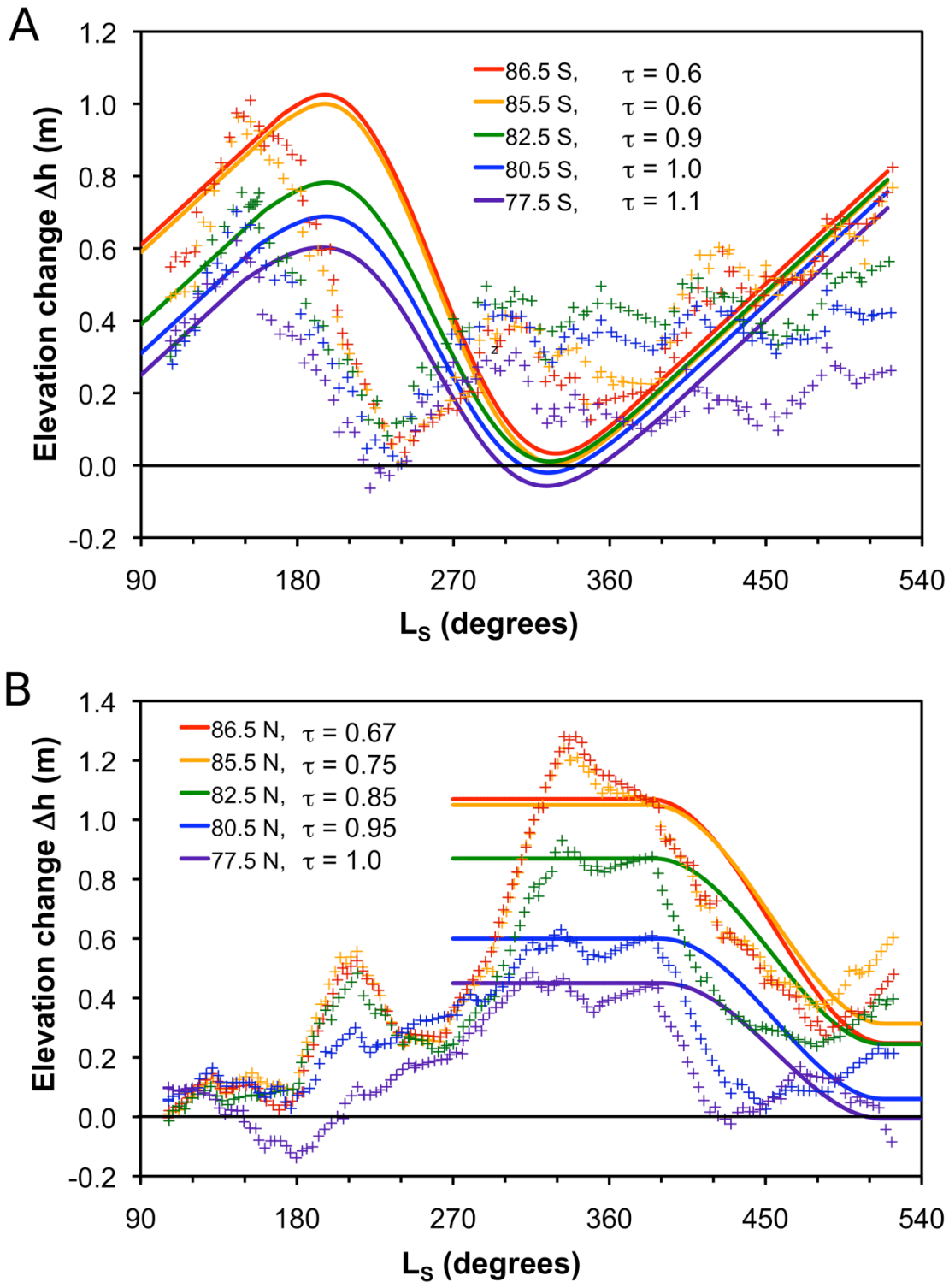

Figure 2.6 – A. *Our sublimation model's prediction of the change in height of the southern seasonal cap (solid lines) compared to MOLA data from (plus signs, Smith et al., 2001) for the south cap at latitudes 86.5 S, 85.5 S, 82.5 S, 80.5 S, and 77.5 °S. Optical*

depth (τ) is the free parameter, and its values were chosen so that total sublimated height matches the MOLA data. ***B.*** *Same as in part A, yet for the northern cap.*

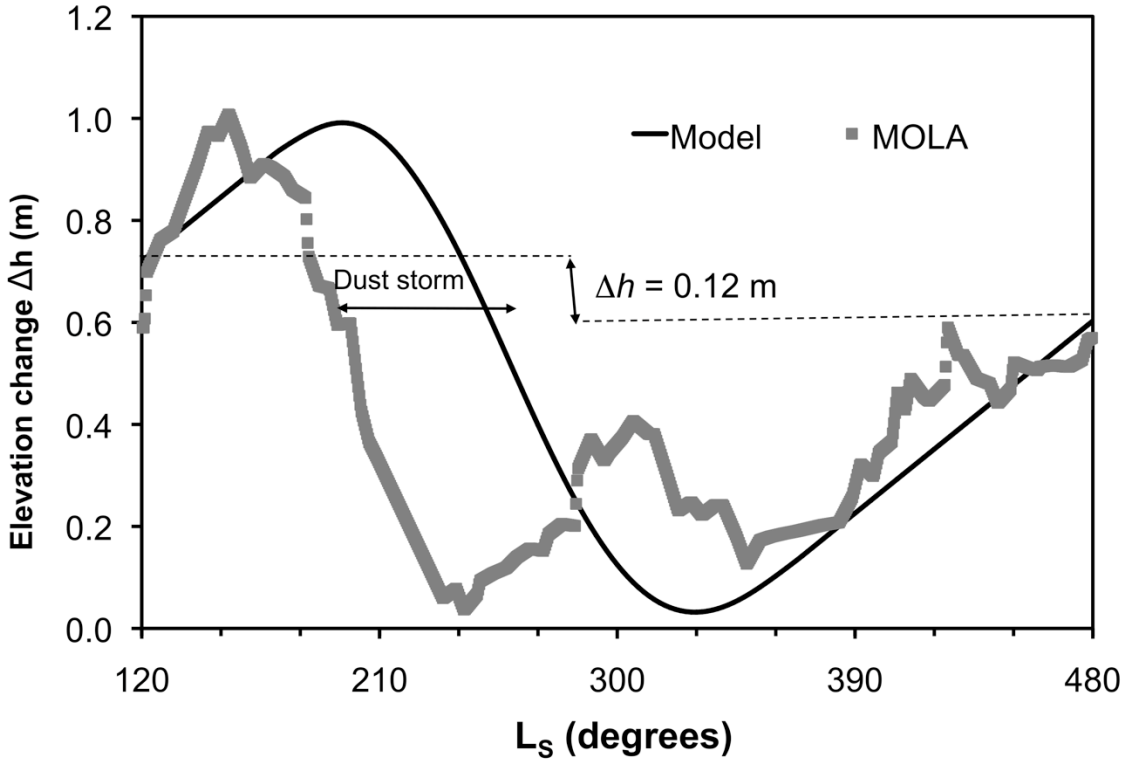

Figure 2.7 *– Our sublimation model's prediction of the change in height of the southern CO_2 cap (solid, black line) compared to MOLA data from (gray squares, Smith et al., 2001) for 86.5 °S and an optical depth of 0.6. The time period from L_S ~ 225° to 245° was marked by global dust storms, and the 35° advance on the sublimation rate was most likely triggered by massive abnormal advection (Smith et al., 2001). Our model predicts a loss of ~ 0.12 m yr^{-1} of CO_2 ice from the southern cap at 86.5 °S if the yearly average for the optical depth is 0.6.*

2.8.3 Seasonal and Perennial Variations in South Polar Features

In order to better understand the precise dynamics of the southern polar cap, we analyzed HiRISE images of different times of the year. Smoother surfaces are observed at higher elevations than layers presenting an irregular surface (Fig. 2.8). To identify the CO_2 ice features in the polar caps, we examined the CRISM observations in the 86ºS region. To compare which features were CO_2 ice versus water ice, we used the CO_2/Water ice indicator from CRISM observations (Murchie *et al.*, 2007). This indicator was based off the ICER1 summary product a CO_2 (1.5 μm) and water ice (1.43 μm) band depth ratio, created with the CRISM Analysis Tool. CRISM observations show that the top flat features are composed of CO_2 ice while the lower irregular layers contain water ice (Fig. 2.8). The water ice layer is visible only during the summer (L_S = 332º), being covered by seasonal CO_2 ice during the winter (L_S = 287, Fig. 2.8). This demonstrates the presence of a seasonal cap of CO_2 on top of a perennial cap composed of CO_2 and water ice and supports the recent findings of exposed water ice by Brown *et al.* (2010).

There is good agreement between our model and MOLA results on a global scale; accordingly we want to verify its applicability on a local scale. Therefore, we studied the evolution of the width of the south perennial CO_2 features at latitude ~86ºS by comparing HiRISE images of the same region, obtained between L_S ~180º and ~360º, i.e. south hemisphere spring and summer (Fig. 2.9C). There are not an abundance of images in the polar region that overlap the same location at least during three different L_S's and include measurable sublimation features; therefore a limited number of images were analyzed (Table 2.2). The widths of the flat tops were measured in HiRISE images at different seasons to create the graph in Fig. 2.9B. Once it was confirmed that the top flat features

were composed of CO_2 ice, measurements of the features were used to determine the sublimation rates. We observe that the local CO_2 ice layer features undergo significant decrease in width by 3 ± 1 m (Fig. 2.9B). Using a ~30º slope (Byrne and Ingersoll, 2003; Fig. 2.9A), this corresponds to a local elevation decrease of ~1.5 m during the summer, similar to our model prediction of ~1.3 m when the average yearly optical depth is set to 0.3. In addition, the sublimation of CO_2 starts at L_S 240º and ends around L_S 330º (Fig. 2.9B), in agreement with our model (Fig. 2.6A).

We observed series of parallel bands or "ripples" with relatively high albedo, along the pit walls of these sublimational features that are separated by higher albedo strips (Fig. 2.10). We did a survey of these features from several images, and the results are displayed in Table 2.3 for 16 observed ripples. We observed that the average distance between each ripple is 3.76 m ± 0.76, all being within the range 3 to 4.5 m, which corresponds well to the 3 m lost from the width of the CO_2 seasonal cap (Fig. 2.9). This close correlation to the CO_2 features' widths (Fig. 2.9B) suggests that the ripples are remnants of the annual sublimation and deposition cycle, probably due to dust previously deposited on the slope of the slab and left after sublimation.

All previous observations focused on annual or shorter timescales, but trends should also be observed in longer timescales. To determine the net perennial variation of the CO_2 caps, we compared MOC images and HiRISE images of the southern polar cap, during the south polar summer. MOC and HiRISE images were either 2 or 3 martian years apart. Of this limited selection of HiRISE images, even fewer of them have MOC images that overlap the same features. Only two locations showed an overlap between MOC and HiRISE images. Despite the very few superimposed pictures, we observed a

systematic retreat of the CO_2 perennial cap (Fig. 2.11). Using the shadows produced by the CO_2 slab at low sun declination, we determined the average thickness of the CO_2 perennial cap to be 2.3 ± 0.4 m in MOC images and 1.03 ± 0.14 m in HiRISE images of the same features separated by 3 martian years. These thicknesses correspond well to the thickness of the region classified as Unit B (1-3 m) of the south polar residual cap, compared to 5-10 m for the larger Unit A region (Thomas et al, 2009). Our thickness difference over both those images separated by 2 or 3 years gives an average sublimation rate of 0.43 ± 0.03 m y^{-1}, fitting exactly the average for our model (0.43 ± 0.04 m y^{-1}) using the optical depths from Vincendon *et al.* (2009) over a similar time span (Fig. 2.4). We argue that this number is higher than the 0.12 m y^{-1} prediction of our model from the MOLA data (Fig. 2.7) because the optical depth and frequency of dust storms was less than at the time Smith *et al.* (2001) monitored elevation changes. Our model's predictions for the south caps are in agreement with findings over the last 8 years of the retreat of the south polar caps (Malin *et al.*, 2001; Byrne and Ingersoll, 2003; Bibring *et al.*, 2004; Zuber *et al.*, 2007; Haberle *et al.*, 2009).

Table 2.2. *MRO-HiRISE images analyzed to determine the sublimation rate of CO_2 ice features in the south polar cap (See text and Fig. 2.9)*

Location	Image	L_S
86º25'18"S 0º47'1"E	PSP-005728-0935	331.8
	PSP-005095-0935	303.7
	PSP-004383-0935	269.7
	PSP-004739-0935	286.9
86º58'12"S 6º19'34"W	PSP-004687-0930	284.5
	PSP-005043-0930	301.3
	PSP-003738-0930	237.9
	PSP-002617-0930	184.9
	PSP-005517-0930	322.7
86º9'34"S 10º11'22"W	PSP-004647-0940	282.5
	PSP-004370-0940	269.0
	PSP-004792-0940	289.5
	PSP-005359-0940	315.7
	PSP-003170-0940	210.3
	PSP-005781-0940	334.1
	PSP-004858-0940	292.6
85º41'24"S 73º55'9"W and 85º41'45"S 74º6'46"W	PSP-003832-0945	242.5
	PSP-006126-0945	348.4
	PSP-002922-0945	198.7
	PSP-003937-0945	247.7
	PSP-004992-0945	298.9

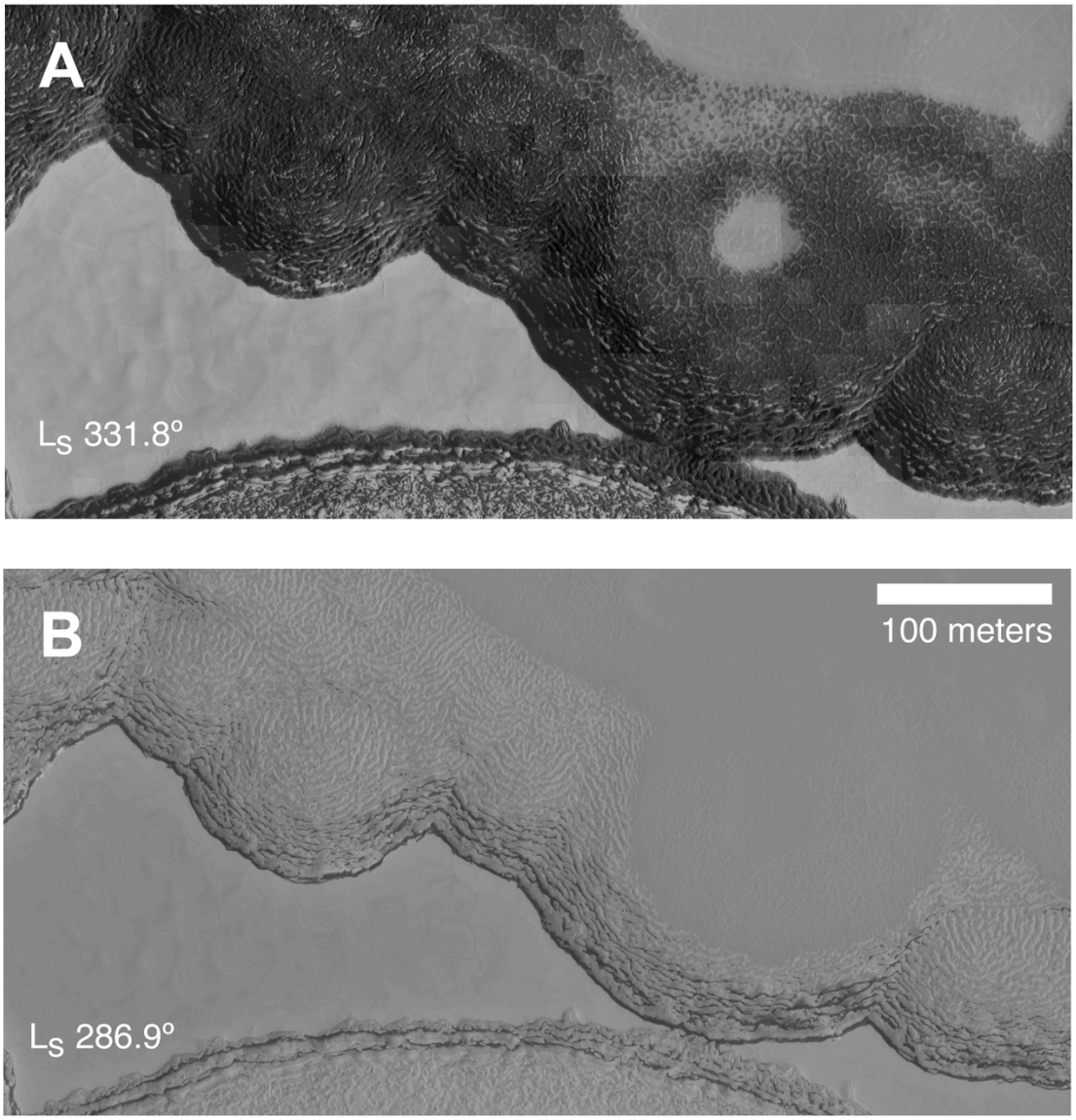

Figure 2.8 – *Infrared MRO CRISM observations of the south polar cap revealing CO_2 (light gray) and water (black) ices. The area shown in A and B is at 86°21'S, 0°7'W.* ***A.*** *Summer observation at L_S 331.8°, a subframe of HiRISE image PSP-005728-0935 with a superimposed CO_2/water ice indicator from infrared CRISM observation FRT000083f2_07. Summer sublimation of CO_2 seasonal cap reveals the water ice underneath.* ***B.*** *Winter observation at L_S 286.9°, a subframe of HiRISE image PSP-004739-0935 with a superimposed CO_2/Water ice indicator from infrared CRISM observation FRT00006df1_07. No water is observed due to coverage by the CO_2 seasonal cap.*

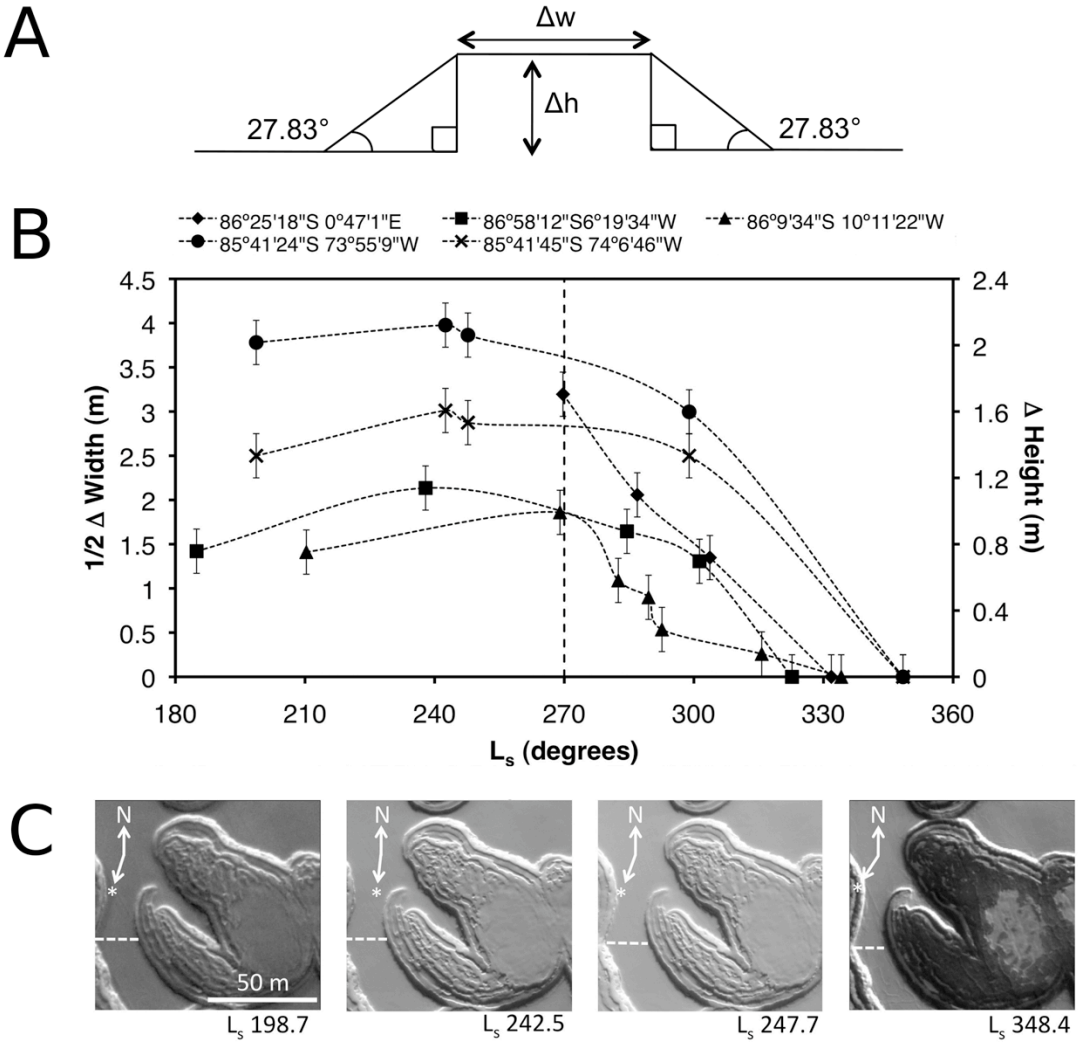

Figure 2.9 *– Summer evolution of the South polar cap on HiRISE images.* ***A.*** *The change in width of the flat tops were measured in order to determine the change in length (1/2 Δw) of the side of the right triangle adjacent to our average 27.83 ± 5.16° slope angle, giving us the change in height by trigonometry.* ***B.*** *Measured half delta width of the tops of CO_2 features at 5 different south polar locations as a function of season.* ***C.*** *Subframes of HiRISE images at 85°41'S, 74°6'W, (from left to right) PSP_002922_0945, PSP_003832_0945, PSP_003937_0945, PSP_006126_0945. The dashed line indicates where a feature width was measured. Arrows indicate direction toward the north (N) and the Sun (*), respectively.*

Table 2.3. *Description of "ripple" observations on MRO-HiRISE images (see text for details)*

Location	Image	L_S	Number	Average Width (m)
85º41'19"S 74º2'15"W	PSP_003937_0945	247.7	4	3.25
86º8'46"S 10º16'0.8"W	PSP_004792_0940	289.5	3	3.18
86º22'2"S 0º11'51"W	PSP_004739_0935	286.9	3	4.04
86º55'58"S 7º0'58"W	PSP_004687_0930	284.5	6	4.24
Average of Total Ripples Surveyed				3.76±0.76

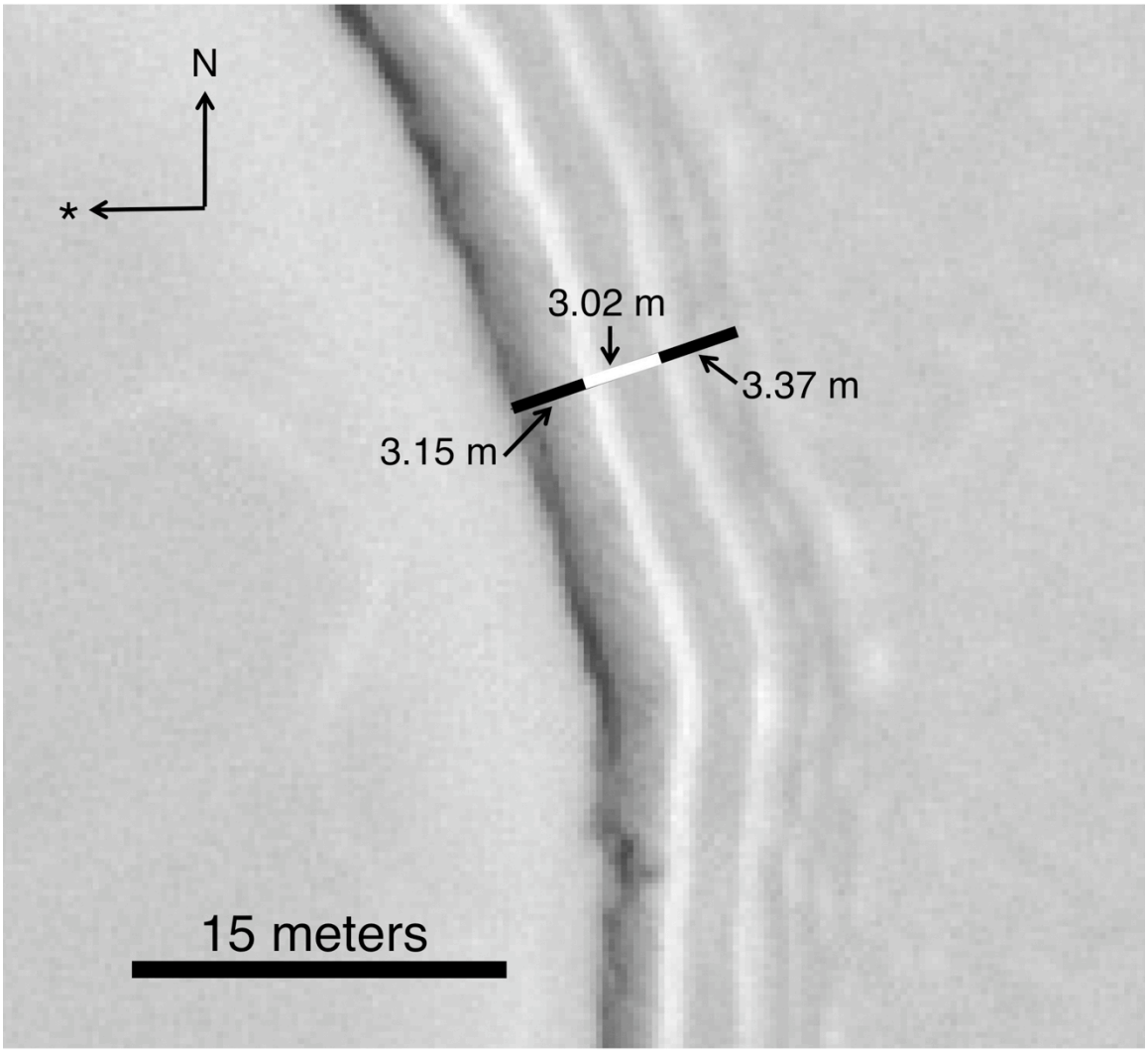

Figure 2.10 *– MRO HiRISE image of parallel fringes or "ripples" on the border of a CO_2 feature. The spacing of these ripples is on average 3.2 ± 0.2 m, similar to the total annual retreat of the seasonal cap, suggesting these are remnants of the seasonal sublimation cycle. The image at 86°8S, 10°15' W is a subframe of HiRISE image PSP-004792-0940.*

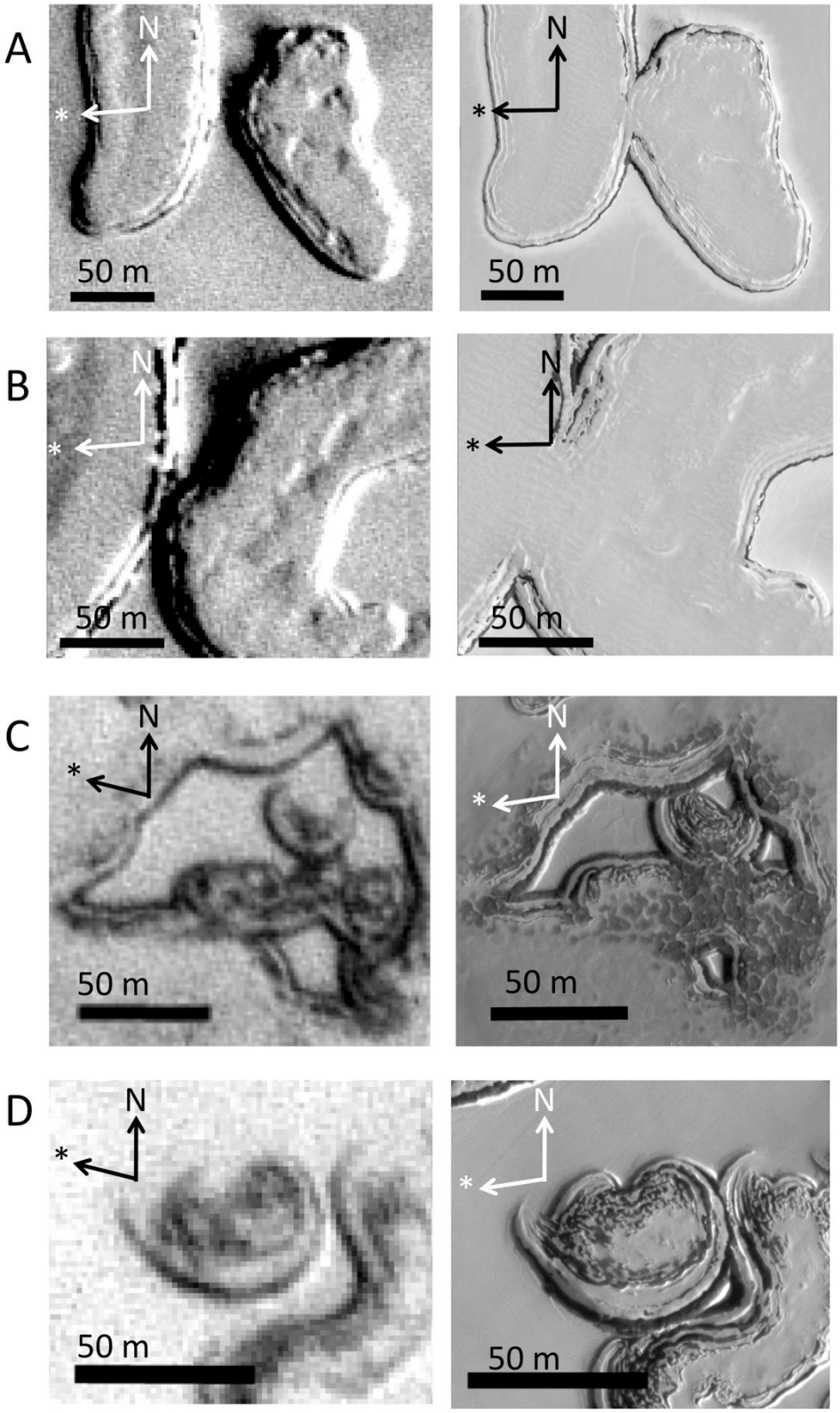

Figure 2.11 *– Comparison between MGS MOC (left) and MRO HiRISE (right) images of the same region, indicating sublimation of the CO_2 features over 2 to 3 martian years. A*

and B are subframes of (left) MOC image E11-00955 and (right) HiRISE image PSP-004792-0940 at approximately the same season, L_S 285.57º and 289.5º, respectively, separated by 3 martian years. C and D are subframes of (left) MOC image R13-01242 and (right) HiRISe image PSP-005728-0935 at approximately the same season, L_S 330.26º and 331.8º, respectively, separated by 2 martian years. Feature heights have retreated an average of 0.43 ± 0.03 m y^{-1}. Arrows indicate direction toward the north (N) and the Sun (*), respectively.

2.8.4 North Polar Cap

In the north polar cap, HiRISE images do not show any measurable geomorphological features. We can, however, apply our model to the northern cap for a limited case. Since the north polar cap only consists of a seasonal cap of CO_2 and exposes H_2O ice for over half of the year, we chose to restrict our model to the period where CO_2 sublimates in the northern spring. We chose an average constant bolometric albedo of 0.5 for the seasonal cap (Paige *et al.*, 1994; Paige and Keegan, 1994). We also chose to keep the emissivity the same as the model for the southern cap (0.91). Our model, then, predicts sublimation between L_S 360º and 540º (Fig. 2.6B). This coincides with Viking Lander 2 pressure measurements, showing a pressure anomaly (as compared to purely thermally controlled) between L_S 360º and 540º (Fig. 2.12) that we attribute to sublimation of the CO_2 seasonal cap in the northern spring, though a dynamic pressure wave, or a Rossby wave, could also be responsible (Hourdin *et al.*, 1995). The reason that the rate is constant in the winter is that we decided to make the rate zero during seasons when the surface is in constant darkness, and we chose initial conditions that were consistent with the CO_2 elevation at the start of sublimation. The winter rate was chosen to be constant because the surface during that time varies from water to carbon dioxide ice; thus, we chose to apply our model only to periods where we were sure that CO_2 dominated the surface. Our slopes are fairly constant due to our choice of a constant albedo, but the MOLA data slopes support the conclusion that the albedo of the seasonal cap slowly increases over time and is consistent with the exposure of the water ice underneath the seasonal cap. The predicted start of sublimation in our model for 86.5 °N is $L_S \sim 390$, compared to the $L_S \sim 330$ measured by Smith *et al.* (2009) for the start of

mass loss for the north polar cap. Furthermore, the higher resulting optical depths between 0.67 and 1 (Fig. 2.6B) suggest that the yearly balance between condensation and sublimation in the northern CO_2 cap would be less than or equal to zero, so that CO_2 ice cannot accumulate (i.e. no perennial cap) and only a seasonal cap is present.

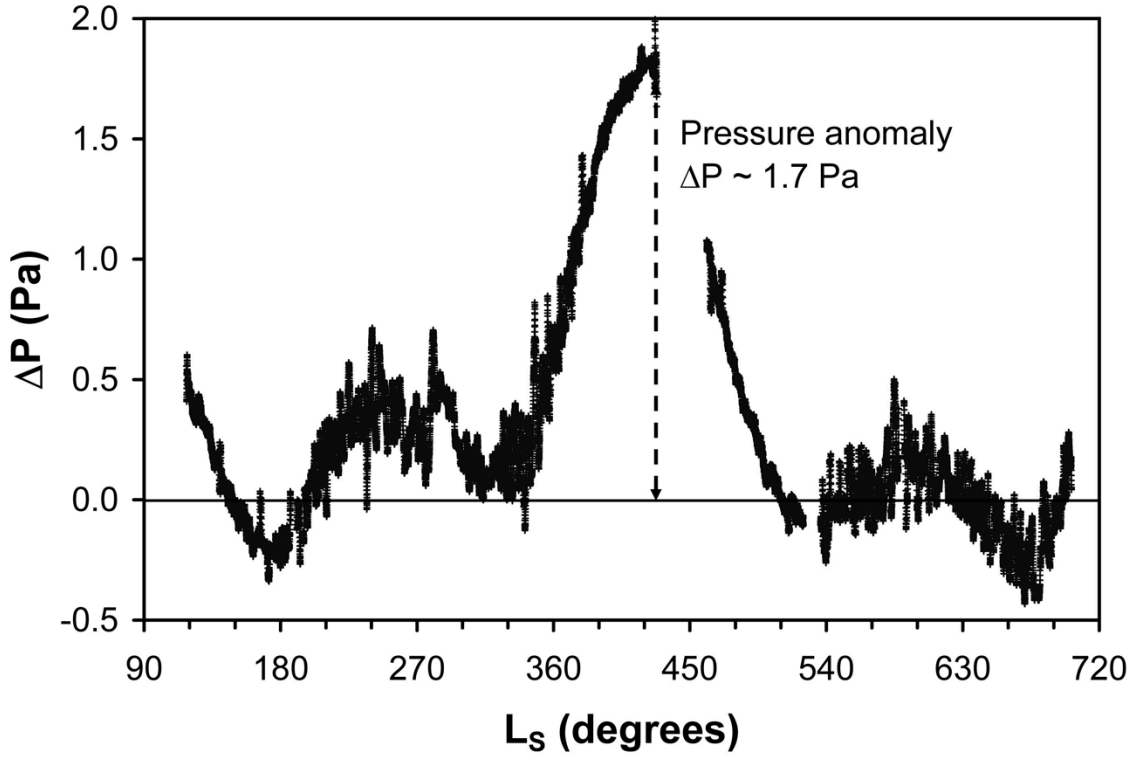

Figure 2.12 *– Pressure data from Viking Lander 2 in Utopia Planitia at 48.27ºN. The absolute pressure has been corrected for temperature variations, assuming the ideal gas law and that standard conditions are 210K and 7.5 mbar. If the pressure followed the temperature variations, then all the data should be aligned on the 0 line. We observe small variations from the ideal case, probably due to adsorption in the regolith (Zent and Quinn, 1995), and a large positive pressure anomaly centered at* L_S *420º, when insolation is maximum in the north hemisphere. Thus, we attribute this rise of pressure to the sublimation of the north polar cap.*

2.9. Conclusions

Our experimental study demonstrates that the dynamics of the polar caps are predominately heat-transfer limited and controlled by the irradiance of the sun and hence the optical depth. Our model, therefore, based on irradiance of the sun, can predict trends in the mass balance of the polar caps. While the high lambert albedos of the residual cap (~0.8) help to buffer the solar insolation in the southern summer (James *et al.*, 2007; Byrne *et al*., 2008), our calculations show that albedo control is not enough to maintain stability of the cap on its own. If the rate of CO_2 loss remains the same (~0.4 m y^{-1}), then the perennial CO_2 cap will disappear in approximately 6-7 martian years, assuming an average thickness of 2.4 meters for the entire residual cap (Thomas *et al.*, 2009). The low optical depths (~0.3) required to sustain that rate of loss are not likely to be maintained due to the frequency of dust storms, both regional and global that originate in the southern hemisphere, although that opacity number is well within the observations of the south polar cap from 2002-2008 by THEMIS (Smith, 2009) and compares well with Vincendon *et al.* (2009). If, however, it is maintained, the migration of CO_2 from the south polar cap will leave the south pole entirely composed of water ice. If this water ice starts to sublimate, then higher humidities in the martian atmosphere should be expected. Alternatively, if the sublimation trend inverts and progression of the south polar cap occurs in this timescale (Piqueux and Chistensen, 2008), then this suggests a short timescale climatic cycle linked to changes in the optical depth and local weather patterns.

2.10 References

Aharonson, O., Schorghofer, N., 2006. Subsurface ice on Mars with rough topography. Journal of Geophysical Research (Planets). 111, 11007.

Bibring, J.P., Langevin, Y., Poulet, F., Gendrin, A., Gondet, B., Berthé, M., Soufflot, A., Drossart, P., Combes, M., Bellucci, G., Moroz, V., Mangold, N., Schmitt, B., 2004. Perennial water ice identified in the south polar cap of Mars. Nature. 428, 627-630.

Bonev, P.B, Hansen, G.B, Glenar, D.A., James, P.B, and Bjorkman, J.E., 2008. Albedo models for the residual south polar cap on Mars: Implications for the stability of the cap under near-perihelion global dust storm conditions. Journal of Geophysical Research. 56, 181-193.

Brown, A.J., Calvin, W.M. McGuire, P.C., Murchie, S.L., 2010. CRISM south polar mapping: first Mars year of observations. Journal of Geophysical Research (Planets) 115, E00D13.

Byrne, S., Ingersoll, A.P., 2003. A Sublimation Model for Martian South Polar Ice Features. Science. 299, 1051-1053.

Byrne, S., Zuber, M.T., Neumann, G.A., 2008. Internannual and seasonal behavior of martian residual ice-cap albedo. Planetary and Space Science. 56, 194-211.

Chevrier, V., Sears, D.W.G., Chittenden, J.D., Roe, L.A., Ulrich, R., Bryson, K., Billingsley, L., Hanley, J., 2007. Sublimation rate of ice under simulated Mars conditions and the effect of layers of mock regolith JSC Mars-1. Geophysical Research Letters. 34(2), 02203.

Chittenden, J.D., Chevrier, V., Roe, L.A., Bryson, K., Pilgrim, R., Sears, D.W.G., 2008. Experimental study of the effect of wind on the stability of water ice on Mars. Icarus. 196, 477-487.

Eluszkiewicz, J., Moncet, J.-L., 2003. A coupled microphysical/radiative transfer model of albedo and emissivity of planetary surfaces covered by volatile ices. Icarus. 166, 375-384.

Fanale, F.P., Banerdt, W.B., Saunders, R.S., Johansen, L.A., Salvail, J.R., 1982. Seasonal carbon dioxide exchange between the regolith and atmosphere of Mars: experimental and theoretical studies. Journal of Geophysical Research. 87(B12), 10215-10225.

Fanale, F.P., Cannon, W.A., 1971. Adsoprtion on the martian regolith. Nature. 230, 502-504.

Fishbaugh, K.E., Head III, J.W., 2001. Comparison of the North and South Polar Caps of Mars: New Observations from MOLA Data and Discussion of Some Outstanding Questions. Icarus. 154, 145-161.

Forget, F., Hourdin, F., Talagrand, O., 1998. CO_2 Snowfall on Mars: Simulation with a General Circulation Model. Icarus. 131, 302-316.

Giauque, W. F.; Egan, C. J., 1937. Carbon dioxide: The heat capacity and vapor pressure of the solid. the heat of sublimation. thermodynamic and spectroscopic values of the entropy. J. Chem. Phys. 5, 45– 54.

Haberle, R.M., Forget, F., Colaprete, A., Schaeffer, J., Boynton, W.V., Kelly, N.J., and Chamberlain, M.A., (2008). The effect of ground ice on the martian seasonal CO_2 cycle. Planetary and Space Science. 56, 251-255.

Haberle, R.M., Kahre, M.A., Malin, M., Thomas, P.C., 2009. The disappearing south residual cap on Mars: Where is the CO_2 going? International Workshop on Mars Polar Energy Balance and CO_2 Cycle. Abstract 7002.

Hourdin, F., Forget, F., Talagrand, O., 1995. The sensitivity of the Martian surface pressure and atmospheric mass budget to various parameters: A comparison between numerical simulations and Viking observations. Journal of Geophysical Research. 100, 5501-5523.

Ingersoll, A.P., 1970. Mars: Occurence of liquid water. Science. 168(3934), 972-973.

James, P.B., Thomas, P.C., Wolff, M.J., Bonev, B.P., 2007. MOC observations of four Mars year variations in the south polar residual cap of Mars. Icarus. 192, 318-326.

Kaviany, M., 2002. Principles of heat transfer. New York: Wiley.

Kieffer, H.H., Martin, T.Z., Peterfreund, A.R., Jakosky, B.M., Miner, E.D., Palluconi, F.D., 1977. Thermal and albedo mapping of Mars during the Viking primary mission. Journal of Geophysical Research. 82, 4249-4291.

Langevin, Y., Poulet, F., Bibring, J.-P., Schmitt, B., Douté, S., Gondet, B., 2005. Summer evolution of the North Polar Cap of Mars as observed by OMEGA/Mars Express. Science. 307, 1581-1584.

Leighton, R.B., Murray, B.C., 1966. Behavior of carbon dioxide and other volatiles on Mars. Science. 153, 136-144.

Malin, M.C., Caplinger, M.A., Davis, S.D., 2001. Observational Evidence for an Active Surface Reservoir of Solid Carbon Dioxide on Mars. Science. 294, 2146-2148.

Moore, S.R., Sears, D.W.G., 2006. On laboratory simulation and the effect of small temperature oscillations about the freezing point and ice formation on the evaporation rate of water on Mars. Astrobiology. 6(4), 644-650.

Murchie, S., Guinness, E., Slavney, S., 2007. Mars Reconnaissance Orbiter CRISM data product software interface specification. Version 1.3.3.

Paige, D.A., Bachman, J.E., Keegan, K.D., 1994. Thermal and albedo mapping of the polar regions of Mars using Viking thermal mapper observations: 1. North polar region. Journal of Geophysical Research. 99, 25959-25991.

Paige, D.A., Keegan, K.D., 1994. Thermal and albedo mapping of the polar regions of Mars using Viking thermal mapper observations: 2. South polar region. Journal of Geophysical Research. 99, 25993-26013.

Piqueux, S., Chistensen, P.R., 2008. Deposition of CO_2 and erosion of the martian south perennial cap between 1972 and 2004: Implications for current climate change. Journal of Geophysical Research. 113, 02006.

Pollack, J.B., Haberle, R.M., Murphy, J.R., Schaeffer, J., Lee, H., 1990. Simulations of the general circulation of the martian atmosphere. I - Polar Processes. Journal of Geophysical Research. 95, 1447-1473.

Pollack J.B. Haberle, R.M., Murphys, J.R., Schaeffer, J., Lee, H., 1993. Simulations of the general circulation of the martian atmosphere II – Seasonal pressure variations. Journal of Geophysicsl Research. 98, 3149-3181.

Rapp, D. (2008) Human missions to Mars: Enabling technologies for exploring the red planet. Praxis Publishing, Chichester, UK.

Rivera-Valentin, E. G., Chevrier, V.F., and Ulrich, R. (2009) Time depdendent model for heat transfer and water vapor diffusion/adsorption at the phoenix landing site. Workshop on Modeling of Martian Hydrous Environments, Abstract 4020.

Schmidt, F., DoutÈ, S., Schmitt, B., Vincendon, M., Bibring, J.-P., Langevin, Y., 2009. Albedo control of seasonal South Polar cap recession on Mars. Icarus. 200(2), 374-294.

Sears, D.W.G., Chittenden, J.D., 2005. On laboratory simulation and the temperature dependence of evaporation rate of brine on Mars. Geophysical Research Letters. 32(L23203),

Sears, D.W.G., Moore, S.R., 2005. On laboratory simulation and the evaporation rate of water on Mars. Geophysical Research Letters. 32(L16202),

Smith, D.E., Zuber, M.T., Neumann, G.A., 2001. Seasonal variation of snow depth on Mars. Science. 294, 2141-2146.

Smith, D.E., Zuber, M.T., Torrence, M.H., Dunn, P.J., Neumann, G.A., Lemoine, F.G., Fricke, S.K., 2009. Time variations of Mars' gravitational field and seasonal changes in the masses of the polar ice caps. Journal of Geophysical Research (Planets). 114, 05002.

Smith, M.D., 2009. THEMIS observations of Mars aerosol optical depth from 2002-2008. Icarus. 202, 444-452.

Thomas, P.C., James, P.B, Calvin, W.M., Haberle, R, Malin, M.C., 2009. Residual south polar cap of Mars: Stratigraphy, history, and implications of recent changes. Icarus. 203, 352-375.

Titus, T.N., Kieffer, H.H., Chistensen, P.R., 2003. Exposed Water Ice Discovered near the South Pole of Mars. Science. 299, 1048-1051.

Vincendon, M., Langevin, Y., Poulet, F., Bibring, J.-P., Gondet, B., Jougle, D., OMEGA Team, 2008. Dust aerosols above the south polar cap of Mars as seen by OMEGA. Icarus. 196, 488-505.

Vincendon, M., Langevin, Y., Douté, S., Bibring, J.-P., 2009. 3 Mars years of dust optical depth mapping by OMEGA above the south pole. Third International Workshop on Mars Polar Energy Balance and CO_2 Cycle. Abstract 7022.

Warren, S.G., Wiscombe, W.J., Firestone, J.F., 1990. Spectral albedo and emissivity of CO_2 in martian polar caps - Model results. Journal of Geophysical Research. 95, 14717-14741.

Zent, A.P., Quinn, R.C., 1995. Simutaneous adsorption of CO_2 and H_2O under Mars-like conditions and application to the evolution of the martian climate. Journal of Geophysical Research. 100, 5341-5349.

Zuber, M.T., Phillips, R.J., Andrews-Hanna, J.C., Asmar, S.W., Konopliv, A.S., Lemoine, F.G., Plaut, J.J., Smith, D.E., Smrekar, S.E., 2007. Density of Mars' South Polar Layered Deposits. Science. 317, 1718-1719.

APPENDIX A

Author's personal copy

Planetary and Space Science 58 (2010) 780–791

Contents lists available at ScienceDirect

Planetary and Space Science

journal homepage: www.elsevier.com/locate/pss

Sublimation kinetics of CO_2 ice on Mars

David G. Blackburn [a,*], Kathryn L. Bryson [a,b], Vincent F. Chevrier [a], Larry A. Roe [a,c], Krista F. White [a,d]

[a] Arkansas Center for Space and Planetary Sciences, 202 Old Museum Building, University of Arkansas, Fayetteville, AR 72701, USA
[b] Bay Area Environmental Research Institute, Sonoma, CA 95476, USA
[c] Department of Mechanical Engineering, University of Arkansas, Fayetteville, AR 72701, USA
[d] Department of Physics and Astronomy, Ball State University, Muncie, IN 47306, USA

ARTICLE INFO

Article history:
Received 2 August 2009
Received in revised form
14 November 2009
Accepted 16 December 2009
Available online 29 December 2009

Keywords:
Mars
Polar caps
Mass balance
Sublimation
CO_2 ice

ABSTRACT

Dynamic models of the martian polar caps are in abundance, but most rely on the assumption that the rate of sublimation of CO_2 ice can be calculated from heat transfer and lack experimental verification. We experimentally measured the sublimation rate of pure CO_2 ice under simulated martian conditions as a test of this assumption, developed a model based on our experimental results, and compared our model's predictions with observations from several martian missions (MRO, MGS, Viking). We show that sun irradiance is the primary control for the sublimation of CO_2 ice on the martian poles with the amount of radiation penetrating the surface being controlled by variations in the optical depth, ensuring the formation and sublimation of the seasonal cap. Our model confirmed by comparison of MGS-MOC and MRO-HiRISE images, separated by 2–3 martian years, shows that ~0.4 m are currently being lost from the south perennial cap per martian year. At this rate, the ~2.4-m-thick south CO_2 perennial cap will disappear in about 6–7 martian years, unless a short-scale climatic cycle alters this rate of retreat.

© 2009 Elsevier Ltd. All rights reserved.

1. Introduction

The martian polar caps represent the most active geological features on the surface of Mars today. The polar caps are composed predominately of water ice at their base, covered by a seasonal cap of CO_2 and H_2O ice in the North and a perennial and seasonal CO_2 cap in the South (Bibring et al., 2004; Langevin et al., 2005). Early modeling of the polar caps suggested that they were in equilibrium with the ~6 mbar CO_2 atmosphere (Leighton and Murray, 1966), and various observations have shown a cyclicity of growth and retreat, following martian seasons (Smith et al., 2001). Other studies show that CO_2 ice is only a thin veneer on the surface of a probably much thicker ice layer (Bibring et al., 2004; Zuber et al., 2007). This veneer is too small for the caps to be in equilibrium with the atmosphere (Byrne and Ingersoll, 2003; Malin et al., 2001), suggesting that the polar caps are very young (Fishbaugh and Head III, 2001). Therefore, either larger unidentified CO_2 reservoirs in the martian subsurface are required, including possibly adsorbed CO_2 in the regolith (Fanale et al., 1982; Fanale and Cannon, 1971), to buffer the much larger atmosphere or the total budget of CO_2 is present in the atmosphere. With the later case, it requires that Mars today has much less CO_2 than other terrestrial planets.

Dynamic models of the polar caps on Mars are in abundance, and the majority are based on energy gain/loss to estimate the mass balance. A radiative energy balance as the primary modeling mechanism was first suggested by Leighton and Murray (1966). Forget et al. (1998) introduced the emissivity of the ice as an important component to the radiation balance, and Schmidt et al. (2009) demonstrated an albedo control on the cap recession.

The majority of dynamic models of the polar caps are based on CO_2 ice sublimation, lacking laboratory confirmation that heat transfer controls the rate of sublimation. Experimental verification of this process under simulated martian conditions is of interest, as it has been shown previously (Ingersoll, 1970; Moore and Sears, 2006; Sears and Chittenden, 2005; Sears and Moore, 2005) that the kinetics of water ice sublimation into a CO_2 atmosphere is best modeled by ice surface temperature and diffusion limitation. We report in this paper the experimentally measured sublimation rate of pure CO_2 ice under simulated martian conditions and derive an experimentally based model of CO_2 sublimation on Mars. Finally, we compare our predictions to data from Mars Global Surveyor (MGS) Mars Orbiter Laser Altimeter (MOLA), Mars Orbiter Camera (MOC), Mars Express Observatoire pour la Mineralogie l'Eau les Glaces et l'Activite (OMEGA), and Mars Reconnaissance Orbiter (MRO) High Resolution Imaging Science Experiment (HiRISE) and Compact Reconnaissance Imaging Spectrometer for Mars (CRISM).

* Corresponding author. Tel.: +1 870 612 0524.
E-mail addresses: dgblackb@uark.edu, garrisonbyz@gmail.com (D.G. Blackburn).

0032-0633/$ - see front matter © 2009 Elsevier Ltd. All rights reserved.
doi:10.1016/j.pss.2009.12.004

Author's personal copy

2. Experimental

We performed 10 experiments where we determined the rate of CO_2 ice sublimation on a variety of grain sizes. In these experiments, we compared the differences between CO_2 powder, gravel or pellets, and solid blocks. CO_2 ice pellets (on average 1–2 cm in radius) were acquired from VMR International and solid blocks from Airgas. In the case of the CO_2 powder, we ground pellets of CO_2 ice down with a mortar and pestle to below 1 cm radii to a snow-like consistency. The CO_2 samples were packed into a beaker with a thermocouple above the surface of the dry ice and, in some experiments a second thermocouple was inserted inside the dry ice in order to look for any thermal variation by depth within the ice itself. We used a 0.6 m^3 environmental chamber (Fig. 1), previously described in several publications (Chevrier et al., 2007; Sears and Chittenden, 2005; Sears and Moore, 2005). The chamber was evacuated to <0.09 mbar, filled with dry gaseous CO_2 (g) to 1 atm, and cooled to $\sim$263 or 273 K. The chamber was then opened, and the sample was placed on top a loading analytical balance. The platform supporting the balance and the sample were then lowered into the chamber. The chamber was evacuated to 7 mbar (700 Pa) and allowed to equilibrate for 30 min, and the mass, pressure, temperature (of the atmosphere, walls, sample, and coolant), and humidity were recorded every 1–2 min for $\sim$1 h, but the results were only considered significant for the mass loss rates after equilibration indicated by zero on the x-axis in Fig. 2B. Pressure and atmospheric temperature were maintained between 6.7 and 7.2 mbar and at 263 ± 1 or 273 ± 1 K, respectively. Before and after each experiment, the height and diameter of the dry ice were measured, as well as the surface area and volume.

3. Results

The mass loss of CO_2 appears extremely linear, with R^2 coefficients systematically above 0.99 (Fig. 2A). The mass loss in g min^{-1} was converted into sublimation rate, E_S, in mm h^{-1} using the density (ρ_{ice}=1562 kg m^{-3}) and surface area of the sample. Results are summarized in Table 1 and show remarkably constant values, validating the reproducibility of our experiments. We compared the differences between CO_2 powder, gravel, and solid blocks and observed that the effect of particle size was considered negligible, yet the rate for the powdered samples was slightly higher (up to 1.66 mm h^{-1}) than for larger blocks (up to 1.06 mm h^{-1}). No noticeable difference of sublimation rate was observed between the experiments performed at atmospheric temperature of 263 and 273 K. We determined that the average sublimation rate of CO_2 ice is 1.20 ± 0.27 mm h^{-1}.

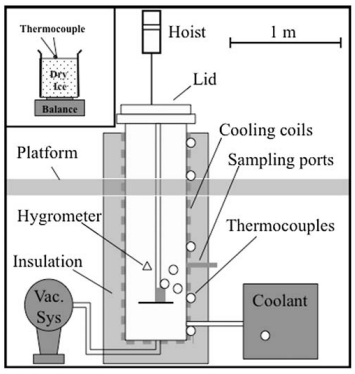

Fig. 1. Schematic diagram of the simulation chamber. (Inset) Experimental setup for the present experiments, which is placed on the platform inside the chamber. The 61 cm diameter and 208 cm deep chamber is equipped with cooling system, vacuum system, thermocouples, hygrometer, and pressure gauge.

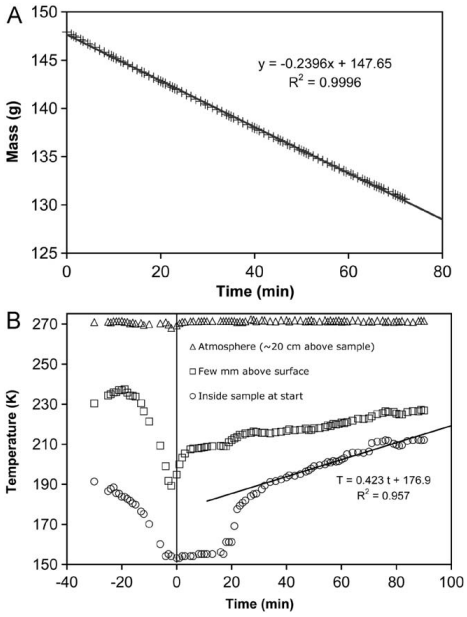

Fig. 2. Experimental results of the sublimation of CO_2 ice. (A) mass of CO_2 ice as a function of time. Dividing the mass loss (slope of the regression line) by the surface area of the sample and the density of CO_2 ice (ρ_{ice}=1562 kg m^{-3}) gives the sublimation rate in mm h^{-1}. (B) Evolution of temperature measured at three different locations: triangles: atmosphere temperature (20 cm above the sample), squares: a few mm above the sample, circles: the thermocouple is initially a few mm below the surface, in the dry ice; with time, the surface regresses due to sublimation, and the thermocouple reaches the surface ($\sim$20 min). Then, the thermocouple measures the heat transfer by conduction from the atmosphere, and t=0 corresponds to the end of the pumping period when the pressure reaches 7 mbar.

4. Temperature profile

We measured the temperature profiles below the surface of the sample ($\sim$0.5 cm), $\sim$0.5 cm above the surface and 20 cm above the sample (Fig. 2B). The temperature of the atmosphere (i.e. 20 cm above the sample) remained very constant during the experiments (either at 263 K or at 273 K), as well as the sample temperature at $\sim$153 K, which corresponds to the equilibrium temperature of CO_2 at 7 mbar. This is exactly what is observed on the surface of Mars, where the polar caps are usually at $\sim$150 K (Titus et al., 2003), thus in thermal equilibrium with the atmospheric pressure. The temperature a few mm above the surface was 30–60 K higher, as a result of the strong temperature gradient between the surface and the atmosphere (Fig. 2B). The sudden increase in the near-surface temperature at $t\sim$20 min (Fig. 2B) resulted from the fact that the thermocouple, which is

Author's personal copy

Table 1
Experimental data of solid CO_2 ice sublimation. T_s is the temperature inside the sample near the surface; $T_{s'}$ is the temperature a few mm above the surface; T_{atm} is the temperature 20 cm above the sample; and R_h is the relative humidity (defined as the measured water vapor pressure divided by the saturation pressure at the atmospheric temperature).

Type	Grain size radius	Avg. T_S (K)	Avg. $T_{s'}$ (K)	Avg. T_{atm} (K)	Avg. R_h (%)	Duration (min)	Sublimation rate E_S (mm h^{-1})
Gravel	~1 cm	–	218 ± 6	261 ± 1	2.86 ± 0.60	110	1.06
Solid block	N/A	–	219 ± 1	265 ± 1	5.08 ± 0.52	79	1.01
Solid block	N/A	–	218 ± 2	264 ± 1	4.46 ± 0.34	92	0.99
Powder	~1 mm	–	213 ± 3	263 ± 1	2.06 ± 0.24	92	1.36
Powder	~1 mm	–	214 ± 4	263 ± 1	2.64 ± 0.36	81	1.63
Powder	~1 mm	–	208 ± 4	264 ± 1	3.40 ± 0.53	85	1.68
Loose powder	~2 mm	186 ± 20	218 ± 10	271 ± 1	3.30 ± 2.17	67	1.22
Loose powder	~2 mm	159 ± 13	193 ± 7	271 ± 1	3.33 ± 2.08	90	1.09
Packed powder	~1 mm	151 ± 1	240 ± 4	272 ± 1	2.28 ± 0.09	78	0.91
Packed powder	~1 mm	152 ± 2	238 ± 7	272 ± 1	2.16 ± 0.12	82	1.04

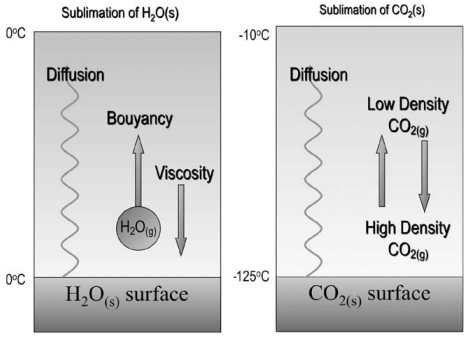

Fig. 3. Comparison between sublimation processes of H_2O and CO_2 ice on Mars. Water ice sublimation is mostly driven by diffusion and buoyancy into the heavier CO_2 atmosphere (Ingersoll, 1970; Sears and Moore, 2005). In our experiments, the density gradient is reversed since the CO_2 atmosphere is warmer than the surface. This situation simplifies the heat transfer to radiation from the walls only (no possible convection, and very low conduction from the gas phase, see section 5 for details).

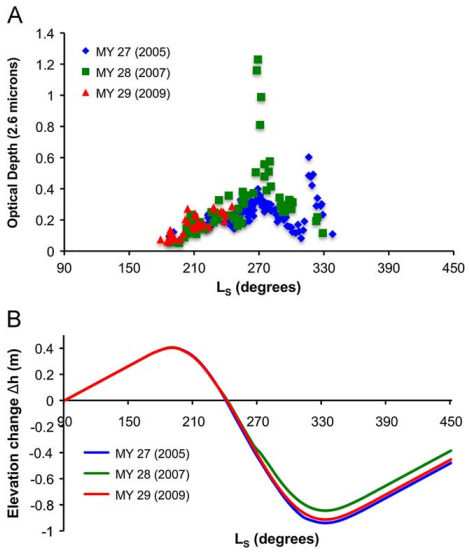

Fig. 4. (A) Optical depth vs. L_S for Mars years (MY) 27, 28, and 29, using the measured optical depth from Vincendon et al. (2009). (B) Predicted elevation change of the CO_2 seasonal cap vs. L_S for Mars years 27, 28, and 29, using the measured optical depth from Vincendon et al. (2009), showing a net loss of 0.47, 0.38, and 0.45 m over these martian years, corresponding to an average of 0.43 ± 0.04 m $year^{-1}$ that may manifest itself in the residual cap.

initially inside the sample, reaches the surface when the ice is recessing due to sublimation. After this sudden transition, the temperature increased linearly at an average rate of 0.3 ± 0.1 K min^{-1} or about 4.7 ± 1.9 K mm^{-1}, which was obtained by dividing the rate of temperature increase by the sublimation rate.

5. CO_2 sublimation process

We modeled the CO_2 sublimation process as being governed by heat transfer between the chamber and the ice and by diffusion of the sublimated molecules away from the surface. There are three possible heat transfer processes: conduction from the ice surface into the ice interior, heat transfer from the warmer atmosphere to the cooler ice surface, and radiation from the chamber walls to the ice surface. From conservation of energy, the net heat transfer to the surface will equal the rate at which the ice is sublimated:

$$Q_{solid} + Q_{gas} + Q_{rad} = J \times \Delta H^{sub}_{150\,K,0.07\,bar} \quad (1)$$

where Q_{solid} is the rate at which energy is transferred between the surface and the body of the ice, Q_{gas} is the rate at which the surface receives energy from the chamber atmosphere, Q_{rad} is the rate of radiative heat transfer from the warmer chamber walls to the surface, J is the sublimation rate in mol s^{-1} m^{-2}, and $\Delta H^{sub}_{150\,K,0.07\,bar}$ is the enthalpy of sublimation of CO_2 ice, which is 590×10^3 J kg^{-1} at 155 K (Schmidt et al., 2009). At the beginning of the experiment (t=0), the temperature measured below the ice surface is 148–153 K (Fig. 2B), indicating that conduction has caused the ice to reach internal thermal equilibrium during the approximately 30 min pump-down. As a result, the surface and interior of the ice were at the same temperature. At this point, the ice surface reached the solid–vapor equilibrium temperature associated with the chamber pressure (7 mbar, 150 K, Fig. 2B). This condition is maintained by sublimation of the surface: any heat input to the surface causes a constant-temperature

Author's personal copy

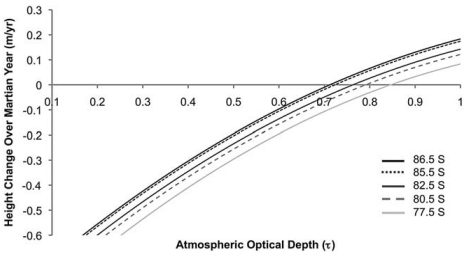

Fig. 5. Elevation change of the CO_2 seasonal cap vs. average yearly atmospheric optical depth for the latitudes 86.5, 85.5, 82.5, 80.5, and 77.5°S. In the case of latitude 86.5S, for optical depths above ~0.71, the CO_2 cap would experience a net growth over a martian year and a net loss for values lower than 0.71. *Note*: At much higher optical depths (approaching ~2), dust storms would provide a source of heat for sublimation by themselves (Bonev et al., 2008).

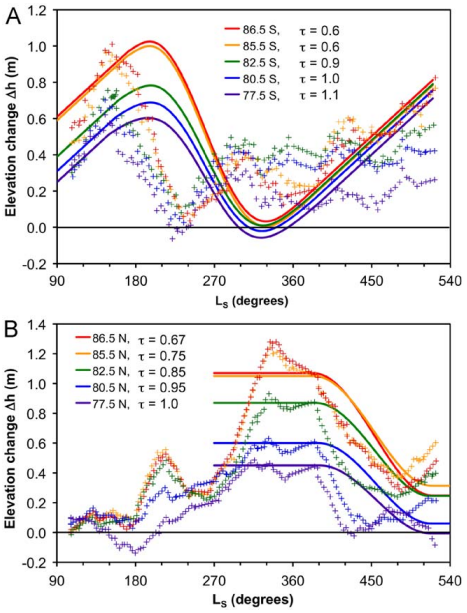

Fig. 6. (A) Our sublimation model's prediction of the change in height of the southern seasonal cap (solid lines) compared to MOLA data from (plus signs, Smith et al., 2001) for the south cap at latitudes 86.5, 85.5, 82.5, 80.5, and 77.5°S. Optical depth (τ) is the free parameter, and its values were chosen so that total sublimated height matches the MOLA data. (B) Same as in part A, yet for the northern cap.

sublimation of the affected layer, preventing a thermal gradient in the ice, thus eliminating conduction into the solid. This leaves conduction from the gas phase or radiation as the possible drivers for the sublimation process.

Heat transfer from the chamber atmosphere to the ice surface is purely gaseous conduction. Since the ice surface is considerably colder than the atmosphere, there are no buoyancy effects creating free convection, and there is no wind to create forced convection. In this case, the heat conduction is defined by the

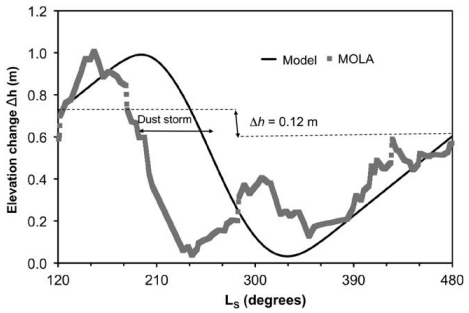

Fig. 7. Our sublimation model's prediction of the change in height of the southern CO_2 cap (solid, black line) compared to MOLA data from (grey squares, Smith et al., 2001) for latitude 86.5°S and an optical depth of 0.6. The time period from L_S~225° to 245° was marked by global dust storms, and the 35° advance on the sublimation rate was most likely triggered by massive abnormal advection (Smith et al., 2001). Our model predicts a loss of ~0.12 m year^{-1} of CO_2 ice from the southern cap at 86.5°S if the yearly average for the optical depth is 0.6.

following equation:

$$\frac{Q_{gas}}{A} = k_{CO_2}\frac{(T_{atm}-T_S)}{L} \quad (2)$$

where A is the sample surface area, k_{CO2} is the thermal conductivity of CO_2 gas at the average temperature of the thermal boundary layer (4.48×10^{-3} W m^{-1} K^{-1}), and L is the thermal boundary layer thickness. The measured temperature gradient (4.7 K mm^{-1}, Fig. 2B) allows us to estimate that the average conductive flux from the atmosphere to the surface Q_{gas}/A is 66 ± 26 W m^{-2}. Therefore, sublimation occurs because the atmosphere is too warm compared to the cold ice surface (263–273 K against 150 K). Thermal conduction in the CO_2 atmosphere is too low to be the dominant process in the chamber, as its contribution alone corresponds to a sublimation rate of 0.26 ± 0.10 mm h^{-1}.

Neglecting atmospheric absorption and re-radiation and assuming a shape factor of one, the radiative heat transfer between the ice surface (treating the ice as an opaque material, a condition verified in our experiments) and chamber walls is defined by

$$\frac{Q_{rad}}{A} = \sigma(1-\alpha)(T_W^4-T_S^4) \quad (3)$$

where T_W is the temperature of the walls of the chamber, T_S is the temperature of the ice surface, σ is the Stefan–Boltzmann constant and $(1-\alpha)$ is the absorptivity of CO_2 ice at the characteristic wavelength of the emitted radiation (α being the albedo). Eq. (3) can be utilized, in this case, because we are assuming that the ice is a gray body and that the walls of our chamber represent a blackbody, which makes the absorptivity equal to the emissivity and is a common technique in heat transfer (Kaviany, 2002). Using Wien's displacement law, we calculated that the peak in the blackbody radiation spectrum for the wall surface at 263 K is 11 μm. At this wavelength, the estimated surface absorptivity of CO_2 ice is ~0.9 (Warren et al., 1990). The calculated radiative heat flux Q_{rad}/A under these assumptions is 220 ± 20 W m^{-2}. Therefore, in our experiments, the sublimation of CO_2 ice is in majority controlled by radiation from the walls (220 W m^{-2}), with a minor contribution due to conduction from the gas phase (66 W m^{-2}). Combining

Author's personal copy

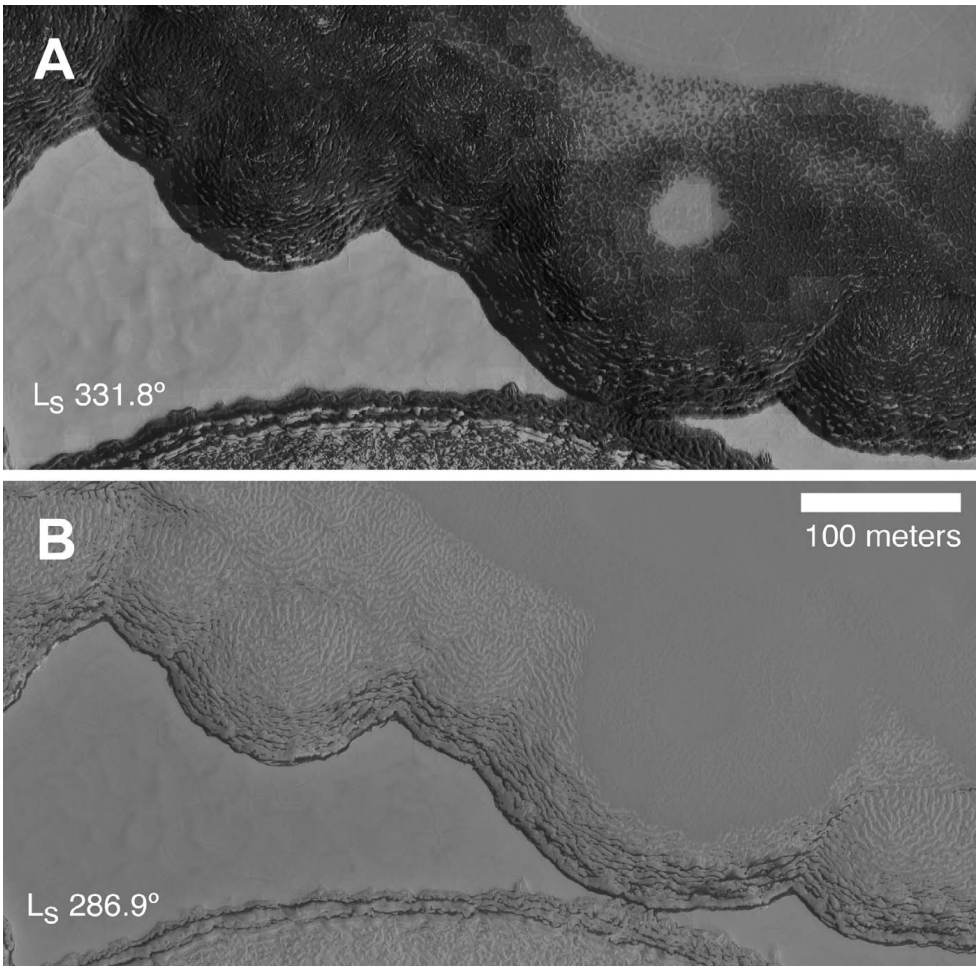

Fig. 8. Infrared MRO-CRISM observations of the south polar cap revealing CO_2 (light grey) and water (black) ices. The area shown in A and B is at 86°21′S, 0°7′W. (A) Summer observation at L_S 331.8°, a subframe of HiRISE image PSP-005728-0935 with a superimposed CO_2/water ice indicator from infrared CRISM observation FRT000083f2_07. Summer sublimation of CO_2 seasonal cap reveals the water ice underneath. (B) Winter observation at L_S 286.9°, a subframe of HiRISE image PSP-004739-0935 with a superimposed CO_2/water ice indicator from infrared CRISM observation FRT00006df1_07. No water is observed due to coverage by the CO_2 seasonal cap.

Eqs. (1)–(3) leads to the following equation describing CO_2 ice sublimation:

$$E_S = \frac{\sigma(1-\alpha)(T_W^4 - T_S^4) + k_{CO_2}(T_{atm} - T_S)/L}{\rho_{ice}\Delta H^{sub}_{150\,K,0.07\,bar}} \quad (4)$$

In Eq. (4), ρ_{ice} is the measured density of the CO_2 ice (1562 kg m^{-3}) and $\Delta H^{sub}_{150\,K,0.07\,bar}$ is the measured heat of sublimation for CO_2 at 150 K and 0.07 bar (590×10^3 J kg^{-1}, Giauque and Egan, 1937; Schmidt et al., 2009).

Combining the radiative energy from the walls at 263 K (~220 W m^{-2}), with the conductive flux from the atmosphere (~66 W m^{-2}), gives a sublimation rate of 1.12 ± 0.18 mm h^{-1}, a value identical to our experimental results (1.20 ± 0.27 mm h^{-1}) within the error margin.

6. Comparison to H_2O ice sublimation

It has been shown previously that ice surface and gas boundary layer temperatures control the sublimation rate of water ice (Chevrier et al., 2007; Chittenden et al., 2008; Ingersoll, 1970). This is due to the strong temperature dependency of the saturation pressure of the gas phase on the surface of the solid,

Author's personal copy

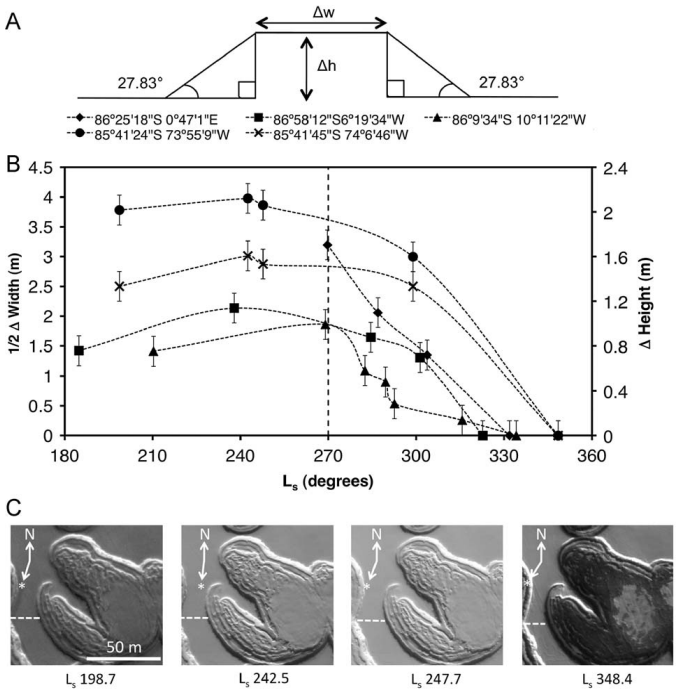

Fig. 9. Summer evolution of the South polar cap on HiRISE images. (A) The change in width of the flat tops were measured in order to determine the change in length (1/2 Δw) of the side of the right triangle adjacent to our average $27.83 \pm 5.16^{\circ}$ slope angle, giving us the change in height by trigonometry. (B) Measured half delta width of the tops of CO_2 features at 5 different south polar locations as a function of time. (C) Subframes of HiRISE images at 85°41′S, 74°6′W, (from left to right) PSP_002922_0945, PSP_003832_0945, PSP_003937_0945, PSP_006126_0945. The dashed line indicates where a feature width was measured. Arrows indicate direction toward the north (N) and the Sun (*), respectively.

which determines the concentration gradient. However, in the case of the CO_2 ice, there is no concentration gradient, since CO_2 is the dominant gas. This effect helps to simplify prediction of the sublimation rate of CO_2 ice by heat transfer control as illustrated in Fig. 3, while the sublimation rate for water ice depends on temperatures and includes terms for the diffusion of water into a CO_2 atmosphere, gravity, and humidity (Ingersoll, 1970).

7. Application to the martian polar caps

Now that we have experimentally confirmed that the kinetics are heat-transfer limited, we can use our experimentally derived equation as a basis for a new model for change in the elevation of the seasonal and residual CO_2 cap of the south pole of Mars by correcting to the appropriate heat flux on Mars. In addition to confirm our model and heat-transfer limitation, we chose to compare our predictions with observational data from MOLA, MOC, HiRISE and CRISM.

7.1. Sublimation model

On Mars, there is no blackbody emission like the walls of our chamber. Instead, the irradiance of the surface comes predominately from the sun with a minor contribution from infrared emission of the atmosphere. In this case Eq. (4) becomes

$$E_S = \frac{Q_{DirectSolar} + Q_{IndirectSolar} + Q_{IR} - Q_{Emission}}{\rho_{ice} \Delta H^{sub}_{150\,K,0.07\,bar}} \quad (5)$$

In Eq. (5), $Q_{DirectSolar}$ is the radiation from direct solar illumination; $Q_{IndirectSolar}$ is the scattering component, due to the presence of dust in the atmosphere; Q_{IR} is the infrared emission from the atmosphere that strikes the surface; and $Q_{Emission}$ is the infrared emission of the ice itself. The conduction from the martian atmosphere is not included in Eq. (5) and can be neglected (as a first approximation) since the maximum difference of temperature between the martian atmosphere and the CO_2 surface is ~70 K (Titus et al., 2003), which is less than the 110–120 K difference in our experiments and corresponds to a maximum heat input of $\sim 42\,W\,m^{-2}$. In Eq. (5), $Q_{DirectSolar}$ is defined as follows:

$$Q_{DirectSolar} = (1-\alpha_{VIS}) S_0 \cos(z) \left(\frac{\bar{r}}{r}\right) \psi \quad (6)$$

S_0 is the mean irradiance at Mars' distance from the sun ($590\,W\,m^{-2}$), $\bar{r}/r$ is the normalized distance to the sun, z is the zenith angle, ψ is the atmospheric transmission coefficient, and α_{VIS} is the albedo of the CO_2 ice in the visible wavelengths. The

Author's personal copy

Table 2
MRO-HiRISE images analyzed to determine the sublimation rate of CO_2 ice features in the south polar cap (see text and Fig. 9).

Location	Image	L_S(deg.)
86°25′18″S 0°47′1″E	PSP-005728-0935	331.8
	PSP-005095-0935	303.7
	PSP-004383-0935	269.7
	PSP-004739-0935	286.9
86°58′12″S 6°19′34″W	PSP-004687-0930	284.5
	PSP-005043-0930	301.3
	PSP-003738-0930	237.9
	PSP-002617-0930	184.9
	PSP-005517-0930	322.7
86°9′34″S 10°11′22″W	PSP-004647-0940	282.5
	PSP-004370-0940	269.0
	PSP-004792-0940	289.5
	PSP-005359-0940	315.7
	PSP-003170-0940	210.3
	PSP-005781-0940	334.1
	PSP-004858-0940	292.6
85°41′24″S 73°55′9″W and 85°41′45″S 74°6′46″W	PSP-003832-0945	242.5
	PSP-006126-0945	348.4
	PSP-002922-0945	198.7
	PSP-003937-0945	247.7
	PSP-004992-0945	298.9

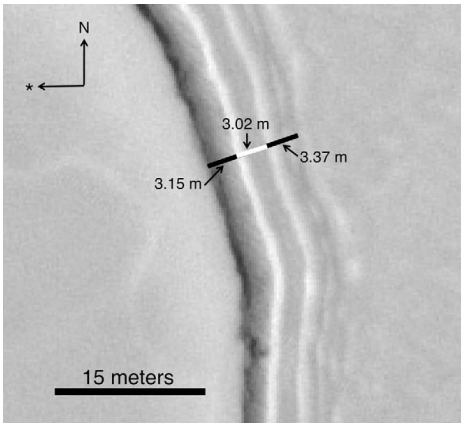

Fig. 10. MRO-HiRISE image of parallel fringes or "ripples" on the border of a CO_2 feature. The spacing of these ripples is on average 3.2 ± 0.2 m, similar to the total annual retreat of the seasonal cap, suggesting these are remnants of the seasonal sublimation cycle. The image at 86°8S, 10°15′W is a subframe of HiRISE image PSP-004792-0940.

transmission coefficient is taken from Pollack et al. (1990) and is a function of the zenith angle and optical depth, calculated by dividing the net downward flux in Pollack et al. (1990) by (1−α). This result is presented in Rapp (2008) in table format for varying optical depths and zenith angles. From their data, we produced polynomial best fits for various optical depths. For example, for τ=0.5, the resultant degree four polynomial as a function of zenith angle is

$$\psi = -0.36459z^4 + 0.65774z^3 + 0.46207z^2 + 0.076182z + 0.89927 \quad (7)$$

The indirect solar irradiance is taken from Rivera-Valentin et al. (2009), which is an adaption of Kieffer et al. (1977), Aharonson and Schorghofer (2006) and Schmidt et al. (2009):

$$Q_{IndirectSolar} = (1-\alpha_{VIS}) f_{ID} S_0 \left(\frac{\bar{r}}{r}\right)^2 (1-\psi)\cos^2\left(\frac{\gamma}{2}\right) \quad \text{for} \quad \cos(z) > 0 \quad (8)$$

For indirect solar, γ is the slope angle of the terrain, and f_{ID} is the 2 percent contribution used by Kieffer et al. (1977), Aharonson and Schorghofer (2006), Schmidt et al. (2009), and Rivera-Valentin et al. (2009). $Q_{IndirectSolar}$ is zero when cos(z) is below zero, i.e. during the night time. The infrared emission from the atmosphere on the surface of the ice is defined as

$$Q_{IR} = (1-\alpha_{IR}) f_{IR} S_0 \left(\frac{\bar{r}}{r}\right)^2 \cos^2\left(\frac{\gamma}{2}\right)\cos(z_{noon}) \quad \text{for } \cos(z_{noon}) > 0 \quad (9)$$

Infrared emission from the atmosphere (Eq. (9)) was approximated in the same manner as previous models (Aharonson and Schorghofer, 2006; Kieffer et al., 1977; Schmidt et al., 2009) as 4 percent of the noon direct sunlight (f_{IR}), and α_{IR}, the ice albedo in the infrared, is equal to $1-\varepsilon$ (Warren et al., 1990), where ε is the emissivity. The z_{noon} is the zenith angle at noon. The infrared emission of the ice $Q_{Emission}$ is defined as

$$Q_{Emission} = \varepsilon\sigma T_{ice}^4 \quad (10)$$

where σ is the Stephan–Boltzman constant and T_{ice} is the mean CO_2 ice temperature (148 K, Titus et al., 2003). We used a standard value of 0.91 for the emissivity, measured by Eluszkiewicz and Moncet (2003), used by Pollack et al. (1993) and Schmidt et al. (2009) and within the range of Haberle et al.'s (2008) model for considering ground ice effects.

For our model, we determined the daily average flux for $Q_{DirectSolar}$ by using the following equation:

$$\overline{Q}_{DirectSolar} = (1-\alpha_{VIS})\frac{S_0}{\pi}\left(\frac{\bar{r}}{r}\right)[\cos\delta\cos\varphi\sin H + H\sin\delta\sin\varphi]\,\Psi_{avg} \quad (11)$$

where

$$\cos H = -\tan\varphi\tan\delta \quad (12)$$

In this daily average for direct solar insolation, δ is the solar declination, ϕ is the latitude, and H is the hour angle defined in

Author's personal copy

Table 3
Description of "ripple" observations on MRO-HiRISE images (see text for details).

Location	Image	L_S	Number	Average width (m)
85°41′19″S 74°2′15″W	PSP_003937_0945	247.7	4	3.25
86°8′46″S 10°16′0.8″W	PSP_004792_0940	289.5	3	3.18
86°22′2″S 0°11′51″W	PSP_004739_0935	286.9	3	4.04
86°55′58″S 7°0′58″W	PSP_004687_0930	284.5	6	4.24
Average of ripples surveyed				3.76 ± 0.76

Eq. 12. In Eq. 11, ψ_{avg} is the value for the transmission coefficient at the average zenith angle during a day.

Schmidt et al. (2009) determined a relationship between L_S and the bolometric albedo at visual wavelengths (α_{VIS}) from OMEGA images. In the south polar cap, the albedo relationship with L_S differs between the cryptic (between longitude 60°E and 260°E) and the anti-cryptic sectors (between longitude 100°W and 60°E). Using a weighted average from the extent of these sectors, we derived the following equation to describe the change in the CO_2 ice visible bolometric albedo over a martian year for $178^\circ < L_S < 368^\circ$ (when the average daily flux from the sun is above zero and visible albedo becomes relevant):

$$\alpha_{VIS} = \left(\frac{200}{360}\right)(-0.1967 + 0.0029L_S) + \left(\frac{160}{360}\right)MIN(-0.392 + 0.0044L_S, 0.63) \quad (13)$$

In Eq. (13), the *MIN* means to take the minimum of the two values in the series, and values for visible bolometric albedo span from 0.33 to 0.76 for L_S from 178° to 368°, respectively. While Schmidt et al. (2009) only used this relation though L_S 320°, we found that continuing the model though 368° fit well with albedo observations of the residual cap, which is exposed after ~L_S 320° (Byrne et al., 2008).

Our experiments showed that the behavior of CO_2 ice on Mars is largely dependent on the intensity of surface insolation, which is heavily dependent on optical depth τ, our remaining free parameter due to the variation in dustiness from year to year (Vincendon et al., 2009, 2008; Bonev et al., 2008). We used the measurements of optical depth over the southern cap provided by Vincendon et al. (2009) spanning 3 martian years (27, 28 and 29) as a baseline to constrain our model (Fig. 4A). For our model, we calculated the average E_S corresponding to all L_S values. Once the averages were determined by L_S, the result was integrated over a martian year to produce a predicted change in elevation for the south polar cap (Fig. 4B). All 3 years showed very similar trends with two general periods: (1) sublimation of ~1.3 m of cap thickness during the summer between L_S 180° and 330° and (2) condensation of CO_2 ice the rest of the year. Also, we observed for all 3 years a net loss of CO_2 ice between condensation and sublimation of 0.43 ± 0.04 m for each martian year. The slight difference in year 28 compared to the 2 other years is due to a peak in atmospheric dust at L_S 270°, which reduced the sublimation rate during that period.

After comparing a yearly-averaged optical depth of 0.3 with the variation in optical depth over season provided by Vincendon et al. (2009), we found the difference in net loss of elevation negligible (< 0.05 m year^{-1}). Thus, to compare the changes with more and less dusty years than the three sampled by Vincendon et al. (2009), we calculated the net change in height Δh over a martian year for various latitudes and yearly-averaged optical depths between 0.1 and 1.0 (Fig. 5). We observed that for optical depths below 0.7–0.8, there is a net loss over 1 martian year, while higher optical depths result in a net gain.

7.2. Comparison to MOLA data

We applied our model to height changes of the south polar seasonal caps determined from longitudinally averaged MOLA observations over varying ranges of latitudes (Fig. 6A). These observations were acquired by MGS during martian years 24 and 25, for which there is no detailed optical depth measurement. Therefore, we fitted optical depths that allowed our model to match the highest and lowest point for the elevation change throughout the year. Since we wanted to compare these values to longitudinally averaged MOLA data (Smith et al., 2001), we used a zero value for the slope angle to get an average for all topographies. Our model applied over 1 martian year (Fig. 7) predicts a net loss of 0.12 m yr^{-1} of CO_2 from the south polar cap at 86.5°S when the optical depth is set to 0.6. This higher number for the optical depth than the ~0.3 yearly average value found by Vincendon et al. (2009) is expected, considering the regional dust storms during MOLA data acquisition. However, the elevation changes analyzed in the MOLA altimeter data expressed in Smith et al. (2001) may be inaccurate and altered by compaction of CO_2 snow, which lowers the elevation over time (Smith, 2009, personal communication). Our model predicts that sublimation starts at L_S~198° (Fig. 7), which is later than L_S~163° predicted by the CO_2 mass loss from the Ames GCMS and from time variations in Mars' gravitational field (Smith et al., 2009); yet they were based on total mass loss of the poles, and at 86.5°S latitude, we are far from the polar cap edge that will begin sublimating first. Regional dust storms occurred in the southern hemisphere between L_S~225° and 245°, most likely dramatically affecting global-scale advection, providing an early heat source, and resulting in sublimation of the south seasonal cap about 35° L_S prior to the start of substantial solar insolation.

7.3. Seasonal and perennial variations in South polar features

In order to better understand the precise dynamics of the southern polar cap, we analyzed HiRISE images of different times of the year. Smoother surfaces are observed at higher elevations than layers presenting an irregular surface (Fig. 8). To identify the CO_2 ice features in the polar caps, we examined the CRISM observations in the 86°S region. To compare which features were CO_2 ice versus water ice, we used the CO_2/water ice indicator from CRISM observations (Murchie et al., 2007). This indicator was based off the ICER1 summary product a CO_2 (1.5 μm) and water ice (1.43 μm) band depth ratio, created with the CRISM Analysis Tool. CRISM observations show that the top flat features are composed of CO_2 ice while the lower irregular layers contain water ice (Fig. 8). The water ice layer is visible only during the summer (L_S=332°), being covered by seasonal CO_2 ice during the winter (L_S=287°, Fig. 8). This demonstrates the presence of a

Author's personal copy

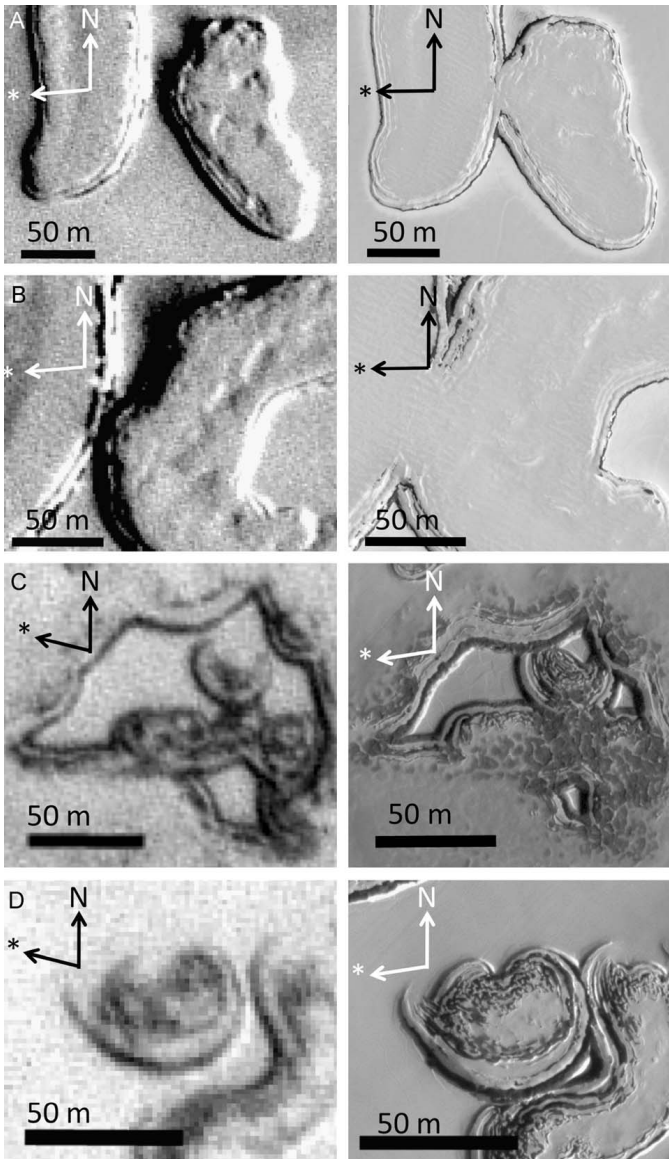

Fig. 11. Comparison between MGS-MOC (left) and MRO-HiRISE (right) images of the same region, indicating sublimation of the CO_2 features over 2–3 martian years. A and B are subframes of (left) MOC image E11-00955 and (right) HiRISE image PSP-004792-0940 at approximately the same season, L_S 285.57° and 289.5°, respectively, separated by 3 martian years. C and D are subframes of (left) MOC image R13-01242 and (right) HiRISe image PSP-005728-0935 at approximately the same season, L_S 330.26° and 331.8°, respectively, separated by 2 martian years. Feature heights have retreated an average of 0.43 ± 0.03 m year^{-1}. Arrows indicate direction toward the north (N) and the Sun (*), respectively.

Author's personal copy

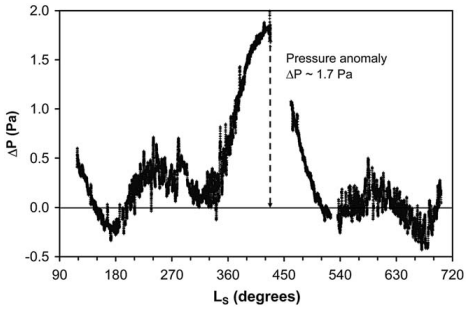

Fig. 12. Pressure data from Viking Lander 2 in Utopia Planitia at 48.27°N. The absolute pressure has been corrected for temperature variations, assuming the ideal gas law and that standard conditions are 210 K and 7.5 mbar. If the pressure followed the temperature variations, then all the data should be aligned on the 0 line. We observe small variations from the ideal case, probably due to adsorption in the regolith (Zent and Quinn, 1995), and a large positive pressure anomaly centered at L_S 420°, when insolation is maximum in the north hemisphere. Thus, we attribute this rise of pressure to the sublimation of the north polar cap.

seasonal cap of CO_2 on top of a perennial cap composed of CO_2 and water ice and supports the recent findings of exposed water ice by Brown et al. (2010).

There is good agreement between our model and MOLA results on a global scale; accordingly we want to verify its applicability on a local scale. Therefore, we studied the evolution of the width of the south perennial CO_2 features at latitude ~86°S by comparing HiRISE images of the same region, obtained between L_S~180° and ~360°, i.e. south hemisphere spring and summer (Fig. 9C). There are not an abundance of images in the polar region that overlap the same location at least during three different L_S's and include measurable sublimation features; therefore a limited number of images were analyzed (Table 2). The widths of the flat tops were measured in HiRISE images at different seasons to create the graph in Fig. 9B. Once it was confirmed that the top flat features were composed of CO_2 ice, measurements of the features were used to determine the sublimation rates. We observe that the local CO_2 ice layer features undergo significant decrease in width by 3 ± 1 m (Fig. 9B). Using a ~30° slope (Byrne and Ingersoll, 2003; Fig. 9A), this corresponds to a local elevation decrease of ~1.5 m during the summer, similar to our model prediction of ~1.3 m when the average yearly optical depth is set to 0.3. In addition, the sublimation of CO_2 starts at L_S 240° and ends around L_S 330° (Fig. 9B), in agreement with our model (Fig. 6A).

We observed series of parallel bands or "ripples" with relatively high albedo, along the pit walls of these sublimational features that are separated by higher albedo strips (Fig. 10). We did a survey of these features from several images, and the results are displayed in Table 3 for 16 observed ripples. We observed that the average distance between each ripple is 3.76 ± 0.76 m, all being within the range 3–4.5 m, which corresponds well to the 3 m lost from the width of the CO_2 seasonal cap (Fig. 9). This close correlation to the CO_2 features' widths (Fig. 9B) suggests that the ripples are remnants of the annual sublimation and deposition cycle, probably due to dust previously deposited on the slope of the slab and left after sublimation.

All previous observations focused on annual or shorter timescales, but trends should also be observed in longer timescales. To determine the net perennial variation of the CO_2 caps, we compared MOC images and HiRISE images of the southern polar cap, during the south polar summer. MOC and HiRISE images were either 2 or 3 martian years apart. Of this limited selection of HiRISE images, even fewer of them have MOC images that overlap the same features. Only two locations showed an overlap between MOC and HiRISE images. Despite the very few superimposed pictures, we observed a systematic retreat of the CO_2 perennial cap (Fig. 11). Using the shadows produced by the CO_2 slab at low sun declination, we determined the average thickness of the CO_2 perennial cap to be 2.3 ± 0.4 m in MOC images and 1.03 ± 0.14 m in HiRISE images of the same features separated by 3 martian years. These thicknesses correspond well to the thickness of the region classified as Unit B (1–3 m) of the south polar residual cap, compared to 5–10 m for the larger Unit A region (Thomas et al., 2009). Our thickness difference over both those images separated by 2 or 3 years gives an average sublimation rate of 0.43 ± 0.03 m yr^{-1}, fitting exactly the average for our model (0.43 ± 0.04 m yr^{-1}) using the optical depths from Vincendon et al. (2009) over a similar time span (Fig. 4). We argue that this number is higher than the 0.12 m yr^{-1} prediction of our model from the MOLA data (Fig. 7) because the optical depth and frequency of dust storms was less than at the time Smith et al. (2001) monitored elevation changes. Our model's predictions for the south caps are in agreement with findings over the last 8 years of the retreat of the south polar caps (Malin et al., 2001; Byrne and Ingersoll, 2003; Bibring et al., 2004; Zuber et al., 2007; Haberle et al., 2009).

7.4. North polar cap

In the north polar cap, HiRISE images do not show any measurable geomorphological features. We can, however, apply our model to the northern cap for a limited case. Since the north polar cap only consists of a seasonal cap of CO_2 and exposes H_2O ice for over half of the year, we chose to restrict our model to the period where CO_2 sublimates in the northern spring. We chose an average constant bolometric albedo of 0.5 for the seasonal cap (Paige et al., 1994; Paige and Keegan, 1994). We also chose to keep the emissivity the same as the model for the southern cap (0.91). Our model, then, predicts sublimation between L_S 360° and 540° (Fig. 6B). This coincides with Viking Lander 2 pressure measurements, showing a pressure anomaly (as compared to purely thermally controlled) between L_S 360° and 540° (Fig. 12) that we attribute to sublimation of the CO_2 seasonal cap in the northern spring, though a dynamic pressure wave, or a Rossby wave, could also be responsible (Hourdin et al., 1995). The reason that the rate is constant in the winter is that we decided to make the rate zero during seasons when the surface is in constant darkness, and we chose initial conditions that were consistent with the CO_2 elevation at the start of sublimation. The winter rate was chosen to be constant because the surface during that time varies from water to carbon dioxide ice; thus, we chose to apply our model only to periods where we were sure that CO_2 dominated the surface. Our slopes are fairly constant due to our choice of a constant albedo, but the MOLA data slopes support the conclusion that the albedo of the seasonal cap slowly increases over time and is consistent with the exposure of the water ice underneath the seasonal cap. The predicted start of sublimation in our model for 86.5°N is L_S~390°, compared to the L_S~330° measured by Smith et al. (2009) for the start of mass loss for the north polar cap. Furthermore, the higher resulting optical depths between 0.67 and 1 (Fig. 6B) suggest that the yearly balance between condensation and sublimation in the northern CO_2 cap would be less than or equal to zero, so that CO_2 ice cannot accumulate (i.e. no perennial cap) and only a seasonal cap is present.

Author's personal copy

8. Conclusions

Our experimental study demonstrates that the dynamics of the polar caps are predominately heat-transfer limited and controlled by the irradiance of the sun and hence the optical depth. Our model, therefore, based on irradiance of the sun, can predict trends in the mass balance of the polar caps. While the high Lambert albedos of the residual cap ($\sim$0.8) help to buffer the solar insolation in the southern summer (James et al., 2007; Byrne et al., 2008), our calculations show that albedo control is not enough to maintain stability of the cap on its own. If the rate of CO_2 loss remains constant ($\sim$0.4 m yr^{-1}), then the perennial CO_2 cap will disappear in approximately 6–7 martian years, assuming an average thickness of 2.4 m for the entire residual cap (Thomas et al., 2009). The low optical depths ($\sim$0.3) required to sustain that rate of loss are not likely to be maintained due to the frequency of dust storms, both regional and global that originate in the southern hemisphere, although that opacity number is well within the observations of the south polar cap from 2002 to 2008 by THEMIS (Smith, 2009) and compares well with Vincendon et al. (2009). If, however, it is maintained, the migration of CO_2 from the south polar cap will leave the south pole entirely composed of water ice. If this water ice starts to sublimate, then higher humidities in the martian atmosphere should be expected. Alternatively, if the sublimation trend inverts and progression of the south polar cap occurs in this timescale (Piqueux and Chistensen, 2008), then this suggests a short timescale climatic cycle linked to changes in the optical depth and local weather patterns.

Acknowledgments

The authors would like to acknowledge the help of Edgard Rivera-Valentin for his assistance with constraining some of the parameters of our model, Walter Graupner for laboratory assistance, David Smith for helpful conversation, and the suggestions of Mathieu Vincendon and an anonymous reviewer, which improved the quality of our manuscript.

References

Aharonson, O., Schorghofer, N., 2006. Subsurface ice on Mars with rough topography. Journal of Geophysical Research (Planets) 111, 11007.
Bibring, J.P., Langevin, Y., Poulet, F., Gendrin, A., Gondet, B., Berthé, M., Soufflot, A., Drossart, P., Combes, M., Bellucci, G., Moroz, V., Mangold, N., Schmitt, B., 2004. Perennial water ice identified in the south polar cap of Mars. Nature 428, 627–630.
Bonev, P.B, Hansen, G.B, Glenar, D.A., James, P.B, Bjorkman, J.E., 2008. Albedo models for the residual south polar cap on Mars: implications for the stability of the cap under near-perihelion global dust storm conditions. Planetary and Space Science 56, 181–193.
Brown, A.J., Calvin, W.M., McGuire, P.C., Murchie, S.L., 2010. CRISM south polar mapping: first Mars year of observations. Journal of Geophysical Research (Planets) 115, E00D13.
Byrne, S., Ingersoll, A.P., 2003. A sublimation model for martian south polar ice features. Science 299, 1051–1053.
Byrne, S., Zuber, M.T., Neumann, G.A., 2008. Internannual and seasonal behavior of martian residual ice-cap albedo. Planetary and Space Science 56, 194–211.
Chevrier, V., Sears, D.W.G., Chittenden, J.D., Roe, L.A., Ulrich, R., Bryson, K., Billingsley, L., Hanley, J., 2007. Sublimation rate of ice under simulated Mars conditions and the effect of layers of mock regolith JSC Mars-1. Geophysical Research Letters 34 (2), 02203.
Chittenden, J.D., Chevrier, V., Roe, L.A., Bryson, K., Pilgrim, R., Sears, D.W.G., 2008. Experimental study of the effect of wind on the stability of water ice on Mars. Icarus 196, 477–487.
Eluszkiewicz, J., Moncet, J.-L., 2003. A coupled microphysical/radiative transfer model of albedo and emissivity of planetary surfaces covered by volatile ices. Icarus 166, 375–384.
Fanale, F.P., Banerdt, W.B., Saunders, R.S., Johansen, L.A., Salvail, J.R., 1982. Seasonal carbon dioxide exchange between the regolith and atmosphere of Mars: experimental and theoretical studies. Journal of Geophysical Research 87 (B12), 10215–10225.
Fanale, F.P., Cannon, W.A., 1971. Adsoprtion on the martian regolith. Nature 230, 502–504.
Fishbaugh, K.E., Head III, J.W., 2001. Comparison of the north and south polar caps of Mars: new observations from MOLA data and discussion of some outstanding questions. Icarus 154, 145–161.
Forget, F., Hourdin, F., Talagrand, O., 1998. CO_2 snowfall on Mars: simulation with a general circulation model. Icarus 131, 302–316.
Giauque, W.F., Egan, C.J., 1937. Carbon dioxide: the heat capacity and vapor pressure of the solid. the heat of sublimation. thermodynamic and spectroscopic values of the entropy. Journal of Chemical Physics 5, 45–54.
Haberle, R.M., Forget, F., Colaprete, A., Schaeffer, J., Boynton, W.V., Kelly, N.J., Chamberlain, M.A., 2008. The effect of ground ice on the martian seasonal CO_2 cycle. Planetary and Space Science 56, 251–255.
Haberle, R.M., Kahre, M.A., Malin, M., Thomas, P.C., 2009. The disappearing south residual cap on Mars: where is the CO_2 going? In: International Workshop on Mars Polar Energy Balance and CO_2 Cycle, Abstract 7002.
Hourdin, F., Forget, F., Talagrand, O., 1995. The sensitivity of the martian surface pressure and atmospheric mass budget to various parameters: a comparison between numerical simulations and Viking observations. Journal of Geophysical Research 100, 5501–5523.
Ingersoll, A.P., 1970. Mars: occurence of liquid water. Science 168 (3934), 972–973.
James, P.B., Thomas, P.C., Wolff, M.J., Bonev, B.P., 2007. MOC observations of four Mars year variations in the south polar residual cap of Mars. Icarus 192, 318–326.
Kaviany, M., 2002. In: Principles of Heat Transfer. Wiley, New York.
Kieffer, H.H., Martin, T.Z., Peterfreund, A.R., Jakosky, B.M., Miner, E.D., Palluconi, F.D., 1977. Thermal and albedo mapping of Mars during the Viking primary mission. Journal of Geophysical Research 82, 4249–4291.
Langevin, Y., Poulet, F., Bibring, J.-P., Schmitt, B., Douté, S., Gondet, B., 2005. Summer evolution of the north polar cap of Mars as observed by OMEGA/Mars express. Science 307, 1581–1584.
Leighton, R.B., Murray, B.C., 1966. Behavior of carbon dioxide and other volatiles on Mars. Science 153, 136–144.
Malin, M.C., Caplinger, M.A., Davis, S.D., 2001. Observational evidence for an active surface reservoir of solid carbon dioxide on Mars. Science 294, 2146–2148.
Moore, S.R., Sears, D.W.G., 2006. On laboratory simulation and the effect of small temperature oscillations about the freezing point and ice formation on the evaporation rate of water on Mars. Astrobiology 6 (4), 644–650.
Murchie, S., Guinness, E., Slavney, S., 2007. Mars Reconnaissance Orbiter CRISM data product software interface specification, Version 1.3.3.
Paige, D.A., Bachman, J.E., Keegan, K.D., 1994. Thermal and albedo mapping of the polar regions of Mars using Viking thermal mapper observations: 1. North polar region. Journal of Geophysical Research 99, 25959–25991.
Paige, D.A., Keegan, K.D., 1994. Thermal and albedo mapping of the polar regions of Mars using Viking thermal mapper observations: 2. South polar region. Journal of Geophysical Research 99, 25993–26013.
Piqueux, S., Chistensen, P.R., 2008. Deposition of CO_2 and erosion of the martian south perennial cap between 1972 and 2004: implications for current climate change. Journal of Geophysical Research 113, 02006.
Pollack, J.B., Haberle, R.M., Murphy, J.R., Schaeffer, J., Lee, H., 1990. Simulations of the general circulation of the martian atmosphere. I—Polar processes. Journal of Geophysical Research. 95, 1447–1473.
Pollack, J.B., Haberle, R.M., Murphys, J.R., Schaeffer, J., Lee, H., 1993. Simulations of the general circulation of the martian atmosphere II—Seasonal pressure variations. Journal of Geophysical Research 98, 3149–3181.
Rapp, D., 2008. In: Human Missions to Mars: Enabling Technologies for Exploring the Red Planet. Praxis Publishing, Chichester, UK.
Rivera-Valentin, E.G., Chevrier, V.F., Ulrich, R., 2009. Time depdendent model for heat transfer and water vapor diffusion/adsorption at the phoenix landing side. In: Workshop on Modeling of Martian Hydrous Environments, Abstract 4020.
Schmidt, F., DoutÈ, S., Schmitt, B., Vincendon, M., Bibring, J.-P., Langevin, Y., 2009. Albedo control of seasonal South Polar cap recession on Mars. Icarus 200 (2), 374–394.
Sears, D.W.G., Chittenden, J.D., 2005. On laboratory simulation and the temperature dependence of evaporation rate of brine on Mars. Geophysical Research Letters 32 (L23203).
Sears, D.W.G., Moore, S.R., 2005. On laboratory simulation and the evaporation rate of water on Mars. Geophysical Research Letters 32 (L16202).
Smith, D.E., Zuber, M.T., Neumann, G.A., 2001. Seasonal variation of snow depth on Mars. Science 294, 2141–2146.
Smith, D.E., Zuber, M.T., Torrence, M.H., Dunn, P.J., Neumann, G.A., Lemoine, F.G., Fricke, S.K., 2009. Time variations of Mars' gravitational field and seasonal changes in the masses of the polar ice caps. Journal of Geophysical Research (Planets) 114, 05002.
Smith, M.D., 2009. THEMIS observations of Mars aerosol optical depth from 2002 to 2008. Icarus 202, 444–452.
Thomas, P.C., James, P.B, Calvin, W.M., Haberle, R, Malin, M.C., 2009. Residual south polar cap of Mars: stratigraphy, history, and implications of recent changes. Icarus 203, 352–375.

Author's personal copy

Titus, T.N., Kieffer, H.H., Chistensen, P.R., 2003. Exposed water ice discovered near the south pole of Mars. Science 299, 1048–1051.
Vincendon, M., Langevin, Y., Poulet, F., Bibring, J.-P., Gondet, B., Jougle, D., Team, OMEGA, 2008. Dust aerosols above the south polar cap of Mars as seen by OMEGA. Icarus 196, 488–505.
Vincendon, M., Langevin, Y., Douté, S., Bibring, J.-P., 2009. 3 Mars years of dust optical depth mapping by OMEGA above the south pole. In: Third International Workshop on Mars Polar Energy Balance and CO_2 Cycle, Abstract 7022.
Warren, S.G., Wiscombe, W.J., Firestone, J.F., 1990. Spectral albedo and emissivity of CO_2 in martian polar caps—model results. Journal of Geophysical Research 95, 14717–14741.
Zent, A.P., Quinn, R.C., 1995. Simutaneous adsorption of CO_2 and H_2O under Mars-like conditions and application to the evolution of the martian climate. Journal of Geophysical Research 100, 5341–5349.
Zuber, M.T., Phillips, R.J., Andrews-Hanna, J.C., Asmar, S.W., Konopliv, A.S., Lemoine, F.G., Plaut, J.J., Smith, D.E., Smrekar, S.E., 2007. Density of Mars' south polar layered deposits. Science 317, 1718–1719.

| Print

Journal Publishing Agreement

Elsevier Ltd

Your details

Article:	Sublimation Kinetics of CO2 Ice on Mars
Corresponding author:	Mr. David Garrison Blackburn
E-mail address:	
Journal:	Planetary and Space Science
Our reference	PSS2781
PII:	S0032-0633(09)00361-4
DOI:	10.1016/j.pss.2009.12.004

Your Status

- I am one author signing on behalf of all co-authors of the manuscript
- I am not a US Government employee but some of my co-authors are

Assignment of publishing rights

I hereby assign toElsevier Ltdthe copyright in the manuscript identified above (government authors not electing to transfer agree to assign a non-exclusive licence) and any supplemental tables, illustrations or other information submitted therewith that are intended for publication as part of or as a supplement to the manuscript (the "Article") in all forms and media (whether now known or hereafter developed), throughout the world, in all languages, for the full term of copyright, effective when and if the article is accepted for publication. This transfer includes the right to provide the Article in electronic and online forms and systems. No revisions, additional terms or addenda to this Agreement can be accepted without our express written consent. Authors at institutions that place restrictions on copyright assignments, including those that do so due to policies about local institutional repositories, are encouraged to obtain a waiver from those institutions so that the author can accept our publishing agreement.

Retention of Rights for Scholarly Purposes

I understand that I retain or am hereby granted (without the need to obtain further permission) rights to use certain versions of the Article for certain scholarly purposes, as described and defined below ("Retained Rights"), and that no rights in patents, trademarks or other intellectual property rights are transferred to the journal.

The Retained Rights include the right to use the Pre-print or Accepted Author Manuscript for Personal Use, Internal Institutional Use and for Scholarly Posting; and the Published Journal Article for Personal Use and Internal Institutional Use.

Author Representations / Ethics and Disclosure

Author representations

- The article I have submitted to the journal for review is original, has been written by the stated authors and has not been published elsewhere.
- The article is not currently being considered for publication by any other journal and will not be submitted for

such review while under review by this journal.
- The article contains no libellous or other unlawful statements and does not contain any materials that violate any personal or proprietary rights of any other person or entity.
- I have obtained written permission from copyright owners for any excerpts from copyrighted works that are included and have credited the sources in my article.
-
- If the article was prepared jointly with other authors, I have informed the co-author(s) of the terms of this publishing agreement and that I am signing on their behalf as their agent, and I am authorized to do so.

Funding agency requirements and other policies

For more information about the definitions relating to this agreement click here.

☑ **I have read and agree to the terms of the Journal Publishing Agreement. .**

22nd December 2009

T-copyright-v15/2009

-
-
-

Copyright (c) 2009 Elsevier B.V. All rights reserved.

DEFINITIONS

ACCEPTED AUTHOR MANUSCRIPT ("AAM")

Author's version of the manuscript of an article that has been accepted for publication and which may include any author-incorporated changes suggested through the processes of submission processing, peer review, and editor-author communications. AAMs should not include other publisher value-added contributions such as copy-editing, formatting and (if relevant) pagination, and should include the Appropriate Bibliographic Citation and a link to the final publication (generally through the relevant DOI).

APPROPRIATE BIBLIOGRAPHIC CITATION

Authors posting Accepted Author Manuscript online should later add a citation for the Published Journal Article indicating that the Article was subsequently published, and may mention the journal title provided they add the following text at the beginning of the document:

> "NOTICE: this is the author's version of a work that was accepted for publication in Planetary and Space Science. Changes resulting from the publishing process, such as peer review, editing, corrections, structural formatting, and other quality control mechanisms may not be reflected in this document. Changes may have been made to this work since it was submitted for publication. A definitive version was subsequently published in PUBLICATION, [VOL#, ISSUE#, (DATE)] DOI#"

COMMERCIAL USE

The use or posting of articles for commercial gain or to substitute for the services provided directly by the journal including:

the posting by companies of their employee-authored works for use by customers of such companies (e.g. pharmaceutica physician-prescribers); and

commercial exploitation such as directly associating advertising with such posting or the charging of fees for document de

INTERNAL INSTITUTIONAL USE

Use by the author's institution for classroom teaching at the institution (including distribution of copies, paper or electronic, and use in coursepacks and courseware programs) for scholarly purposes. For authors employed by companies, the use by that company for internal training purposes.

PERSONAL USE

Use by an author in the author's classroom teaching (including distribution of copies, paper or electronic), distribution of copies to research colleagues for their personal use, use in a subsequent compilation of the author's works, inclusion in a thesis or dissertation, preparation of other derivative works such as extending the article to book-length form, or otherwise using or re-using portions or excerpts in other works (with full acknowledgment of the original publication of the article).

PERMITTED SCHOLARLY POSTING

Voluntary posting of AAMs or Preprints by an author on open Web sites operated by the author or the author's institution for scholarly purposes, as determined by the author, or (in connection with Preprints) on preprint servers, but not for Commercial Use or Systematic Distribution. The author should include the Appropriate Bibliographic Citation when posting AAMs. Deposit in or posting to subject-oriented or centralised repositories (such as PubMed Central), or institutional repositories with mandates for systematic postings, is permitted only under specific agreements between the publisher and the repository, agency or institution, and only consistent with the Copyright Owner's policies concerning such repositories. To learn more about the publisher's policies and agreements with such agencies or institutions go to http://www.elsevier.com/fundingbodyagreements.

PREPRINT

Author's own write-up of research results and analysis that has not been refereed, nor had any other value added to it by a publisher (such as formatting, copy-editing, and the like).

PUBLISHED JOURNAL ARTICLE

The definitive final record of published research that appears or will appear in the journal and embodies all value-adding publisher activities including copy-editing, formatting and (if relevant) pagination.

SYSTEMATIC DISTRIBUTION

Policies or other mechanisms designed to aggregate and openly disseminate manuscripts or articles, or to substitute for journal-provided services, including:

the systematic distribution to others via e-mail lists or listservers (to parties other than known colleagues), whether for a

the posting of links to sponsored articles by commercial third parties including pharmaceutical companies;

institutional, funding body or government manuscript posting policies or mandates that aim to aggregate and openly distri peer reviewed manuscripts or published journal articles authored by its researchers or funded researchers; and

subject repositories that aim to aggregate and openly distribute accepted peer reviewed manuscripts or published journal researchers in specific subject areas.

CHAPTER 3

SOLAR PHASE CURVES AND PHASE INTEGRALS FOR THE LEADING AND TRAILING HEMISPHERES OF IAPETUS FROM THE *CASSINI* VISUAL INFRARED MAPPING SPECTROMETER

In this chapter, we look at the directional scattering properties of Iapetus' surface in order to derive the necessary phase integrals to produce a bolometric Bond albedo map for Iapetus; this chapter was published in the journal *Icarus*. Joel A. Mosher collected the disk-integrated observations of Iapetus, and Dr. Bonnie J. Buratti supplied the idea and contributed her vast knowledge of surface photometry. Dr. Richard Ulrich provided the funding as PI of the proposal that supported this project through the Arkansas Space Grant Consortium. I performed the data analysis of the disk-integrated data set, collected and analyzed the disk-resolved observations of the bright material, calculated the phase integrals for Iapetus, and all remaining details not listed.

3.1 Abstract

We performed photometry of *Cassini* Visual Infrared Mapping Spectrometer (VIMS) observations of Iapetus to produce the first phase integrals calculated directly from solar phase curves of Iapetus for the leading hemisphere and to estimate the phase integrals for the trailing hemisphere. We also explored the phase integral dependence on wavelength and geometric albedo. The extreme dichotomy of the brightness of the leading and trailing sides of Iapetus is reflected in their phase integrals. Our phase integrals, which are lower than the results of Morrison *et al*. (1975) and Squyres *et al*. (1984), have profound implications on the energy balance and volatile transport on this icy satellite.

3.2. Introduction

In the saturnian system, Iapetus exhibits the most extreme variations in albedo of the satellites, with an extremely dark, leading hemisphere and a much brighter, trailing hemisphere. The dark material might be composed of hydrocarbon polymers (Cruikshank *et al*., 2008) along with a CO_2 absorption band, while the bright side is mostly water ice (Buratti *et al*., 2005). In recent high-resolution images of the border regions, this dark material is juxtaposed with the bright, icy material; although the demarcations are not sudden in terms of regional albedo, this effect creates a Dalmatian-like, spotty surface appearance on the local scale. This surface dichotomy produces a possibly dynamic system with volatile transport of carbon dioxide and water vapor from the large differences in surface temperature (Palmer and Brown, 2007).

In light of this unique variation and due to the limited previous work, Iapetus is a prime target for a photometric study of the changes in brightness with phase angle. Morrison *et al*. (1975) estimated a phase integral of 1.3 for the bright side from radiometry. After the Voyager fly-by, Squyres *et al*. (1984) estimated a phase integral of 0.3 for the dark hemisphere and 0.9 for the light from disk-resolved photometry from the Voyager camera centered at 0.47 microns.

Observations obtained by the *Cassini* Visual Infrared Mapping Spectrometer over the portion of the solar spectrum that includes 99% of the radiated power and over a full range of solar phase angles provide an unprecedented opportunity to study the photometric and thermal properties of icy satellites. Since the bolometric Bond albedo describes the energy balance on a planetary surface, measurements obtained over 99% of the solar spectrum is significant. For the case of Iapetus, this opportunity is particularly

compelling because thermal segregation is believed to help create and sustain its unusual albedo dichotomy (Spencer and Denk, 2010; Denk *et al*., 2010). As a first step in understanding the thermal properties of Iapetus, we have calculated the phase integrals of Iapetus between 0.36 and 5.12 microns, though noise was a major factor beyond 2.5 microns for the trailing hemisphere.

The phase integral, which is a numerical representation of the directional scattering properties of a planet or satellite, is also the ratio between the Bond albedo, which is crucial for thermal modeling and energy balance, and the geometric albedo. Yet, an extensive study of the phase integrals at every wavelength has yet to be performed for Iapetus. In this paper, we took advantage of the phase angle and wavelength coverage of *Cassini*'s VIMS instrument to produce the first phase integrals calculated directly from solar phase curves of the leading side and to estimate the phase integrals for the trailing side. We also explored the wavelength dependence of the phase integrals and the dependence of the phase integrals on the geometric albedo. Given the large albedo differences on Iapetus, this exercise also affords a prime opportunity to study the effects of albedo and wavelength on the phase curves of airless bodies.

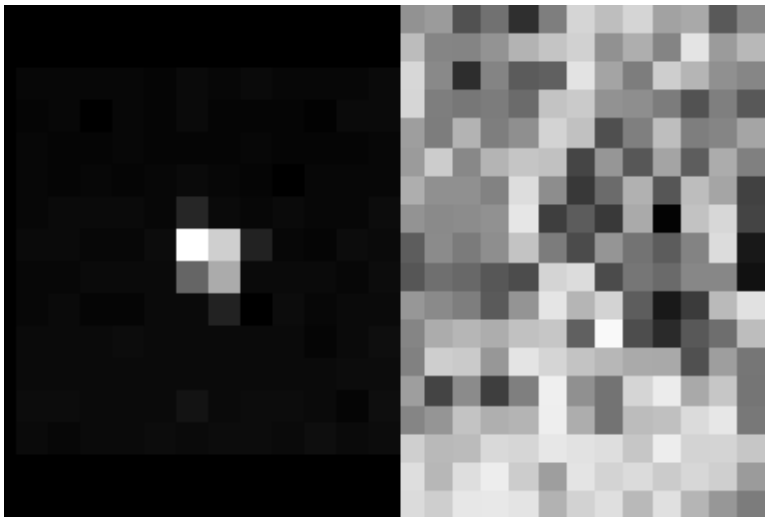

Figure 3.1 *– (left) Band 1 of Cassini VIMS-IR cube 1536445566_1 included in the disk-integrated phase curve for the leading hemisphere; the range is 3,217,420 km. (right) Band 1 of Cassini VIMS-IR cube 1568131937_1 used in the high-resolution disk-resolved photometry of the bright material; the image was taken at a range of 11,766 km during the 2007 targeted flyby of the trailing hemisphere.*

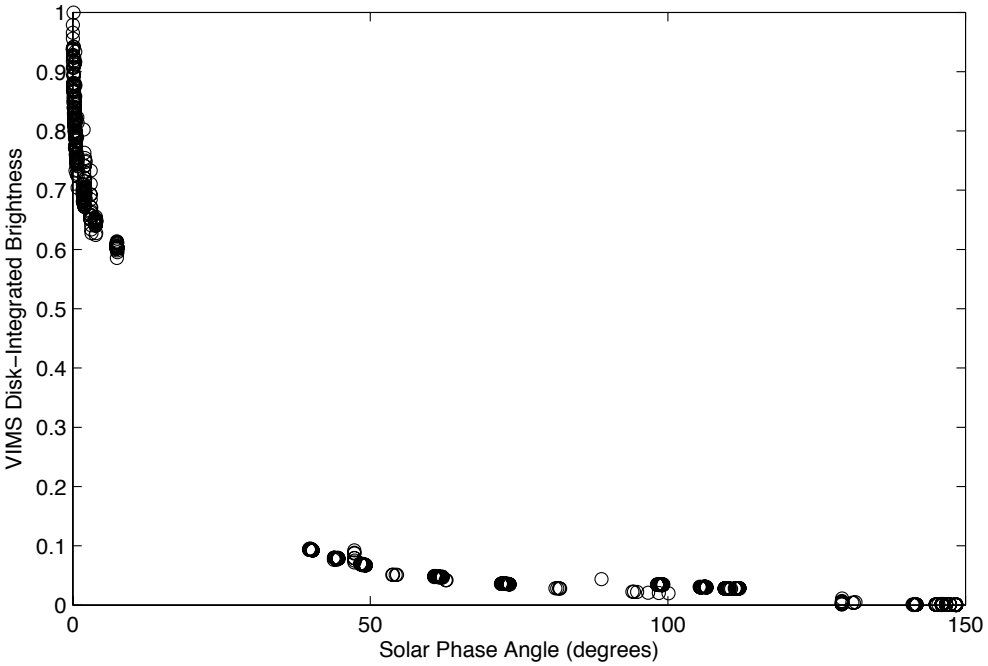

Figure 3.2 *– VIMS disk-integrated brightness $\phi(\alpha)$ versus solar phase angle α for the dark, leading hemisphere at 1.15 microns (Band 17 of VIMS-IR).*

3.3. Data Analysis – Leading Hemisphere

For the dark leading hemisphere (0-180°W longitude), we used all available non-proprietary VIMS cubes of Iapetus that captured a full disk of the leading side (totaling 451, Fig. 3.1) and performed disk-integrated photometry at every band of the VIMS instrument (96 for VIMS-VIS and 256 for VIMS-IR). These observations were created by summing the flux in every pixel that included a signal from the leading side and then correcting for spacecraft distance. Figure 3.2 displays the solar phase curve at 0.47 microns for the dark material. At each band of the VIMS instrument, we normalized disk-integrated brightness to be 1 at $\alpha = 0°$. Four VIMS cubes (CM_1536468302_1, CM_1536468456_1, CM_1536468321_1, CM_1536468475_1) that all had a phase angle of 0.05° were averaged for the normalization to 0°. From the available solar phase angle coverage (~0 – 10°, 40-150°), we calculated the phase integral directly by definition (Russell, 1916; Veverka, 1977):

$$q = 2\int_0^{\pi} \phi(\alpha)\sin(\alpha)d\alpha \qquad (3.1.)$$

where q is the phase integral; $\Phi(\alpha)$ is the normalized disk-integrated brightness (Fig. 3.2); and α is the solar phase angle. The phase integral describes the directional scattering properties of a planetary body; in effect it is the "beam pattern" of the object. To calculate the phase integral, normalized disk-integrated brightness was derived from third-order polynomial fits of the data spanning the total available phase angle coverage. It should be noted that since these solar phase curves include the entire leading hemisphere, the phase integral calculated here is more an average of the phase integral for the leading hemisphere and not the phase integral for only dark material, as the

leading hemisphere contains the largest albedo variations on Iapetus (Squyres *et al.*, 1984).

3.4. Data Analysis – Trailing Hemisphere

Unfortunately, the coverage of the bright, trailing side (180-359° W longitude) was not sufficient (~ 33°, 100-140°) to produce phase integrals with an acceptable margin for error using the technique above, as the opposition region (α < 3 degrees) is crucial to normalizing the values correctly. Instead, we chose to use disk-resolved photometry of twelve high-resolution VIMS cubes (Table 3.1, Fig. 3.1) spanning phase angles (~13-33°) of the brightest areas available, noting that the decrease in the surface phase function was quite linear at 0.47 microns from previous disk-resolved photometry of *Voyager* data from Squyres *et al.* (1984).

From our high resolution cubes, we developed our own surface phase functions (Fig. 3.3) for the purpose of estimating phase integrals for the bright material. The surface phase function represents the decrease in brightness of the surface material as a function of solar phase angle and was calculated by the following equation from Hapke (1963), Irvine (1966), and Squyres *et al*. (1984):

$$I(i,\varepsilon,\alpha) = F\left(\frac{\mu_0}{\mu_0 + \mu}\right) f(\alpha) \qquad (3.2.)$$

where i = incidence angle, ε = emission angle, α = phase angle, μ = cos ε, μ_0 = cos i, I = intensity of scattered light, F = incident solar flux at i = 0 divided by pi, and $f(\alpha)$ = surface phase function.

Table 3.1. *High Resolution VIMS Cubes of the Bright Material*

Cube	Phase Angle	Latitude	Longitude	Pixels
1568131937_1	24.25	-10	234	324
1568129331_1	13.42	-45	208	900
1568129201_1	12.68	-41	201	900
1568129461_1	14.47	-42	206	900
1568129671_1	16.07	-43	201	25
1568136573_1	29.06	-10	247	144
1568131010_1	24.39	0	199	4
1568136449_1	29.12	11	246	144
1568135049_1	28.74	-12	219	16
1568139139_1	30.79	12	225	16
1568138316_1	30.81	45	216	16
1568163600_1	33.37	47	220	1

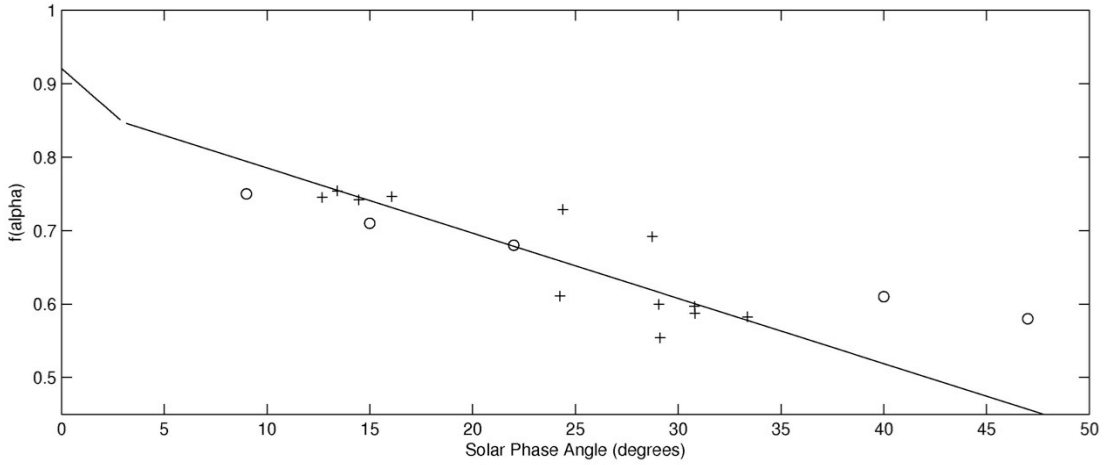

Figure 3.3 – *The surface phase function for the bright material at 0.47 microns is a linear fit (black line) to our data from the twelve sampled cubes (pluses). At less than 3˚, we modified the slope to reflect the known phase coefficient (0.03 mag/deg) for the bright hemisphere from Noland et al. (1974) and Cruikshank (1979). We compared our results to a surface phase function by Squyres et al. (1984) (circles) from Voyager ISS clear-filter images to verify our method.*

Once surface phase functions were produced for each wavelength of the VIMS instrument, we were able to approximate the disk-integrated brightness by assuming a spherical body and using the following equation:

$$\phi(\alpha) = \frac{f(\alpha)\left(1 - \sin\frac{\alpha}{2}\tan\frac{\alpha}{2}\ln\left(\cot\frac{\alpha}{4}\right)\right)}{f(0°)} \qquad (3.3.)$$

which is the formula used by Buratti and Veverka (1983) when *A*, a weighting parameter between a lunar-like and Lambert scattering function, is set to 1 for a lunar-like surface. Then, phase integrals at each wavelength for the trailing side were calculated using Eq. 3.1, extrapolating a linear fit from our limited phase angle coverage (Fig. 3.2); our fit compares well with Voyager results from Squyres *et al*. (1984) at 0.47 microns at the wavelengths in which VIMS data were available (Fig. 3.3). In order to estimate *f(0)*, we chose to include the opposition surge effect, which has been shown to typically affect the other icy satellites inside of ~3° (Buratti *et al.* (2009); Pitman *et al.* (2010). Therefore, we modified the slope at 3° to the phase coefficient 0.03 mag/deg, which has been determined by ground-based observations and has shown little wavelength dependency between the ultraviolet and near-infrared filters (Noland *et al*., 1974; Cruikshank, 1979).

3.5. Results

Our calculated phase integrals for the leading and trailing hemispheres are shown in Fig 3.4B and Fig 3.5B, respectively. We compared our results to spectra from normal reflectance of the leading hemisphere from a mosaic of VIMS cubes and of the bright material using our derived $f(\alpha)$ curves and plotted the relationship for each wavelength covered by the VIMS instrument (Fig. 3.4A and 3.5A). For the leading side normal reflectance (Fig. 3.4A), we used a lunar-like scattering law (Eq. 3.2) and surface phase

functions determined from high-resolution cubes of the leading hemisphere to approximate the average normal reflectance for the leading hemisphere and to adjust appropriately for the bright material contamination evident in the leading hemisphere phase curves. For the trailing side (Fig 3.5A), since we used high-resolution cubes of the bright material, we determined the normal reflectance from our surface phase function curves, noting that half of *f(0)* is equal to the normal reflectance. Since the effects of multiple scattering do not become significant until normal reflectance rises above ~0.6 (Buratti, 1984; Buratti and Veverka, 1985), the normal reflectance is a close approximation of the geometric albedo for Iapetus. Our spectra compare well with the findings of Buratti *et al.* (2005). Clearly, the phase integral corresponds to changes in geometric albedo for both the dark regions (absorption feature at 3 microns) and light (key water ice absorption bands at 1.5 and 2.1 microns): as the albedo increases, the value for the phase integral also increases. To illustrate the relationship between geometric albedo and phase integral more clearly, we chose to plot the phase integral versus geometric albedo at each band of the VIMS instrument for both the leading (pluses) and trailing (circles) hemispheres (Fig. 3.6) and to compare our results for Iapetus with the findings of the other saturnian icy satellites by Pitman *et al.* (2010). Plotting the Pitman *et al.* (2010) data onto Figure 3.6 revealed highly linear trends, and we chose to use a linear best-fit line that included both the visible and near infrared to represent the slopes of Enceladus, Tethys, Dione, Mimas, and Rhea in relation to Iapetus.

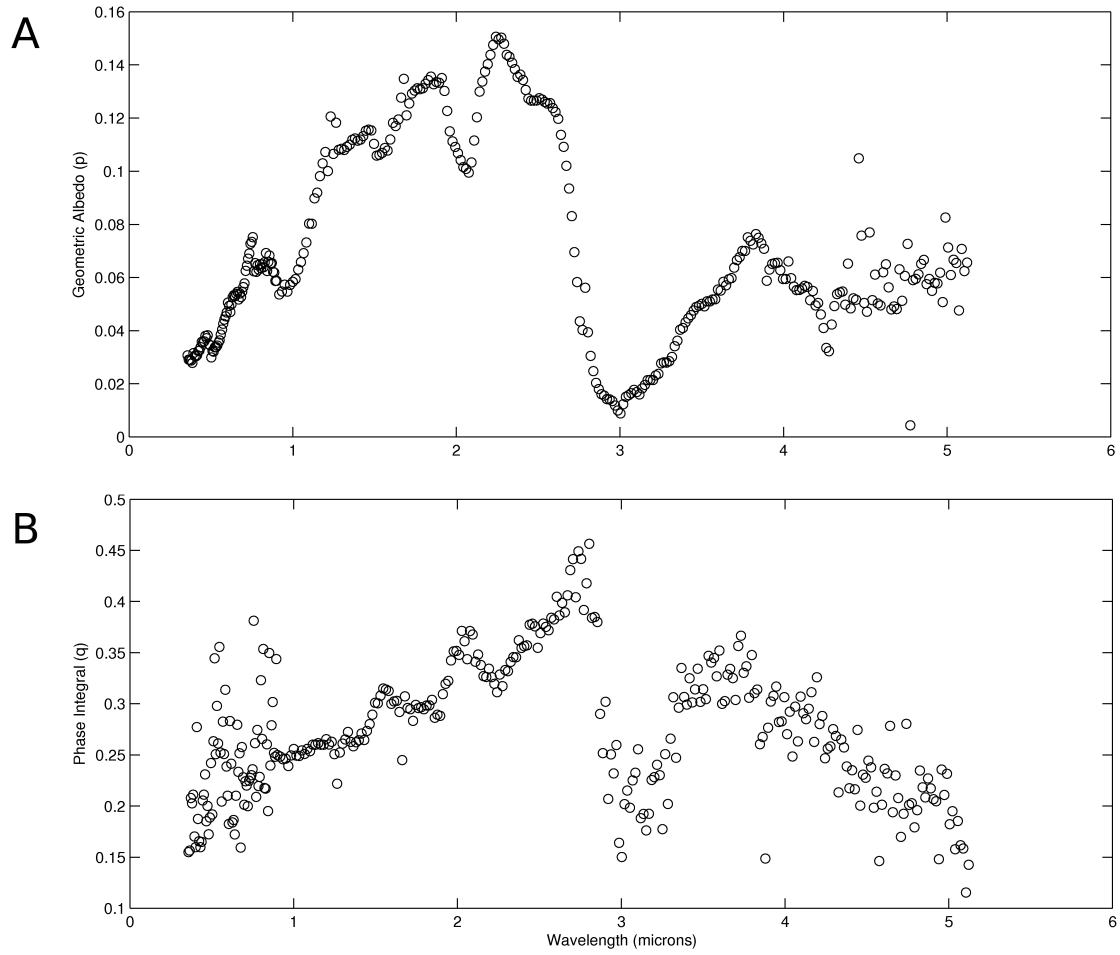

Figure 3.4 *– **A)** Geometric albedo of the leading side versus wavelength from normalized reflectance from VIMS cubes. **B)** Phase integrals calculated using disk-integrated photometry for the leading side versus wavelength.*

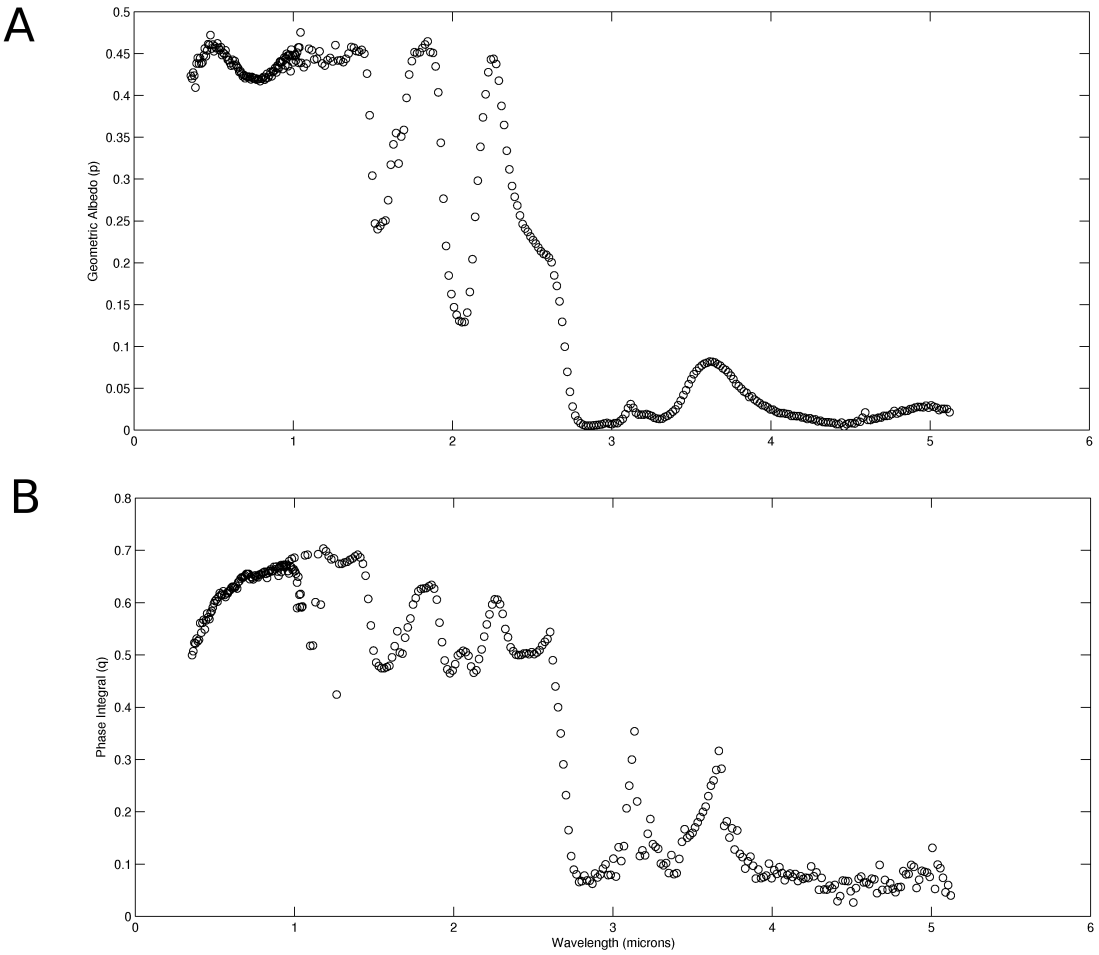

Figure 3.5 *– **A**) Geometric albedo of the trailing side versus wavelength from half of f(0). **B**) Phase integrals estimated using disk-resolved photometry for the trailing side versus wavelength.*

3.6 Discussion and Summary

It is well known that generally for a planetary body the phase integral increases with geometric albedo while the intensity of the opposition surge effect decreases with increasing geometric albedo (Veverka, 1977), and our results conform to that trend. This relationship is expected, because as the albedo increases, the degree of multiple scattering, which tends to be more isotropic than single scattered radiation, also increases. These multiple-scattered photons tend to make the phase curve more "Lambertian", which increases the area under the normalized integrated phase curve. Multiple scattering also isotropizes the single scattering phase function and partly illuminates primary shadows: both effects increase the area under the normalized integrated phase curve. Although most of the increase in the phase integral is from an increased geometric albedo, another component is from additional effects of illuminated shadows caused by rough features and the properties of the surface - particle size and shape, for example - which affect the single particle phase function (Buratti and Veverka, 1985). This texture difference clearly alters the slope between the leading and the trailing hemispheres (Fig. 3.6). The remaining deviance is from noise and error in the measurement. The scatter in the data in Fig. 3.6 is indicative of two factors for the dark material: at low albedos, noise affecting the VIMS instrument competes with the signal at the surface, and at higher wavelengths, differences in the noise levels of individual cubes produces scatter in our data near the opposition surge region even after the bands had been filtered by averaging the 11 adjacent bands. For the light material, at longer wavelengths (> 2.5 microns) where water ice absorbs nearly all light, the noise becomes a relevant factor as well, since the

signal is very weak; also, the limitation in number of high-resolution cubes (12) needed for disk-resolved photometry precluded having data with a good signal.

Palmer and Brown (2007) extrapolated a linear approximation of the relationship between the phase integral and geometric albedo from two solitary points, one of which was not based on Iapetus, in order to make a map of the Bond albedo. The two points used by Palmer and Brown (2007) for their line included one from the dark material estimated from Squyres *et al*. (1984) and the other from an extrapolation to Europa from Buratti and Veverka (1983) with the assumption that the brightest area on Iapetus (p = 0.65) had a phase integral of 1. The slope (1.23) from their fit compared to Figure 3.6 produces an overestimation of the phase integral on Iapetus, though our geometric albedos include the opposition surge, which may account for some of the variance. Our graph (Fig. 3.6) also illustrates that a purely linear approximation for all of Iapetus is not valid, as the slopes for the leading and trailing hemispheres are slightly different. Lower values for the phase integrals translate into lower Bond albedos and will hence increase the rates of volatile transport of CO_2 modeled by Palmer and Brown (2007).

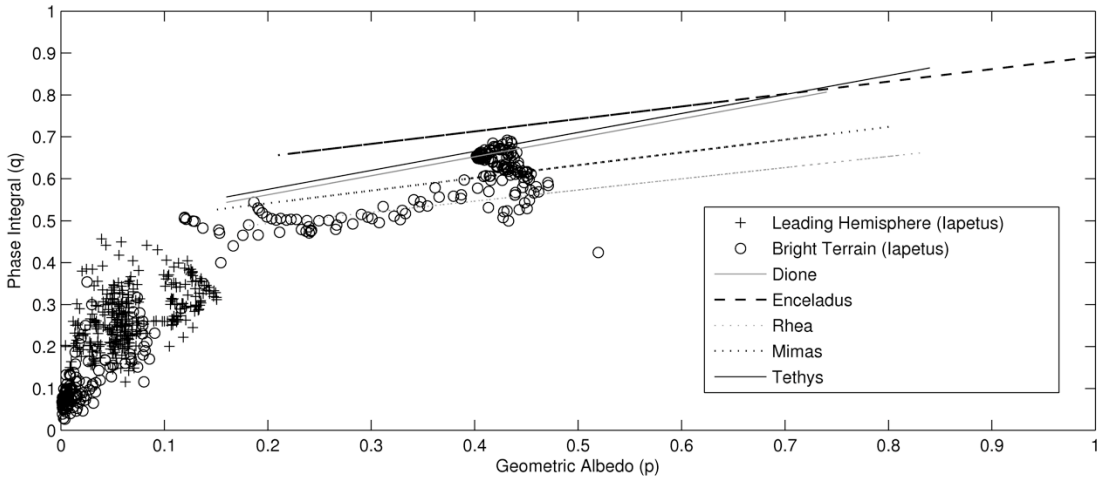

Figure 3.6 – *Phase integral versus geometric albedo for Iapetus for the dark, leading side pluses) and the bright, trailing side (circles). The lines are linear fits to the Pitman et al. (2010) results for Dione, Enceladus, Rhea, Mimas, and Tethys.*

Table 3.2. *Phase integrals from our results on Iapetus compared to the other saturnian icy satellites from Pitman et al. (2010) at selected wavelengths.*

	VIMS-VIS λ (μm)						Average of VIMS-VIS and VIMS-IR λ (μm)		VIMS-IR λ (μm)				
	0.35	**0.40**	**0.51**	**0.60**	**0.70**	**0.81**	**0.90**	**1.00**	**1.52**	**1.80**	**2.02**	**2.23**	**3.60**
Iapetus													
q_{lead}	0.16 ± 0.04	0.16 ± 0.04	0.26 ± 0.05	0.18 ± 0.06	0.22 ± 0.05	0.35 ± 0.04	0.25 ± 0.05	0.26 ± 0.04	0.31 ± 0.05	0.30 ± 0.05	0.37 ± 0.04	0.32 ± 0.04	0.35 ± 0.05
q_{trial}	0.50 ± 0.10	0.52 ± 0.09	0.61 ± 0.10	0.63 ± 0.10	0.65 ± 0.10	0.66 ± 0.11	0.67 ± 0.09	0.67 ± 0.08	0.47 ± 0.11	0.63 ± 0.11	0.50 ± 0.09	0.58 ± 0.10	0.23 ± 0.13
Rhea													
q	0.55 ± 0.06	0.60 ± 0.04	0.64 ± 0.04	0.66 ± 0.05	0.69 ± 0.04	0.70 ± 0.05	0.68 ± 0.04	0.67 ± 0.05	0.60 ± 0,05	0.66 ± 0.05	0.56 ± 0.07	0.67 ± 0.05	0.45 ± 0.10
q_{lead}	0.58 ± 0.05	0.64 ± 0.05	0.68 ± 0.06	0.70 ± 0.05	0.73 ± 0.08	0.74 ± 0.09	0.72 ± 0.06	0.72 ± 0.06	0.60 ± 0.05	0.70 ± 0.07	0.58 ± 0.08	0.70 ± 0.06	0.50 ± 0.10
q_{trial}	0.54 ± 0.06	0.57 ± 0.06	0.61 ± 0.06	0.63 ± 0.06	0.66 ± 0.08	0.68 ± 0.09	0.63 ± 0.07	0.64 ± 0.11	0.60 ± 0.05	0.63 ± 0.05	0.55 ± 0.07	0.64 ± 0.05	0.40 ± 0.11
Dione													
q	0.78 ± 0.05	0.82 ± 0.07	0.77 ± 0.06	0.75 ± 0.07	0.78 ± 0.06	0.76 ± 0.06	0.81 ± 0.10	0.85 ± 0.09	0.66 ± 0.05	0.83 ± 0.16	0.55 ± 0.07	0.80 ± 0.15	0.58 ± 0.06
q_{lead}	0.89 ± 0.05	0.93 ± 0.07	0.84 ± 0.06	0.86 ± 0.07	0.88 ± 0.06	0.88 ± 0.06	0.87 ± 0.10	0.93 ± 0.09	0.70 ± 0.15	0.86 ± 0.16	0.58 ± 0.07	0.87 ± 0.15	0.65 ± 0.06
q_{trial}	0.68 ± 0.05	0.74 ± 0.06	0.71 ± 0.06	0.68 ± 0.07	0.71 ± 0.05	0.68 ± 0.05	0.72 ± 0.08	0.73 ± 0.06	0.64 ± 0.02	0.72 ± 0.09	0.56 ± 0.07	0.75 ± 0.09	0.57 ± 0.06
Tethys													
q	-	-	-	-	-	-	0.68 ± 0.07	0.66 ± 0.05	0.77 ± 0.05	0.86 ± 0.05	0.67 ± 0.02	0.86 ± 0.05	0.48 ± 0.11
q_{lead}	-	-	-	-	-	-	0.68 ± 0.07	0.66 ± 0.05	0.76 ± 0.05	0.86 ± 0.05	0.67 ± 0.02	0.86 ± 0.05	0.49 ± 0.11
q_{trial}	-	-	-	-	-	-	0.69 ± 0.03	0.72 ± 0.03	0.86 ± 0.02	0.92 ± 0.02	0.75 ± 0.02	0.92 ± 0.02	0.42 ± 0.08
Mimas													
q	-	-	-	-	-	-	0.80 ± 0.05	0.79 ± 0.03	0.83 ± 0.05	0.85 ± 0.05	0.86 ± 0.05	0.85 ± 0.05	0.80 ± 0.05
q_{lead}	-	-	-	-	-	-	0.80 ± 0.02	0.78 ± 0.02	0.82 ± 0.04	0.84 ± 0.04	0.84 ± 0.04	0.85 ± 0.03	0.80 ± 0.06
q_{trial}	-	-	-	-	-	-	0.84 ± 0.04	0.82 ± 0.03	0.90 ± 0.07	0.89 ± 0.05	0.96 ± 0.07	0.90 ± 0.05	0.85 ± 0.05
Enceladus													
q	-	-	-	-	-	-	0.85 ± 0.10	0.90 ± 0.13	0.73 ± 0.06	0.83 ± 0.09	0.69 ± 0.03	0.84 ± 0.09	0.57 ± 0.06
q_{lead}	-	-	-	-	-	-	0.87 ± 0.08	0.90 ± 0.13	0.71 ± 0.04	0.81 ± 0.08	0.68 ± 0.02	0.83 ± 0.08	0.55 ± 0.07
q_{trial}	-	-	-	-	-	-	0.90 ± 0.10	0.91 ± 0.11	0.76 ± 0.05	0.84 ± 0.10	0.72 ± 0.07	0.85 ± 0.10	0.59 ± 0.03

When compared with other icy satellites (Table 3.2), the dark material has a phase integral closer to the dark surface of Phoebe ($q = 0.29 \pm 0.03$); however, Phoebe's phase integral showed no significant wavelength dependence (Buratti *et al*., 2008). The slope and magnitude of our measurements for the bright, icy material on Iapetus compare best to the satellites of Dione, Rhea, and Mimas (Pitman *et al*., 2010). The phase integrals of Rhea and Dione would be expected to be more similar to Iapetus, as these icy satellites also exhibit insignificant multiple scattering and are more lunar-like than the brighter satellites of Mimas, Tethys, and Enceladus (Buratti, 1984); however since their geometric albedos are slightly higher (Table 3.2), the phase integrals at each wavelength band are not as comparable. Since the albedoes and morpholology of Dione and Rhea are similar to the bright side of Iapetus, it is reasonable to assume that the surface texture of Dione and Rhea is also similar to the bright side of Iapetus. (except perhaps for some accumulation on their surfaces of micron-sized particles from the E-ring). The dark material on Iapetus may have settled onto a moon that looked more like a "typical" icy saturnian satellite.

Compared with previous results, our phase integrals for the bright side are lower than the estimates of Morrison *et al*. (1975) ($q \sim 1.3$) based on radiometry, yet Morrison used inaccurate numbers for Iapetus' radius and the average geometric albedo for the trailing side (835 km and 0.35 instead of 730 km and 0.42 (Squyres et al., 1984)). Our results for the bright and dark hemispheres at 0.47 microns are 0.58 ± 0.10 and 0.20 ± 0.06, respectively, compared to the results of Squyres *et al*. (1984) of ~0.9 and ~0.3. The difference in the phase integral for the bright region can be explained based on the coverage of the *Cassini* spacecraft relative to *Voyager*. *Voyager* provided excellent

coverage of the north polar region (Squyres *et al*., 1984), where geometric albedos approach 0.65, and a phase integral closer to 1 like on Europa's surface is not surprising. Our twelve high-resolution images centered on a region where the average geometric albedo is 0.43 near the equator, since *Cassini* had poor coverage of both poles of Iapetus. Yet, *Cassini* had better coverage of the dark region, which is of course weighted more in our approximation of the leading hemisphere since we included every cube available. However, if Iapetus follows a similar trend to the other icy satellites of Saturn (Fig 3.6; Pitman *et al.*, 2010), which is likely to be the case, then extrapolating the slope up to the highest albedo region (0.65) would produce a phase integral of ~0.7. Squyres et al. (1984) explain that they used a derived value twice the average geometric albedo of the trailing side (2 x 0.42) as their $f(0)$, yet the locations they sampled for their $f(\alpha)$ have actual geometric albedoes closer to 0.5 from their own normal reflectance maps; this would also result in inflated estimates for the phase integral for the bright terrain. Our results of lower phase integrals than previous findings will translate into lower Bond albedos and higher temperatures in thermal models, which may have profound implications on volatile transport on Iapetus (Palmer and Brown, 2007; Spencer and Denk, 2010).

3.7 References

Cruikshank, D.P. and 26 coauthors, 2008. Hydrocarbons on Saturn's satellites Iapetus and Phoebe. Icarus 193, 334-343.

Buratti, B.J and Veverka, J., 1983. Voyager photometry of Europa. Icarus 55, 93-110.

Buratti, B.J., 1984. Voyager disk resolved photometry of the saturnian satellites. Icarus. 59, 392-405.

Buratti, B.J. and Veverka, J., 1985. Photometry of rough planetary surfaces: The role of multiple scattering. Icarus. 64, 320-328.

Buratti, B.J. and 28 co-authors, 2005. Cassini Visual and Infrared Mapping Spectrometer observations of Iapetus: Detection of CO_2. Astrophys. J. 622, L149-L152.

Buratti, B.J, Soderlund, K., Bauer, J., Mosher, J.A., Hicks, M.D., Simonelli, D.P., Jaumann, R., Clark, R.N., Brown, R.H., Cruikshank, D.P., Momary, T., 2008. Infrared (0.83-5.1 μm) photometry of Phoebe from the Cassini Visual Infrared Mapping Spectrometer. Icarus. 193, 309-322.

Buratti, B.J., Mosher, J.A., Abramson, L., Akhter, N., Clark, R.N., Brown, R.H, Baines, K.H., Nicholson, P.D., DeWet, S., 2009. Opposition surges of the satellites of Saturn from the Cassini Visual infrared mapping spectrometer. LPSC XV, Abstract 1738.

Cruikshank, D.P., 1979. The surfaces and interiors of Saturn's satellites. Rev. Geophys. Space Phys. 17, 165-176.

Denk, T., Neukum, G., Roatsch, T., Porco, C.C., Burns, J.A., Galuba, G.G., Schmedemann, N., Helfenstein, P., Thomas, P.C., Wagner, R.J., West, R.A., 2010. Iapetus: Unique surface properties and a global color dichotomy from Cassini imaging. Science 327, 435-439.

Hapke, B. W., 1963. A theoretical photometric function for the lunar surface. J. Geophys. Res. 68, 4571-4586.

Irvine, W.M., 1966. The shadowing effect in diffuse reflection. J. Geophys. Res. 71, 2931-2937.

Morrison, D., Jones, T.J., Cruikshank, D.P. Murphy, R.E., 1975. 2 faces of Iapetus. Icarus 24, 157-171.

Noland, M., Veverka, J., Morrison, D., Cruikshank, D.P., Lazarewicz, A.R., Morrison, N.D., Elliot, J.L., Goguen, J., Burns, J.A., 1974. Six-color photometry of Iapetus, Titan, Rhea, Dione, and Tethys. Icarus 23, 334-354.

Palmer, E.E. and Brown, R.H., 2007. The stability and transport of carbon dioxide on Iapetus. Icarus 195, 434-446.

Pitman, K.M., Buratti, B.J., Mosher, J.A, 2010. Disk-integrated bolometric Bond albedos and rotational light curves of saturnian satellites from *Cassini* Visual and Infrared Mapping Spectrometer. Icarus 206, 537-560.

Russell, H. N, 1916. On the albedo of planets and their satellities. Astrophys. J. 43, 173-195.

Spencer, J.R., Denk, T., 2010. Formation of Iapetus' extreme albedo dichotomy by exogenically triggered thermal ice migration. Science 327, 432-435.

Squyres, S.W., Buratti, B.J., Veverka, J., Sagan, C., 1984. Voyager photometry of Iapetus. Icarus 59, 426-435.

Veverka, J., 1977. Photometry of satellite surfaces. In Planetary Satellites. J.A. Burns, Ed., 171-231. Univ. of Arizona Press, Tucson.

APPENDIX B

Author's personal copy

Icarus 209 (2010) 738–744

Contents lists available at ScienceDirect

Icarus

journal homepage: www.elsevier.com/locate/icarus

Solar phase curves and phase integrals for the leading and trailing hemispheres of Iapetus from the *Cassini* Visual Infrared Mapping Spectrometer

David G. Blackburn [a,*], Bonnie J. Buratti [b], Richard Ulrich [a], Joel A. Mosher [b]

[a] Arkansas Center for Space and Planetary Sciences, University of Arkansas, 202 Old Museum Bldg., Fayetteville, AR 72701, United States
[b] Jet Propulsion Laboratory, California Institute of Technology, 4800 Oak Drove Dr. 183-501, Pasadena, CA 91109, United States

ARTICLE INFO

Article history:
Received 9 December 2009
Revised 12 April 2010
Accepted 14 April 2010
Available online 28 April 2010

Keywords:
Iapetus
Photometry
Satellites, Surfaces

ABSTRACT

We performed photometry of *Cassini* Visual Infrared Mapping Spectrometer observations of Iapetus to produce the first phase integrals calculated directly from solar phase curves of Iapetus for the leading hemisphere and to estimate the phase integrals for the trailing hemisphere. We also explored the phase integral dependence on wavelength and geometric albedo. The extreme dichotomy of the brightness of the leading and trailing sides of Iapetus is reflected in their phase integrals. Our phase integrals, which are lower than the results of Morrison et al. (Morrison, D., Jones, T.J., Cruikshank, D.P., Murphy, R.E. [1975]. Icarus 24, 157–171) and Squyres et al. (Squyres, S.W., Buratti, B.J., Veverka, J., Sagan, C. [1984]. Icarus 59, 426–435), have profound implications on the energy balance and volatile transport on this icy satellite.

© 2010 Elsevier Inc. All rights reserved.

1. Introduction

In the saturnian system, Iapetus exhibits the most extreme variations in albedo of the satellites, with an extremely dark, leading hemisphere and a much brighter, trailing hemisphere. The dark material might be composed of hydrocarbon polymers (Cruikshank et al., 2008) along with a CO_2 absorption band, while the bright side is mostly water ice (Buratti et al., 2005). In recent high-resolution images of the border regions, this dark material is juxtaposed with the bright, icy material; although the demarcations are not sudden in terms of regional albedo, this effect creates a Dalmatian-like, spotty surface appearance on the local scale. This surface dichotomy produces a possibly dynamic system with volatile transport of carbon dioxide and water vapor from the large differences in surface temperature (Palmer and Brown, 2007).

In light of this unique variation and due to the limited previous work, Iapetus is a prime target for a photometric study of the changes in brightness with phase angle. Morrison et al. (1975) estimated a phase integral of 1.3 for the bright side from radiometry. After the Voyager fly-by, Squyres et al. (1984) estimated a phase integral of 0.3 for the dark hemisphere and 0.9 for the light from disk-resolved photometry from the Voyager camera centered at 0.47 μm.

Observations obtained by the *Cassini* Visual Infrared Mapping Spectrometer over the portion of the solar spectrum that includes 99% of the radiated power and over a full range of solar phase angles provide an unprecedented opportunity to study the photometric and thermal properties of icy satellites. Since the bolometric Bond albedo describes the energy balance on a planetary surface, measurements obtained over 99% of the solar spectrum is significant. For the case of Iapetus, this opportunity is particularly compelling because thermal segregation is believed to help create and sustain its unusual albedo dichotomy (Spencer and Denk, 2010; Denk et al., 2010). As a first step in understanding the thermal properties of Iapetus, we have calculated the phase integrals of Iapetus between 0.36 and 5.12 μm, though noise was a major factor beyond 2.5 μm for the trailing hemisphere.

The phase integral, which is a numerical representation of the directional scattering properties of a planet or satellite, is also the ratio between the Bond albedo, which is crucial for thermal modeling and energy balance, and the geometric albedo. Yet, an extensive study of the phase integrals at every wavelength has yet to be performed for Iapetus. In this paper, we took advantage of the phase angle and wavelength coverage of *Cassini*'s VIMS instrument to produce the first phase integrals calculated directly from solar phase curves of the leading side and to estimate the phase integrals for the trailing side. We also explored the wavelength dependence of the phase integrals and the dependence of the phase integrals on the geometric albedo. Given the large albedo differences on Iapetus, this exercise also affords a prime opportunity to study the effects of albedo and wavelength on the phase curves of airless bodies.

2. Data analysis – leading hemisphere

For the dark leading hemisphere (0–180°W longitude), we used all available non-proprietary VIMS cubes of Iapetus that captured a

* Corresponding author.
E-mail address: dgblackb@uark.edu (D.G. Blackburn).

0019-1035/$ - see front matter © 2010 Elsevier Inc. All rights reserved.
doi:10.1016/j.icarus.2010.04.011

Author's personal copy

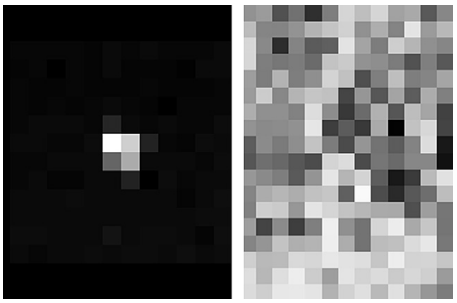

Fig. 1. (left) Band 1 (0.88 microns) of *Cassini* VIMS–IR cube 1536445566_1 included in the disk-integrated phase curve for the leading hemisphere; the range is 3,217,420 km. (right) Band 1 of *Cassini* VIMS–IR cube 1568131937_1 used in the high-resolution disk-resolved photometry of the bright material; the image was taken at a range of 11,766 km during the 2007 targeted fly-by of the trailing hemisphere.

full disk of the leading side (totaling 451, Fig. 1) and performed disk-integrated photometry at every band of the VIMS instrument (96 for VIMS–VIS and 256 for VIMS–IR). These observations were created by summing the flux in every pixel that included a signal from the leading side and then correcting for spacecraft distance. Fig. 2 displays the solar phase curve at 0.47 μm for the dark material. At each band of the VIMS instrument, we normalized disk-integrated brightness to be 1 at $\alpha = 0°$. Four VIMS cubes (CM_1536468302_1, CM_1536468456_1, CM_1536468321_1, and CM_1536468475_1) that all had a phase angle of 0.05° were averaged for the normalization to 0°. From the available solar phase angle coverage (~0–10°, 40–150°), we calculated the phase integral directly by definition (Russell, 1916; Veverka, 1977):

$$q = 2\int_0^{\pi} \phi(\alpha)\sin(\alpha)d\alpha \tag{1}$$

where q is the phase integral; $\phi(\alpha)$ is the normalized disk-integrated brightness (Fig. 2); and α is the solar phase angle. The phase integral describes the directional scattering properties of a planetary body; in effect it is the "beam pattern" of the object. To calculate the phase integral, normalized disk-integrated brightness was derived from third-order polynomial fits of the data spanning the total available phase angle coverage. It should be noted that since these solar phase curves include the entire leading hemisphere, the phase integral calculated here is more an average of the phase integral for the leading hemisphere and not the phase integral for only dark material, as the leading hemisphere contains the largest albedo variations on Iapetus (Squyres et al., 1984).

3. Data analysis – trailing hemisphere

Unfortunately, the coverage of the bright, trailing side (180–359°W longitude) was not sufficient (~33°, 100–140°) to produce phase integrals with an acceptable margin for error using the technique above, as the opposition region ($\alpha < 3°$) is crucial to normalizing the values correctly. Instead, we chose to use disk-resolved photometry of 12 high-resolution VIMS cubes (Table 1 and Fig. 1) spanning phase angles (~13–33°) of the brightest areas available, noting that the decrease in the surface phase function was quite linear at 0.47 μm from previous disk-resolved photometry of *Voyager* data from Squyres et al. (1984).

From our high-resolution cubes, we developed our own surface phase functions (Fig. 3) for the purpose of estimating phase integrals for the bright material. The surface phase function represents the decrease in brightness of the surface material as a function of solar phase angle and was calculated by the following equation from Hapke (1963), Irvine (1966), and Squyres et al. (1984):

$$I(i,\varepsilon,\alpha) = F\left(\frac{\mu_0}{\mu_0+\mu}\right)f(\alpha) \tag{2}$$

where i = incidence angle, ε = emission angle, α = phase angle, $\mu = \cos\varepsilon$, $\mu_0 = \cos i$, I = intensity of scattered light, F = incident solar flux at $i = 0$ divided by π, and $f(\alpha)$ = surface phase function.

Once surface phase functions were produced for each wavelength of the VIMS instrument, we were able to approximate the disk-integrated brightness by assuming a spherical body and using the following equation:

$$\phi(\alpha) = \frac{f(\alpha)\left(1-\sin\frac{\alpha}{2}\tan\frac{\alpha}{2}\ln\left(\cot\frac{\alpha}{4}\right)\right)}{f(0°)} \tag{3}$$

which is the formula used by Buratti and Veverka (1983) when A, a weighting parameter between a lunar-like and Lambert

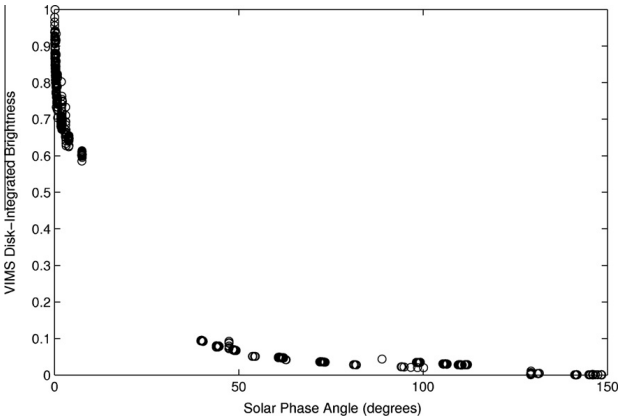

Fig. 2. VIMS disk-integrated brightness $\phi(\alpha)$ versus solar phase angle α for the dark, leading hemisphere at 1.15 μm (Band 17 of VIMS–IR).

Author's personal copy

Table 1
High resolution VIMS cubes of the bright material.

Cube	Phase angle	Latitude	Longitude	Pixels
1568131937_1	24.25	−10	234	324
1568129331_1	13.42	−45	208	900
1568129201_1	12.68	−41	201	900
1568129461_1	14.47	−42	206	900
1568129671_1	16.07	−43	201	25
1568136573_1	29.06	−10	247	144
1568131010_1	24.39	0	199	4
1568136449_1	29.12	11	246	144
1568135049_1	28.74	−12	219	16
1568139139_1	30.79	12	225	16
1568138316_1	30.81	45	216	16
1568163600_1	33.37	47	220	1

scattering function, is set to 1 for a lunar-like surface. Then, phase integrals at each wavelength for the trailing side were calculated using Eq. (1), extrapolating a linear fit from our limited phase angle coverage (Fig. 2); our fit compares well with Voyager results from Squyres et al. (1984) at 0.47 μm at the wavelengths in which VIMS data were available (Fig. 3). In order to estimate $f(0)$, we chose to include the opposition surge effect, which has been shown to typically affect the other icy satellites inside of ∼3° (Buratti et al., 2009; Pitman et al., 2010). Therefore, we modified the slope at 3° to the phase coefficient 0.03 mag/deg, which has been determined by ground-based observations and has shown little wavelength dependency between the ultraviolet and near-infrared filters (Noland et al., 1974; Cruikshank, 1979).

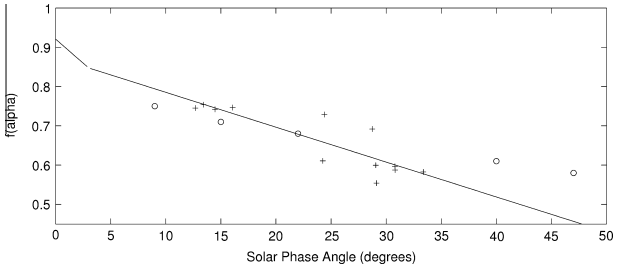

Fig. 3. The surface phase function for the bright material at 0.47 μm is a linear fit (black line) to our data from the 12 sampled cubes (pluses). At less than 3°, we modified the slope to reflect the known phase coefficient (0.03 mag/deg) for the bright hemisphere from Noland et al. (1974) and Cruikshank (1979). We compared our results to a surface phase function by Squyres et al. (1984) (circles) from *Voyager* ISS clear-filter images to verify our method.

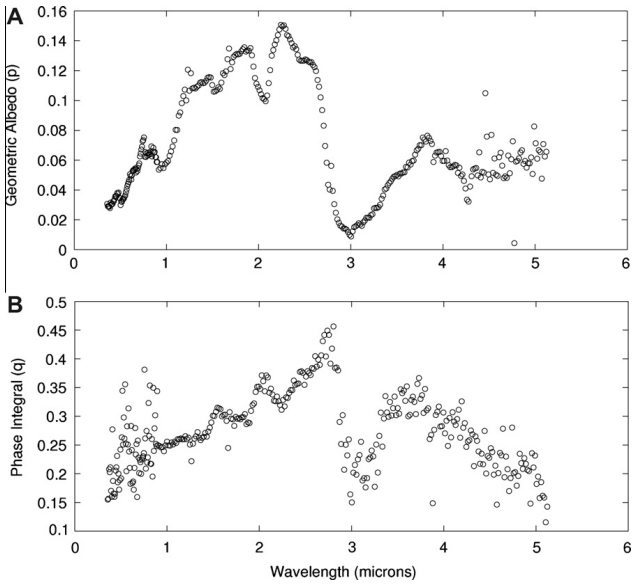

Fig. 4. (A) Geometric albedo of the leading side versus wavelength from normalized reflectance from VIMS cubes. (B) Phase integrals calculated using disk-integrated photometry for the leading side versus wavelength.

Author's personal copy

4. Results

Our calculated phase integrals for the leading and trailing hemispheres are shown in Figs. 4B and 5B, respectively. We compared our results to spectra from normal reflectance of the leading hemisphere from a mosaic of VIMS cubes and of the bright material using our derived $f(\alpha)$ curves and plotted the relationship for each wavelength covered by the VIMS instrument (Figs. 4A and 5A). For the leading side normal reflectance (Fig. 4A), we used a lunar-like scattering law (Eq. (2)) and surface phase functions determined from high-resolution cubes of the leading hemisphere to approximate the average normal reflectance for the leading hemisphere and to adjust appropriately for the bright material contamination evident in the leading hemisphere phase curves. For the trailing side (Fig. 5A), since we used high-resolution cubes of the bright material, we determined the normal reflectance from our surface phase function curves, noting that half of $f(0)$ is equal to the normal reflectance. Since the effects of multiple scattering do not become significant until normal reflectance rises above ~0.6 (Buratti, 1984; Buratti and Veverka, 1985), the normal reflectance is a close approximation of the geometric albedo for Iapetus. Our spectra compare well with the findings of Buratti et al. (2005). Clearly, the phase integral corresponds to changes in geometric albedo for both the dark regions (absorption feature at 3 μm) and light (key water ice absorption bands at 1.5 and 2.1 μm): as the albedo increases, the value for the phase integral also increases. To illustrate the relationship between geometric albedo and phase integral more clearly, we chose to plot the phase integral versus geometric albedo at each band of the VIMS instrument for both the leading (pluses) and trailing (circles) hemispheres (Fig. 6) and to compare

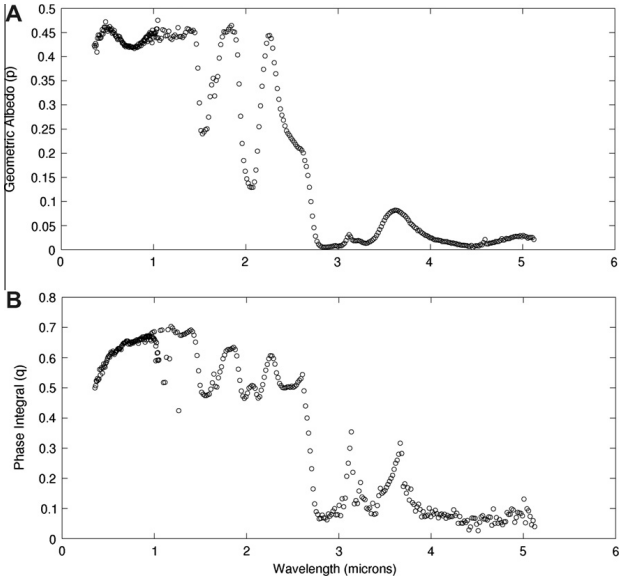

Fig. 5. (A) Geometric albedo of the trailing side versus wavelength from half of $f(0)$. (B) Phase integrals estimated using disk-resolved photometry for the trailing side versus wavelength.

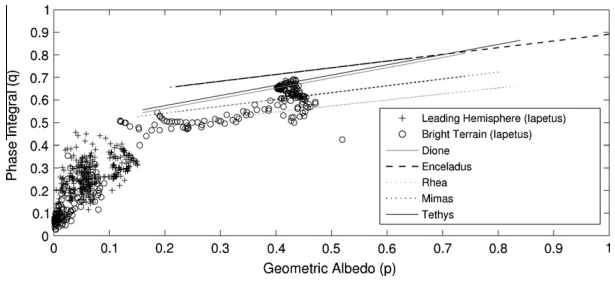

Fig. 6. Phase integral versus geometric albedo for Iapetus for the dark, leading side (pluses) and the bright, trailing side (circles). The lines are linear fits to the Pitman et al. (2010) results for Dione, Enceladus, Rhea, Mimas, and Tethys.

Author's personal copy

Table 2
Phase integrals from our results on Iapetus compared to the other saturnian icy satellites from Pitman et al. (2010) at selected wavelengths.

	VIMS–VIS λ (μm)						Average of VIMS–VIS and VIMS–IR λ (μm)		VIMS–IR λ (μm)				
	0.35	0.40	0.51	0.60	0.70	0.81	0.90	1.00	1.52	1.80	2.02	2.23	3.60
Iapetus													
q_{lead}	0.16 ± 0.04	0.16 ± 0.04	0.26 ± 0.05	0.18 ± 0.06	0.22 ± 0.05	0.35 ± 0.04	0.25 ± 0.05	0.26 ± 0.04	0.31 ± 0.05	0.30 ± 0.05	0.37 ± 0.04	0.32 ± 0.04	0.35 ± 0.05
q_{trial}	0.50 ± 0.10	0.52 ± 0.09	0.61 ± 0.10	0.63 ± 0.10	0.65 ± 0.10	0.66 ± 0.11	0.67 ± 0.09	0.67 ± 0.08	0.47 ± 0.11	0.63 ± 0.11	0.50 ± 0.09	0.58 ± 0.10	0.23 ± 0.13
Rhea													
q	0.55 ± 0.06	0.60 ± 0.04	0.64 ± 0.04	0.66 ± 0.05	0.69 ± 0.04	0.70 ± 0.05	0.68 ± 0.04	0.67 ± 0.05	0.60 ± 0.05	0.66 ± 0.05	0.56 ± 0.07	0.67 ± 0.05	0.45 ± 0.10
q_{lead}	0.58 ± 0.05	0.64 ± 0.05	0.68 ± 0.06	0.70 ± 0.05	0.73 ± 0.08	0.74 ± 0.09	0.72 ± 0.06	0.72 ± 0.06	0.60 ± 0.05	0.70 ± 0.07	0.58 ± 0.08	0.70 ± 0.06	0.50 ± 0.10
q_{trial}	0.54 ± 0.06	0.57 ± 0.06	0.61 ± 0.06	0.63 ± 0.06	0.66 ± 0.08	0.68 ± 0.09	0.63 ± 0.07	0.64 ± 0.11	0.60 ± 0.05	0.63 ± 0.05	0.55 ± 0.07	0.64 ± 0.05	0.40 ± 0.11
Dione													
q	0.78 ± 0.05	0.82 ± 0.07	0.77 ± 0.06	0.75 ± 0.07	0.78 ± 0.06	0.76 ± 0.06	0.81 ± 0.10	0.85 ± 0.09	0.66 ± 0.05	0.83 ± 0.16	0.55 ± 0.07	0.80 ± 0.15	0.58 ± 0.06
q_{lead}	0.89 ± 0.05	0.93 ± 0.07	0.84 ± 0.06	0.86 ± 0.07	0.88 ± 0.06	0.88 ± 0.06	0.87 ± 0.10	0.93 ± 0.09	0.70 ± 0.15	0.86 ± 0.16	0.58 ± 0.07	0.87 ± 0.15	0.65 ± 0.06
q_{trial}	0.68 ± 0.05	0.74 ± 0.06	0.71 ± 0.06	0.68 ± 0.07	0.71 ± 0.05	0.68 ± 0.05	0.72 ± 0.08	0.73 ± 0.06	0.64 ± 0.02	0.72 ± 0.09	0.56 ± 0.07	0.75 ± 0.09	0.57 ± 0.06
Tethys													
q	–	–	–	–	–	–	0.68 ± 0.07	0.66 ± 0.05	0.77 ± 0.05	0.86 ± 0.05	0.67 ± 0.02	0.86 ± 0.05	0.48 ± 0.11
q_{lead}	–	–	–	–	–	–	0.68 ± 0.07	0.66 ± 0.05	0.76 ± 0.05	0.86 ± 0.05	0.67 ± 0.02	0.86 ± 0.05	0.49 ± 0.11
q_{trial}	–	–	–	–	–	–	0.69 ± 0.03	0.72 ± 0.03	0.86 ± 0.02	0.92 ± 0.02	0.75 ± 0.02	0.92 ± 0.02	0.42 ± 0.08
Mimas													
q	–	–	–	–	–	–	0.80 ± 0.05	0.79 ± 0.03	0.83 ± 0.05	0.85 ± 0.05	0.86 ± 0.05	0.85 ± 0.05	0.80 ± 0.05
q_{lead}	–	–	–	–	–	–	0.80 ± 0.02	0.78 ± 0.02	0.82 ± 0.04	0.84 ± 0.04	0.84 ± 0.04	0.85 ± 0.03	0.80 ± 0.06
q_{trial}	–	–	–	–	–	–	0.84 ± 0.04	0.82 ± 0.03	0.90 ± 0.07	0.89 ± 0.05	0.96 ± 0.07	0.90 ± 0.05	0.85 ± 0.05
Enceladus													
q	–	–	–	–	–	–	0.85 ± 0.10	0.90 ± 0.13	0.73 ± 0.06	0.83 ± 0.09	0.69 ± 0.03	0.84 ± 0.09	0.57 ± 0.06
q_{lead}	–	–	–	–	–	–	0.87 ± 0.08	0.90 ± 0.13	0.71 ± 0.04	0.81 ± 0.08	0.68 ± 0.02	0.83 ± 0.08	0.55 ± 0.07
q_{trial}	–	–	–	–	–	–	0.90 ± 0.10	0.91 ± 0.11	0.76 ± 0.05	0.84 ± 0.10	0.72 ± 0.07	0.85 ± 0.10	0.59 ± 0.03

Author's personal copy

our results for Iapetus with the findings of the other saturnian icy satellites by Pitman et al. (2010). Plotting the Pitman et al. (2010) data onto Fig. 6 revealed highly linear trends, and we chose to use a linear best-fit line that included both the visible and near-infrared to represent the slopes of Enceladus, Tethys, Dione, Mimas, and Rhea in relation to Iapetus.

5. Discussion and summary

It is well known that generally for a planetary body the phase integral increases with geometric albedo while the intensity of the opposition surge effect decreases with increasing geometric albedo (Veverka, 1977), and our results conform to that trend. This relationship is expected, because as the albedo increases, the degree of multiple scattering, which tends to be more isotropic than single scattered radiation, also increases. These multiple-scattered photons tend to make the phase curve more ''Lambertian'', which increases the area under the normalized integrated phase curve. Multiple scattering also isotropizes the single scattering phase function and partly illuminates primary shadows: both effects increase the area under the normalized integrated phase curve. Although most of the increase in the phase integral is from an increased geometric albedo, another component is from additional effects of illuminated shadows caused by rough features and the properties of the surface – particle size and shape, for example – which affect the single particle phase function (Buratti and Veverka, 1985). This texture difference clearly alters the slope between the leading the trailing hemispheres (Fig. 6). The remaining deviance is from noise and error in the measurement. The scatter in the data in Fig. 6 is indicative of two factors for the dark material: at low albedos, noise affecting the VIMS instrument competes with the signal at the surface, and at higher wavelengths, differences in the noise levels of individual cubes produces scatter in our data near the opposition surge region even after the bands had been filtered by averaging the 11 adjacent bands. For the light material, at longer wavelengths (>2.5 μm) where water ice absorbs nearly all light, the noise becomes a relevant factor as well since the signal is very weak; also, the limitation in number of high-resolution cubes (12) needed for disk-resolved photometry precluded having data with a good signal.

Palmer and Brown (2007) extrapolated a linear approximation of the relationship between the phase integral and geometric albedo from two solitary points, one of which was not based on Iapetus, in order to make a map of the Bond albedo. The two points used by Palmer and Brown (2007) for their line included one from the dark material estimated from Squyres et al. (1984) and the other from an extrapolation to Europa from Buratti and Veverka (1983) with the assumption that the brightest area on Iapetus ($p = 0.65$) had a phase integral of 1. The slope (1.23) from their fit compared to Fig. 6 produces an overestimation of the phase integral on Iapetus, though our geometric albedos include the opposition surge, which may account for some of the variance. Our graph (Fig. 6) also illustrates that a purely linear approximation for all of Iapetus is not valid, as the slopes for the leading and trailing hemispheres are slightly different. Lower values for the phase integrals translate into lower Bond albedos and will hence increase the rates of volatile transport of CO_2 modeled by Palmer and Brown (2007).

When compared with other icy satellites (Table 2), the dark material has a phase integral closer to the dark surface of Phoebe ($q = 0.29 \pm 0.03$); however, Phoebe's phase integral showed no significant wavelength dependence (Buratti et al., 2008). The slope and magnitude of our measurements for the bright, icy material on compare best to the satellites of Dione, Rhea, and Mimas (Pitman et al., 2010). The phase integrals of Rhea and Dione would be expected to be more similar to Iapetus, as these icy satellites also exhibit insignificant multiple scattering and are more lunar-like than the brighter satellites of Mimas, Tethys, and Enceladus (Buratti, 1984); however since their geometric albedos are slightly higher (Table 2), the phase integrals at each wavelength band are not as comparable. Since the albedos and morphology of Dione and Rhea are similar to the bright side of Iapetus, it is reasonable to assume that the surface texture of Dione and Rhea is also similar to the bright side of Iapetus (except perhaps for some accumulation on their surfaces of micron-sized particles from the E-ring). The dark material on Iapetus may have settled onto a moon that looked more like a "typical" icy saturnian satellite.

Compared with previous results, our phase integrals for the bright side are lower than the estimates of Morrison et al. (1975) ($q \sim 1.3$) based on radiometry, yet Morrison used inaccurate numbers for Iapetus' radius and the average geometric albedo for the trailing side (835 km and 0.35 instead of 730 km and 0.42 (Squyres et al., 1984)). Our results for the bright and dark hemispheres at 0.47 μm are 0.58 ± 0.10 and 0.20 ± 0.06, respectively, compared to the results of Squyres et al. (1984) of ∼0.9 and ∼0.3. The difference in the phase integral for the bright region can be explained based on the coverage of the *Cassini* spacecraft relative to *Voyager*. *Voyager* provided excellent coverage of the north polar region (Squyres et al., 1984), where geometric albedos approach 0.65, and a phase integral closer to 1 like on Europa's surface is not surprising. Our 12 high-resolution images centered on a region where the average geometric albedo is 0.43 near the equator, since *Cassini* had poor coverage of both poles of Iapetus. Yet, *Cassini* had better coverage of the dark region, which is of course weighted more in our approximation of the leading hemisphere since we included every cube available. However, if Iapetus follows a similar trend to the other icy satellites of Saturn (Fig. 6; Pitman et al., 2010), which is likely to be the case, then extrapolating the slope up to the highest albedo region (0.65) would produce a phase integral of ∼0.7. Squyres et al. (1984) explain that they used a derived value twice the average geometric albedo of the trailing side (2×0.42) as their $f(0)$, yet the locations they sampled for their $f(\alpha)$ have actual geometric albedos closer to 0.5 from their own normal reflectance maps; this would also result in inflated estimates for the phase integral for the bright terrain. Our results of lower phase integrals than previous findings will translate into lower Bond albedos and higher temperatures in thermal models, which may have profound implications on volatile transport on Iapetus (Palmer and Brown, 2007; Spencer and Denk, 2010).

Acknowledgments

This research was carried out at the Jet Propulsion Laboratory, California Institute of Technology, and was sponsored by the National Aeronautics and Space Administration's Space Grant Program. We would like to thank the University of Arkansas and the Arkansas Space Grant Consortium for support, as well as helpful conversation with Mike Hicks, Ken Lawrence, Karly Pitman, and Sean Faulk. We would also like to thank the comments and suggestions from two anonymous reviewers who improved the quality of our manuscript.

References

Buratti, B.J., 1984. Voyager disk resolved photometry of the saturnian satellites. Icarus 59, 392–405.
Buratti, B.J., Veverka, J., 1983. Voyager photometry of Europa. Icarus 55, 93–110.
Buratti, B.J., Veverka, J., 1985. Photometry of rough planetary surfaces: The role of multiple scattering. Icarus 64, 320–328.
Buratti, B.J., and 28 colleagues, 2005. *Cassini* Visual and Infrared Mapping Spectrometer observations of Iapetus: Detection of CO_2. Astrophys. J. 622, L149–L152.
Buratti, B.J., and 10 colleagues, 2008. Infrared (0.83–5.1 μm) photometry of Phoebe from the *Cassini* Visual Infrared Mapping Spectrometer. Icarus 193, 309–322.

Author's personal copy

Buratti, B.J., Mosher, J.A., Abramson, L., Akhter, N., Clark, R.N., Brown, R.H, Baines, K.H., Nicholson, P.D., DeWet, S., 2009. Opposition surges of the satellites of Saturn from the *Cassini* Visual Infrared Mapping Spectrometer. Lunar Planet. Sci. XV. Abstract 1738.

Cruikshank, D.P., 1979. The surfaces and interiors of Saturn's satellites. Rev. Geophys. Space Phys. 17, 165–176.

Cruikshank, D.P., and 26 colleagues, 2008. Hydrocarbons on Saturn's satellites Iapetus and Phoebe. Icarus 193, 334–343.

Denk, T., and 10 colleagues, 2010. Iapetus: Unique surface properties and a global color dichotomy from *Cassini* imaging. Science 327, 435–439.

Hapke, B.W., 1963. A theoretical photometric function for the lunar surface. J. Geophys. Res. 68, 4571–4586.

Irvine, W.M., 1966. The shadowing effect in diffuse reflection. J. Geophys. Res. 71, 2931–2937.

Morrison, D., Jones, T.J., Cruikshank, D.P., Murphy, R.E., 1975. 2 faces of Iapetus. Icarus 24, 157–171.

Noland, M., Veverka, J., Morrison, D., Cruikshank, D.P., Lazarewicz, A.R., Morrison, N.D., Elliot, J.L., Goguen, J., Burns, J.A., 1974. Six-color photometry of Iapetus, Titan, Rhea, Dione, and Tethys. Icarus 23, 334–354.

Palmer, E.E., Brown, R.H., 2007. The stability and transport of carbon dioxide on Iapetus. Icarus 195, 434–446.

Pitman, K.M., Buratti, B.J., Mosher, J.A., 2010. Disk-integrated bolometric Bond albedos and rotational light curves of saturnian satellites from *Cassini* Visual and Infrared Mapping Spectrometer. Icarus 206, 537–560.

Russell, H.N., 1916. On the albedo of planets and their satellites. Astrophys. J. 43, 173–195.

Spencer, J.R., Denk, T., 2010. Formation of Iapetus' extreme albedo dichotomy by exogenically triggered thermal ice migration. Science 327, 432–435.

Squyres, S.W., Buratti, B.J., Veverka, J., Sagan, C., 1984. Voyager photometry of Iapetus. Icarus 59, 426–435.

Veverka, J., 1977. Photometry of satellite surfaces. In: Burns, J.A. (Ed.), Planetary Satellites. University of Arizona Press, Tucson, pp. 171–231.

| Print

Journal Publishing Agreement

Elsevier Inc.

Your article details

Article:	Solar Phase Curves and Phase Integrals for the Leading and Trailing Hemispheres of Iapetus from the Cassini Visual Infrared Mapping Spectrometer
Corresponding author:	Mr. David G. Blackburn
E-mail address:	
Journal:	Icarus
Our reference	YICAR9408
PII:	S0019-1035(10)00159-4
DOI:	10.1016/j.icarus.2010.04.011

Your Status

- I am one author signing on behalf of all co-authors of the manuscript
- I am not a US Government employee but some of my co-authors are

Data Protection

- I do not wish to receive news, promotions and special offers about products and services from Elsevier Inc. and its affiliated companies worldwide.

Assignment of publishing rights

I hereby assign toElsevier Inc.the copyright in the manuscript identified above (government authors not electing to transfer agree to assign a non-exclusive licence) and any supplemental tables, illustrations or other information submitted therewith that are intended for publication as part of or as a supplement to the manuscript (the "Article") in all forms and media (whether now known or hereafter developed), throughout the world, in all languages, for the full term of copyright, effective when and if the article is accepted for publication. This transfer includes the right to provide the Article in electronic and online forms and systems. No revisions, additional terms or addenda to this Agreement can be accepted without our express written consent. Authors at institutions that place restrictions on copyright assignments, including those that do so due to policies about local institutional repositories, are encouraged to obtain a waiver from those institutions so that the author can accept our publishing agreement.

Retention of Rights for Scholarly Purposes

I understand that I retain or am hereby granted (without the need to obtain further permission) rights to use certain versions of the Article for certain scholarly purposes, as described and defined below ("Retained Rights"), and that no rights in patents, trademarks or other intellectual property rights are transferred to the journal.

The Retained Rights include the right to use the Pre-print or Accepted Author Manuscript for Personal Use, Internal Institutional Use and for Scholarly Posting; and the Published Journal Article for Personal Use and Internal Institutional Use.

Author Representations / Ethics and Disclosure

Author representations

- The article I have submitted to the journal for review is original, has been written by the stated authors and has not been published elsewhere.
- The article is not currently being considered for publication by any other journal and will not be submitted for such review while under review by this journal.
- The article contains no libellous or other unlawful statements and does not contain any materials that violate any personal or proprietary rights of any other person or entity.
- I have obtained written permission from copyright owners for any excerpts from copyrighted works that are included and have credited the sources in my article.
-
- If the article was prepared jointly with other authors, I have informed the co-author(s) of the terms of this publishing agreement and that I am signing on their behalf as their agent, and I am authorized to do so.

Funding agency requirements and other policies

For more information about the definitions relating to this agreement click here.

☑ **I have read and agree to the terms of the Journal Publishing Agreement. .**

22nd April 2010

T-copyright-v15/2009

-
-
-

Copyright (c) 2010 Elsevier B.V. All rights reserved.

DEFINITIONS

ACCEPTED AUTHOR MANUSCRIPT ("AAM")

Author's version of the manuscript of an article that has been accepted for publication and which may include any author-incorporated changes suggested through the processes of submission processing, peer review, and editor-author communications. AAMs should not include other publisher value-added contributions such as copy-editing, formatting and (if relevant) pagination, and should include the Appropriate Bibliographic Citation and a link to the final publication (generally through the relevant DOI).

APPROPRIATE BIBLIOGRAPHIC CITATION

Authors posting Accepted Author Manuscript online should later add a citation for the Published Journal Article indicating that the Article was subsequently published, and may mention the journal title provided they add the following text at the beginning of the document:

> "NOTICE: this is the author's version of a work that was accepted for publication in Planetary and Space Science. Changes resulting from the publishing process, such as peer review, editing, corrections, structural formatting, and other quality control mechanisms may not be reflected in this document. Changes may have been made to this work since it was submitted for publication. A definitive version was subsequently published in PUBLICATION, [VOL#, ISSUE#, (DATE)] DOI#"

COMMERCIAL USE

The use or posting of articles for commercial gain or to substitute for the services provided directly by the journal including:

the posting by companies of their employee-authored works for use by customers of such companies (e.g. pharmaceutica physician-prescribers); and

commercial exploitation such as directly associating advertising with such posting or the charging of fees for document de

INTERNAL INSTITUTIONAL USE

Use by the author's institution for classroom teaching at the institution (including distribution of copies, paper or electronic, and use in coursepacks and courseware programs) for scholarly purposes. For authors employed by companies, the use by that company for internal training purposes.

PERSONAL USE

Use by an author in the author's classroom teaching (including distribution of copies, paper or electronic), distribution of copies to research colleagues for their personal use, use in a subsequent compilation of the author's works, inclusion in a thesis or dissertation, preparation of other derivative works such as extending the article to book-length form, or otherwise using or re-using portions or excerpts in other works (with full acknowledgment of the original publication of the article).

PERMITTED SCHOLARLY POSTING

Voluntary posting of AAMs or Preprints by an author on open Web sites operated by the author or the author's institution for scholarly purposes, as determined by the author, or (in connection with Preprints) on preprint servers, but not for Commercial Use or Systematic Distribution. The author should include the Appropriate Bibliographic Citation when posting AAMs. Deposit in or posting to subject-oriented or centralised repositories (such as PubMed Central), or institutional repositories with mandates for systematic postings, is permitted only under specific agreements between the publisher and the repository, agency or institution, and only consistent with the Copyright Owner's policies concerning such repositories. To learn more about the publisher's policies and agreements with such agencies or institutions go to http://www.elsevier.com/fundingbodyagreements.

PREPRINT

Author's own write-up of research results and analysis that has not been refereed, nor had any other value added to it by a publisher (such as formatting, copy-editing, and the like).

PUBLISHED JOURNAL ARTICLE

The definitive final record of published research that appears or will appear in the journal and embodies all value-adding publisher activities including copy-editing, formatting and (if relevant) pagination.

SYSTEMATIC DISTRIBUTION

Policies or other mechanisms designed to aggregate and openly disseminate manuscripts or articles, or to substitute for journal-provided services, including:

the systematic distribution to others via e-mail lists or listservers (to parties other than known colleagues), whether for a

the posting of links to sponsored articles by commercial third parties including pharmaceutical companies;

institutional, funding body or government manuscript posting policies or mandates that aim to aggregate and openly distri peer reviewed manuscripts or published journal articles authored by its researchers or funded researchers; and

subject repositories that aim to aggregate and openly distribute accepted peer reviewed manuscripts or published journal researchers in specific subject areas.

CHAPTER 4

A BOLOMETRIC BOND ALBEDO MAP OF IAPETUS: OBSERVATIONS FROM *CASSINI* VIMS AND ISS AND *VOYAGER* ISS

In this chapter, we continue our study of the reflectance properties of Iapetus by producing a bolometric Bond albedo map of the surface of Iapetus. This chapter is published in the journal *Icarus.* Dr. Richard Ulrich was the PI on the continuing proposal from the Arkansas Space Grant Consortium and the University of Arkansas and provided helpful conversation. Dr. Bonnie J. Buratti provided the idea, facilities, and technical support for the theory behind the project. I gathered the data, performed the analysis, produced the subsequent map, and all remaining details not listed.

4.1 Abstract

We utilized *Cassini* VIMS, *Cassini* ISS, and *Voyager* ISS observations of Iapetus to produce the first bolometric Bond albedo map of Iapetus. The average albedo values for the leading and trailing hemispheres are 0.06 ± 0.01 and 0.25 ± 0.03, respectively. However, the bright material in high-resolution ISS images has a value of 0.38 ± 0.04, highlighting the importance of resolution in determining accurate albedo values for Iapetus due to the speckling of localized regions of dark material into the trailing hemisphere. The practical application of this map is determining more accurate surface temperatures in thermal models; these albedo values translate into first order blackbody temperatures of 118.4 K and 125.5 K for the trailing and leading hemispheres at the semi-major axis.

4.2 Introduction

Iapetus, discovered by Giovanni Domenico Cassini in 1671, is being explored by a craft bearing his name. In terms of brightness, Iapetus is the most diverse satellite in the saturnian system, and its albedo dichotomy makes it a prime target for a study of the reflectance and thermal properties of icy satellites in general. Not only is the origin of the low-albedo material indicative of a unique process altering a planetary surface (or at least an extreme example of such a process), but the extreme changes in albedo and thus temperature may drive volatile transport and segregation on the moon. Previous observations by *Voyager 2* were too deficient in spatial resolution, spectral range and viewing geometry to accurately map the albedo variations on the body and to fully understand the energy balance.

Following the *Voyager 2* results of Smith *et al*. (1982) showing the stark dichotomy in albedo between the leading and trailing hemispheres, Squyres and Sagan (1983) demonstrated that the darkest area on the surface is not only on the apex of motion for the satellite, but that the albedo changes gradually from the low albedo to high albedo regions. As Figure 4.1 illustrates, the dark material drapes over into the trailing hemisphere, producing a pattern much like a baseball cover. Various theories have been proposed as the source of this dichotomy, including endogenic sources such as volcanic flows (Smith *et al.*, 1981) and exogenic sources from the remnants of collisions and micro-meteoritic bombardment involving the outer irregular satellites, including Phoebe and Hyperion (Soter, 1974; Cruikshank *et al.*, 1983; Matthews, 1992; Buratti and Mosher, 1995; Vilas *et al.*, 1996; Owen *et al.*, 2001). The discovery of a large, tenuous dust ring at the orbit of Phoebe ring provided final validation for the exogenic class of models

(Verbiscer *et al*., 2009), and at present the exogenic source as the origin of the dark material is more widely favored due to the dark material residing on the apex of motion. Consequently, Spencer and Denk (2010) have shown that thermal segregation is a probable mechanism for creating the pattern that is present today if the leading hemisphere were seeded by an exogenic coating in the past, a process originally proposed by Mendis and Axford (1974). In addition, Denk *et al*. (2010) have shown that both dark and light materials on the leading side have redder spectra than their counterparts on the trailing hemisphere.

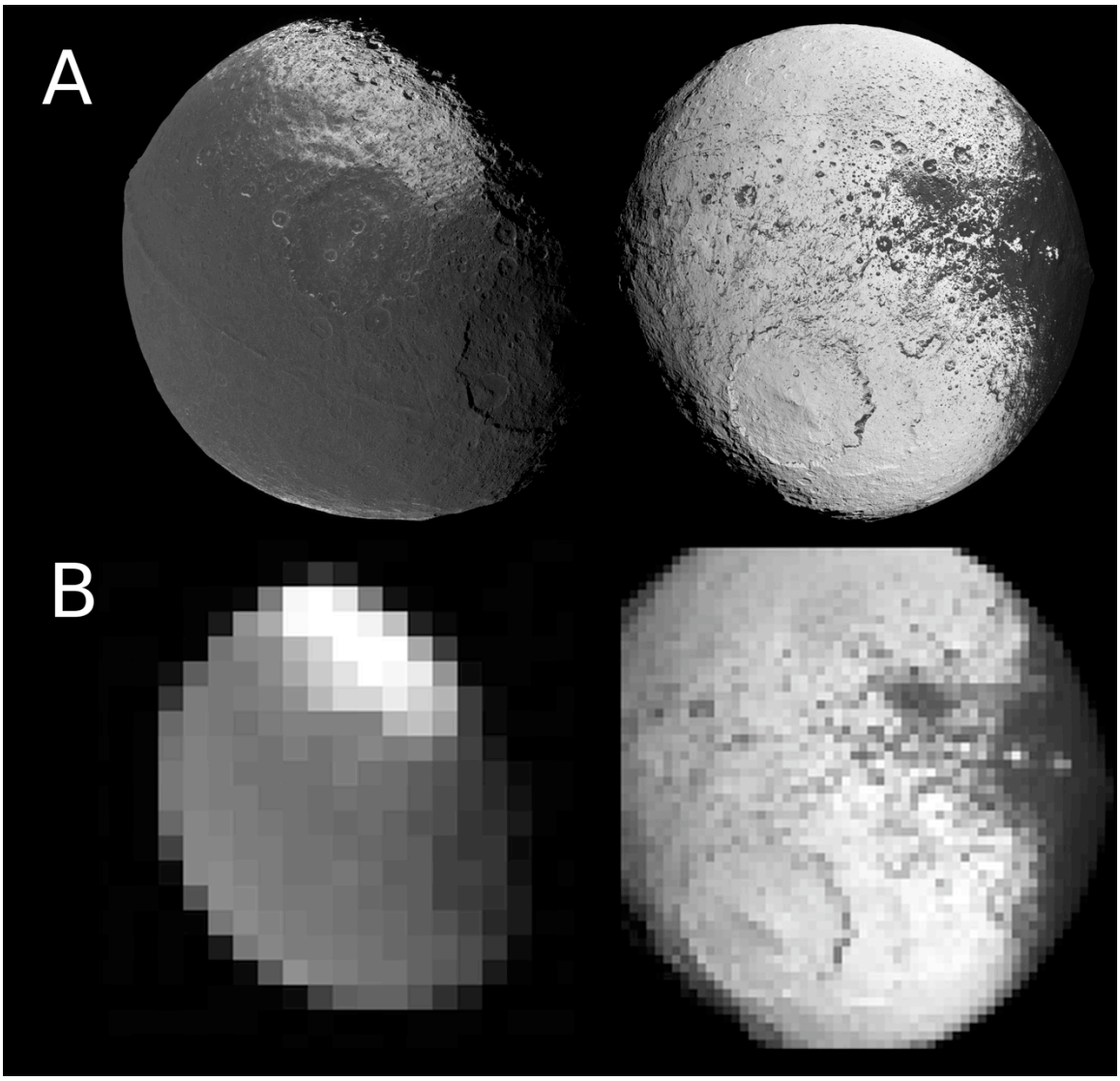

Figure 4.1 *– Images from the two targeted flybys of Iapetus, (left) of the leading hemisphere on December 31, 2004 and (right) of the trailing hemisphere on September 10, 2007.* ***A****. Cassini ISS point-perspective mosaic.* ***B****. Band 2 (0.90 microns) from VIMS-IR Cubes 1483156810_1 (left) and 1568145604_1 (right).*

In this paper, we take advantage of the extraordinary wavelength and solar phase angle coverage of the *Cassini* Visual and Infrared Mapping Spectrometer (VIMS), coupled with observations from the *Cassini* and *Voyager 1 & 2* Imaging Science Subsystems (ISS), to produce the first bolometric Bond albedo map of Iapetus. Blackburn *et al.* (2010) provided the first phase integrals measured directly from photometry at solar phase angles between 0° and 140° at wavelengths ranging from 0.36 to 5.12 microns, which we will use to produce the albedo map in this study. Since the *Cassini* Visual Infrared Mapping Spectrometer provides reflectance over 99% of the total radiated power of the solar spectrum, it is ideal for deriving the bolometric Bond albedo that is integrated over all wavelengths of the solar spectrum.

4.3 Data Analysis

In order to achieve the map with the best possible coverage of the surface, we chose to include multiple data sets including the *Cassini* Visual and Infrared Mapping Spectrometer, the *Cassini* Imaging Science Subsystem, and the *Voyager 1 & 2* Imaging Science Subsystem. Figure 4.1 illustrates the difference in resolution between *Cassini* ISS and VIMS data sets; while the resolution is higher with ISS, VIMS image sets were preferred due to the increased spectral range (0.36-5.12 microns). *Cassini* ISS and *Voyager* ISS images were used primarily to fill in the gaps in VIMS coverage. All image manipulations, calculations, and projections were performed with the Integrated Software for Imagers and Spectrometers (ISIS) package versions 2 & 3. All *Cassini* VIMS cubes were acquired and calibrated to *I/F* internally by the VIMS team as described in Brown *et al*. (2004), while *Voyager* ISS and *Cassini* ISS images were obtained from the Planetary Data System (PDS) and converted to *I/F* via the SPICE information and instrument

specifications embedded in routines native to the open source ISIS software; the SPICE kernels within ISIS also provided the necessary ephemeris data for the projections. In some cases, limb fits and manual adjusting were necessary to refine the pointing information. All of the data used in this study were nonproprietary and accessible via the PDS.

4.3.1 *Cassini* VIMS

4.3.1.1 Normal Reflectance Maps

Cassini VIMS allowed the production of separate normal reflectance maps (Fig. 4.3) at all 352 bands covering wavelengths from 0.35 – 5.12 microns. In order to correct to normal reflectance, we first chose a photometric function to account for scattering and minimize the effects of limb darkening. Previously, it has been shown that a lunar-like scattering law representing single scattering is appropriate for Iapetus since the majority of the surface has a geometric albedo less than 0.6 (Squyres *et al.*, 1984; Buratti and Veverka, 1985). This Lommel-Seeliger photometric function is defined as:

$$I(i,\varepsilon,\alpha) = F\left(\frac{\mu_0}{\mu_0 + \mu}\right) f(\alpha) \tag{4.1}$$

where i = incidence angle, ε = emission angle, α = phase angle, $\mu = \cos \varepsilon$, $\mu_0 = \cos i$, I = intensity of scattered light, πF = incident solar flux at $i = 0$, and $f(\alpha)$ = phase function of the surface (Chandrasekhar, 1960; Hapke, 1963; Irvine, 1966; Squyres *et al.*, 1984).

In order to correct to a normal reflectance in which the solar phase angle is zero and both μ and μ_0 equal unity, we utilized VIMS high-resolution cubes (Table 4.1) to produce our own surface phase functions (Fig. 4.2). The surface phase function represents the decrease in brightness of the surface material as a function of solar phase

angle alone, and it also represents physical attributes of the surface such as macroscopic roughness, particle size, and compaction state. We utilized all the high-resolution VIMS cubes from the 2007 targeted flyby, combined them with a handful of images from the 2004 untargeted flyby (Table 4.1), and selected regions of the brightest and the darkest terrain possible. Individual $f(\alpha)$s were calculated by correcting the I/F values in the high resolution cubes via eq. (4.1), and the resulting data points were used to build a separate set of surface phase functions for the light and dark material (Fig. 4.2) for each of the 352 VIMS bands.

Table 4.1 *VIMS high-resolution cubes utilized for production of surface phase functions (Fig 4.2).*

Cube	Phase Angle	Latitude	Longitude	Pixels	Terrain
1568131937_1	24.25	-10	234	324	Light
1568129331_1	13.42	-45	208	900	Light
1568129201_1	12.68	-41	201	900	Light
1568129461_1	14.47	-42	206	900	Light
1568129671_1	16.07	-43	201	25	Light
1568136573_1	29.06	-10	247	144	Light
1568131010_1	24.39	0	199	4	Light
1568136449_1	29.12	11	246	144	Light
1568135049_1	28.74	-12	219	16	Light
1568139139_1	30.79	12	225	16	Light
1568138316_1	30.81	45	216	16	Light
1568163600_1	33.37	47	220	1	Light
1568126375_1	97.35	1	194	1026	Dark
1568128380_1	12.77	-13	208	256	Dark
1568124369_1	131.55	12	220	144	Dark
1568124533_1	130.63	-1	222	16	Dark
1568124800_1	128.64	0	218	16	Dark
1483233838_1	113.2	40	318	16	Dark
1483224693_1	105.68	51	302	9	Dark
1483157059_4	53.8	0	270	9	Dark
1483224693_1	105.73	40	276	4	Dark
1483172847_1	62.78	12	287	4	Dark
1483194809_1	79.09	20	286	9	Dark
1568124753_1	129.85	0	213	4	Dark
1568125677_1	121.32	0	192	4	Dark
1568128091_1	11.3	-10	196	4096	Dark
1568127937_1	13.53	-11	193	900	Dark

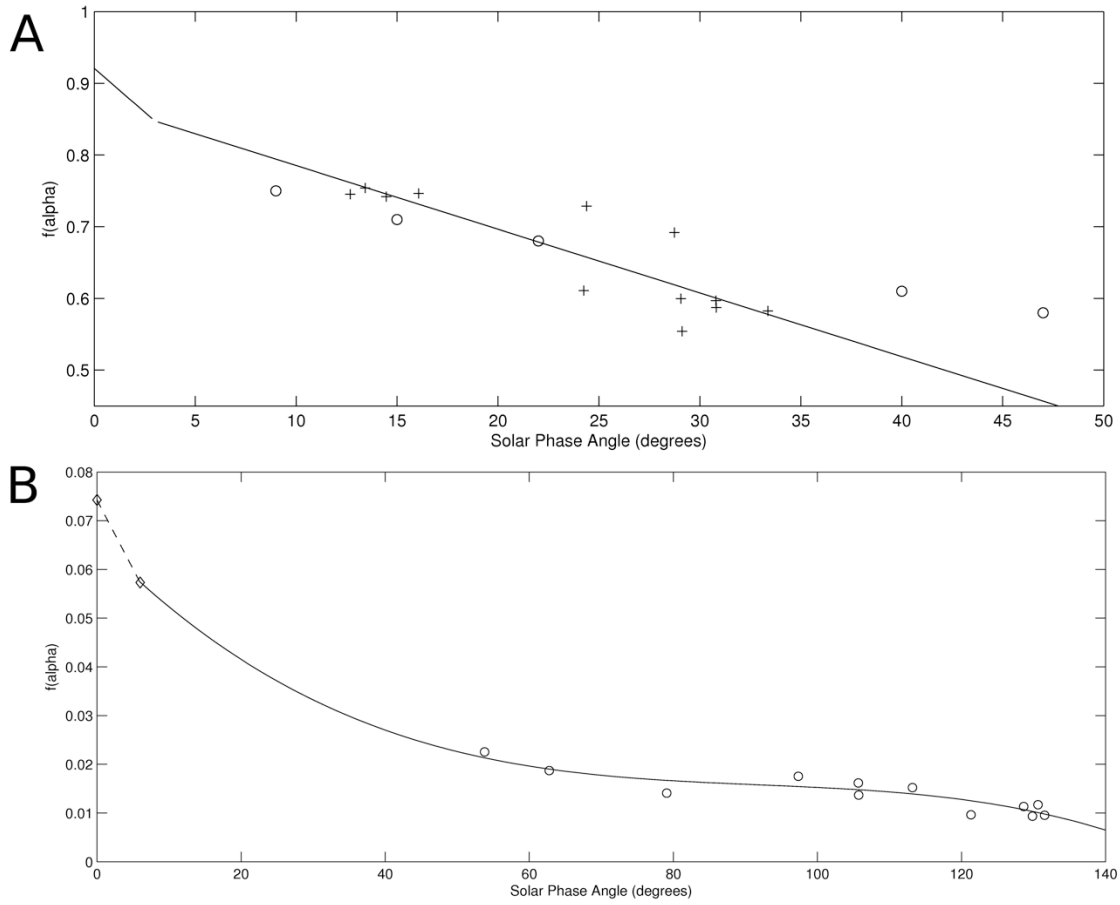

Figure 4.2 – A. *The surface phase function for the bright material at 0.47 μm is a linear fit (black line) to our data from the 12 sampled cubes (pluses). At less than 3°, we modified the slope to reflect the known phase coefficient (0.03 mag/deg) for the bright hemisphere from Noland et al. (1974) and Millis (1977). We compared our results to a surface phase function by Squyres et al. (1984) (circles) from Voyager ISS clear-filter images to verify our method. We used precisely the same surface phase function for bright material as Blackburn et al. (2010).* ***B.*** *For the dark material, the surface phase function for 0.47 μm is also displayed. The circles represent data from high-resolution VIMS cubes (all over 50° phase angle). The diamond at 0° is twice the normal reflectance of Cruikshank et al., 2008, and the dotted line shows the opposition surge at that wavelength, corresponding to a phase coefficient of 0.05 deg/mag (Squyres et al., 1984; Noland et al, 1974; Millis, 1977).*

A vital component of the surface phase function is the value for *f(0)*, which is equal to twice the normal reflectance. For the light material (Fig. 2A), we utilized the Noland *et al.* (1974) and Squyres *et al.* (1984) values for the opposition surge to correct for the lack of high-resolution VIMS cubes at low phase angles for Iapetus; we used the same surface phase functions for the bright material as Blackburn *et al.* (2010) by using the same data to achieve the same result. In the case of the dark material (Fig 4.2B), we utilized the normalized spectra from Cruikshank *et al.* (2008) as half of our *f(0)*, which is a compilation of Bell *et al.* (1985) and Owen *et al.* (2001) data, scaled to the geometric albedo of 0.14 at 2.2 microns; this spectrum was carefully obtained via ground-based telescopes in order to eliminate contamination by light material from the poles on the leading side. In order to determine normal reflectance, we then fit third-order polynomials to all of the surface phase functions and developed a scaling relationship to account for the contrast in albedo on the surface and the change in concavity of the surface phase functions between the dark and light material:

$$s = \frac{R_{data} - R(\alpha)_D}{R(\alpha)_L - R(\alpha)_D} \tag{4.2}$$

$$R_{data} = \left(\frac{I}{F}\right)_{data}\left(\frac{\mu_0 + \mu}{\mu_0}\right) \tag{4.3}$$

$$r = R_{data}\frac{f(0)}{2f(\alpha)} = R_{data}\frac{sR(0)_L + (1-s)R(0)_D}{2\left[sR(\alpha)_L + (1-s)R(\alpha)_D\right]} \tag{4.4}$$

where R_D and R_L are the surface phase functions for the dark and light material (third-order polynomials in terms of the phase angle α); R_{data} is a correction factor applied to each individual I/F_{data} pixel to reduce limb darkening in the data set and allow for a comparison with the surface phase functions; s is our scaling ratio of the percentage of

light material; and r is the normal reflectance. It should be noted that the value for R_{data} is twice the I/F_{data} when emission and incidence angles are at unity for the image undergoing transformation to normal reflectance. Such a scaling relationship is necessary in order to acquire the proper normal reflectance in the mixed albedo regions. Thus, equations 4.2-4.4 are used on each pixel in a VIMS cube of I/F to calculate normal reflectance, and each scaling relationship is unique for each VIMS band or wavelength.

As normal reflectance has been shown to be a good approximation for the geometric albedo at values less than ~0.6 since the effects of multiple scattering are minimized (Squyres *et al.*, 1984; Buratti and Veverka, 1985), we assumed the values to be equivalent. Based on instrument specification documents regarding the accuracy of the *Cassini* VIMS and ISS instruments (Brown *et al.*, 2004; Porco *et al*., 2004) and the error within our surface phase functions, we estimate an average error across all wavelengths of 2.1 % for our geometric albedo values of the brighter material, while the error in the darker material is worse (5.0 %) due to the low signal to noise ratios. Geometric albedos for the trailing hemispheres and leading hemispheres have been reported as 0.42 ± 0.05 and 0.08 ± 0.01 at 0.55 microns (Squyres et al, 1984; Owen et al., 2001); the same averages of VIMS data at 0.55 microns (Band 28 of VIMS-VIS) corrected to normal reflectance in this study are 0.41 ± 0.03 and 0.08 ± 0.01, respectively.

Table 4.2 *Cassini VIMS cubes utilized in our mosaics.*

Cube	Phase Angle	Subspacecraft Longitude	Pixel Size (km)
1483156810_1	54	69	82
1510369274_1	61	29	121
1568145604_1	32	245	22
1568163600_1	33	247	42
1568163922_1	33	247	43
High-Resolution Border Cubes	15-29	205-241	1-5

High-Resolution Border Cube List

1568128091_1	1568130559_1	1568131994_1	1568134531_1
1568128380_1	1568130636_1	1568132105_1	1568134703_1
1568128681_1	1568130786_1	1568132282_1	1568134877_1
1568128811_1	1568130860_1	1568132454_1	1568135049_1
1568128941_1	1568131010_1	1568132626_1	1568135222_1
1568129071_1	1568131083_1	1568132801_1	1568135394_1
1568129201_1	1568131233_1	1568133146_2	1568135570_1
1568129331_1	1568131307_1	1568133319_1	1568135798_3
1568129461_1	1568131457_1	1568133492_1	1568135915_1
1568129671_1	1568131468_1	1568133665_1	1568136232_1
1568129948_1	1568131605_1	1568133838_1	1568136342_1
1568130180_1	1568131937_1	1568134011_1	1568136449_1
1568130330_1	1568131972_1	1568134183_1	1568136573_1
1568130409_1	1568131983_1	1568134357_1	

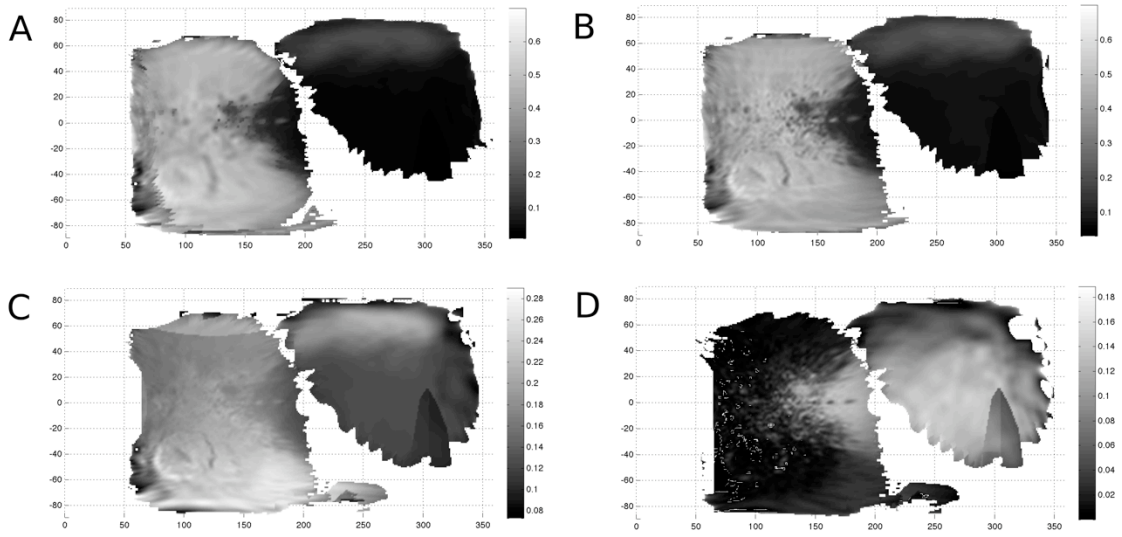

Figure 4.3 *– Cassini VIMS normal reflectance maps.* ***A.*** *0.53 μm* ***B****. 1.00 μm* ***C.*** *2.12 μm (water adsorption feature)* ***D.*** *4.11 μm (brightness reversal)*

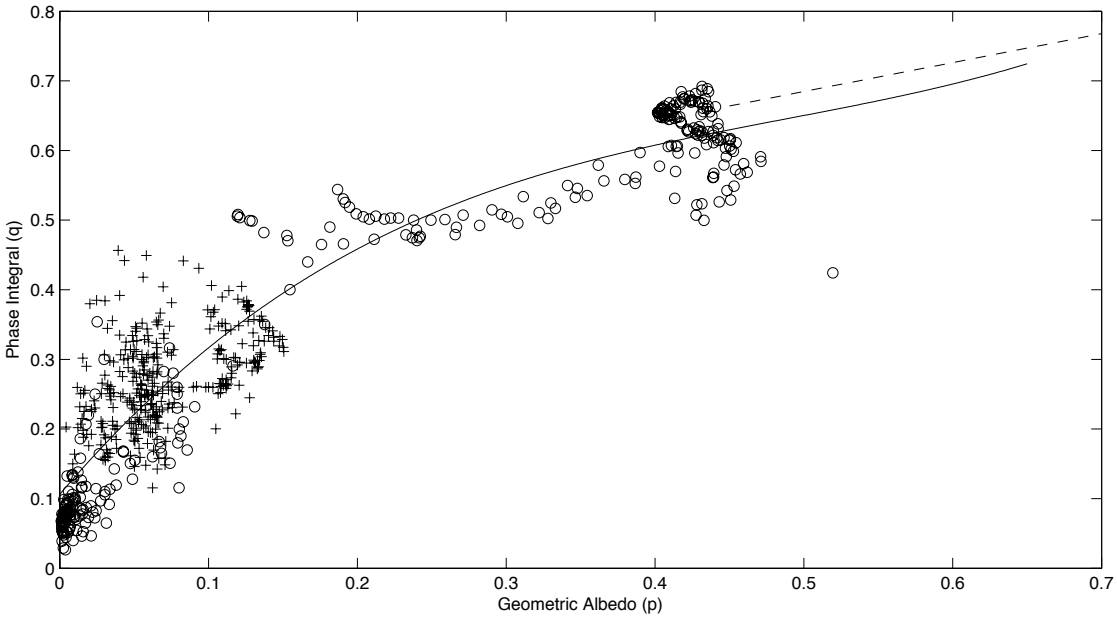

Figure 4.4 *– Our relationship (solid black line) between the geometric albedo and the phase integral by comparing data for the leading hemisphere (pluses) with the trailing (circles). The dotted line shows the relationship for a "typical" saturnian satellite by averaging the linear fits for Mimas, Tethys, Rhea, and Dione from Pitman et al. (2010).*

4.3.1.2 Phase Integral Determination

Blackburn *et al.* (2010) showed that the phase integral could be effectively predicted by the geometric albedo. While the curvature in the data shown in their Fig. 4.5 is most likely the result of a textural difference for the dark material, a third-order polynomial fit this difference well. From that study, we have derived this estimation for the phase integral plotted in Fig 4.4:

$$q = 2.9583p^3 - 4.3155p^2 + 2.5066p + 0.1061 \qquad 0 < p < 0.65 \qquad (4.5)$$

where q is the phase integral and p is the geometric albedo. Since the brightest terrain on Iapetus has a geometric albedo of ~0.65 and the Blackburn et al. (2010) data did not extend into albedos that high, we used the slope of the average of a linear fit from Pitman *et al.* (2010) phase integral values for Tethys, Mimas, Dione, and Rhea as a guide for extrapolation. We altered the coefficients in our fit (eq. 4.5) until the slope matched the one from their data beyond geometric albedoes of 0.55 (Fig. 4.4), which resulted in an estimation of the phase integral of 0.72 ± 0.10 for the brightest terrain on Iapetus. Equation 4.5 was vital to produce 352 individual phase integral maps (Fig. 4.5) for each of the VIMS bands by applying the equation over every pixel of the normal reflectance maps. The scatter in the data (Fig. 4.4) produces an estimated error of ± 0.06 for the values of the phase integrals in our map (Fig. 4.5).

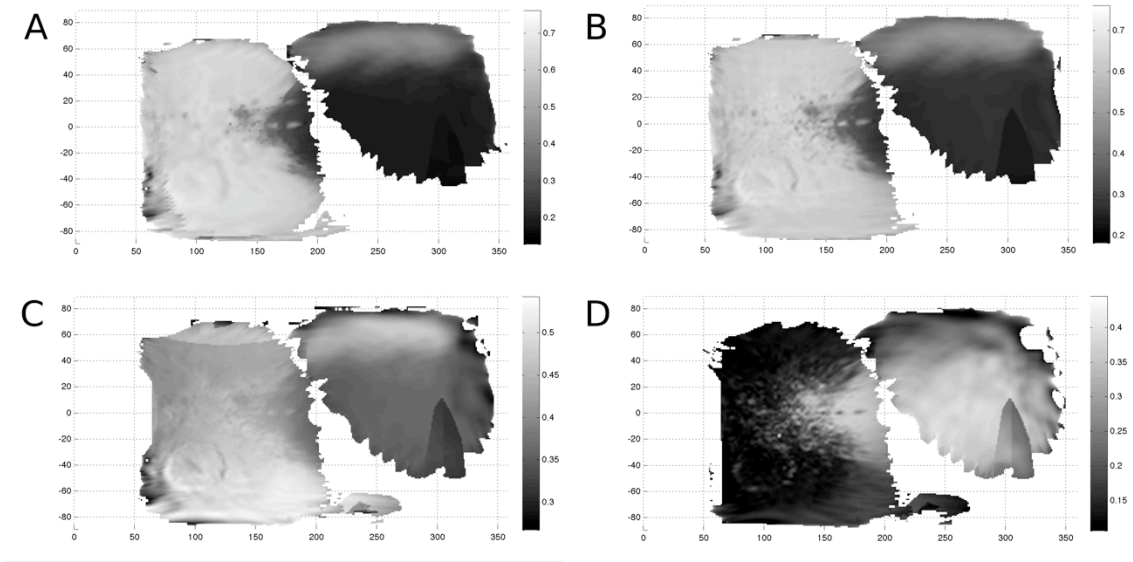

Figure 4.5*– Cassini VIMS phase integral maps.* ***A.*** *0.53 μm* ***B****. 1.00 μm* ***C.*** *2.12 μm (water adsorption feature)* ***D.*** *4.11 μm (brightness reversal)*

4.3.1.3 Bolometric Bond Albedo

The Bond albedo (Fig. 4.6) is simply the product of the phase integral and the geometric albedo, and we calculated this value for all 352 bands. However, the Bond albedo is wavelength dependent because its aforementioned factors are, and thus, the bolometric Bond albedo (Fig. 4.7) is integrated over all wavelengths, taking into account the intensity of the solar flux at each wavelength:

$$A_B = \frac{\int_0^\infty q(\lambda)p(\lambda)F(\lambda)d\lambda}{\int_0^\infty F(\lambda)d\lambda} \tag{4.6}$$

where q is the phase integral, p is the geometric albedo, F is the intensity of the solar flux, and λ is wavelength. When performing this integration, we were careful to compare the results from the overlapping bands from VIMS-VIS and VIMS-IR and noticed that their differences were negligible. In addition to the low-resolution mosaic depicted in Fig 4.7, we also created a higher resolution mosaic (4 pixels per degree lat/long, ~5 km per pixel) from VIMS cubes from the Sept 10, 2007 flyby (Fig 4.8). For error determination, we used the following relationship for the errors in the individual Bond albedos:

$$A_{Bond.err} = A_{Bond}\sqrt{\left(\frac{p_{err}}{p}\right)+\left(\frac{q_{err}}{q}\right)} \tag{4.7}$$

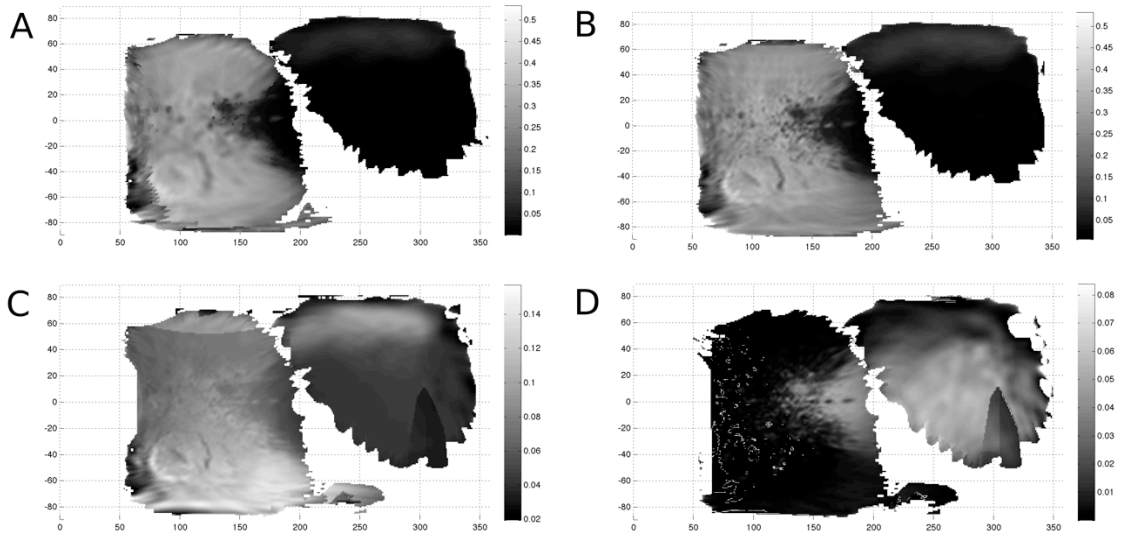

Figure 4.6 *– Cassini VIMS Bond albedo maps.* ***A.*** *0.53 μm* ***B****. 1.00 μm* ***C.*** *2.12 μm (water adsorption feature)* ***D.*** *4.11 μm (brightness reversal)*

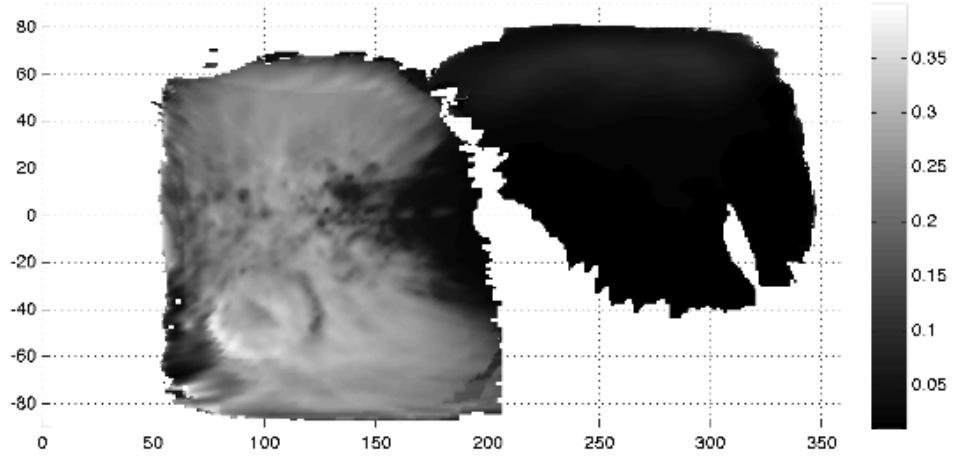

Figure 4.7 *– Cassini VIMS bolometric Bond albedo map in equirectangular projection.*

4.3.2 *Voyager* ISS

Given the lack of coverage by *Cassini* of Iapetus's northern pole, we have scaled *Voyager* ISS images (Fig 4.10) in order to approximate the bolometric Bond albedo there. By evaluating equation 4.6 for our *Cassini* VIMS data over the wavelength range of the *Voyager* clear filter (350 – 650 nm) to produce a Bond albedo map with the weighting of the solar flux at those wavelengths and comparing to the same map over all wavelengths (Fig 4.7), we were able to determine a scaling ratio in order to fit *Voyager* ISS observations into our map (Table 4.3). In the case of the light material, the ratio is 0.911, and in the case of the dark material, it is 2.44. These values show that the albedo is brighter for the dark material at wavelengths higher than 0.65 microns and the reverse for the light material, a fact that is corroborated by published spectra (Cruikshank *et al.*, 2008; Blackburn *et al.*, 2010).

We used Squyres' normal reflectance map as a point of reference and two *Voyager* ISS images (FDS counts 3497658 and 4390708) to add coverage of the northern polar cap, which is important for modeling the possibility of a CO_2 polar cap on Iapetus and its stability. Our normal reflectance values compare well to the normal reflectance maps produced from *Voyager* ISS observations by Squyres *et al.* (1984) and Buratti and Mosher (1995). In regions of overlap between *Voyager* ISS and *Cassini* VIMS, we ratioed the overlap regions with the numerator being the *Voyager* results as a consistency check; the pixels in this ratioed mosaic on average were 1.01 ± 0.34.

4.3.3 *Cassini* ISS

We used *Cassini* ISS narrow angle images N1562601817_1 taken in the BL1/CL2 filters (404 - 507 nm) and N1482859953_2 in the CL1/CL2 filters (200 – 1100 nm).

Employing the same procedure as in section 2.2 for *Voyager* (scaling ratios are in Table 4.3), we translated these images to a full bolometric Bond albedo for the purpose of adding regions of Iapetus for which no VIMS cubes are available (Fig 10). We also used an ISS wide-angle camera image W1568130503_2 with the CL1/CL2 filters (380-1100 nm) to produce a high resolution bolometric Bond albedo map of the border region (Fig 4.9). *Cassini* ISS (CL1/CL2) clear filter images required a different scale than *Voyager* ISS, i.e. 9.111 for light and 2.411 for dark (Table 4.3) because of the broader range in wavelengths 0.2 – 1.1 μm. We noted no noticeable change for the scaling factors necessary for the narrow verses the wide-angle CL1/CL2 filter images. We performed the same consistency check as in the case of *Voyager* by comparing *Cassini* ISS versus VIMS in overlap regions with ISS being in the numerator of this ratio; we found the average of the pixels in the overlap region of this comparison to be 1.08 ± 0.18.

4.4 Results

Since sufficient coverage for the South was not available, we flipped the northern hemisphere to provide estimates for the values in the South; this procedure was also performed by Palmer and Brown (2008), corresponds well with the results of Spencer and Denk (2010), and is supported by the contour lines at the edges of our mosaics. At other points where no data was available or only in phase angles higher than 90 degrees, we used the contour lines of albedo nearby to project their values (Fig 4.10). For our mosaics, which were produced from the cubes and images listed in Table 4.2, we were careful to avoid the terminator or limb in our camera images, since the photometric function we used can depart from true values at those edges. Most of our mosaics (Figs 4.3, 4.5-4.9, 4.11) are in an equirectangular projection view, and all except for the two of the border

region (Figs 4.8 & 4.9) are in a resolution of 1 pixel per degree lat/long (~10 km per pixel). In order to focus on the values at the northern cap, we also projected the values from Fig 4.11 into a polar stereographic view (Fig. 4.12) where the highest value in the north is 0.40 ± 0.07. In regards to the dark terrain, the darkest material is located in the center of the apex and has a bolometric Bond albedo of 0.015 ± 0.012. Using an equal-area projection mode (sinusoidal), we calculated an average bolometric Bond albedo of 0.250 ± 0.032 for the trailing hemisphere (0 to 180 ˚E) and 0.056 ± 0.014 for the leading (180 to 360 ˚E).

Table 4.3 *Scaling factors for conversion to bolometric Bond albedo.*

Instrument	**Filter(s)**	**Wavelength Range (nm)**	**Dark**	**Light**
Voyager ISS NAC	Clear	310-650	1.857	0.917
Cassini ISS NAC	BL1/CL2	404-507	1.790	0.920
	CL1/CL2	200-1100	1.440	0.940
Cassini ISS WAC	CL1/CL2	380-1100	1.440	0.940

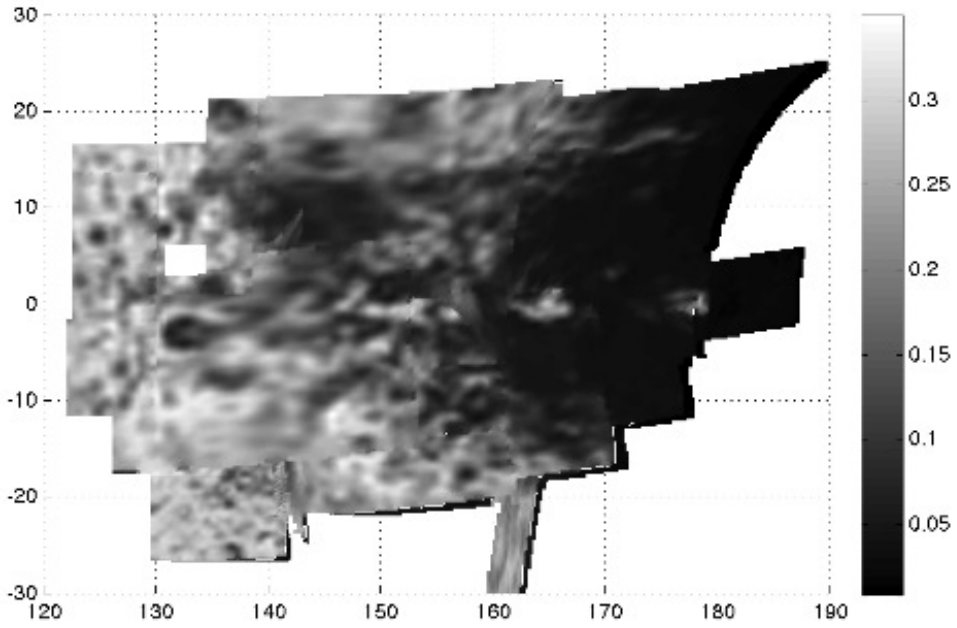

Figure 4.8– *Bolometric Bond albedo of the border region from high resolution Cassini VIMS cubes in Table 4.2.*

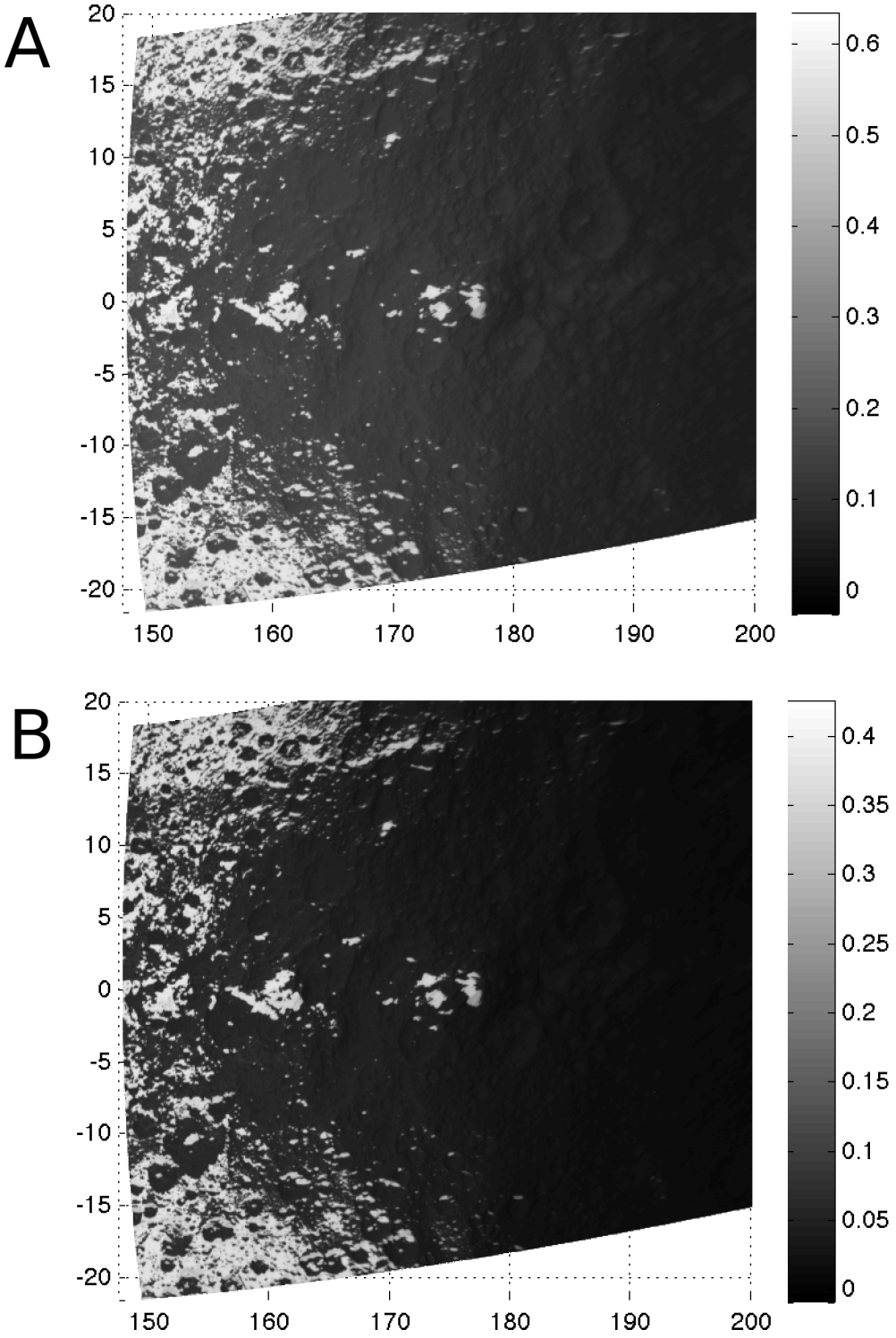

Figure 4.9 *– Cassini ISS wide angle camera image W1568130503_2 in equirectangular projection view.* ***A.*** *Normal reflectance, i.e. geometric albedo set to grey scale.* ***B.*** *Bolometric Bond albedo set to grey scale.*

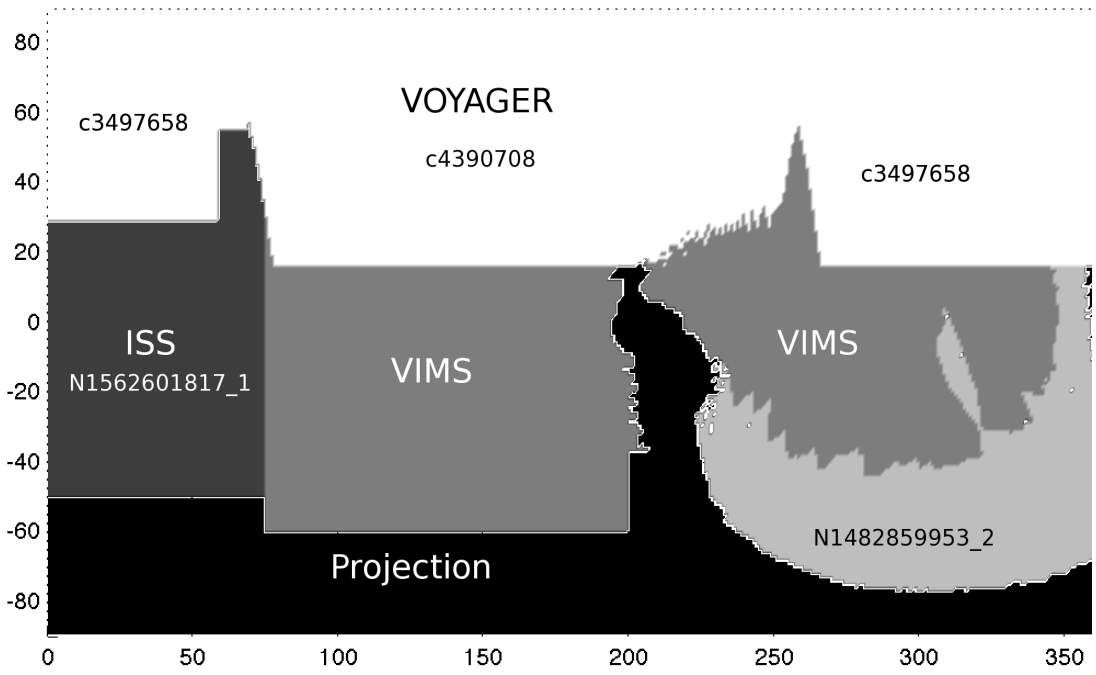

Figure 4.10 – *Guide to mosaics for Figures 4.11 and 4.12.*

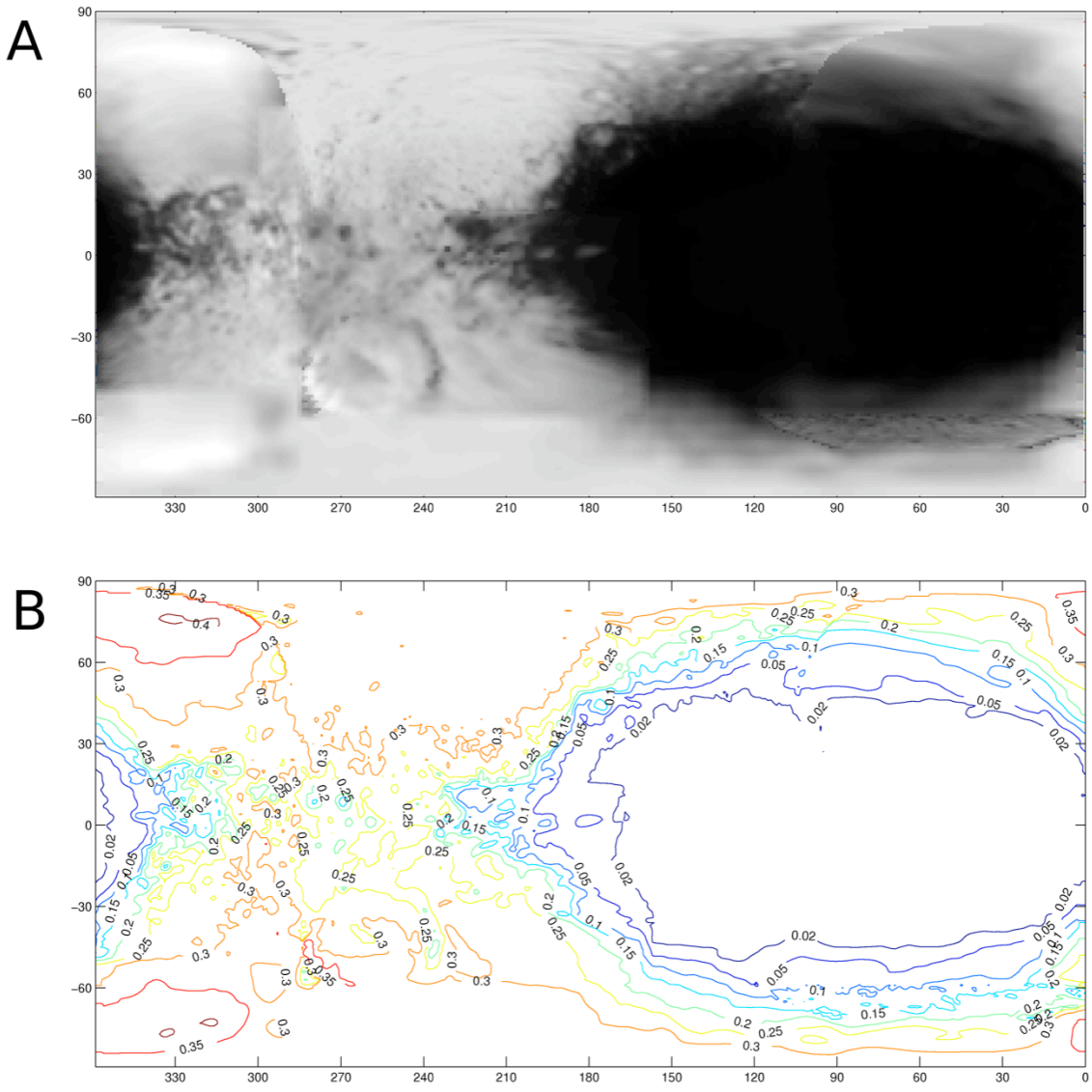

Figure 4.11 *– Our complete coverage bolometric Bond albedo map in an equirectangular projection, mosaicked using the order outlined in Figure 4.10.* ***A.*** *Values converted into grayscale image.* ***B****. Contour map of the values.*

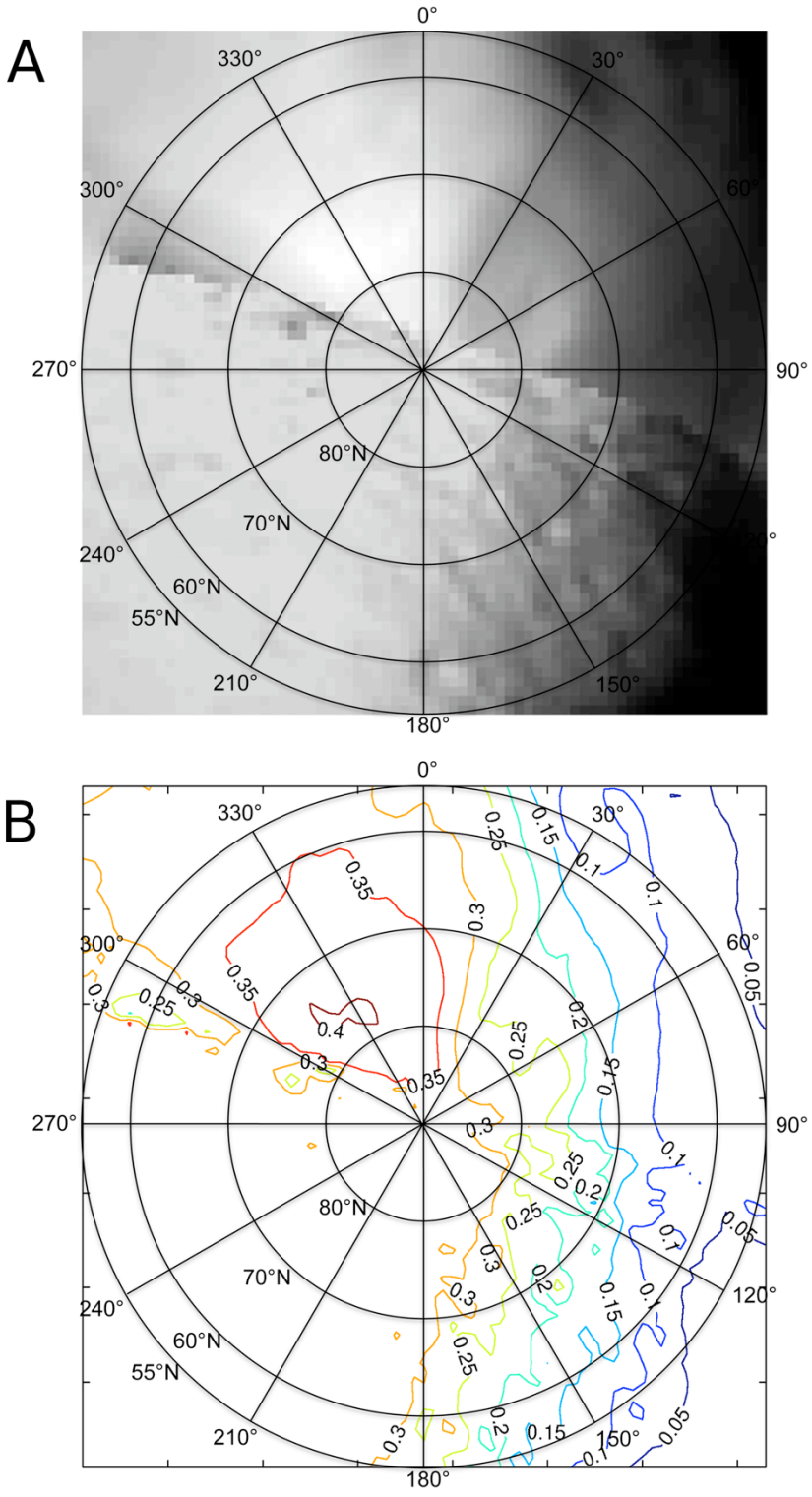

Figure 4.12 *– Polar stereographic view of the northern pole (55 to 90 degrees N latitude) bolometric Bond albedo map.* ***A.*** *Values converted into grayscale image.* ***B****. Contour map of the values.*

4.5 Discussion

Given the contrast in albedo within the leading hemisphere and the opportunity provided by the Sept 10, 2007 flyby of Iapetus, we chose to investigate the bolometric Bond albedo change of the border region centered at ~0°N and 150°E with both the VIMS (Fig. 4.8) and the ISS (Fig 4.9) cameras. Clearly, as the resolution increases, the contrast in albedo becomes more evident, indicating a problem of resolution with determining the albedo of the bright material, also noticed by Spencer and Denk (2010). While the average bolometric Bond albedo of the trailing hemisphere is 0.25, the brighter, purer material has an albedo of 0.38 ± 0.01. This evidence contradicts previous claims in the literature about a very gradual transition in albedo (Squryes *et al.*, 1984; Buratti and Mosher, 1995) from relying on the lower resolution *Voyager* observations yet supports the observations of Denk *et al*., 2010. While the change appears gradual (Fig. 4.3), higher resolution images show that it is a deception caused by averaging light material with isolated regions of dark material that appear to be speckled into the equatorial regions of the trailing hemisphere (Fig. 4.1). The *Cassini* CIRS instrument has provided another method of determining the bolometric Bond albedo from the peak temperatures (Howett *et al.*, 2010; Spencer and Denk, 2010). Howett *et al.* (2010) calculated values of 0.31 for the trailing and 0.10 for the leading hemisphere. The FP1 data as described by Spencer and Denk (2010) give a bright side albedo of 0.31, though they note that the fits of the bright terrain peak temperatures from the higher spatial resolution FP3 data match 0.39, compared to our value of 0.38 ± 0.04 at higher resolution (Fig 4.9). Thus, our results correspond well with Spencer and Denk (2010) in this respect. The difference in the values between Figure 4.8 and 4.9 highlights the difficulty in

estimating the bolometric Bond albedo for so called "light" and "dark" material. In the higher resolution ISS image of the border region (Fig 4.9), it is clear that the boundary is a harsh contrast (0.37 for bright and 0.04 for dark), but in Fig 4.11, the albedo change appears gradual, as would be expected from an average of the pixels. This problem makes the accuracy of the results from a thermal model highly dependent on the resolution of that model, as a model with lower resolution would clearly give an average temperature of a wide region.

Previous estimates for the bolometric Bond albedo are quite limited, but we compared our results to the reported values available. Compared with the Bond albedo map provided by Palmer and Brown (2008), our values are lower for the trailing hemisphere for two reasons: (1) Palmer and Brown (2008) estimated that the phase integral for the brightest region on Iapetus was 1 by applying values from Europa compared to our estimate of 0.72, and (2) they used only reflectance values in the visible range from the *Voyage*r ISS clear filter, which results in an overestimation of about 11 percent due to the spectra of the trailing side (Blackburn *et al.*, 2010). However, our average value of 0.06 ± 0.01 for the leading hemisphere is roughly equivalent to theirs (0.04). We find our results difficult to reconcile with the Morrison *et al*. (1975) values for the trailing hemisphere of a Bond albedo of 0.5, a phase integral of 1.3, and an average geometric albedo of 0.34 determined from radiometry. We argue that part of the discrepancy here is due to inaccurate values for Iapetus' radius of 835 km instead of the more recent measurement (~730 km) that Morrison *et al*. (1975) relied upon for their calculation.

With regard to the northern hemisphere, it is clear that this area has higher bolometric Bond albedos than the trailing hemisphere at equatorial latitudes. However, our scaling of *Voyager* data here is based on the assumption that bright material spectra at the equatorial and mid-latitudes covered by the VIMS instrument are a good match for the icy material at Iapetus's poles. If however, a CO_2 cap with a different spectrum is present, as some have suggested (Palmer and Brown, 2008), then values for the North may be different due to that reason or a texture difference that alters the scattering and hence the phase integral. With these limitations in mind, we have applied a conservative error of 0.40 ± 0.07 for the value of bolometric Bond albedo for the brightest region on Iapetus.

4.6 Equilibrium Surface Temperatures

The ultimate practical outcome of this study is to determine surface temperatures via thermal models. As a first-order approximation of the equilibrium blackbody temperature, we chose to use a simple equilibrium temperature equation:

$$T_{eff} = \sqrt[4]{\left(\frac{1-A}{\sigma_B}\right)\left(\frac{F_{sun}}{R^2}\right)} \tag{4.8}$$

where A is the bolometric Bond albedo, σ_B is the Stefan-Boltzman constant, F_{sun} is the solar constant at 1 AU, and R is the distance from the sun in AU. For R, we used the semi-major axis for Saturn. Our values for the effective temperatures give a maximum blackbody temperature at low latitudes of 125.5 K for leading and 118.4 K for the trailing; essentially, these temperatures represent the average maximum temperature of the two hemispheres at the equator at the semi-major axis of Saturn's orbit. Equation 4.8 assumes that the body is in equilibrium with the ambient solar flux, which is appropriate

due to Iapetus' status as a slow rotator (~79 earth days). Thus, these temperatures correspond to low latitude midday temperatures only; we leave further development of an advanced thermal model for Iapetus to another study.

4.7. Conclusions

Exploring key questions on Iapetus in greater detail, such as thermal segregation and volatile transport, will require advanced thermal models. Our map provides the most accurate fundamental framework for thermal modeling of Iapetus' surface temperatures and surface processes to date, and we also demonstrate that resolution is key when comparing albedo values correctly for Iapetus. In general bolometric Bond albedoes for the northern polar region on Iapetus have been overstated in some previous thermal models (Palmer and Brown, 2007), as values peak at ~0.4. This adjustment in values comes primarily from the phase integrals, which previously had to be estimated for Iapetus until the *Cassini* tour allowed the opportunity to measure brightness at phase angles up to 140 degrees.

4.8. References

Blackburn, D.G., Buratti, B.J., Ulrich, R., Mosher, J., 2010. Solar phase curves and phase integrals for the leading and trailing hemispheres of Iapetus from the *Cassini* Visual and Infrared Mapping Spectrometer. Icarus, 209, 738-744.

Bell, J.F., Cruikshank, D.P., Gaffey, M.J., 1985. The composition and origin of the Iapetus dark material. Icarus 61, 192-207.

Brown, R.H., and 21 colleagues, 2004. The *Cassini* Visual and Infrared Mapping Spectrometer (VIMS) investigation. Space Sci. Reviews 155, 111-168.

Buratti, B.J., Mosher, J.A., 1995. The dark side of Iapetus: Additional evidence for an exogenic origin. Icarus 115, 219-227.

Buratti, B.J, Veverka, J., 1985. Photometry of rough planetary surfaces: the role of multiple scattering. Icarus 64, 320-328.

Chandrasekhar, S. 1960. Radiative Transfer. Dover Press, New York.

Cruikshank, D.P., Bell, J.F., Gaffey, M.J., Brown, R.H., Howell, R. Beerman, C., Rognstad, M., 1983. The dark side of Iapetus. Icarus, 53, 90-104.

Cruikshank, D.P., and 26 coauthors, 2008. Hydrocarbons on Saturn's satellites Iapetus and Phoebe. Icarus 193, 334-343.

Denk, T. and 10 co-authors, 2010. Iapetus: Unique surface properties and a global color dichotomy from Cassini imaging. Science 327, 435-439.

Hapke, B. W., 1963. A theoretical photometric function for the lunar surface. J. Geophys. Res. 68, 4571-4586.

Howett, C.J.A., Spencer, J.R., Pearl, J., Segura, M., 2010. Thermal inertia and bolometric Bond albedo values for Mimas, Enceladus, Tethys, Dione, Rhea, and Iapetus as derived from Cassini/CIRS measurements. Icarus 206, 573-593.

Irvine, W.M., 1966. The shadowing effect in diffuse reflection. J. Geophys. Res. 71, 2931-2937.

Matthews, R. A. J. 1992. The darkening of Iapetus and the origin of Hyperion. Q.J.R. astr. Soc. 33, 253-258.

Mendis, D. A., Axford, W. I., 1974. Satellites and magnetospheres of the outer planets. Annu. Rev. of Earth & Planet. Sci. 2, 419-474.

Millis, R.L., 1977. UBV photometry of Iapetus: Results from five apparitions. Icarus 31, 81-88.

Morrison, D., Jones, T.J., Cruikshank, D.P. Murphy, R.E., 1975. 2 faces of Iapetus. Icarus 24, 157-171.

Noland, M., Veverka, J., Morrison, D., Cruikshank, D.P., Lazarewicz, A.R., Morrison, N.D., Elliot, J.L., Goguen, J., Burns, J.A., 1974. Six-color photometry of Iapetus, Titan, Rhea, Dione, and Tethys. Icarus 23, 334-354.

Owen, T.C., Cruikshank, D.P., Dalle Ore, C.M., Geballe, T.R., Roush, T.L., de Bergh, C., Meier, R., Pendleton, Y.J., Khare, B.N., 2001. Decoding the domino: The dark side of Iapetus. Icarus 149, 160-172.

Palmer, E.E. and Brown, R.H., 2008. The stability and transport of carbon dioxide on Iapetus. Icarus 195, 434-446.

Pitman, K.M., Buratti, B.J., Mosher, J.A, 2010. Disk-integrated bolometric bond albedos and rotational light curves of saturnian satellites from Cassini VIMS. Icarus 206, 537-560.

Porco, C.C. and 19 coauthors, 2004. Cassini imaging science: Instrument characterizations and anticipated scientific investigations at Saturn. Space Science Reviews 115, 363-497.

Smith, B.A. and 26 coauthors, 1981. Encounter with Saturn: Voyager 1 imaging science results. Science 212, 163-191.

Smith, B.A. et al., 1982. A new look at the Saturn system - The Voyager 2 images. Science 215, 504-537.

Soter, S., 1974. Remarks on origin of Iapetus' photometric asymmetry. Paper presented at the 28th IAU Colloquium on Planetary Satellites, Cornell University.

Spencer, J.R. and Denk, T., 2010. Formation of Iapetus' extreme albedo dichotomy by exogenically triggered thermal ice migration. Science 327, 432-435.

Squyres, S.W., Buratti, B.J., Veverka, J., Sagan, C., 1984. Voyager photometry of Iapetus. Icarus 59, 426-435.

Squyres, S.W., Sagan, C., 1983. Albedo asymmetry of Iapetus. Nature 303, 782-785.

Verbiscer, A. J., M. Skrutskie, Hamilton D., 2009. Saturn's largest ring. Nature 461, 1098-1100.

Vilas, F., Larson, S.M., Stockstill, K.R., Gaffey, M.J., 1996. Unraveling the zebra: Clues to the Iapetus dark material composition. Icarus 124, 262-267.

APPENDIX C

Author's personal copy

Icarus 212 (2011) 329–338

Contents lists available at ScienceDirect

Icarus

journal homepage: www.elsevier.com/locate/icarus

A bolometric Bond albedo map of Iapetus: Observations from *Cassini* VIMS and ISS and *Voyager* ISS

David G. Blackburn [a,*], Bonnie J. Buratti [b], Richard Ulrich [c]

[a] Arkansas Center for Space and Planetary Sciences, University of Arkansas, 202 Old Museum Bldg., Fayetteville, AR 72701, United States
[b] Jet Propulsion Laboratory, California Institute of Technology, 4800 Oak Drove Dr. 183-501, Pasadena, CA 91109, United States
[c] Department of Chemical Engineering, University of Arkansas, 3202 Bell Engineering Center, Fayetteville, AR 72701, United States

ARTICLE INFO

Article history:
Received 24 June 2010
Revised 13 December 2010
Accepted 19 December 2010
Available online 31 December 2010

Keywords:
Iapetus
Photometry
Satellites, Surfaces

ABSTRACT

We utilized *Cassini* VIMS, *Cassini* ISS, and *Voyager* ISS observations of Iapetus to produce the first bolometric Bond albedo map of Iapetus. The average albedo values for the leading and trailing hemispheres are 0.06 ± 0.01 and 0.25 ± 0.03, respectively. However, the bright material in high-resolution ISS images has a value of 0.38 ± 0.04, highlighting the importance of resolution in determining accurate albedo values for Iapetus due to the speckling of localized regions of dark material into the trailing hemisphere. The practical application of this map is determining more accurate surface temperatures in thermal models; these albedo values translate into first order blackbody temperatures of 125.5 K and 118.4 K for the trailing and leading hemispheres at the semi-major axis.

© 2010 Elsevier Inc. All rights reserved.

1. Introduction

Iapetus, discovered by Giovanni Domenico Cassini in 1671, is being explored by a craft bearing his name. In terms of brightness, Iapetus is the most diverse satellite in the saturnian system, and its albedo dichotomy makes it a prime target for a study of the reflectance and thermal properties of icy satellites in general. Not only is the origin of the low-albedo material indicative of a unique process altering a planetary surface (or at least an extreme example of such a process), but the extreme changes in albedo and thus temperature may drive volatile transport and segregation on the moon. Previous observations by *Voyager 2* were too deficient in spatial resolution, spectral range and viewing geometry to accurately map the albedo variations on the body and to fully understand the energy balance.

Following the *Voyager 2* results of Smith et al. (1982) showing the stark dichotomy in albedo between the leading and trailing hemispheres, Squyres and Sagan (1983) demonstrated that the darkest area on the surface is not only on the apex of motion for the satellite, but that the albedo changes gradually from the low albedo to high albedo regions. As Fig. 1 illustrates, the dark material drapes over into the trailing hemisphere, producing a pattern much like a baseball cover. Various theories have been proposed as the source of this dichotomy, including endogenic sources such as volcanic flows (Smith et al., 1981) and exogenic sources from the remnants of collisions and micro-meteoritic bombardment involving the outer irregular satellites, including Phoebe and Hyperion (Soter, 1974; Cruikshank et al., 1983; Matthews, 1992; Buratti and Mosher, 1995; Vilas et al., 1996; Owen et al., 2001). The discovery of a large, tenuous dust ring at the orbit of Phoebe ring provided final validation for the exogenic class of models (Verbiscer et al., 2009), and at present the exogenic source as the origin of the dark material is more widely favored due to the dark material residing on the apex of motion. Consequently, Spencer and Denk (2010) have shown that thermal segregation is a probable mechanism for creating the pattern that is present today if the leading hemisphere were seeded by an exogenic coating in the past, a process originally proposed by Mendis and Axford (1974). In addition, Denk et al. (2010) have shown that both dark and light materials on the leading side have redder spectra than their counterparts on the trailing hemisphere.

In this paper, we take advantage of the extraordinary wavelength and solar phase angle coverage of the *Cassini* Visual and Infrared Mapping Spectrometer (VIMS), coupled with observations from the *Cassini* and *Voyager 1 & 2* Imaging Science Subsystems (ISS), to produce the first bolometric Bond albedo map of Iapetus. Blackburn et al. (2010) provided the first phase integrals measured directly from photometry at solar phase angles between 0° and 140° at wavelengths ranging from 0.36 to 5.12 μm, which we will use to produce the albedo map in this study. Since the *Cassini* Visual Infrared Mapping Spectrometer provides reflectance over 99% of the total radiated power of the solar spectrum, it is ideal for deriving the bolometric Bond albedo that is integrated over all wavelengths of the solar spectrum.

* Corresponding author.
E-mail address: dgblackb@uark.edu (D.G. Blackburn).

0019-1035/$ - see front matter © 2010 Elsevier Inc. All rights reserved.
doi:10.1016/j.icarus.2010.12.022

Author's personal copy

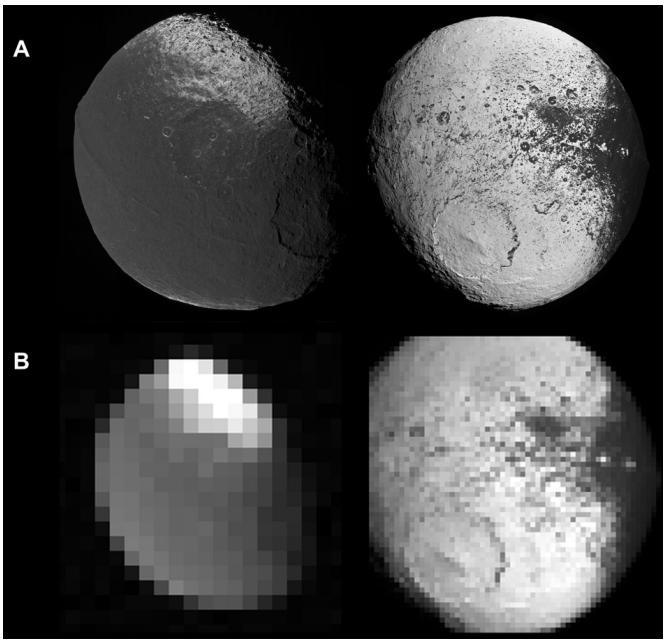

Fig. 1. Images from the two targeted flybys of Iapetus, (left) of the leading hemisphere on December 31, 2004 and (right) of the trailing hemisphere on September 10, 2007. (A) *Cassini* ISS point-perspective mosaic. (B) Band 2 (0.90 μm) from VIMS-IR Cubes 1483156810_1 (left) and 1568145604_1 (right).

2. Data analysis

In order to achieve the map with the best possible coverage of the surface, we chose to include multiple data sets including the *Cassini* Visual and Infrared Mapping Spectrometer, the *Cassini* Imaging Science Subsystem, and the *Voyager 1 & 2* Imaging Science Subsystem. Fig. 1 illustrates the difference in resolution between *Cassini* ISS and VIMS data sets; while the resolution is higher with ISS, VIMS image sets were preferred due to the increased spectral range (0.36–5.12 μm). *Cassini* ISS and *Voyager* ISS images were used primarily to fill in the gaps in VIMS coverage. All image manipulations, calculations, and projections were performed with the Integrated Software for Imagers and Spectrometers (ISIS) package versions 2 & 3. All *Cassini* VIMS cubes were acquired and calibrated to *I*/*F* internally by the VIMS team as described in Brown et al. (2004), while *Voyager* ISS and *Cassini* ISS images were obtained from the Planetary Data System (PDS) and converted to *I*/*F* via the SPICE information and instrument specifications embedded in routines native to the open source ISIS software; the SPICE kernels within ISIS also provided the necessary ephemeris data for the projections. In some cases, limb fits and manual adjusting were necessary to refine the pointing information. All of the data used in this study were nonproprietary and accessible via the PDS.

2.1. Cassini VIMS

2.1.1. Normal reflectance maps

Cassini VIMS allowed the production of separate normal reflectance maps (Fig. 3) at all 352 bands covering wavelengths from 0.35 to 5.12 μm. In order to correct to normal reflectance, we first chose a photometric function to account for scattering and minimize the effects of limb darkening. Previously, it has been shown that a lunar-like scattering law representing single scattering is appropriate for Iapetus since the majority of the surface has a geometric albedo

Table 1
VIMS high-resolution cubes utilized for production of surface phase functions (Fig. 2).

Cube	Phase angle	Latitude	Longitude	Pixels	Terrain
1568131937_1	24.25	−10	234	324	Light
1568129331_1	13.42	−45	208	900	Light
1568129201_1	12.68	−41	201	900	Light
1568129461_1	14.47	−42	206	900	Light
1568129671_1	16.07	−43	201	25	Light
1568136573_1	29.06	−10	247	144	Light
1568131010_1	24.39	0	199	4	Light
1568136449_1	29.12	11	246	144	Light
1568135049_1	28.74	−12	219	16	Light
1568139139_1	30.79	12	225	16	Light
1568138316_1	30.81	45	216	16	Light
1568163600_1	33.37	47	220	1	Light
1568126375_1	97.35	1	194	1026	Dark
1568128380_1	12.77	−13	208	256	Dark
1568124369_1	131.55	12	220	144	Dark
1568124533_1	130.63	−1	222	16	Dark
1568124800_1	128.64	0	218	16	Dark
1483233838_1	113.2	40	318	16	Dark
1483224693_1	105.68	51	302	9	Dark
1483157059_4	53.8	0	270	9	Dark
1483224693_1	105.73	40	276	4	Dark
1483172847_1	62.78	12	287	4	Dark
1483194809_1	79.09	20	286	9	Dark
1568124753_1	129.85	0	213	4	Dark
1568125677_1	121.32	0	192	4	Dark
1568128091_1	11.3	−10	196	4096	Dark
1568127937_1	13.53	−11	193	900	Dark

Author's personal copy

less than 0.6 (Squyres et al., 1984; Buratti and Veverka, 1985). This Lommel–Seeliger photometric function is defined as:

$$I(i,\varepsilon,\alpha) = F\left(\frac{\mu_0}{\mu_0+\mu}\right)f(\alpha) \quad (1)$$

where i = incidence angle, ε = emission angle, α = phase angle, $\mu = \cos\varepsilon$, $\mu_0 = \cos i$, I = intensity of scattered light, πF = incident solar flux at $i = 0$, and $f(\alpha)$ = phase function of the surface (Chandrasekhar, 1960; Hapke, 1963; Irvine, 1966; Squyres et al., 1984).

In order to correct to a normal reflectance in which the solar phase angle is zero and both μ and μ_0 equal unity, we utilized VIMS high-resolution cubes (Table 1) to produce our own surface phase functions (Fig. 2). The surface phase function represents the decrease in brightness of the surface material as a function of solar phase angle alone, and it also represents physical attributes of the surface such as macroscopic roughness, particle size, and compaction state. We utilized all the high-resolution VIMS cubes from the 2007 targeted flyby, combined them with a handful of images from the 2004 untargeted flyby (Table 1), and selected regions of the brightest and the darkest terrain possible. Individual $f(\alpha)$s were calculated by correcting the I/F values in the high-resolution cubes via Eq. (1), and the resulting data points were used to build a separate set of surface phase functions for the light and dark material (Fig. 2) for each of the 352 VIMS bands.

A vital component of the surface phase function is the value for $f(0)$, which is equal to twice the normal reflectance. For the light material (Fig. 2A), we utilized the Noland et al. (1974) and Squyres et al. (1984) values for the opposition surge to correct for the lack of high-resolution VIMS cubes at low phase angles for Iapetus; we used the same surface phase functions for the bright material as Blackburn et al. (2010) by using the same data to achieve the same result. In the case of the dark material (Fig. 2B), we utilized the normalized spectra from Cruikshank et al. (2008) as half of our $f(0)$, which is a compilation of Bell et al. (1985) and Owen et al. (2001) data, scaled to the geometric albedo of 0.14 at 2.2 μm; this spectrum was carefully obtained via ground-based telescopes in order to eliminate contamination by light material from the poles on the leading side. In order to determine normal reflectance, we then fit third-order polynomials to all of the surface phase functions and developed a scaling relationship to account for the contrast in albedo on the surface and the change in concavity of the surface phase functions between the dark and light material:

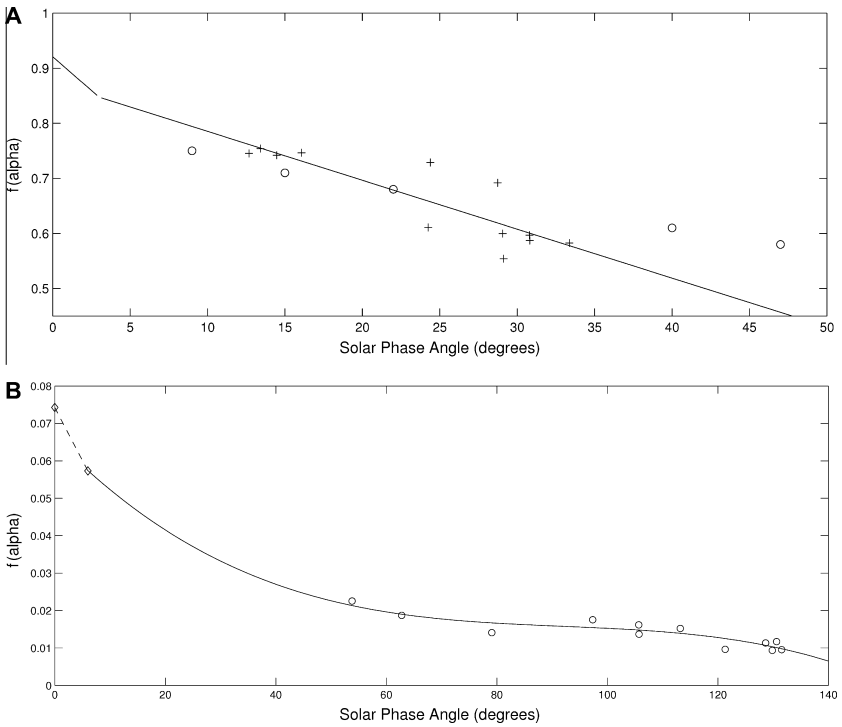

Fig. 2. (A) The surface phase function for the bright material at 0.47 μm is a linear fit (black line) to our data from the 12 sampled cubes (pluses). At less than 3°, we modified the slope to reflect the known phase coefficient (0.03 mag/deg) for the bright hemisphere from Noland et al. (1974) and Millis (1977). We compared our results to a surface phase function by Squyres et al. (1984) (circles) from Voyager ISS clear-filter images to verify our method. We used precisely the same surface phase function for bright material as Blackburn et al. (2010). (B) For the dark material, the surface phase function for 0.47 μm is also displayed. The circles represent data from high-resolution VIMS cubes (all over 50° phase angle). The diamond at 0° is twice the normal reflectance of Cruikshank et al., 2008, and the dotted line shows the opposition surge at that wavelength, corresponding to a phase coefficient of 0.05 deg/mag (Squyres et al., 1984; Noland et al., 1974; Millis, 1977).

Author's personal copy

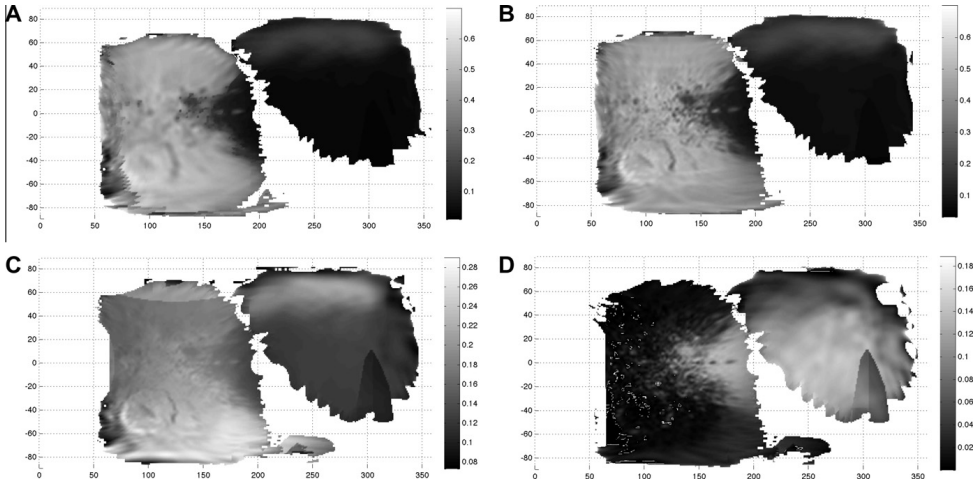

Fig. 3. Cassini VIMS normal reflectance maps. (A) 0.53 μm, (B) 1.00 μm, (C) 2.12 μm (water adsorption feature), (D) 4.11 μm (brightness reversal).

$$s = \frac{R_{data} - R(\alpha)_D}{R(\alpha)_L - R(\alpha)_D} \tag{2}$$

$$R_{data} = \left(\frac{I}{F}\right)_{data}\left(\frac{\mu_0 + \mu}{\mu_0}\right) \tag{3}$$

$$r = R_{data}\frac{f(0)}{2f(\alpha)} = R_{data}\frac{sR(0)_L + (1-s)R(0)_D}{2[sR(\alpha)_L + (1-s)R(\alpha)_D]} \tag{4}$$

where R_D and R_L are the surface phase functions for the dark and light material (third-order polynomials in terms of the phase angle α); R_{data} is a correction factor applied to each individual I/F_{data} pixel to reduce limb darkening in the data set and allow for a comparison with the surface phase functions; s is our scaling ratio of the percentage of light material; and r is the normal reflectance. It should be noted that the value for R_{data} is twice the I/F_{data} when emission and incidence angles are at unity for the image undergoing transformation to normal reflectance. Such a scaling relationship is necessary in order to acquire the proper normal reflectance in the mixed albedo regions. Thus, Eqs. (2)–(4) are used on each pixel in a VIMS cube of I/F to calculate normal reflectance, and each scaling relationship is unique for each VIMS band or wavelength.

As normal reflectance has been shown to be a good approximation for the geometric albedo at values less than ~0.6 since the effects of multiple scattering are minimized (Squyres et al., 1984; Buratti and Veverka, 1985), we assumed the values to be equivalent. Based on instrument specification documents regarding the accuracy of the *Cassini* VIMS and ISS instruments (Brown et al., 2004; Porco et al., 2004) and the error within our surface phase functions, we estimate an average error across all wavelengths of 2.1% for our geometric albedo values of the brighter material, while the error in the darker material is worse (5.0%) due to the low signal to noise ratios. Geometric albedos for the trailing hemispheres and leading hemispheres have been reported as 0.42 ± 0.05 and 0.08 ± 0.01 at 0.55 μm (Squyres et al., 1984; Owen et al., 2001); the same averages of VIMS data at 0.55 μm (Band 28 of VIMS-VIS) corrected to normal reflectance in this study are 0.41 ± 0.03 and 0.08 ± 0.01, respectively.

2.1.2. Phase integral determination

Blackburn et al. (2010) showed that the phase integral could be effectively predicted by the geometric albedo. While the curvature in the data shown in their Fig. 5 is most likely the result of a textural difference for the dark material, a third-order polynomial fit this difference well. From that study, we have derived this estimation for the phase integral plotted in Fig. 4:

$$q = 2.9583p^3 - 4.3155p^2 + 2.5066p + 0.1061, \quad 0 < p < 0.65 \tag{5}$$

where q is the phase integral and p is the geometric albedo. Since the brightest terrain on Iapetus has a geometric albedo of ~0.65 and the Blackburn et al. (2010) data did not extend into albedos that high, we used the slope of the average of a linear fit from Pitman et al. (2010) phase integral values for Tethys, Mimas, Dione, and Rhea as a guide for extrapolation. We altered the coefficients in our fit (Eq. (5)) until the slope matched the one from their data beyond geometric albedoes of 0.55 (Fig. 4), which resulted in an estimation of the phase integral of 0.72 ± 0.10 for the brightest terrain on Iapetus. Eq. (5) was vital to produce 352 individual phase integral maps (Fig. 5) for each of the VIMS bands by applying the equation over every pixel of the normal reflectance maps. The scatter in the data (Fig. 4) produces an estimated error of ±0.06 for the values of the phase integrals in our map (Fig. 5).

2.1.3. Bolometric Bond albedo

The Bond albedo (Fig. 6) is simply the product of the phase integral and the geometric albedo, and we calculated this value for all 352 bands. However, the Bond albedo is wavelength dependent because its aforementioned factors are, and thus, the bolometric Bond albedo (Fig. 7) is integrated over all wavelengths, taking into account the intensity of the solar flux at each wavelength:

$$A_B = \frac{\int_0^\infty q(\lambda)p(\lambda)F(\lambda)d\lambda}{\int_0^\infty F(\lambda)d\lambda} \tag{6}$$

where q is the phase integral, p is the geometric albedo, F is the intensity of the solar flux, and λ is wavelength. When performing this integration, we were careful to compare the results from the

Author's personal copy

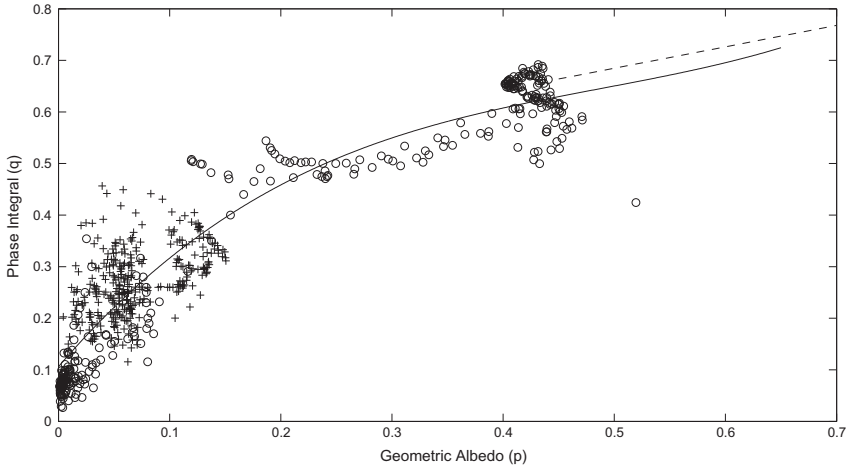

Fig. 4. Our relationship (solid black line) between the geometric albedo and the phase integral by comparing data for the leading hemisphere (pluses) with the trailing (circles). The dotted line shows the relationship for a "typical" saturnian satellite by averaging the linear fits for Mimas, Tethys, Rhea, and Dione from Pitman et al. (2010).

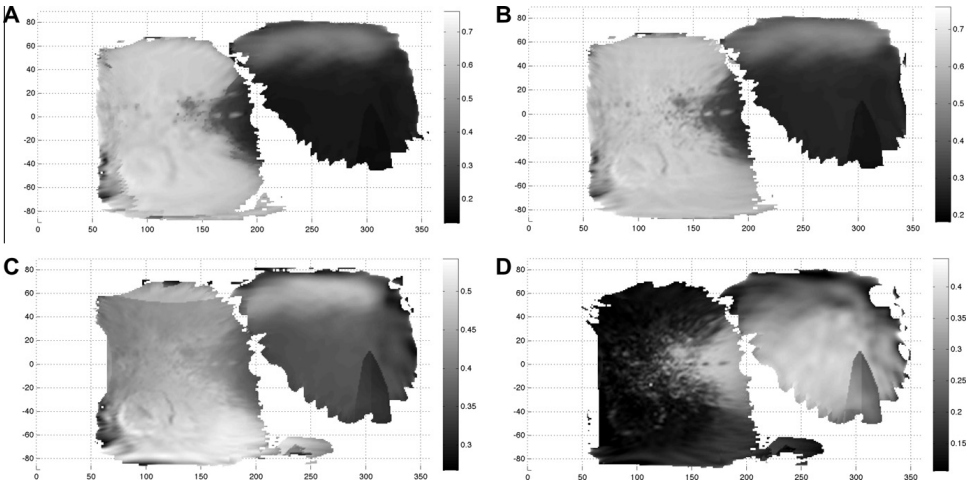

Fig. 5. Cassini VIMS phase integral maps. (A) 0.53 μm, (B) 1.00 μm, (C) 2.12 μm (water adsorption feature), (D) 4.11 μm (brightness reversal).

overlapping bands from VIMS-VIS and VIMS-IR and noticed that their differences were negligible. In addition to the low-resolution mosaic depicted in Fig 7, we also created a higher resolution mosaic (4 pixels per degree lat/long, ~5 km per pixel) from VIMS cubes from the September 10, 2007 flyby (Fig. 8). For error determination, we used the following relationship for the errors in the individual Bond albedos:

$$A_{Bond.err} = A_{Bond}\sqrt{\left(\frac{p_{err}}{p}\right) + \left(\frac{q_{err}}{q}\right)} \quad (7)$$

2.2. Voyager ISS

Given the lack of coverage by *Cassini* of Iapetus's northern pole, we have scaled *Voyager* ISS images (Fig. 10) in order to approximate the bolometric Bond albedo there. By evaluating Eq. (6) for our *Cassini* VIMS data over the wavelength range of the *Voyager* clear filter (350–650 nm) to produce a Bond albedo map with the weighting of the solar flux at those wavelengths and comparing to the same map over all wavelengths (Fig. 7), we were able to determine a scaling ratio in order to fit *Voyager* ISS observations

Author's personal copy

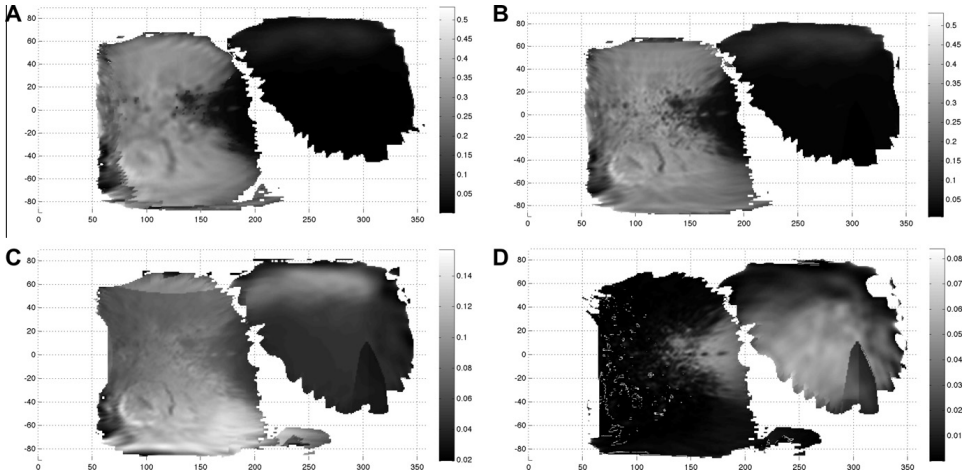

Fig. 6. Cassini VIMS Bond albedo maps. (A) 0.53 μm, (B) 1.00 μm, (C) 2.12 μm (water adsorption feature), (D) 4.11 μm (brightness reversal).

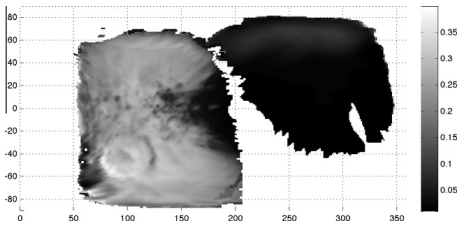

Fig. 7. Cassini VIMS bolometric Bond albedo map in equirectangular projection.

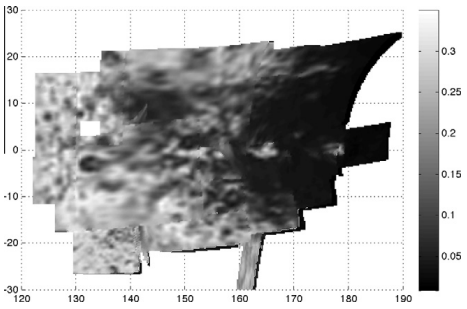

Fig. 8. Bolometric Bond albedo of the border region from high resolution *Cassini* VIMS cubes in Table 2.

into our map (Table 3). In the case of the light material, the ratio is 0.911, and in the case of the dark material, it is 2.44. These values show that the albedo is brighter for the dark material at wavelengths higher than 0.65 μm and the reverse for the light material, a fact that is corroborated by published spectra (Cruikshank et al., 2008; Blackburn et al., 2010).

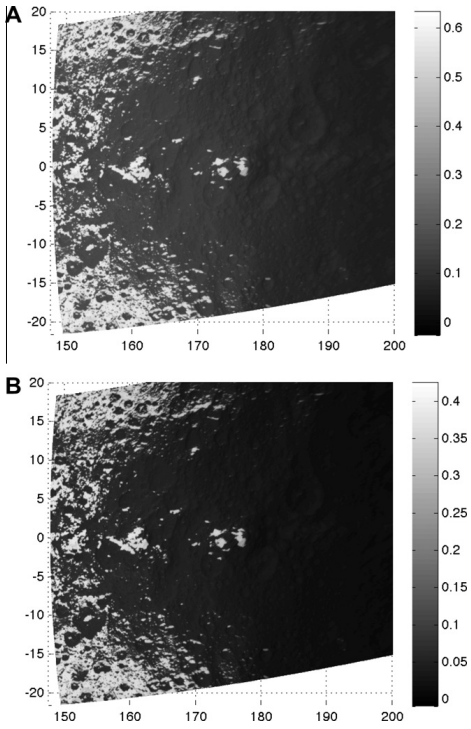

Fig. 9. *Cassini* ISS wide-angle camera image W1568130503_2 in equirectangular projection view. (A) Normal reflectance, i.e. geometric albedo set to grey scale. (B) Bolometric Bond albedo set to grey scale.

Author's personal copy

We used Squyres' normal reflectance map as a point of reference and two *Voyager* ISS images (FDS counts 3,497,658 and 4,390,708) to add coverage of the northern polar cap, which is important for modeling the possibility of a CO_2 polar cap on Iapetus and its stability. Our normal reflectance values compare well to the normal reflectance maps produced from *Voyager* ISS observations by Squyres et al. (1984) and Buratti and Mosher (1995). In regions of overlap between *Voyager* ISS and *Cassini* VIMS, we ratioed the overlap regions with the numerator being the *Voyager* results as a consistency check; the pixels in this ratioed mosaic on average were 1.01 ± 0.34.

2.3. Cassini ISS

We used *Cassini* ISS narrow angle images N1562601817_1 taken in the BL1/CL2 filters (404–507 nm) and N1482859953_2 in the CL1/CL2 filters (200–1100 nm). Employing the same procedure as in Section 2.2 for *Voyager* (scaling ratios are in Table 3), we translated these images to a full bolometric Bond albedo for the purpose of adding regions of Iapetus for which no VIMS cubes are available (Fig. 10). We also used an ISS wide-angle camera image W1568130503_2 with the CL1/CL2 filters (380–1100 nm) to produce a high resolution bolometric Bond albedo map of the border region (Fig. 9). *Cassini* ISS (CL1/CL2) clear-filter images required a different scale than *Voyager* ISS, i.e. 9.111 for light and 2.411 for dark (Table 3) because of the broader range in wavelengths 0.2–1.1 μm. We noted no noticeable change for the scaling factors necessary for the narrow verses the wide-angle CL1/CL2 filter images. We performed the same consistency check as in the case of *Voyager* by comparing *Cassini* ISS versus VIMS in overlap regions with ISS being in the numerator of this ratio; we found the average of the pixels in the overlap region of this comparison to be 1.08 ± 0.18.

3. Results

Since sufficient coverage for the South was not available, we flipped the northern hemisphere to provide estimates for the values in the South; this procedure was also performed by Palmer and Brown (2008), corresponds well with the results of Spencer and Denk (2010), and is supported by the contour lines at the edges

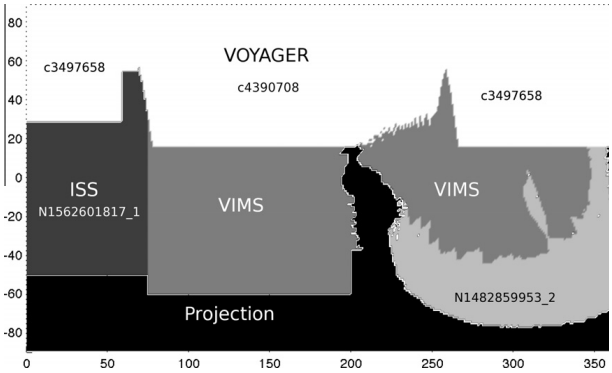

Fig. 10. Guide to mosaics for Figs. 11 and 12.

Table 2
Cassini VIMS cubes utilized in our mosaics.

Cube	Phase angle	Subspacecraft longitude	Pixel size (km)
1483156810_1	54	69	82
1510369274_1	61	29	121
1568145604_1	32	245	22
1568163600_1	33	247	42
1568163922_1	33	247	43
High-resolution border cubes	15–29	205–241	1–5
High-resolution border cube list			
1568128091_1	1568130559_1	1568131994_1	1568134531_1
1568128380_1	1568130636_1	1568132105_1	1568134703_1
1568128681_1	1568130786_1	1568132282_1	1568134877_1
1568128811_1	1568130860_1	1568132454_1	1568135049_1
1568128941_1	1568131010_1	1568132626_1	1568135222_1
1568129071_1	1568131083_1	1568132801_1	1568135394_1
1568129201_1	1568131233_1	1568133146_2	1568135570_1
1568129331_1	1568131307_1	1568133319_1	1568135798_3
1568129461_1	1568131457_1	1568133492_1	1568135915_1
1568129671_1	1568131468_1	1568133665_1	1568136232_1
1568129948_1	1568131605_1	1568133838_1	1568136342_1
1568130180_1	1568131937_1	1568134011_1	1568136449_1
1568130330_1	1568131972_1	1568134183_1	1568136573_1
1568130409_1	1568131983_1	1568134357_1	

Author's personal copy

of our mosaics. At other points where no data was available or only in phase angles higher than 90°, we used the contour lines of albedo nearby to project their values (Fig. 10). For our mosaics, which were produced from the cubes and images listed in Table 2, we were careful to avoid the terminator or limb in our camera images, since the photometric function we used can depart from true values at those edges. Most of our mosaics (Figs. 3, 5–9 and 11) are in an equirectangular projection view, and all except for the two of the border region (Figs. 8 and 9) are in a resolution of 1 pixel per degree lat/long (~10 km per pixel). In order to focus on the values at the northern cap, we also projected the values from Fig. 11 into a polar stereographic view (Fig. 12) where the highest value in the north is 0.40 ± 0.07. In regards to the dark terrain, the darkest material is located in the center of the apex and has a bolometric Bond albedo of 0.015 ± 0.012. Using an equal-area projection mode (sinusoidal), we calculated an average bolometric Bond albedo of 0.250 ± 0.032 for the trailing hemisphere (0–180°E) and 0.056 ± 0.014 for the leading (180–360°E).

Table 3
Scaling factors for conversion to bolometric Bond albedo.

Instrument	Filter (s)	Wavelength range (nm)	Dark	Light
Voyager ISS NAC	Clear	310–650	1.857	0.917
Cassini ISS NAC	BL1/CL2	404–507	1.790	0.920
	CL1/CL2	200–1100	1.440	0.940
Cassini ISS WAC	CL1/CL2	380–1100	1.440	0.940

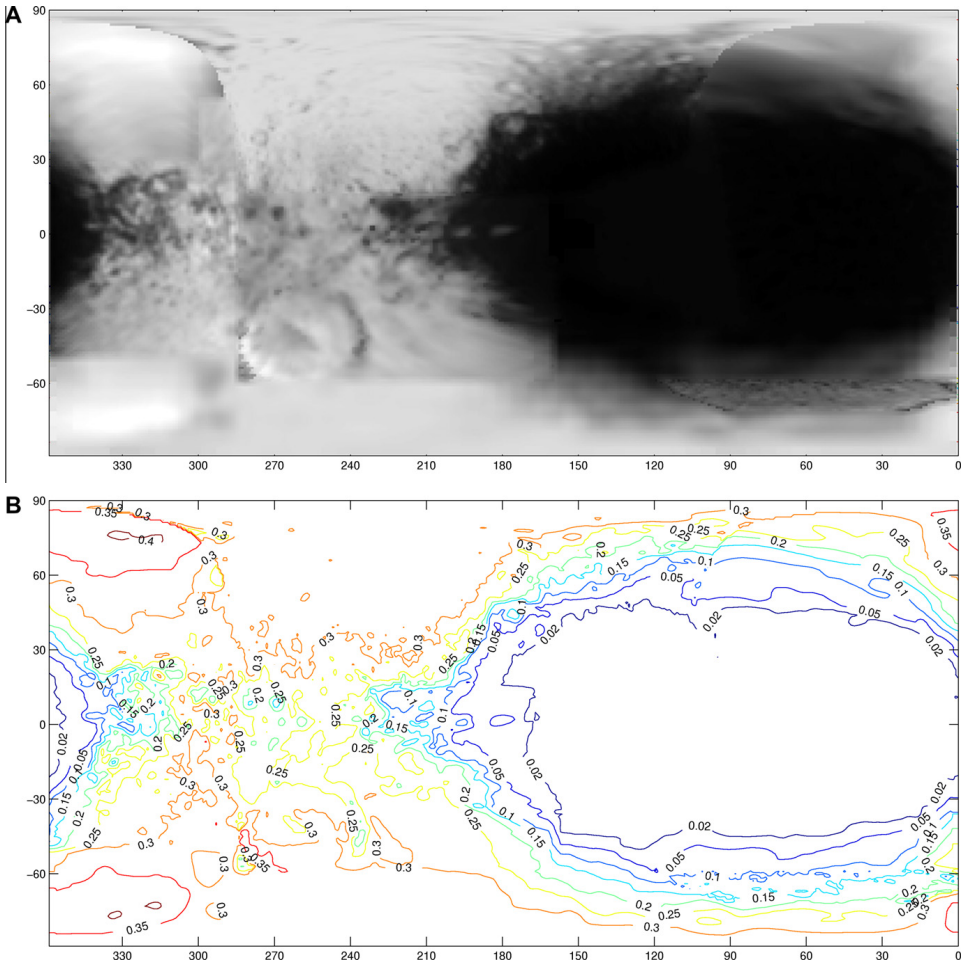

Fig. 11. Our complete coverage bolometric Bond albedo map in an equirectangular projection, mosaicked using the order outlined in Fig. 10. (A) Values converted into grayscale image. (B) Contour map of the values.

Author's personal copy

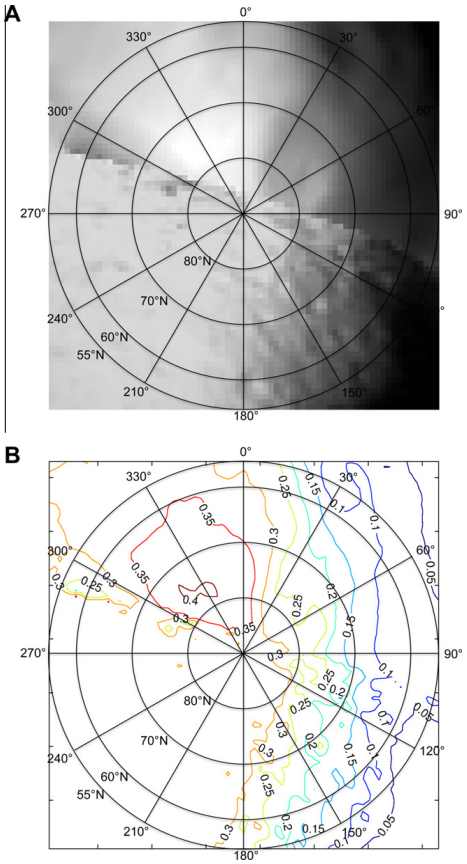

Fig. 12. Polar stereographic view of the northern pole (55–90°N latitude) bolometric Bond albedo map. (A) Values converted into grayscale image. (B) Contour map of the values.

4. Discussion

Given the contrast in albedo within the leading hemisphere and the opportunity provided by the September 10, 2007 flyby of Iapetus, we chose to investigate the bolometric Bond albedo change of the border region centered at ~0°N and 150°E with both the VIMS (Fig. 8) and the ISS (Fig. 9) cameras. Clearly, as the resolution increases, the contrast in albedo becomes more evident, indicating a problem of resolution with determining the albedo of the bright material, also noticed by Spencer and Denk (2010). While the average bolometric Bond albedo of the trailing hemisphere is 0.25, the brighter, purer material has an albedo of 0.38 ± 0.01. This evidence contradicts previous claims in the literature about a very gradual transition in albedo (Squyres et al., 1984; Buratti and Mosher, 1995) from relying on the lower resolution *Voyager* observations yet supports the observations of Denk et al., 2010. While the change appears gradual (Fig. 3), higher resolution images show that it is a deception caused by averaging light material with isolated regions of dark material that appear to be speckled into the equatorial regions of the trailing hemisphere (Fig. 1). The *Cassini* CIRS instrument has provided another method of determining the bolometric Bond albedo from the peak temperatures (Howett et al., 2010; Spencer and Denk, 2010). Howett et al. (2010) calculated values of 0.31 for the trailing and 0.10 for the leading hemisphere. The FP1 data as described by Spencer and Denk (2010) give a bright side albedo of 0.31, though they note that the fits of the bright terrain peak temperatures from the higher spatial resolution FP3 data match 0.39, compared to our value of 0.38 ± 0.04 at higher resolution (Fig. 9). Thus, our results correspond well with Spencer and Denk (2010) in this respect. The difference in the values between Figs. 8 and 9 highlights the difficulty in estimating the bolometric Bond albedo for so called "light" and "dark" material. In the higher resolution ISS image of the border region (Fig. 9), it is clear that the boundary is a harsh contrast (0.37 for bright and 0.04 for dark), but in Fig. 11, the albedo change appears gradual, as would be expected from an average of the pixels. This problem makes the accuracy of the results from a thermal model highly dependent on the resolution of that model, as a model with lower resolution would clearly give an average temperature of a wide region.

Previous estimates for the bolometric Bond albedo are quite limited, but we compared our results to the reported values available. Compared with the Bond albedo map provided by Palmer and Brown (2008), our values are lower for the trailing hemisphere for two reasons: (1) Palmer and Brown (2008) estimated that the phase integral for the brightest region on Iapetus was 1 by applying values from Europa compared to our estimate of 0.72, and (2) they used only reflectance values in the visible range from the *Voyager* ISS clear filter, which results in an overestimation of about 11% due to the spectra of the trailing side (Blackburn et al., 2010). However, our average value of 0.06 ± 0.01 for the leading hemisphere is roughly equivalent to theirs (0.04). We find our results difficult to reconcile with the Morrison et al. (1975) values for the trailing hemisphere of a Bond albedo of 0.5, a phase integral of 1.3, and an average geometric albedo of 0.34 determined from radiometry. We argue that part of the discrepancy here is due to inaccurate values for Iapetus' radius of 835 km instead of the more recent measurement (~730 km) that Morrison et al. (1975) relied upon for their calculation.

With regard to the northern hemisphere, it is clear that this area has higher bolometric Bond albedos than the trailing hemisphere at equatorial latitudes. However, our scaling of *Voyager* data here is based on the assumption that bright material spectra at the equatorial and mid-latitudes covered by the VIMS instrument are a good match for the icy material at Iapetus's poles. If however, a CO_2 cap with a different spectrum is present, as some have suggested (Palmer and Brown, 2008), then values for the North may be different due to that reason or a texture difference that alters the scattering and hence the phase integral. With these limitations in mind, we have applied a conservative error of 0.40 ± 0.07 for the value of bolometric Bond albedo for the brightest region on Iapetus.

5. Equilibrium surface temperatures

The ultimate practical outcome of this study is to determine surface temperatures via thermal models. As a first-order approximation of the equilibrium blackbody temperature, we chose to use a simple equilibrium temperature equation:

$$T_{eff} = \sqrt[4]{\left(\frac{1-A}{\sigma_B}\right)\left(\frac{F_{Sun}}{R^2}\right)} \tag{8}$$

where A is the bolometric Bond albedo, σ_B is the Stefan–Boltzman constant, F_{Sun} is the solar constant at 1 AU, and R is the distance from the Sun in AU. For R, we used the semi-major axis for Saturn.

Author's personal copy

Our values for the effective temperatures give a maximum blackbody temperature at low latitudes of 125.5 K for leading and 118.4 K for the trailing; essentially, these temperatures represent the maximum temperature of the two hemispheres at the equator at the semi-major axis of Saturn's orbit. Eq. (8) assumes that the body is in equilibrium with the ambient solar flux, which is appropriate due to Iapetus' status as a slow rotator (~79 Earth days). Thus, these temperatures correspond to low latitude midday temperatures only; we leave further development of an advanced thermal model for Iapetus to another study.

6. Conclusions

Exploring key questions on Iapetus in greater detail, such as thermal segregation and volatile transport, will require advanced thermal models. Our map provides the most accurate fundamental framework for thermal modeling of Iapetus' surface temperatures and surface processes to date, and we also demonstrate that resolution is key when comparing albedo values correctly for Iapetus. In general bolometric Bond albedoes for the northern polar region on Iapetus have been overstated in some previous thermal models (Palmer and Brown, 2008), as values peak at ~0.4. This adjustment in values comes primarily from the phase integrals, which previously had to be estimated for Iapetus until the *Cassini* tour allowed the opportunity to measure brightness at phase angles up to 140°.

Acknowledgments

This research was carried out at the Jet Propulsion Laboratory, California Institute of Technology, and the University of Arkansas and sponsored by the National Aeronautics and Space Administration's Space Grant Program. We would like to thank the University of Arkansas and the Arkansas Space Grant Consortium for support, as well as helpful conversation with Mike Hicks, Ken Lawrence, Karly Pitman, and Edgard Rivera-Valentin. We also appreciate the comments and suggestions of John Spencer and an anonymous reviewer that improved the quality of our manuscript.

References

Bell, J.F., Cruikshank, D.P., Gaffey, M.J., 1985. The composition and origin of the Iapetus dark material. Icarus 61, 192–207.
Blackburn, D.G., Buratti, B.J., Ulrich, R., Mosher, J., 2010. Solar phase curves and phase integrals for the leading and trailing hemispheres of Iapetus from the *Cassini* Visual and Infrared Mapping Spectrometer. Icarus 209, 738–744.
Brown, R.H. et al., 2004. The *Cassini* Visual and Infrared Mapping Spectrometer (VIMS) investigation. Space Sci. Rev. 155, 111–168.
Buratti, B.J., Veverka, J., 1985. Photometry of rough planetary surfaces: the role of multiple scattering. Icarus 64, 320–328.
Buratti, B.J., Mosher, J.A., 1995. The dark side of Iapetus: Additional evidence for an exogenic origin. Icarus 115, 219–227.
Chandrasekhar, S., 1960. Radiative Transfer. Dover Press, New York.
Cruikshank, D.P., Bell, J.F., Gaffey, M.J., Brown, R.H., Howell, R., Beerman, C., Rognstad, M., 1983. The dark side of Iapetus. Icarus 53, 90–104.
Cruikshank, D.P. et al., 2008. Hydrocarbons on Saturn's satellites Iapetus and Phoebe. Icarus 193, 334–343.
Denk, T. et al., 2010. Iapetus: Unique surface properties and a global color dichotomy from Cassini imaging. Science 327, 435–439.
Hapke, B.W., 1963. A theoretical photometric function for the lunar surface. J. Geophys. Res. 68, 4571–4586.
Howett, C.J.A., Spencer, J.R., Pearl, J., Segura, M., 2010. Thermal inertia and bolometric Bond albedo values for Mimas, Enceladus, Tethys, Dione, Rhea, and Iapetus as derived from Cassini/CIRS measurements. Icarus 206, 573–593.
Irvine, W.M., 1966. The shadowing effect in diffuse reflection. J. Geophys. Res. 71, 2931–2937.
Matthews, R.A.J., 1992. The darkening of Iapetus and the origin of Hyperion. Q. J. R. Astron. Soc. 33, 253–258.
Mendis, D.A., Axford, W.I., 1974. Satellites and magnetospheres of the outer planets. Annu. Rev. Earth Planet. Sci. 2, 419–474.
Millis, R.L., 1977. UBV photometry of Iapetus: Results from five apparitions. Icarus 31, 81–88.
Morrison, D., Jones, T.J., Cruikshank, D.P., Murphy, R.E., 1975. 2 faces of Iapetus. Icarus 24, 157–171.
Noland, M., Veverka, J., Morrison, D., Cruikshank, D.P., Lazarewicz, A.R., Morrison, N.D., Elliot, J.L., Goguen, J., Burns, J.A., 1974. Six-color photometry of Iapetus, Titan, Rhea, Dione, and Tethys. Icarus 23, 334–354.
Owen, T.C., Cruikshank, D.P., Dalle Ore, C.M., Geballe, T.R., Roush, T.L., de Bergh, C., Meier, R., Pendleton, Y.J., Khare, B.N., 2001. Decoding the domino: The dark side of Iapetus. Icarus 149, 160–172.
Palmer, E.E., Brown, R.H., 2008. The stability and transport of carbon dioxide on Iapetus. Icarus 195, 434–446.
Pitman, K.M., Buratti, B.J., Mosher, J.A., 2010. Disk-integrated bolometric bond albedos and rotational light curves of saturnian satellites from Cassini VIMS. Icarus 206, 537–560.
Porco, C.C. et al., 2004. Cassini imaging science: Instrument characterizations and anticipated scientific investigations at Saturn. Space Sci. Rev. 115, 363–497.
Smith, B.A. et al., 1981. Encounter with Saturn: Voyager 1 imaging science results. Science 212, 163–191.
Smith, B.A. et al., 1982. A new look at the Saturn system – The Voyager 2 images. Science 215, 504–537.
Soter, S., 1974. Remarks on origin of Iapetus' photometric asymmetry. Paper presented at the 28th IAU Colloquium on Planetary Satellites, Cornell University.
Spencer, J.R., Denk, T., 2010. Formation of Iapetus' extreme albedo dichotomy by exogenically triggered thermal ice migration. Science 327, 432–435.
Squyres, S.W., Sagan, C., 1983. Albedo asymmetry of Iapetus. Nature 303, 782–785.
Squyres, S.W., Buratti, B.J., Veverka, J., Sagan, C., 1984. Voyager photometry of Iapetus. Icarus 59, 426–435.
Verbiscer, A.J., Skrutskie, M., Hamilton, D., 2009. Saturn's largest ring. Nature 461, 1098–1100.
Vilas, F., Larson, S.M., Stockstill, K.R., Gaffey, M.J., 1996. Unraveling the zebra: Clues to the Iapetus dark material composition. Icarus 124, 262–267.

| Print

Journal Publishing Agreement

Elsevier Inc.

Your article details

Article:	A Bolometric Bond Albedo Map of Iapetus: Observations from Cassini VIMS and ISS and Voyager ISS
Corresponding author:	Mr. David G. Blackburn
E-mail address:	
Journal:	Icarus
Our reference	YICAR9673
PII:	S0019-1035(10)00490-2
DOI:	10.1016/j.icarus.2010.12.022

Your Status

- I am one author signing on behalf of all co-authors of the manuscript
- I am not a US Government employee but some of my co-authors are

Data Protection & Privacy

- I do not wish to receive news, promotions and special offers about products and services from Elsevier Inc. and its affiliated companies worldwide.

Assignment of publishing rights

I hereby assign to Elsevier Inc. the copyright in the manuscript identified above (government authors not electing to transfer agree to assign an exclusive publishing and distribution license) and any supplemental tables, illustrations or other information submitted therewith that are intended for publication as part of the manuscript (the "Article") in all forms and media (whether now known or hereafter developed), throughout the world, in all languages, for the full term of copyright, effective when and if the article is accepted for publication. This transfer includes the right to provide the Article in electronic and online forms and systems. With respect to supplemental data that I wish to make accessible through a link in the Article, I hereby grant a non-exclusive license for such linking. If I have agreed with Elsevier Inc. to make available such supplemental data on a site or through a service of Elsevier Inc., I hereby grant a non-exclusive license for such publication, posting and making available, and further permit indexing and archiving.

Revisions and Addenda

I understand that no revisions, additional terms or addenda to this Agreement can be accepted without Elsevier Inc.'s express written consent.

Note: authors at institutions that place restrictions on copyright assignments or that assert an institutional right to distribute or provide access to the works of institutional authors, must obtain an express waiver from those institutions releasing the author from such restrictions to enable the acceptance of this publishing agreement.

Retention of Rights for Scholarly Purposes

I understand that I retain or am hereby granted (without the need to obtain further permission) the Retained Rights (see description below), and that no rights in patents, trademarks or other intellectual property rights are transferred to Elsevier Inc..

The Retained Rights include:

- the right to use the Preprint or Accepted Author Manuscript for Personal Use, Internal Institutional Use and for Permitted Scholarly Posting; and
- the right to use the Published Journal Article for Personal Use and Internal Institutional Use.

but in each case as noted in the Definitions excluding Commercial Use or Systematic Distribution (unless expressly agreed in writing by Elsevier Inc.).

Author Representations / Ethics and Disclosure

Author representations

- The article I have submitted to the journal for review is original, has been written by the stated authors and has not been published elsewhere.
- The article is not currently being considered for publication by any other journal and will not be submitted for such review while under review by this journal.
- The article contains no libellous or other unlawful statements and does not contain any materials that violate any personal or proprietary rights of any other person or entity.
- I have obtained written permission from copyright owners for any excerpts from copyrighted works that are included and have credited the sources in my article.
-
- If the article was prepared jointly with other authors, I have informed the co-author(s) of the terms of this publishing agreement and that I am signing on their behalf as their agent, and I am authorized to do so.

Funding agency and Sponsorship Options

For more information about the definitions relating to this agreement click here.

☑ **I have read and agree to the terms of the Journal Publishing Agreement..**

29th December 2010

T-copyright-v17/2009

- Privacy Policy
- Terms & Conditions
-

Copyright (c) 2010 Elsevier Ltd. All rights reserved.

DEFINITIONS

ACCEPTED AUTHOR MANUSCRIPT ("AAM")

Author's version of the manuscript of an article that has been accepted for publication and which may include any author-incorporated changes suggested through the processes of submission processing, peer review, and editor-author communications. AAMs should not include other publisher value-added contributions such as copy-editing, formatting and (if relevant) pagination, and should include the Appropriate Bibliographic Citation and a link to the final publication (generally through the relevant DOI).

APPROPRIATE BIBLIOGRAPHIC CITATION

Authors posting Accepted Author Manuscript online should later add a citation for the Published Journal Article indicating that the Article was subsequently published, and may mention the journal title provided they add the following text at the beginning of the document:

> "NOTICE: this is the author's version of a work that was accepted for publication in Planetary and Space Science. Changes resulting from the publishing process, such as peer review, editing, corrections, structural formatting, and other quality control mechanisms may not be reflected in this document. Changes may have been made to this work since it was submitted for publication. A definitive version was subsequently published in PUBLICATION, [VOL#, ISSUE#, (DATE)] DOI#"

COMMERCIAL USE

The use or posting of articles for commercial gain or to substitute for the services provided directly by the journal including:

the posting by companies of their employee-authored works for use by customers of such companies (e.g. pharmaceutica physician-prescribers); and

commercial exploitation such as directly associating advertising with such posting or the charging of fees for document de

INTERNAL INSTITUTIONAL USE

Use by the author's institution for classroom teaching at the institution (including distribution of copies, paper or electronic, and use in coursepacks and courseware programs) for scholarly purposes. For authors employed by companies, the use by that company for internal training purposes.

PERSONAL USE

Use by an author in the author's classroom teaching (including distribution of copies, paper or electronic), distribution of copies to research colleagues for their personal use, use in a subsequent compilation of the author's works, inclusion in a thesis or dissertation, preparation of other derivative works such as extending the article to book-length form, or otherwise using or re-using portions or excerpts in other works (with full acknowledgment of the original publication of the article).

PERMITTED SCHOLARLY POSTING

Voluntary posting of AAMs or Preprints by an author on open Web sites operated by the author or the author's institution for scholarly purposes, as determined by the author, or (in connection with Preprints) on preprint servers, but not for Commercial Use or Systematic Distribution. The author should include the Appropriate Bibliographic Citation when posting AAMs. Deposit in or posting to subject-oriented or centralised repositories (such as PubMed Central), or institutional repositories with mandates for systematic postings, is permitted only under specific agreements between the publisher and the repository, agency or institution, and only consistent with the Copyright Owner's policies concerning such repositories. To learn more about the publisher's policies and agreements with such agencies or institutions go to http://www.elsevier.com/fundingbodyagreements.

PREPRINT

Author's own write-up of research results and analysis that has not been refereed, nor had any other value added to it by a publisher (such as formatting, copy-editing, and the like).

PUBLISHED JOURNAL ARTICLE

The definitive final record of published research that appears or will appear in the journal and embodies all value-adding publisher activities including copy-editing, formatting and (if relevant) pagination.

SYSTEMATIC DISTRIBUTION

Policies or other mechanisms designed to aggregate and openly disseminate manuscripts or articles, or to substitute for journal-provided services, including:

the systematic distribution to others via e-mail lists or listservers (to parties other than known colleagues), whether for a

the posting of links to sponsored articles by commercial third parties including pharmaceutical companies;

institutional, funding body or government manuscript posting policies or mandates that aim to aggregate and openly distri peer reviewed manuscripts or published journal articles authored by its researchers or funded researchers; and

subject repositories that aim to aggregate and openly distribute accepted peer reviewed manuscripts or published journal researchers in specific subject areas.

CHAPTER 5

THE UPPER BOUND FOR CO_2 TRANSPORT ON IAPETUS: NARROWING IN ON THE NATURE OF THE DARK MATERIAL

In this chapter, the bolometric Bond albedo map and insights gained from studying the kinetics of CO_2 sublimation on the martian polar caps were employed to investigate the potential candidates for the nature of the CO_2 in the dark material on Iapetus and to explore the stability of a hypothetical dry ice polar ice cap; this chapter is in manuscript form and ready for submission to the journal *Planetary Science*. Dr. Richard Ulrich and Dr. Larry Roe provided helpful conversation throughout the study. Edgard Rivera-Valentin supplied the thermal model, contributed towards the sublimation theory and relevant equations, and provided helpful insights into the best process by which to rule out kinetic possibilities. I added the ballistic transport code, the code to calculate the sublimation parameters in Fig 5.1, provided computational support with the JPL and University of Arkansas supercomputers, analyzed the results, and finished all remaining unmentioned details.

5.1. Abstract

A sheet of dry ice on the surface of the dark material has been suggested as a possible source for the CO_2 adsorption feature detected by *Cassini* VIMS. Through proof by contradiction, we show that if dry ice is the source, it produces an impossible scenario where an extensive polar cap is produced along with incorrect temperatures for the dark material at equatorial latitudes. After ruling out surface dry ice as the source, we set strict upper limits on the amount of CO_2 transport on Iapetus to prevent formation of a polar cap.

5.2. Introduction

Iapetus, two-faced in its surface composition and brightness, is positioned in the outskirts of the saturnian system. Further beyond its orbit lie Phoebe and the more recently discovered Phoebe ring, which are prime candidates for the origin of the dark material in the exogenic models (Verbiscer *et al.*, 2009). Concentrated primarily in the dark material, Buratti *et al*. (2005) discovered a signature of CO_2; subsequent studies have mapped its distribution, finding the 4.26 micron absorption band depth to strengthen approaching the boundary between the dark and light material (Clark *et al*., 2011; Cruikshank *et al.*, 2008; 2010). In addition to CO_2, nano-phase hematite, amorphous carbon, and trace amounts of water ice have also been suggested to be the major constituents of the surface (Buratti *et al.,* 2005; Clark *et al.,* 2010). The detection of CO_2 in the dark material is problematic due to its instability at Saturn's solar radius, which was first shown by Lebofsky (1975). Palmer and Brown (2008) have shown that CO_2 remains for longer time scales when considering the effect of gravity, which could possibly permit formation of a seasonal or residual polar cap.

Possibilities for the nature of CO_2 in the dark material include adsorption on the surface, in solid inclusions within water ice, complexed, clathrate hydrate, solid ice (Buratti *et al*., 2005; Palmer and Brown, 2008), or some combination of these. In the case of adsorbed carbon dioxide, the source for the CO_2 could indeed be a reservoir beneath the dark overburden at the interface between the carbon-enriched overburden and the water-rich ice beneath. Cosmic rays could then produce the CO_2, creating a subsurface reservoir that diffuses out slowly and adsorbs on the surface at night. Alternatively, carbon dioxide could be a natural impurity in the water ice beneath the

overburden as part of the original constituents that formed the satellite. The extensive possibilities for kinetics make a model that explores CO_2 sublimation from the dark material highly problematic and case-limited.

Palmer and Brown (2011) showed that the detected signal would correspond to on average a 31 nm layer of dry ice over the dark material. In this study, we take the approach of proof by contradiction, a common form of the argument class called *reductio ad absurdum*. Our claim is that surface dry ice from the dark material is not a plausible candidate for the detected signal. We therefore assume that it is the source, which translates into the following situations: (1) surface dry ice is sublimating from the dark material and (2) dry ice polar cap(s) on Iapetus (Palmer and Brown, 2007; 2008). We therefore produced a sublimation model for dry ice evaporating from both the northern pole (since the coverage by *Voyager* and *Cassini* of the southern pole was highly limited) and for the dark material in the equatorial and mid-latitude regions of Iapetus. This model also has the advantage of providing the opportunity to set an upper limit on the amount of CO_2 that can enter the polar region without forming a polar cap, which will further constrain the choices on kinetics available.

5.3. Methods

Consider the possibilities for a solitary carbon dioxide molecule on the surface of a hypothetical polar cap on Iapetus for any given time period (Fig. 5.1). A carbon dioxide molecule could be destroyed by UV, sublimate, or remain on the surface. If it sublimates, then it either makes a hop or reaches escape velocity. If it hops, then it also faces the possibility of destruction en route or ends up back on the surface; thus, this process is recursive. Also, a molecule in transit may either return to the pole or leave the

hypothetical polar cap latitude boundary. Since there is a finite surface area by which to sublimate, a recursive algorithm is not necessary as the evaporative fluxes are fixed as long as the amount that leave the fixed area (polar cap boundary) is tracked. We assume that the percentage of molecules photodissociated in flight is negligible for the purposes of this exercise, which is reasonable considering the average flight time for a molecule at the poles (1.7×10^3 s) and the photochemical time scale for CO_2 (1.7×10^7 s) differ by almost exactly four orders of magnitude (Palmer and Brown, 2008). The loss rate from the polar cap system can then be expressed as the sum of the rates of photodissociation on the surface, the escape rate, and the rate of molecules hopping outside the polar boundary.

The photodissociation rate from ultraviolet light J_P can be calculated from the following formula:

$$J_P = \eta \int_{1nm}^{227nm} \Phi(\lambda)\sigma(\lambda)d\lambda \tag{5.1}$$

where σ is the radiometric cross section of CO_2, Φ is the solar flux reaching Iapetus' surface, both of which are dependent on the wavelength of light λ, and η is the number density (Shemansky, 1972; Lewis and Carver 1983; Woods *et al*. 1998; Chan *et al*. 1993; Palmer and Brown, 2011). For the escape rate, we use the velocity distributions determined from Section 5.3 and identify molecules that have left Iapetus as those that have achieved or exceeded the escape velocity of Iapetus (591 m s^{-1}).

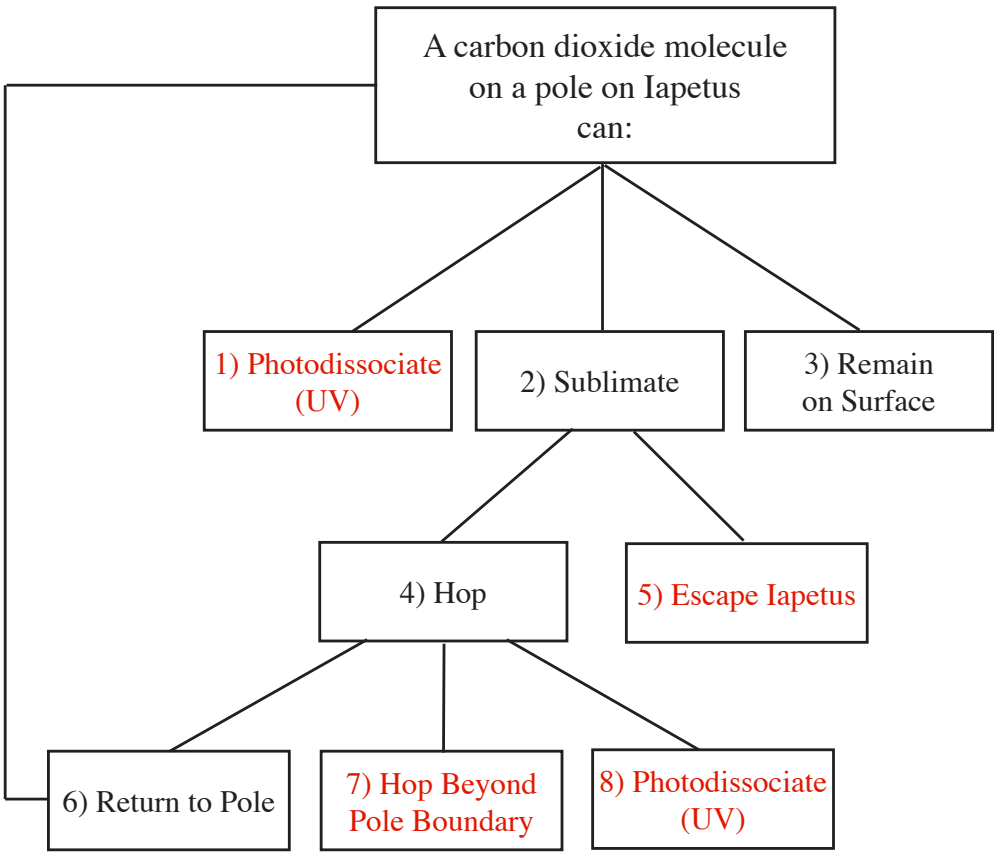

Figure 5.1 *Possibilities for a carbon dioxide molecule on one of Iapetus' poles.*

5.3.1 Sublimation Rate

We calculated the loss rates using the Hertz-Knudsen-Langmuir equation, which has been used previously on Iapetus (Palmer and Brown, 2008; Spencer and Denk, 2010) for temperatures greater than 60 K, and the method derived by Rivera-Valentin *et al*. (2011b) for temperatures less than 60 K in which the mean free path is greater than the scale height. The Hertz-Knudsen-Langmuir equation is given by:

$$J_S = P_{sat}\sqrt{\frac{M}{2\pi RT}} \tag{5.2}$$

where M is molecular weight, R is the gas constant, T is temperature, and P_{sat} is the saturation vapor pressure.

Sublimation of volatiles on airless bodies has been commonly interpreted as being in thermal equilibrium where the particles achieve a Maxwell-Boltzmann velocity distribution via collisional transfer of energy. However, under vacuum and low temperature conditions, it can be shown that the mean free path of the molecules is much larger than the scale height, and thus, intermolecular collisions are minimized, preventing thermal equilibrium among sublimated molecules. If we, however, revert our attention to the molecules within the solid matrix that achieve vibrational energies larger than the solid binding energy, we can provide better estimates on the velocity distribution of sublimating particles. Thus, the velocity distribution of sublimated particles is given by:

$$v = \sqrt{\frac{2}{m}\left(E_v - \Delta E\right)} \tag{5.3}$$

where m is molecular mass, E_v is a vibrational energy distribution function for the solid matrix, and ΔE is the molecular binding energy. Thus, this kinetic equation can be reduced to a perturbation factor that can be applied as a fraction of J_S in eq. 5.2; in this

case for CO_2, the perturbation factor of 0.5117 becomes significant for temperatures less than 60 K (Rivera-Valentin *et al*., 2011b).

For the polar region where the temperature is often below 60 K, we maintained a running total of the amount sublimated per solar orbit for the value for the outward polar flux. However, in the interest of reducing computation time for the sublimation code for the dark material, we recorded the average saturation vapor pressure $\langle P_{sat} \rangle$ and average surface temperature $\langle T \rangle$ separately. Thus, over a solar orbit of Saturn, the total amount sublimated can be estimated by extrapolating from the average sublimation rate $\langle J_S \rangle$:

$$\langle J_S \rangle = \langle P_{sat} \rangle \sqrt{\frac{M}{2\pi R \langle T \rangle}} \tag{5.4}$$

An additional advantage of this technique is that the relevant temperature corresponding to $\langle P_{sat} \rangle$ gives the average kinetic energy of the sublimated molecules, which allows the estimation of ballistic transport in bulk for the whole sublimated mass for each localized area instead of tracking each individual molecule.

5.3.2 Ballistic Transport

Ballistic transport is analytically modeled for one molecular hop of the evaporating species originating from the dark material. Consider the flux from one point on the surface of Iapetus (J_L) and suppose a fraction of this flux will reach a particular pole (J_{RP}) such that:

$$J_{RP} = J_L f \tag{5.5}$$

where f is the fraction of the initial flux that is pole bound and is given by partial fractions:

$$f = f_D f_L f_V \tag{5.6}$$

The partial fractions are described as follows:

1) Since launch direction is isotropic each direction has an equal probability. Suppose the molecule may either launch with a vector component primarily to the north or south. Then half of the molecules will travel north ($f_D = ½$).

2) The launch angle is also isotropic. Let θ_{min} equal the minimum launch angle and θ_{max} equal the maximum launch angle required to reach the lower latitudinal limit of what is considered the pole. The fraction of molecules that will be able to travel towards a pole can then be given by:

$$f_L = \frac{\theta_{\max} - \theta_{\min}}{90} \tag{5.7}$$

The angles θ_{min} and θ_{max} are dependent on the velocity of the molecule, which will be determined by the distributions described in the previous section.

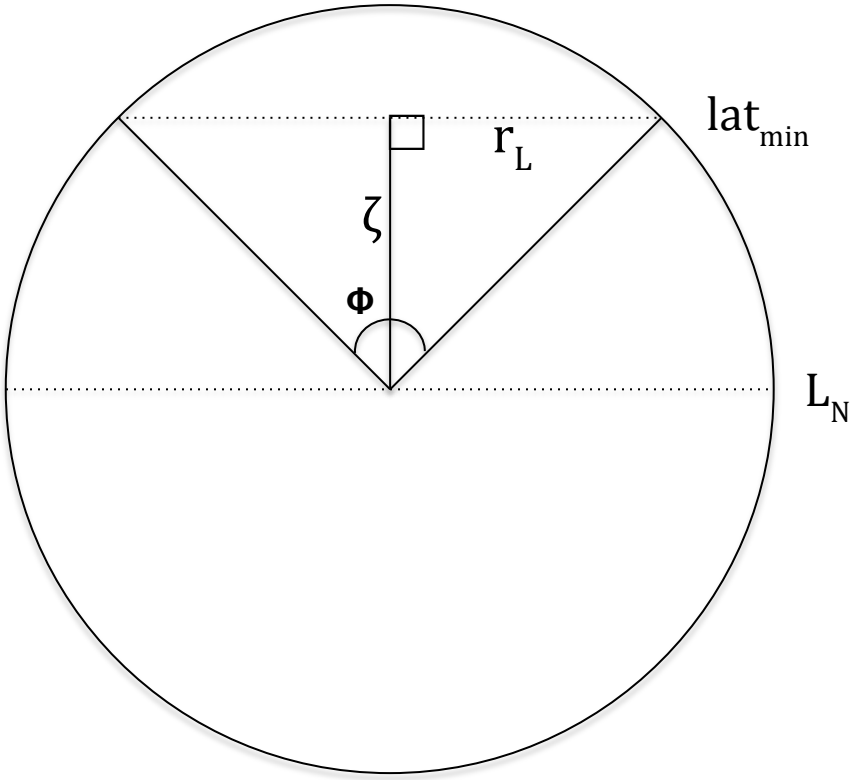

Figure 5.2. *Diagram for deriving the azimuth angle range for a molecule in flight that is capable of entering the polar cap.*

3) Consider the geometry from Figure 5.2 in which ζ is the distance from launch latitude to minimum polar latitude, L_N is the launch latitude (the equator in the figure example), r_I is the radius of Iapetus, and lat_{min} is the minimum latitude designated to be included within the pole. The fraction of those molecules travelling north whose vector is sufficient to enter the polar cap is then given by:

$$f_V = \frac{\varphi}{180} = \frac{2\tan^{-1}\left(\frac{r_L}{\zeta}\right)}{180} = \frac{1}{90}\tan^{-1}\left(\frac{r_L}{\zeta}\right) \tag{5.8}$$

$$r_L = \frac{\pi}{2}\left(1 - \frac{lat_{\min}}{90}\right) r_I \tag{5.9}$$

The value J_P is calculated independently for every pixel in our map corresponding to dark terrain for both the north and the south, and the summation of these fluxes across all pixels produces our estimate for the flux of molecules into the polar systems.

5.3.3 Thermal Model

We used the thermal model for Iapetus established by Rivera-Valentin *et al*. (2011a), incorporating as inputs the bolometric Bond albedo from Blackburn *et al*. (2011) for accurate day-time temperatures and the thermal inertial map from Rivera-Valentin *et al*. (2011a) for refining temperature amplitudes. Since this study concerns the sublimation of CO_2, our thermal model also includes latent heat loss using a heat of sublimation for CO_2 of 590,000 J kg^{-1} (Giauque and Egan, 1937). As Iapetus is an airless body, the one-dimensional thermal diffusion equation will be solved using an Euler

forward finite element procedure as established by various authors (Palmer and Brown, 2008; Ulrich *et al*., 2010; Rivera-Valentin *et al*., 2011a) in order to calculate surface temperatures in the regolith column. Thermal diffusion will be calculated to several times the skin-depth. The bottom boundary condition is adiabatic, and the surface boundary condition is:

$$Q = \varepsilon\sigma T_S^4 - \left(1 - A_{BB}\right)\frac{S_0}{r^2}\cos\zeta \qquad (5.10)$$

where ε is the surface emissivity, σ is Stefan-Boltzmann's constant, A_{BB} is the bolometric Bond albedo, S_0 is the solar flux at 1 AU, T_S is the surface temperature, r is the instantaneous distance from the sun in AU, and ζ is the solar angle to zenith.

5.4. Results

We ran our polar cap sublimation code for one full solar orbit of Saturn to produce a sublimation map for the northern polar cap (Fig. 5.3) and integrated over the polar area to determine the mass loss per solar orbit of Saturn given hypothetical polar cap boundaries of 70, 75, 80, and 85 °N for the individual components from Fig 5.1 (Table 5.1). We then also calculated the sublimation flux rate from the dark terrain using a reduced-pixel albedo map (30x60) and found the temperature corresponding to the average saturation vapor pressure as input into the ballistic transport code for the fractional component that entered the same latitude ranges (Fig 5.4). Table 5.2 demonstrates the comparison between the mass flux into and out of the polar cap: the growth rate increases as the diameter of the hypothetical polar cap decreases. (Note: rates are given in the timeframe of a saturnian orbit of the Sun.)

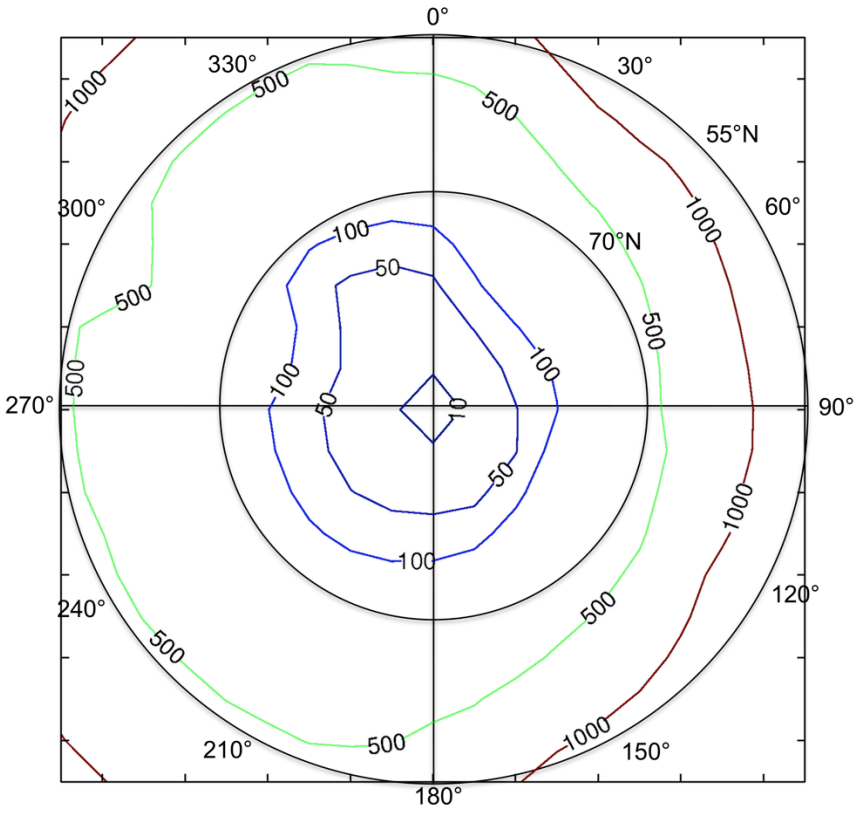

Figure 5.3 *Carbon dioxide sublimation map for the northern pole (units in kg m^{-2} orbit^{-1}).*

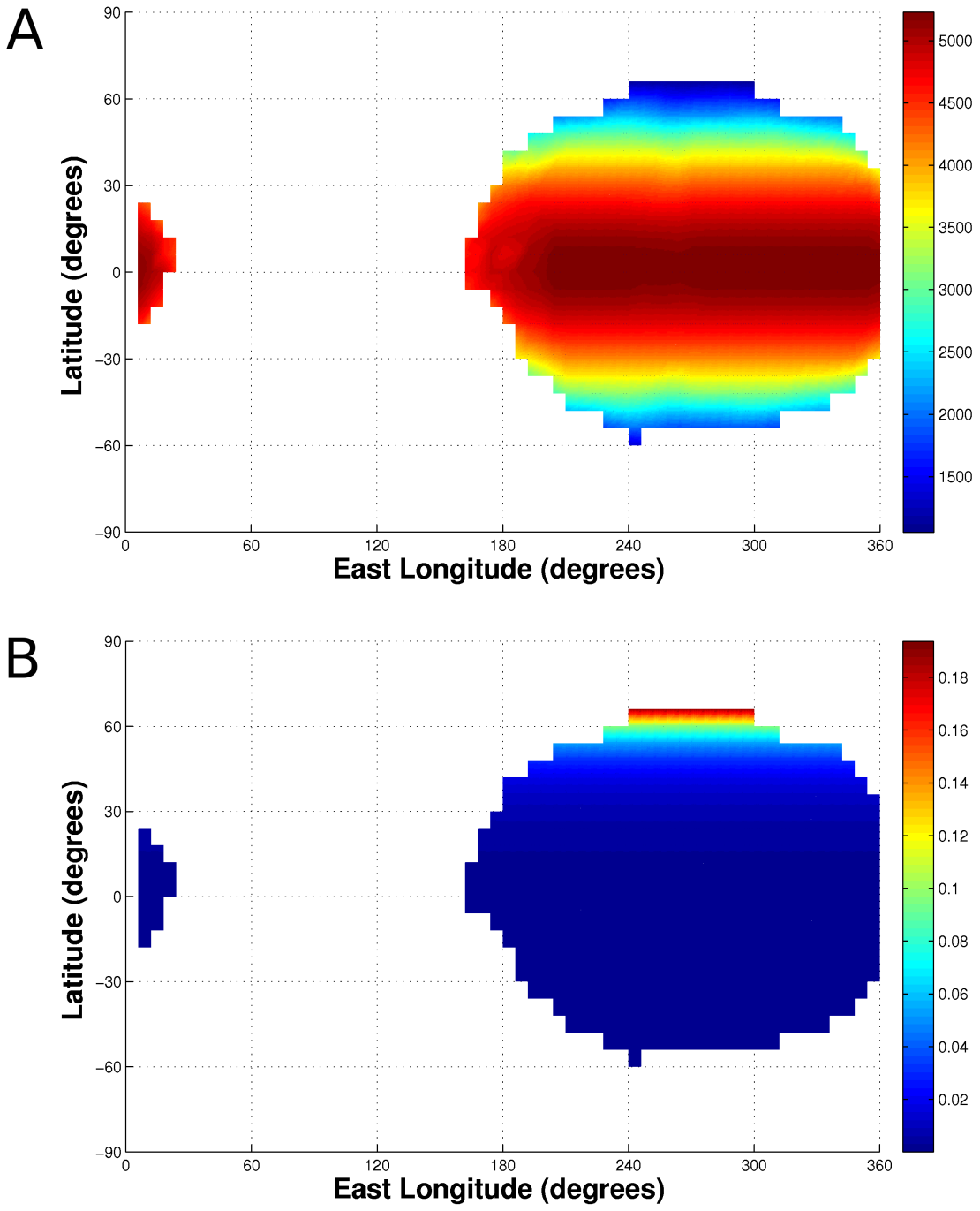

Figure 5.4. *A) Reduced pixel (30 x 60) sublimation map for carbon dioxide on the surface of the dark material (units in kg m^{-2} $orbit^{-1}$). B) Fraction of sublimated molecules that have the kinetic energy, launch angle, and azimuth to land within a polar cap with a boundary defined by 70 °N. The total amount entering at 70 °N polar cap in this case is 7.4 ×10^{13} kg $orbit^{-1}$.*

Table 5.1. *Mass loss components from Fig 5.1 for the hypothetical polar cap boundaries of 70, 75, 80 and 85 °N.*

Pole Boundary (°N)	Sublimated Mass (kg)	Amount of Sublimated that Leaves (kg)	Percentage that Leaves Pole	Escape Mass (kg)	Percentage that Escapes	Mass Destroyed by Ultraviolet (kg)	Total Loss Mass (kg)
70	2.32×10^{13}	9.71×10^{12}	41.9%	5.29×10^{9}	0.023%	19	9.72×10^{12}
75	6.88×10^{12}	3.28×10^{12}	47.7%	1.37×10^{9}	0.020%	4.9	3.28×10^{12}
80	1.34×10^{12}	7.51×10^{11}	56.2%	2.19×10^{8}	0.016%	0.8	7.51×10^{11}
85	1.13×10^{11}	7.85×10^{10}	69.7%	1.32×10^{7}	0.012%	0.05	7.85×10^{10}

Table 5.2. *Total influx into and out of our hypothetical polar cap at the boundaries of 70, 75, 80, and 85 °N.*

Pole Boundary (° N)	Mass Leaving Pole (kg orbit^{-1})	Mass Entering Pole (kg orbit^{-1})
70	9.7×10^{12}	7.4×10^{13}
75	3.3×10^{12}	3.5×10^{13}
80	7.5×10^{11}	1.3×10^{13}
85	7.9×10^{10}	2.9×10^{12}

5.5. Discussion

In the most generous case, eight times as much material enters 70 °N than leaves it, which would result in a rapidly growing polar cap, i.e. albedoes ~0.7-0.9 similar to the southern martian residual cap (Byrne *et al*., 2008; Blackburn *et al*., 2010). Visual evidence from *Voyager* ISS contradicts this result (Fig. 4.12; Squyres *et al.*, 1984; Blackburn *et al*., 2011). Also, surface dry ice sublimating from equatorial regions would buffer the maximum surface temperature, producing a limit of ~93K. Again, *Cassini* CIRS data contradicts this, finding maximum temperatures of ~132K at the same time that VIMS detected the absorption signal (Spencer and Denk, 2010). Therefore since assuming surface dry ice would lead to a polar ice cap and buffered maximum temperatures and we know this not to be true, then surface CO_2 is not feasible, and thus our original claim is proven by contradiction.

Also, our rates of sublimation from the polar region are higher than previous results from Palmer and Brown (2007) and (2008); the discrepancy here is mostly due to the differences in albedo used. Palmer and Brown (2008) used estimated higher phase integrals of 1 for the brighter terrains that resulted in a maximum albedo of 0.65 in their model, while we use 0.40 for the same region. Yet, even if their numbers are used and the phase integrals are higher than our estimates (Blackburn *et al*. 2010; 2011), it only further strengthens the argument for this paper as it shows even less material would be leaving the polar cap.

5.5.1 Upper Limit on Transport

The low albedos present from *Voyager* ISS argue for the lack of a residual CO_2 polar cap in the current obliquity of Iapetus. *Voyager* arrived at Iapetus in 1980 and 1981

during northern spring for Iapetus, and the highest value for bolometric Bond albedo of 0.40 suggests a lack of a residual carbon dioxide polar cap and no detectable seasonal cap (Squyres *et al*., 1984; Blackburn *et al*., 2010; 2011), as CO_2 transport would produce a pristine layer of pure carbon dioxide. Palmer and Brown (2008) also find a residual or seasonal CO_2 cap to be unlikely. Thus, the values from Table 5.2 for the mass flux leaving the polar boundary provide an upper limit on the amount of CO_2 that can enter the polar region from sublimation in the dark material to prevent polar cap formation. This strict upper limit will guide future models for CO_2 transport.

5.5.2 Remaining Candidates

In light of our elimination of dry ice as a candidate, other forms must be considered. Carbon dioxide clathrate is also an unlikely candidate given that the clathrate complex is dominated by H_2O; if clathrate were the form, it is expected that the CO_2 absorption feature would also be present in the bright terrain, yet there is no such indication. Palmer and Brown (2011) performed a series of experiments where they produced carbon dioxide by ultraviolet photolysis in order to determine hypothetical formation rates for Iapetus; the carbon dioxide they produced was trapped in amorphous solid water ice. They concluded that it was not a plausible situation for the surface of Iapetus due to the same dilemma of lack of signal in the bright terrain, as well as the fact that the spectra shows no signs of amorphous ice on the surface (Clark *et al*., 2011). The more likely surface arrangement is complexed, which increases the stability to the lifetime of the solar system (Palmer and Brown, 2008). As noted by Clark *et al*. (2008) and Cruikshank *et al*. (2010), the CO_2 band is also strong in the spectra of Phoebe, Hyperion, and Dione and weakly visible in the spectra of Mimas, Rhea, and Tethys.

Since Phoebe's dark surface also has a carbon dioxide signature, it is indeed possible that the contents of the Phoebe ring or alternative source for the exogenic seeding of Iapetus already contained a complexed species of carbon dioxide that could be stable over the lifetime of the solar system. Also, the presence of a CO_2 adsorption feature on the surfaces of Ganymede and Callisto (McCord *et al*., 1998; Hibbitts *et al*., 2000, 2002, 2003), which reach temperatures approaching ~160 K, strongly argues that the CO_2 there is complexed with materials on the surface.

Subsurface carbon dioxide is also a viable alternative that would increase its stability. Palmer (2010) showed that carbon dioxide could be shielded by grains from ultraviolet dissociation yet still penetrable by infrared and detectable by VIMS. Buratti *et al*. (2005) suggested that cosmic rays could be the source for CO_2 production inside the overburden or beneath it at the carbon/water ice interface. Alternatively, a native carbon dioxide layer or impurity within the ice under the overburden (such as in the form of clathrate) could also provide a source. Carbon dioxide diffusing through an overburden would be in the Knudsen regime, which hinders the kinetics by several orders of magnitudes and would be well below our established upper bound here. As the molecules diffuse through the overburden to the surface, a portion of them would tend to adsorb temporarily on or near the surface and might then be detectable by VIMS.

5.6. Conclusions

We have shown that surface dry ice is not a plausible candidate for the signal detected in the dark material on Iapetus. Thus, the carbon dioxide must be in a different form. We have also set an upper limit on the amount of CO_2 that can enter the polar cap in order to prevent polar cap formation, which should constrain future models. The

authors contend that carbon dioxide in the dark terrain is most likely either complexed or in the subsurface, yet the exact form remains a mystery. We therefore recommend more experiments to attempt to produce the complexed CO_2 in the laboratory given the current predicted ingredients available on the surface of Iapetus (carbon, water ice, possibly hematite) and measure the reflectance spectra of the produced samples.

5.7. References

Blackburn, D.G., Bryson, K.L., Chevrier, V.F., Roe, L.A., White, K.F., 2010. Sublimation kinetics of CO_2 ice on Mars. Planetary and Space Science, 58, 780-791.

Blackburn, D.G., Buratti, B.J., Ulrich, R., 2011. A bolometric Bond albedo map of Iapetus: Observations from *Cassini* VIMS and ISS and *Voyager* ISS. Icarus, 212, 329-338.

Buratti, B.J., and 28 co-authors, 2005. *Cassini* Visual and infrared mapping spectronomer observations of Iapetus: Detection of CO_2. The Astrophysical Journal, 622, L149-L152.

Byrne, S., Zuber, M.T., Neumann, G.A., 2008. Internannual and seasonal behavior of martian residual ice-cap albedo. Planetary and Space Science. 56, 194-211.

Clark, R.N., and 11 colleagues, 2008. Compositional mapping of Saturn's satellite Dione with Cassini VIMS and the implications of dark material in the Saturn system. Icarus 193, 372–386.

Clark, R.N., and 10 colleagues, 2011. The composition of Iapetus: Mapping results from Cassini VIMS. Icarus, submitted for publication.

Chan, W.F., Cooper, G., Brion, C.E., 1993. The electronic spectrum of carbon dioxide: Discrete and continuum photoabsorption oscillator strengths (6-203 eV). Chemical Physics 178, 401-413.

Cruikshank, D.P. and 26 co-authors, 2008. Hydrocarbons on Saturn's satellites Iapetus and Phoebe. Icarus, 193, 334-343.

Cruikshank, D.P. and 17 co-authors, 2010. Carbon dioxide on the satellites of Saturn: Results from Cassini VIMS investigation and revisions to the VIMS wavelength scale. Icarus, 206, 561-572.

Giauque, W.F., Egan., C.J., 1937. Carbon dioxide; the heat capacity and vapor pressure of the solid; the heat of sublimation; thermodynamic and spectroscopic values of the entropy. Journal of Chemical Physics 5, 45-54.

Hibbitts, C.A., McCord, T.B., Hansen, G.B., 2000. Distributions of CO_2 and SO_2 on the surface of Callisto. J. Geophys. Res. 105 (E9), 541–557.

Hibbitts, C.A., Klemaszewski, J.E., McCord, T.B., Hansen, G.B., Greeley, R., 2002. CO2- rich impact craters on Callisto. J. Geophys. Res. 107 (E10), 14-1–12.

Hibbitts, C.A., Pappalardo, R.T., Hansen, G.B., McCord, T.B., 2003. Carbon dioxide on Ganymede. J. Geophys. Res. 108 (E5), 2-1–22.

Lebofsky, L.A., 1975. Stability of frosts in the solar system. Icarus, 25, 205-217.

Lewis, B.R., Carver, J.H., 1983. Temperature dependence of the carbon dioxide photoabsorption cross section between 1200 and 1970 A. J. Quant. Spectrosc. Radiat. Transfer 30, 297-309.

McCord, T.B., and 13 colleagues, 1998. Non-water–ice constituents in the surface material of the icy Galilean satellites from the Galileo near-infrared mapping spectrometer investigation. J. Geophys. Res. 103 (E4), 8603–8626.

Palmer, E.E. and R.H. Brown, 2007. A possible trace carbon dioxide polar cap on Iapetus. The Astrophysical Journal, 666, L125-L128.

Palmer, E.E. and R.H. Brown, 2008. Stability and transport of carbon dioxide on Iapetus Icarus, 195, 434-446.

Palmer, E.E., 2010. The Shielding Effect of Small Regolith Grains on Photodissociation of Carbon Dioxide. DPS meeting #42, #9.04.

Palmer, E.E. and R.H. Brown, 2011. Production and detection of carbon dioxide on Iapetus. Icarus, in press, doi: 10.1016/j.icarus.2010.12.007.

Rivera-Valentin, E.G., D.G. Blackburn, and R. Ulrich, 2011a. Revisiting the thermal inertial of Iapetus: Clues to the thickness of the dark material. *Icarus*, submitted.

Rivera-Valentin, E.G., D.G. Blackburn, R. Ulrich, and L.A. Roe, 2011b. On the current global water ice stability of Iapetus, unpublished manuscript.

Shemansky, D.E., 1972. CO_2 extinction coefficient 1700-3000 A. Journal of Chemical Physics 56, 1582-1587.

Spencer, J.R. and Denk, T., 2010. Formation of Iapetus' extreme albedo dichotomy by exogenically triggered thermal ice migration. Science 327, 432-435.

Squyres, S.W., Buratti, B.J., Veverka, J., Sagan, C., 1984. Voyager photometry of Iapetus. Icarus 59, 426-435.

Verbiscer, A. J., Skrutskie, M. F., Hamilton, D. P., 2009. Saturn's largest ring. Nature. 461**,** 1098.

Woods, T.N., Rottman, G.J., Bailey, S.M., Solomon, S.C., 1998. Solar extreme ultraviolet irradiance measurements during solar cycle 22. Solar Physics 177, 133-146.

CHAPTER 6

CONCLUSIONS AND FUTURE WORK

6.1 Conclusions

The differences between sublimation kinetics of CO_2 ice on Mars and Iapetus is linked mainly to the vast differences in atmospheric pressure. In our martian simulation chamber, we found an energy limitation of heat transfer from infrared radiation and conduction from the atmosphere to be the profound driver of the rates, while on Iapetus, where a vacuum is present, the driver appears to be temperature of the surface in accordance to the Hertz-Knudsen-Langmuir (HKL) evaporation equation. In our martian chamber, the HKL equation predicted significantly higher rates than what was observed (many orders of magnitude too high); yet a heat-transfer limited model described the kinetics most accurately. However, on Iapetus, where conditions are much closer to a vacuum, the kinetics from HKL plus our additional correction factor (Rivera-Valentin *et al*. 2011) provide a better approximation for the rate.

At the current obliquity of Mars, the southern summer is much longer than the northern summer, which adds a greater strain on the long-term stability of the southern cap compared its northern counterpart. We found that the solar insolation striking the southern hemisphere of Mars is too large to sustain the current cap over long periods of time unless opacity is a driving force. While Schmidt *et al*. (2009) found an albedo control of the martian surface, we find that albedo control alone is not sufficient to prevent cap loss. Thus, we determined that the current regime for the martian polar residual cap is unstable, as the cap is currently losing 0.4 meters per martian year in depth. Therefore, unless the system is controlled by local weather activity that affects the

atmospheric opacity (from small-scale dust storms), the martian residual cap will be gone in 6-7 martian years. However, the values used for optical depth from Chapter 2 of 0.3 were from an unusually dust-free span of three years; estimates for the average value range between 0.5-0.6 for the polar caps. Thus, this scenario whereby we are allowed to observe the complete loss of the southern martian residual cap seems unlikely, so a weather-controlled regime is probable.

On Iapetus, we discovered that the phase integrals for the leading hemisphere and trailing hemisphere differ in slope when compared to geometric albedos for the same material or region. Though our results clearly show that the phase integral is closely tied to the geometric albedo, remaining deviations in slope are inherent more in the texture or macroscopic roughness of the material rather than the albedo. We also discovered that the phase integrals are lower than previous estimates, though some of this difference is due to the fact that we included the opposition surge in our measurement.

We produced the first bolometric Bond albedo map for Iapetus, which has a range of albedo from 0.015 ± 0.012 to 0.40 ± 0.07, that can be used by future thermal modelers. We also found that the bolometric Bond albedo is significantly lower than previous estimates (Palmer and Brown, 2008), and this change translates into higher sublimation rates for volatiles on the surface (including both water and carbon dioxide). Concurrently, we showed that resolution plays a key factor in determining albedo for Iapetus, especially in the border terrains.

Unfortunately, infrared spectrometry coverage of the northern hemisphere at 4.26 microns is lacking, and thus no CO_2 polar cap has been confirmed on Iapetus. In terms of a hypothetical polar cap, we found that a current seasonal or residual cap on Iapetus is

unlikely due to the visual albedo from the *Voyager* flybys and high sublimation rates. We developed an upper limit on the amount of CO_2 that can enter the polar region without forming a cap and also used proof by contradiction to narrow the list of candidates for the dark material, effectively demonstrating that the detected CO_2 adsorption signal cannot be dry ice.

6.2 Future Work

Now that it has been shown that dry ice is not sublimating from the dark material on Iapetus, it leaves open the question as to what is the source. Future work here entails exploring the kinetic possibilities of clathrate hydrates and subsurface CO_2 models in order to find the most likely source of the CO_2 detected by *Cassini* VIMS. We will also explore various chemical compositions that complex CO_2. Yet, even if the molecule is thermodynamically stable under the full temperature and pressure range of Iapetus over the lifetime of the solar system, there are still problems with the long-term stability of surface CO_2 due to photolysis from ultraviolet rays, requiring at least some current production mechanism (Palmer and Brown, 2011).

My colleague Edgard Rivera-Valentin is currently producing a sublimation and volatile transport model for water ice (Rivera-Valentin *et al*., 2011) in order to better constrain the contribution of thermal segregation on Iapetus (Spencer and Denk, 2010) versus exogenic deposition (Verbescer, 2009), and I am a contributor to that project. We will be collaborating with Daniel Tamayo and Dr. Joe Burns from Cornell who have developed an exogenic model that describes the depths of exogenic material spatially. Once their team has *Hershel* results constraining the particle size distribution of the Phoebe ring, we will combine our models to produce the most accurate description of the

processes behind the current albedo dichotomy since this new model will combine our bolometric Bond albedo map, a thermal inertia map, and *Hershel* observations of the extent of particles available to coat the leading hemisphere of Iapetus.

Expanding carbon dioxide transport to small bodies, I will also be working on sublimation and volatile transport models for the asteroid Vesta starting in August 2011 at NASA's Jet Propulsion Lab through the NASA Postdoctoral Program. Though most of the volatiles will be water ice, CO_2 could be a component if protected for extended periods of time inside a shaded crater region and then transformed into a volatile during short time periods in the orbit and rotation of the asteroid. A major component of the project is also to describe macroscopic roughness and compaction state of the surface with a model that can provide the effects of roughness for features that are below the resolution limit of the camera (Buratti, *et al*., 2006) and also using similar methodology as in Blackburn *et al*. (2010) and Chapter 3.

6.3 References

Blackburn, D.G., Buratti, B. J., Ulrich, R., and J. A. Mosher, 2010. Solar phase curves and phase integrals for the leading and trailing hemispheres of Iapetus from the *Cassini* Visual Infrared Mapping Spectrometer. Icarus 209, 738-744.

Buratti, B. J. et al. 2006. Titan: preliminary results on surface properties and photometry from VIMS observations of the early flybys. Planet. & Space Sci. 54, 1498-1509.

Palmer, E.E. and R.H. Brown, 2008. Stability and transport of carbon dioxide on Iapetus Icarus, 195, 434-446.

Palmer, E.E. and R.H. Brown, 2011. Production and detection of carbon dioxide on Iapetus. Icarus, in press, doi: 10.1016/j.icarus.2010.12.007.

Rivera-Valentin, E.G., D.G. Blackburn, R. Ulrich, and L.A. Roe, 2011. On the current global water ice stability of Iapetus, unpublished manuscript.

Schmidt, F., DoutÈ, S., Schmitt, B., Vincendon, M., Bibring, J.-P., Langevin, Y., 2009. Albedo control of seasonal South Polar cap recession on Mars. Icarus. 200(2), 374-294.

Spencer, J.R. and Denk, T., 2010. Formation of Iapetus' extreme albedo dichotomy by exogenically triggered thermal ice migration. Science 327, 432-435.

Verbiscer, A. J., M. Skrutskie, Hamilton D., 2009. Saturn's largest ring. Nature 461, 1098-1100.